INFORMATION TO USERS

This manuscript has been reproduced from the microfilm master. UMI films the text directly from the original or copy submitted. Thus, some thesis and dissertation copies are in typewriter face, while others may be from any type of computer printer.

The quality of this reproduction is dependent upon the quality of the copy submitted. Broken or indistinct print, colored or poor quality illustrations and photographs, print bleedthrough, substandard margins, and improper alignment can adversely affect reproduction.

In the unlikely event that the author did not send UMI a complete manuscript and there are missing pages, these will be noted. Also, if unauthorized copyright material had to be removed, a note will indicate the deletion.

Oversize materials (e.g., maps, drawings, charts) are reproduced by sectioning the original, beginning at the upper left-hand corner and continuing from left to right in equal sections with small overlaps.

Photographs included in the original manuscript have been reproduced xerographically in this copy. Higher quality 6" x 9" black and white photographic prints are available for any photographs or illustrations appearing in this copy for an additional charge. Contact UMI directly to order.

Bell & Howell Information and Learning
300 North Zeeb Road, Ann Arbor, MI 48106-1346 USA
800-521-0600

Optical Multisensors Based on Surface Plasmon Resonance

by

Timothy Mark Chinowsky

A dissertation submitted in partial fulfillment of the
requirements for the degree of

Doctor of Philosophy

University of Washington
2000

Department of Electrical Engineering

In presenting this dissertation in partial fulfillment of the requirements for the Doctoral degree at the University of Washington, I agree that the Library shall make its copies freely available for inspection. I further agree that extensive copying of the dissertation is allowable only for scholarly purposes, consistent with "fair use" as prescribed in the U.S. Copyright Law. Requests for copying or reproduction of this dissertation may be referred to Bell and Howell Information and Learning, 300 North Zeeb Road, P.O. Box 1346, Ann Arbor, MI 48106-1346, to whom the author has granted "the right to reproduce and sell (a) copies of the manuscript in microform and/or (b) printed copies of the manuscript made from microform."

Signature 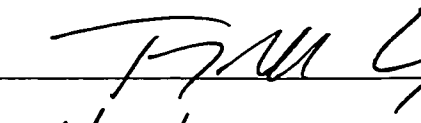

Date 11/29/00

University of Washington
Graduate School

This is to certify that I have examined this copy of a doctoral dissertation by

Timothy Mark Chinowsky

and have found that it is complete and satisfactory in all respects,
and that any and all revisions required by the final
examining committee have been made.

Chair of Supervisory Committee:

Sinclair Yee

Reading Committee:

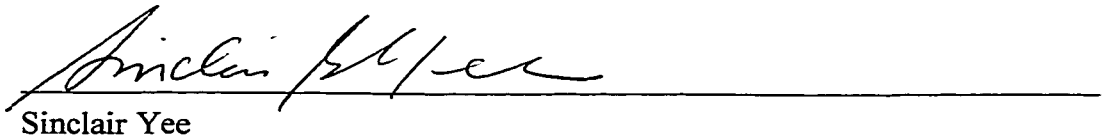

Sinclair Yee

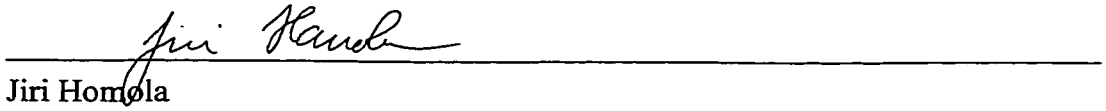

Jiri Homola

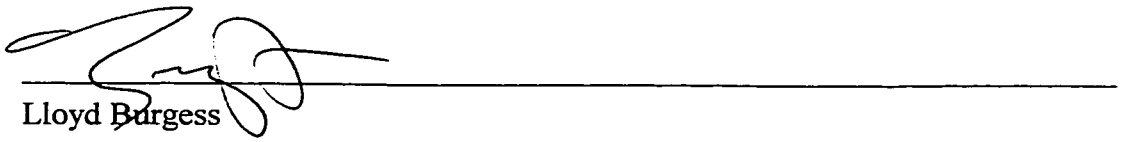

Lloyd Burgess

Date: Nov. 21, 2000

University of Washington
Abstract

Optical Multisensors Based on Surface Plasmon Resonance
by Timothy Mark Chinowsky

Chairperson of the Supervisory Committee
Professor Sinclair S. Yee

Department of Electrical Engineering

Biosensors based on surface plasmon resonance (SPR) detect biological substances through changes in the refractive index (RI) at the sensor surface. We present two optical multisensors designed to improve the robustness of SPR sensing.

Bulk RI interference is a serious drawback of SPR sensing. It has limited the application of SPR to laboratory experiments in which the bulk RI is kept constant. An SPR instrument can solve the problem of bulk RI effects by simultaneously measuring both the SPR response and the bulk RI of the analyte. In our SPR/internal reflection refractometry (IRR) sensor, the bulk RI is measured by critical angle refractometry. In experiments which investigated the ability of the instrument to compensate for bulk effects due to solution composition and temperature, The instrument was found to eliminate 85% to 99% of bulk RI interference.

The SPR/IRR sensor must make high quality measurements of surface RI and bulk RI to realize the benefits of critical angle compensation. These measurements are performed under difficult conditions: the functionalized SPR sensor surface is prone to drift, and the sensor's cost must be minimized. We describe data analysis and calibration techniques which use linear algorithms combined with calibration measurements to produce high quality data under these circumstances.

The SPR/IRR instrument demonstrates that a sensor which combines two sensing techniques can produce more robust measurements than an instrument which relies upon a single technique. We present a new SPR sensor which retains and enhances this multisensing capability in a streamlined configuration. The sensor is based on capillary tubes internally coated with gold. A focused laser beam strikes the capillary

radially and is reflected from the interior surface at a range of angles. The reflected light is then intercepted by an array detector. The versatile optics of capillaries allow the implementation of several types of optical sensing, including critical angle measurement of bulk RI.

Theory, modeling, fabrication, and characterization techniques for SPR capillary sensors are presented. Two techniques for depositing gold in capillaries were found to produce gold layers usable for SPR sensing.

Table of Contents

Page

List of Figures

Number Page

Acknowledgements

I would like to thank my advisor, Sinclair Yee, for the support, freedom, and respect he has given me throughout the work which is described in this dissertation. His well-grounded nature and his dedication to the advancement and well-being of his students are inspirations to me as I consider a career in academia.

I am grateful to my funding sources, the University of Washington Sea Grant Program and Texas Instruments, Inc., for their interest in my research. The Sea Grant/TI Industrial Fellowship jointly funded by these two organizations supported both me and my research; this work could not have been done without it. I look forward to continued contact with these groups.

I am thankful to the many colleagues with whom I have shared enthusiasm. At TI, Jose Melendez, Jerry Elkind, Dwight Bartholomew, Anita Strong, and Andreas Hühmer were a pleasure to work with. In the department of Medical Genetics at UW, Clem Furlong, Scott Jorgensen-Soelberg, Thomas Notides, and Alexei Naimushin have been invaluable collaborators. In the Chemistry department, Charles Campbell, Linda Jung, Hongbo Lu, and Jennifer Shumaker-Perry have likewise been excellent resources. I am grateful to them, and to my fellow students in EE, Kyle Johnston, Garet Nenninger, and Mimi Mar, for teaching me new things.

I thank my committee: Paul Yager, Norman McCormick, Jiri Homola, Lloyd Burgess, and Sinclair, for their time, interest, and contributions towards improving this dissertation.

I would like to thank my parents, Heather and Stanley Chinowsky, my in-laws, Claudia and Bill Anderson, and all of the friends and family who have provided support and babysitting throughout this work. I am very fortunate to have you.

Finally, thanks to my lovely wife Britt for her devotion, forebearance, and excellent prooffreading, and thanks to my son Max for being happy every morning.

Chapter 1: Introduction to surface plasmon resonance (SPR) biosensing

Biosensors combine a biological recognition element with a physical transduction mechanism to achieve a real-time measurement of biological processes [1]. Biosensors can be used to characterize biological reactions, investigate the mechanisms of biological processes, and detect and quantify the presence of biological compounds in samples of unknown composition. The development of biosensors for applications such as clinical and research medicine, drug development, environmental monitoring, industrial process control, food analysis, and military defense is rapidly expanding.

The specificity of a biosensor derives from its biological recognition elements, which are designed to bind the biochemical substance of interest in a manner that creates a measurable physical signal. Biosensors have been constructed using a variety of biological recognition elements, including antibodies, enzymes [2], whole cells [3], DNA [4], and biomimetic substances such as molecularly imprinted polymers.

The physical change which occurs upon binding is converted by the biosensor's transduction mechanism into a quantifiable electrical signal. Biosensor transduction mechanisms which have been employed include electrochemical techniques, mass-sensitive techniques such as the quartz crystal microbalance [5] and surface acoustic wave device, magnetic techniques [6], label-based optical techniques such as fluorescence [7] and chemiluminescence [8], and label-free optical techniques [9] based on surface-sensitive refractometric techniques such ellipsometry, waveguiding, Brewster angle reflectometry, resonant mirrors and surface plasmon resonance (SPR).

This dissertation describes research toward creating the ideal biosensor. This sensor would be (1) capable of universal detection; (2) highly sensitive; (3) able to perform robust measurements, independent of interfering influences; (4) simple in construction, (5) inexpensive to produce, and (6) portable.

This work concerns optical biosensors based on SPR. We believe that SPR is a promising technology for creating the ideal biosensor for the following reasons:

- SPR is an *optical* transduction method which is more resistant to electrical and mechanical interference than electrochemical and mass-sensitive techniques.
- SPR is a *label free* transduction method, which makes it capable in theory of almost universal detection of biological binding events. New applications of SPR can be developed without the need for labeling chemistries.
- SPR is relatively *sensitive*, capable of detecting small amounts of bound material.
- SPR is *simple* to implement - as will be seen below, SPR biosensors can be compact and inexpensive.

This chapter describes the basic SPR biosensing technique, the history and current practice of SPR biosensing, and surveys the applications which could benefit from the use of SPR. We then outline the limitations of the SPR technique which have restricted its application to date, and describe how we intend our research to assist in removing those limitations.

1.1. The basic SPR biosensing technique

The SPR technique detects bound substances through changes in the refractive index (RI) at the sensor surface. For this reason, SPR sensors are theoretically capable of nearly universal detection: Any binding or adsorption process creating a change in RI near the surface may be measured. (For simplicity, all such processes will be referred to as adsorption.)

The SPR sensing principle is illustrated in Fig. 1.1. The body of the sensor consists of a thin (~50 nm) layer of gold deposited onto a transparent optical substrate (typically a glass prism). Transverse-magnetic (TM) polarized monochromatic light reflects from the interface between the substrate and the analyte at a range of angles greater than the critical angle. The reflected light is then analyzed by the SPR instrument.

For certain angles of incidence, part of the incident energy will couple into a surface plasma wave traveling along the interface between the gold layer and the analyte. (The physics of this phenomenon will be discussed further in Chapter 2.) The loss of this energy is observed as a sharp attenuation of reflectivity. The angles at which this occurs vary with the RI of the analyte; therefore, one can measure this RI by

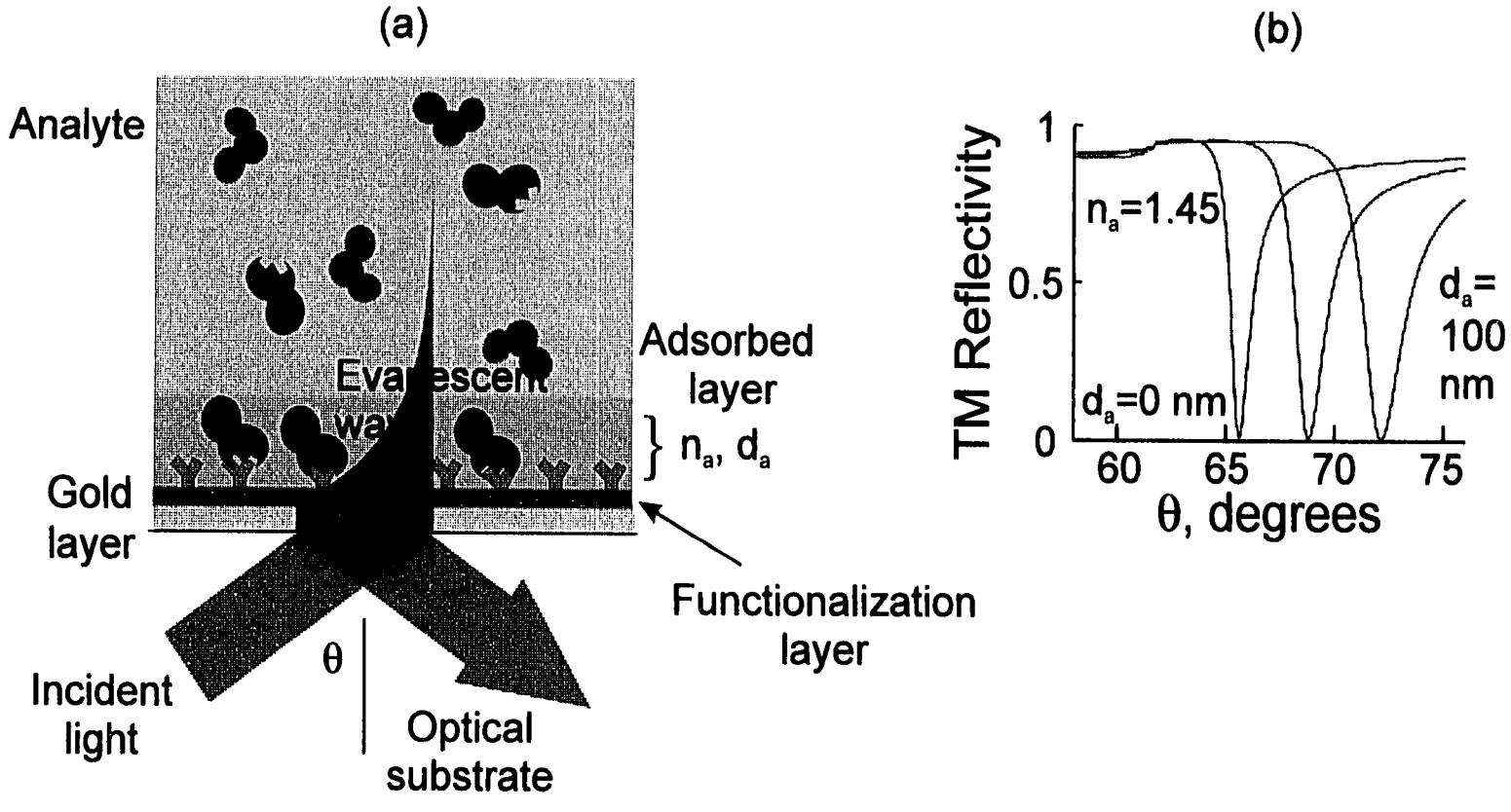

Figure 1.1. SPR sensing principle. (a) Sensing configuration. (b) SPR reflection spectra exhibit a dip in reflectivity which varies in location with the RI of the analyte close to the sensor surface. As a high-RI adsorbed layer (here modeled as a uniform layer of thickness d_a and RI n_a=1.45) increases in thickness, the dip moves to higher angles..

measuring the reflectivity across a range of angles and analyzing the resulting reflection spectrum.

Because the sensor probes the analyte with an evanescent wave, the sensor response depends only on the *surface RI* of the analyte -- the RI within several hundred nanometers from the sensor surface. This, together with the fact that the substance to be sensed (e.g. protein, RI ~ 1.57 [10]) has a different RI than the solution in which it is carried (e.g. water, RI 1.33), allows SPR to sense the adsorption of small amounts of that substance. To make the sensor respond preferentially to a specific substance, the gold surface is chemically functionalized with a biological recognition element, such that only the selected substance will bind. A typical biosensing experiment based on SPR might consist of the following steps:

1) Functionalize the SPR sensing surface with receptors which will specifically bind the desired substance.
2) Begin monitoring the SPR reflection spectrum.
3) Introduce the analyte to the sensor surface. Interpret changes in reflectivity to determine changes in the amount of material adsorbed to the sensor surface.
4) Rinse the sensor surface. Interpret changes in reflectivity to determine adsorbed layer thickness changes resulting from weakly (non-specifically) bound biomolecules being washed from the sensor surface.

1.2 History and current practice of SPR biosensing

The first recorded observation of the optical phenomenon now known as surface plasmon resonance was in 1902 by Wood, who observed reflectivity anomalies on metal-coated diffraction gratings that could not be explained by contemporary grating theory [11]. In an early, accidental observation of SPR in 1959, Turbandar [12] noted dips in reflectivity of an aluminum-coated prism. The practical exploitation of SPR began in earnest with Otto [13], who in 1968 first showed that SPR could be excited on flat metal surfaces using evanescent waves. In 1971, Kretchmann [14], proposed a robust configuration for the optical excitation of SPR and showed how the SPR phenomenon could be used to determine the thickness and optical properties of thin metal films. Because its simplicity, stability, and ease of construction, the

configuration used by Kretchmann became popular. The "Kretchmann configuration" is shown in Fig. 1.1; it remains the SPR configuration most often used for biosensing. The decade following the introduction of the Kretchmann configuration saw SPR used in the laboratory for the investigation of a wide range of phenomena regarding the optics of thin films. SPR was used to characterize metal layers, dyes, Langmuir/Blodgett self-assembled films, changes at electrode surfaces produced in electrochemical experiments [15], and changes in thin layers due to swelling from gas exposure [16]. These measurements were generally performed with experimental setups designed for accurate (but slow) measurement of reflectivity, allowing for detailed comparison of experiment with theory. In a typical experimental setup [16], the angle of incidence of a laser beam is mechanically scanned while the reflected light is measured and recorded.

The field of SPR biosensing began in 1983, when Liedberg, Lundstrom, and Nylander demonstrated that SPR could be used to observe biochemical reactions and quantify their kinetics [17]. In their landmark paper [18], they showed that SPR could quantify the progress of binding of human gamma globulin antibodies to gamma globulin immobilized on the silver-coated surface of a prism.

Their discoveries were commercialized by Pharmacia, who introduced an SPR research instrument named Biacore in 1990. The Biacore instruments (now manufactured by a Pharmacia spin-off named Biacore AB) are optimized for laboratory investigation of binding kinetics. In these instruments, reflected light is measured simultaneously across a range of angles using a converging light beam and a diode array detector, allowing measurements to be made much more quickly than in systems relying upon mechanical scanning. The instruments include an automated fluid handling system which uses a disposable microfluidic cartridge to produces sample injections with very low dispersion [19]. The SPR sensing surface is a gold-coated glass chip which is built into the microfluidic cartridge, and is provided by Biacore with a number of chemistries to allow different biochemical functionalization. In the most popular of these, a dextran matrix coating the gold film provides a structure designed to allow biorecognition elements to be immobilized in a quasi-aqueous environment, while simultaneously resisting non-specific adsorption [20]. The Biacore instruments are large benchtop devices costing over $100,000.

Since the introduction of the Biacore instrument, the number of publications regarding the application of SPR to biomedicine has increased dramatically every year (Fig. 1.2). Most of these publications describe research conducted using the Biacore instrument and its successors. A perusal of recent publications reveals a variety of applications. Researchers seeking to discover new drugs have used SPR to investigate low molecular weight substances which inhibit protein-protein interactions [21] and which bind to DNA [22]. Researchers seeking better control of drug absorption in humans have examined drug dissemination in the intestine [23] and bloodstream [24], using SPR to examine the interaction of various drugs with liposomes and human serum albumin. SPR has been used to investigate various disease mechanisms, including binding of the external envelope protein of human immunodeficiency virus (HIV) with CD4 receptors [25], the interaction between HIV protease and drugs designed to inhibit that enzyme [26], investigation of the affinity of poliovirus for its cellular receptor [27], and the mechanism of toxicity for anthrax [28]. Researchers interested in the uses of SPR for clinical diagnosis have applied it to the detection of human serum antibodies against herpes simplex virus [29] and quantification of hemoglobin in bodily fluids [30]. Others have used SPR to better understand physiologic processes, such as the interaction between steroids and antisteroid antibodies [31], and the role of treponin I mutant proteins in certain types of heart disease [32].

The growing success and demonstrated versatility of Biacore in biomedical applications has stimulated interest in SPR as a biosensing technique, and has given rise to efforts to apply it to a greater range of biosensing applications, both inside and outside the laboratory. The direct and simple nature of SPR sensing has led researchers to investigate the use of SPR to replace other biosensing methods. For instance, pharmaceutical companies are interested in expanding the capabilities of SPR to apply it to applications which screen large numbers of compounds for beneficial properties [33, 34]. SPR biosensors are attractive in the field of medical diagnostics [1, 35] or replacing conventional label-based methods of measuring biological events (such as radioimmunoassay and enzyme immunoassays) and, ultimately, for providing a wide range of diagnostic tests which can be performed at home, similar to existing blood glucose monitors and home pregnancy tests. Outside the laboratory, there is a need for biosensors in environmental testing, such as in the detection of pesticides [36,

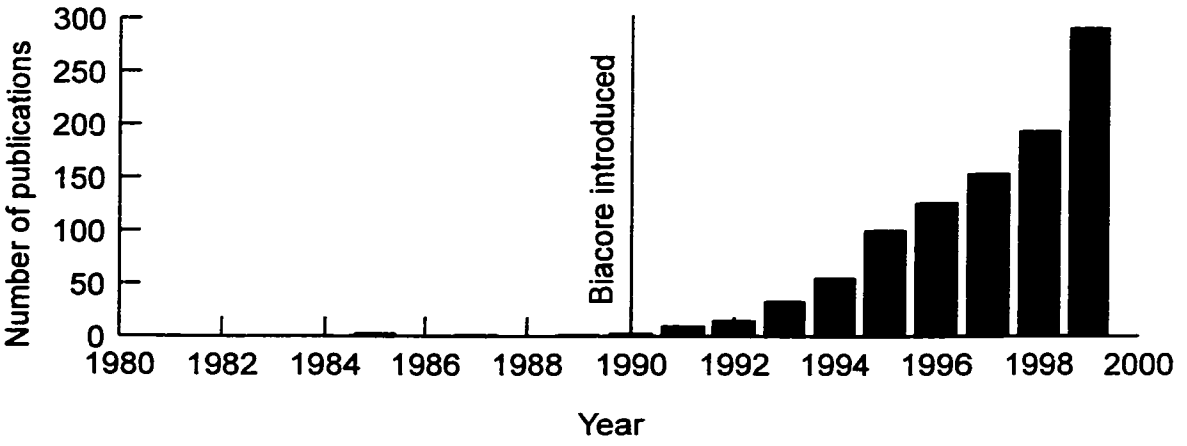

Figure 1.2. Rate of biomedical SPR publishing. Results were obtained from the Medline database using a search for the keyword "plasmon."

37] and industrial pollutants both on land [38] and in marine environments [39]. The possibility of biological warfare and the proliferation of land mines and other unexploded ordnance on land and in the sea have stimulated military interest in biosensor systems for rapid, sensitive detection of biowarfare agents [40, 41] and explosives [42, 43]. Increasing awareness of the dangers of food-borne pathogens such as *E. coli* O157:H7 has led to work on biosensors for detecting such organisms [44].

A simple classification of the range of possible biosensor applications is suggested by the cartoon of Fig. 1.3. We have separated applications based on the number of locations where the sensing is performed and on the number of tests which are performed in each location each day. This figure illustrates the requirements of various biosensing applications relative to the present capabilities of SPR.

To date, the biomedical research performed by users of the Biacore and similar laboratory-based SPR devices represents the only commercial application of SPR. These instruments are large, expensive, and tied to the laboratory, and so are used in relatively few locations. In addition, because experiments must be performed one at a time, and the cost of the sensor's disposable element (the fluidic cartridge) is high, the Biacore is impractical for high-throughput applications.

1.3. Limitations of SPR

Figure 1.3 shows that at present the applications of SPR are limited to one small corner of the total need for biosensors. Some of the factors limiting the application of SPR are related to the limited commercially available instrumentation; other factors are more inherent to the SPR technique. Instrumental factors include:

Cost. If a sensor is to be applied in many locations simultaneously, the instrument should be inexpensive. If many tests are to be performed with a given instrument, any consumable components of the sensor should also be inexpensive.

Size. If the sensing instrumentation is to be portable, so that samples can be analyzed in place rather than transported to a laboratory, the instrument must be small.

Throughput. If many measurements must be performed in a given day, the sensor must either perform measurements quickly or perform a large number of measurements in parallel.

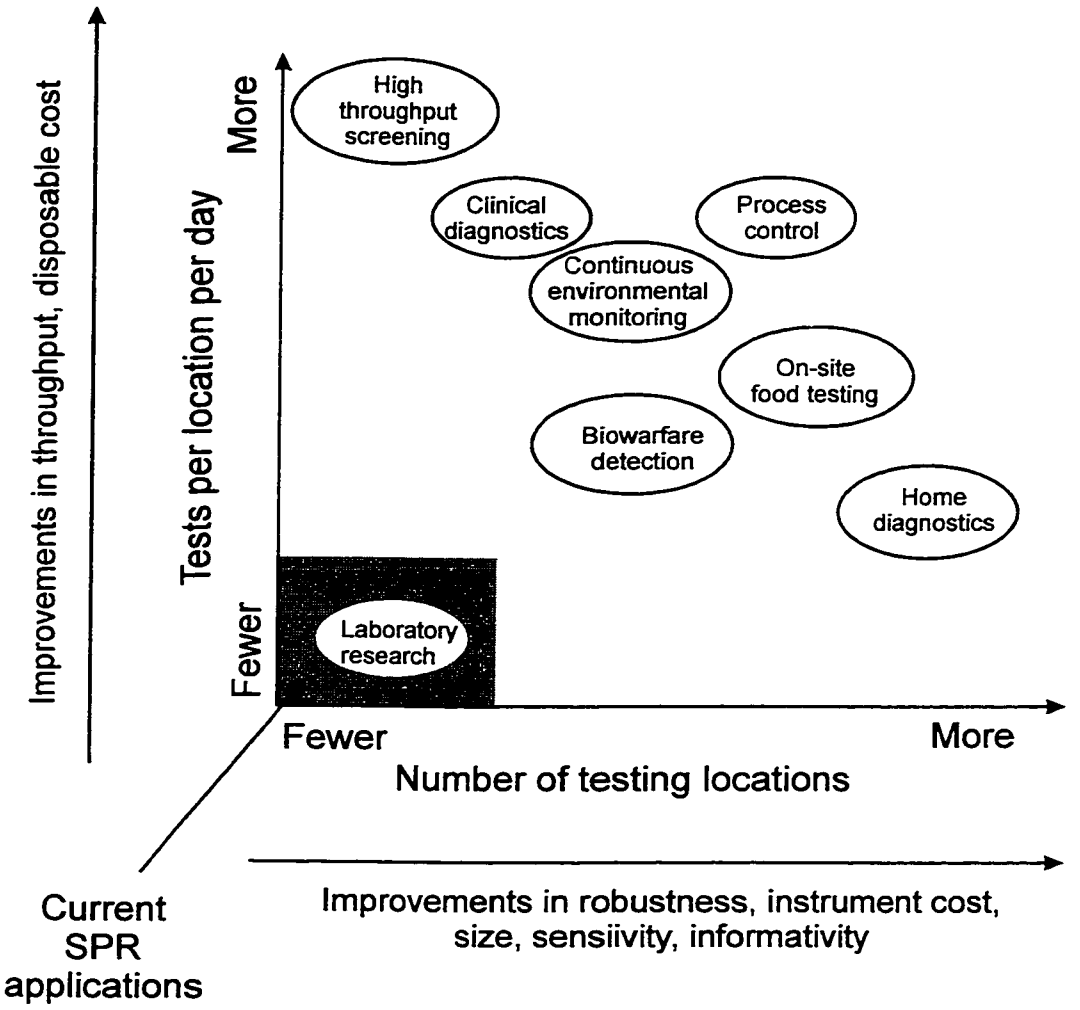

Figure 1.3. Potential SPR sensing applications. Applications are classified by the number of locations at which testing is to be performed and by the number of tests per day which are to be performed at a given location. The improvements in SPR technique which could expand the application of SPR from its current state are listed along each axis.

Limiting factors more inherent to the SPR technique include the following:

Informativity. SPR measurements indicate the amount material adsorbed to the sensor surface. No additional information about the composition of the material is available.

Robustness. The SPR technique is vulnerable to interference from two main sources: non-specific binding and bulk RI effects.

Interference from non-specific binding results from imperfections in the sensor's biological functionalization. Ideally, the substance of interest would completely bind to the sensor surface, while other substances would not bind at all. Deviations from this ideal behavior will result in other substances binding to the sensor and causing an SPR response.

Interference from bulk RI effects can occur because an SPR sensor responds to any RI changes within its sensing range. This range (~500 nm) is greater than the thickness of most adsorbed films of interest. Therefore, the SPR sensor will also respond to changes in the RI of the bulk analyte adjacent to the adsorbed film. The observed sensor response is thus a combination of the desired adsorption response and interference from bulk RI variations. In biosensing, the analyte is typically an aqueous solution containing biologically active molecules. If the temperature or chemical composition of this solution changes, its RI will change. (For example, the RI of water decreases 8×10^{-5} for every degree C increase in temperature [45].) The sensor's response to this change can easily exceed the response resulting from binding of biomolecules.

Sensitivity. Although SPR is sensitive for a RI-based biosensing technique, it is currently not sensitive enough for applications such as detection of bacteria which are pathogenic in very low numbers, and it is not as sensitive as label-based techniques such as fluorescence and chemiluminescence, which achieve very high sensitivity due to the availability of electronic devices such as photomultipliers and CCDs, which can measure very low light levels.

1.4. Current research in SPR

Much of the current research in SPR technology is aimed at overcoming these limitations of SPR. Throughput issues are being addressed by research in SPR

microscopy [46] which allows the monitoring of biochemical interactions simultaneously at many points on the sensor surface. When combined with patterned functionalization chemistry, such an instrument can perform many sensing experiments at once. Increases in the informativity of SPR measurements are pursued by researchers who combine SPR measurements at different wavelengths [47] or who use waveguide modes combined with SPR [48] to gain information about the morphology of adsorbed layers. So-called "hyphenated" techniques, which combine SPR with other analytical techniques such as high-performance liquid chromatography (HPLC) [49] or capillary electrophoresis (CE) [50] enable the composition of the analyte to be analyzed with more specificity than with SPR alone. Increases in the sensitivity of SPR are being pursued through optical refinements of the SPR technique such as interferometric detection of SPR [51] and long-range SPR [11], and also through investigation of chemical ways to amplify the SPR signal through secondary binding of substances such as gold colloid [52]. Efforts to reduce the size of SPR sensors have led to several novel sensing configurations, including the ultraminiature fiber-optic SPR probe developed by Jorgenson and Yee [53] and single mode fiber [54] sensors and planar probe sensors [55]. Researchers have sought to improve the robustness of SPR sensors by investigating compensation for non-specific binding and bulk RI effects [56] and by improvements in functionalization chemistry [57].

Researchers concerned about low cost have investigated SPR devices based on integrated optics to take advantage of the potential cost advantages of integrated fabrication techniques. [58] Johnston *et al.* showed that a chemometric approach to SPR data analysis and calibration allowed simpler and therefore less expensive instrumentation to be used in an SPR sensor [59].

A breakthrough was made in low-cost SPR sensing when Texas Instruments, Inc. (TI) in 1996 introduced a compact, rugged, very inexpensive SPR sensor. Because our collaboration with TI and our experience with their SPR sensor played a fundamental part in shaping this research, it will now be described in detail.

1.5. Taking SPR out of the corner: Spreeta, The TI SPR sensor

In 1996 a group at TI introduced a compact, rugged, integrated SPR sensor in which all sensor components are contained in one small molded package [60, 61].

This sensor, now called Spreeta, is the first commercial SPR sensor intended to be produced in very large quantities. This sensor, developed in conjunction with our group at the University of Washington, is depicted in Fig. 1.4a. The sensor consists of a prism molded to a hybrid microelectronic circuit contained on a printed circuit board (PCB). The circuit contains a light source and a linear diode array detector. The light source consists of an infrared LED, an aperture, and a plastic sheet polarizer. The light source emits a diverging beam that strikes the active sensor surface at a range of angle ranging from approximately 58° to 76°. Because the beam is divergent, a roughly elliptical region on the sensor surface is illuminated. This light reflects from the sensor surface and from the sensor's top mirror, and back onto the PCB. A portion of this light strikes a diode array detector mounted on the PCB. Because each detector pixel will collect light which struck the sensor surface at a different angle, a reflectivity vs. angle spectrum may be obtained by reading each detector pixel in turn. The optical compromises which enable this sensor to be produced for very low cost cause the sensor to have a complicated response relative to many laboratory SPR systems optimized for their match with theory. The LED light source approximates a monochromatic point source, but not particularly well: The emission spectrum of the LED bandwidth is 26 nm. This will cause the SPR spectral dip to be broader and not as deep as a spectrum measured using a true monochromatic light. This is shown in Figs. 1.4b-d. Fig. 1.4b shows SPR spectra predicted for monochromatic light sources of various wavelengths ranging from 750 to 920 nm, while Fig. 1.4c. shows an estimate of the LED emission spectrum. The observed SPR spectrum will effectively be a weighted average of the spectra of Fig. 1.4a, with each spectrum weighted according to the emission intensity at that wavelength.

Other optical complications exist. The polarizer is of relatively poor optical quality. The plastic prism is less transparent than a glass prism, and will have poorer surface quality. Because the active area on the sensing surface is large, any nonuniformity of analyte across the surface will cause corresponding nonuniformities in the spectrum. The active area of the sensor surface is defined by the location of the light source and detector relative to that surface; therefore, the exact location of the active area and the appearance of the reflectivity spectrum is likely to vary from sensor to sensor due to manufacturing tolerances. Finally, diffraction at the sensing surface will distort the reflectivity spectrum, further complicating the relationship between the

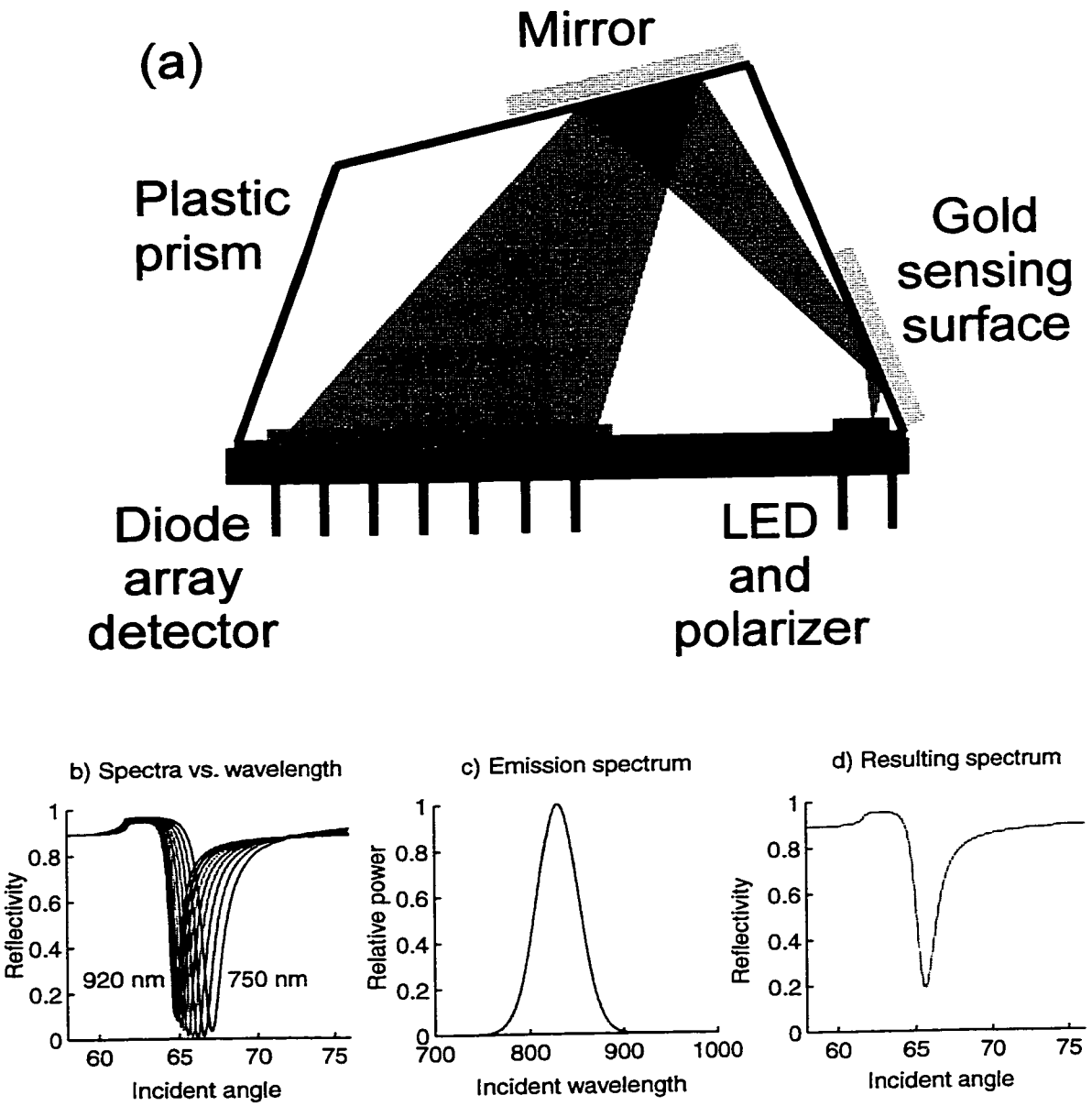

Figure 1.4. The TI SPR sensor. (a) Sensor construction. (b) Simulated SPR spectra for a range of wavelengths: 750 to 920 nm in steps of 20 nm. (c) Approximate emission spectrum of TI LED. (d) SPR spectrum resulting from weighted combination of wavelengths

measured spectrum and the actual reflectivity vs. angle characteristic of the sensor surface.

In spite of these complications, the Spreeta demonstrates good performance. Although the Spreeta at first had very poor resolution (with an RMS noise level of approximately 10^{-4} RI units [60]), subsequent improvements in sensor electronics and fabrication techniques resulted in dramatic improvements in resolution. A more recent report indicates a noise level of 5×10^{-6} [63], and improvements continue. At the time of this writing, the device is reported to be capable of delivering RMS noise levels as good as 3×10^{-7} RI units under some conditions [64] .

1.6. Goals of this research

The TI SPR sensor has gone a long way towards removing two of the factors restricting SPR to its corner of the biosensor market: cost and size. The low cost of the disposable sensor has the potential to increase the number of tests per day that can be practically performed. The increased number of applications which we believe may become practical using the TI SPR sensor is represented by the shaded area in Fig. 1.5a.

However, the throughput attainable using these single-channel devices stops short of that required for high throughput screening applications, and that most of the applications depicted in Fig. 1.5a will remain beyond the reach of the TI sensor as it presently exists. Even though the TI sensor has greatly reduced cost and size relative to other SPR devices, we believe that its use will continue to be confined to relatively few testing locations.

What are the limiting factors which remain? We believe the major limitation is robustness. To move a sensing technology out of a research laboratory means to move it into a less controlled environment containing more sources of interference. A more robust sensor is needed to operate under such circumstances. The goal of the research described in this dissertation is to improve the robustness of SPR sensing. We believe the key to achieving this goal is *multisensing* -- that is, combining SPR with other analytical and sensing techniques in ways which will allow the limitations of SPR to be removed and its advantages to be retained.

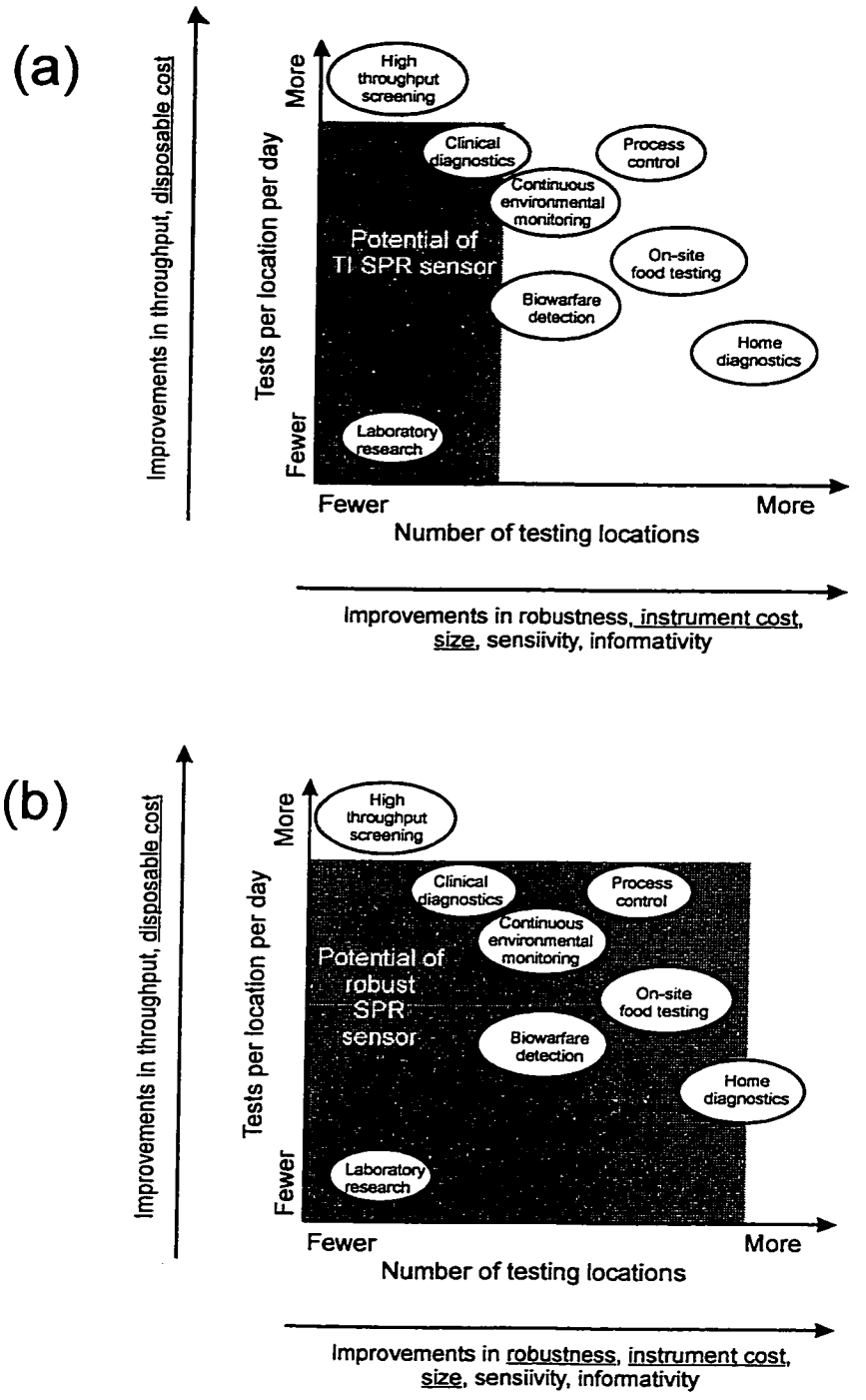

Figure 1.5. Expanding the application of SPR. (a) The low cost of the TI SPR sensor increases the number of tests than can be performed, but does not greatly increase the number of applications that can make use of SPR. (b) A robust, low-cost SPR sensor is needed to reach many applications.

In this dissertation we present two new SPR sensor designs based on this principle. The first, the SPR/internal reflection refractometry (SPR/IRR) sensor, greatly reduces the effects of bulk RI interference on SPR measurements by combining an SPR measurement with an independent measurement of bulk RI. The second, the capillary SPR sensor, explores a novel sensing geometry specifically designed for its potential for implementation of SPR/IRR and other multisensing combinations. We will now introduce these two sensors in more detail by describing their potential benefits and suggesting applications for which they may be suited.

1.7. The SPR/IRR sensor: A robust, low-cost SPR sensor

The SPR/IRR sensor uses a simple modication of the TI SPR sensor design to greatly reduce the effects of bulk RI interference. As described above, bulk RI interference results from changes in the temperature or chemical composition of an analyte which change its bulk RI. This change in RI is misinterpreted by the SPR sensor as a change in the adsorbed layer.

Bulk RI interference has limited the application of SPR to laboratory experiments in which the bulk RI is kept constant by controlling the temperature and composition of the analyte. If this limitation were overcome, SPR would be more applicable to many applications which call for biosensing in less controlled environments. Field-based biosensors, such as the automated airborne biosensor for biological warfare agent detection described by Ligler *et al.* [40] could be implemented using SPR if bulk RI interference due to temperature changes was eliminated. Marine applications, such as detection and monitoring of industrial chemicals and explosives are natural candidates for the use such a sensor -- bulk RI compensation could allow robust SPR measurements in the presence of naturally varying salt concentration and temperature that would otherwise render such measurements impossible. The low cost and small size of the sensor to be widely distributed, for instance to monitor the concentration of underwater contaminants or to map biological activity on the sea floor. The capability for low cost, distributed monitoring could also be useful in industrial process control.

In the laboratory, the bulk RI compensated SPR sensor would be useful in the study of systems in which surface activity is inherently inseparable from bulk RI effects (e.g. detergent adsorption [65]). The sensor would allow facile investigation of

the temperature dependence of chemical and biochemical binding processes such as the formation of thiol monolayers [66] and DNA hybridization [67]. An SPR sensor which can make robust measurements even when temperature is changing rapidly could study the kinetics of the polymerase chain reaction (PCR) [68, 69] with a freedom not now available.

These applications are those for which the bulk RI compensation ability of the SPR/IRR sensor is particularly needed. However, the low cost of the sensor could also make it practical for more general use, such as medical diagnostics in clinical laboratories or in the home. We envision a versatile SPR biosensing device analogous to the fluorescence-based device described by Meusel *et al.* [70] which would allow a wide array of diagnostic tests to be performed by untrained users. Because the technology of the SPR/IRR sensor is simpler and less expensive, our device could even have potential for home use.

However, the sensor will still not be useful for some applications. Bulk RI compensation remedies one of the limitations of SPR sensing, but leaves others untouched. A desire to further expand the applicability of SPR sensors led to the development of the second SPR sensor described in this dissertation, the capillary SPR sensor.

1.8. The capillary SPR sensor: A low-cost SPR multisensor

The SPR/IRR sensor has the potential to eliminate interference in SPR measurements due to bulk RI changes. However, interference due to nonspecific binding remains. Nonspecific binding of analyte components to the sensor surface can be reduced only through improvements in functionalization chemistry; there is a limit to how specific and how robust this chemistry can be. Similarly, the sensitivity of SPR, though good, is unlikely to compete with techniques such as fluorescence and mass spectrometry.

In our opinion, these limitations of SPR technique are more intractable than the problem of bulk RI compensation. Because of these limitations, biosensing applications requiring extreme sensitivity or robust performance in analysis of complex samples will remain beyond the reach of biosensors based on SPR alone. For this reason, we believe the ideal biosensor would use a combination of techniques for

sensitive analysis of complex analytes. For instance, separation technologies such as capillary electrophoresis or chromatography could render complex samples more palatable to an SPR sensor [71], and less universal, but more sensitive techniques (such as fluorescence) could be brought to bear if SPR alone was found to give inconclusive results.

At the same time, because the broad goals of the research is to allow SPR technology to be as widely disseminated as possible, we considered it to be essential that all research was compatible with the eventual production of a low-cost device.

These are the motivations behind the development of the capillary SPR sensor described in chapter 6 of this dissertation. In this sensor, SPR measurements are performed inside glass capillary tubes. The capillary simultaneously serves as an optical element and as a sample conduit and container. The capillary configuration provides for easy handling of liquid samples. Use of the capillary as a disposable optical element allows the sensing surface to be replaced easily and inexpensively. The inside diameter of the capillary tubes can range widely -- very large tubes could be used for process control applications where a large quantity of material is being prepared, and very small tubes can also be used. For instance, implementation of SPR sensing inside of the 75 μm inside diameter capillary tubes commonly used for CE should be possible. The small size and versatility of capillary SPR sensing may make it attractive for integration in portable systems for micro-total chemical analysis (μTAS) [72].

Because a wide array of analytical techniques other than SPR have been developed around the use of capillaries, implementation of capillary sensors using multiple techniques in addition to SPR would be possible. In addition to the IRR measurement which provides bulk RI compensation, measurement of fluorescence, Raman scattering, or UV absorption could be performed simultaneously with the SPR measurement. Use of SPR as an on-column detector for CE or microbore high-performance liquid chromatography (HPLC) could improve ability of SPR to analyze complex samples.

Because the detection apparatus for capillary SPR will be more complicated and expensive than that for the SPR/IRR sensor, we envision the capillary sensor used in laboratories and in field-based sensing applications such as biowarfare agent detection for which the additional capabilities of the capillary sensor are needed and for which

instrument cost is not a critical factor. However, while we anticipate that the cost of the capillary SPR instrument would be relatively high, the cost of the capillary sensing element itself, and therefore the per-test cost, would be as low or lower than that of the SPR/IRR sensor based on the TI sensing configuration. The simplicity and low cost of sample handling using capillaries has attracted other researchers to the use of capillaries for high throughput biochemical processes such as PCR. (The thermal properties of capillaries are also very attractive for this application [69].) For this reason, we believe that the capillary SPR sensor also has potential to address high-throughput applications which are now beyond the reach of current technology.

1.9. Dissertation overview

The remainder of this dissertation describes the theoretical and experimental work we have done in pursuit of the goals described in this chapter. Chapter 2 contains a short review of SPR sensing theory. Chapter 3 begins the description of the SPR/IRR sensing technique with a discussion of theory behind the technique and its capabilities and limitations. Chapter 4 describes the prototype instrument we have built to perform SPR/IRR sensing and presents the results of experiments performed with that instrument. Chapter 5 describes the special data analysis and calibration techniques which we have developed for the SPR/IRR instrument.

Chapter 6 of this dissertation is devoted to the capillary SPR sensor. We present a short history of capillary sensing and the basic theory which we have used to design our capillary SPR sensor. We describe techniques for fabricating the capillary sensing elements and apparatus built to characterize the capillaries and to perform SPR sensing. Experimental results demonstrating capillary SPR sensing is then presented.

The final chapter, Chapter 7, summarizes the results of the previous chapters and enumerates what we feel are the most significant advances to come out of this research. We then outline the problems that remain to be overcome to allow the new sensing technologies described here to reach their full potential.

Notes for Chapter 1

[1] T. Vo-Dinh and B. Cullum, Biosensors and biochips: advances in biological and medical diagnostics, *Fresenius J. Anal. Chem.* **366** (2000) 540-551.

[2] J. F. Liang, Y. T. Li, V. C. Yang, Biomedical application of immobilized enzymes, *J. Pharm. Sci.* **89** (2000) 979-990.

[3] C. Ziegler, Cell-based biosensors, *Fresenius J. Anal. Chem.* **366** (2000) 552-559

[4] Z. Junhai, C. Hong, and Y. Ruifu, DNA-based biosensors, *Biotechnology Advances* **15** (1997) 43-58.

[5] C. K. O'Sullivan and G. G. Guilbault, Commercial quartz crystal microbalances - theory and applications, *Biosens. Bioelectron.* **14** (1999) 663-670.

[6] L. Larsson, K. Kriz, and D. Kriz., Magnetic transducers in biosensors and bioassays, *Analusis* **27** (1999) 617-621.

[7] S. Y. Rabbany, B. L. Donner, and F. S. Ligler, Optical Immunosensors, *Crit. Rev. Biomed. Eng.*, **22** (1994) 307-346.

[8] H. Y. Aboul-Enein, R-I. Stefan, and J. F. Van Staden, Chemiluminescence-based (bio)sensors - an overview, *Crit. Rev. Anal. Chem.*, **29** (1999) 323-331.

[9] H-M Haake, A. Schutz, and G. Gauglitz, Label-free detection of biomolecular interaction by optical sensors, *Fresenius J. Anal. Chem.* **366** (2000) 576-585.

[10] L. S. Jung, C. T. Campbell, T. M. Chinowsky, M. N. Mar, and S. S. Yee, Quantitative interpretation of the response of surface plasmon resonance sensors to adsorbed films, *Langmuir* **14** (1998) 5636-5648.

[11] G. J. Sprokel and J. D. Swalen, Attentuated total internal reflection method, in *Handbook of Optical Constants of Solids II,* Academic Press, 1991.

[12] T. Turbadar, Complete adsorption of light by thin metal films, *Proc. Phys Soc. London* **73** (1959) 40-44.

[13] A. Otto, Excitation of nonradiative surface plasma waves in silver by the method of frustrated total reflection, *Z. Physik* **216** (1968) 398-410.

[14] E. Kretchmann, Die Bestimmung optischer Konstanten von Metallen durch Anregung von Oberflachenplasmaschwingungen, *Z. Physik* **241** (1971) 313-324.

[15] F. Abeles, T. Lopez-Rios, and A. Tadjeddine, Investigation of the metal-electrolyte interface using surface plasma waves with ellipsometric detection, *Solid State Commun.* **16** (1975) 843-847.

[16] C. Nylander, B. Liedberg, and T. Lind, Gas detection by means of surface plasmon resonance, *Sens. Act.* **3** (1982/83) 79-88.

[17] B. Liedberg, C. Nylander, and I. Lundstrom, Biosensing with surface plasmon resonance - how it all started, *Biosens. Bioelectron.* **10** (1995) i-ix.

[18] B. Liedberg, C. Nylander, and I. Lundstrom, Surface plasmon resonance for gas detection and biosensing, *Sens. Act. A* **4** (1983) 299-304.

[19] S. Sjolander and C. Urbaniczky, Integrated fluid handling system for biomolecular interaction analysis, *Anal. Chem.* **63** (1991) 2338-2345.

[20] B. Johnsson, S. Lofas, and G. Lindquist, Immobilization of proteins to a carboxymethydextran-modified gold surface for biospecific interaction analysis in surface plasmon resonance sensors, *Anal. Biochem.* **198** (1991) 268-277.

[21] B. A. Chrunyk, M. H. Rosner, Y. Cong, A. S. McColl, I. G. Otterness, and G. O. Daumy, Inhibiting protein-protein interactions: A model for agonist design, *Biochemistry* **39** (2000) 7092-7099.

[22] R. Gambari, G. Feriotto, C. Rutigliano, N. Bianchi, and C. Mischiati, Biospecific interaction analysis of low-molecular weight DNA-binding drugs, *J. Pharm. Experimental Therapeutics,* **294** (2000) 370-377.

[23] E. Danelian, A. Karlen, R. Karlsson, S. Winiwarter, A. Hansson, S. Lofas, H. Lennernas, and M. D. Hamalainen, SPR biosensor studies of the direct interaction between 27 drugs and a liposome surface: correlation with fraction absorbed in humans, *J. Med. Chem.* **43** (2000) 2083-2086.

[24] A. Frostell-Karlsson, A. Remaeus, H. Roos, K. Andersson, P. Borg, M. Hamalainen, and R. Karlsson, Biosensor analysis of the interaction between immobilized human serum albunin and drug compounds for prediction of human serum albumin binding levels, *J. Med. Chem.* **43** (2000) 1986-1992.

[25] D. G. Myszka, R. W. Sweet, P. Hensley, M. Brigham-Burke, P. D. Kwong, W. A. Hendrickson, R. Wyatt, J. Sodroski, and M. L. Doyle, Energetics of the HIV gp120-CD4 binding reaction, *Proc. Nat. Acad. Sci.* **97** (2000) 9026-9031.

[26] P-O. Markgren, Markku Hamalainen, and U. Helena Danielson, Kinetic Analysis of the interaction between HIV-1 protease and inhibitors using optical biosensor technology, *Anal. Biochem.* **279** (2000) 71-78.

[27] B. M. McDermott, A. H. Rux, R. J. Eisenberg, G. H. Cohen, and V. H. Racaniello, Two distinct binding affinities of poliovirus for its cellular receptor, J. Biol. Chem. **275** (2000) 23089-23096.

[28] J. L. Elliott, J. Mogridge, and R. J. Collier, A quantitative study of the interactions of *bacillus anthracis* edema factor and lethal factor with activated protective antigen, *Biochemistry* **39** (2000) 6706-6713.

[29] C. Wittekindt, B. Fleckenstein, K-H. Wiesmuller, B. R. Eing, and J. E. Kuhn, Detection of human serum antibodies against type-specifically reactive peptides from the N-terminus of glycoprotein B of herpes simplex virus type 1 and type 2 by surface plasmon resonance, *J. Virol. Meth.* **87** (2000) 133-144.

[30] S. Sonezaki, S. Yagi, E. Ogawa, A. Kondo, Analysis of the interaction between monoclonal antibodies and human hemoglobin (native and cross-linked) using a surface plasmon resonance (SPR) biosensor, *J. Immunol. Meth.* **238** (2000) 99-106.

[31] T. Kaiser, P. Gudat, W. Stock, G. Pappert, M. Grol, D. Neumeier, and P. B. Luppa, Biotinylated steroid derivatives as ligands for biospecific interaction analysis with monoclonal antibodies using immunosensor devices, *Anal. Biochem.* **282** (2000) 173-186.

[32] K. Elliott, H. Watkins, and C. S. Redwood, Altered regulatory properties of human cardiac troponin I mutants that cause hypertrophic cardiomyopathy, *J. Biol. Chem.* **275** (2000) 22069-22074.

[33] C. Williams, Biotechnology match making: screening orphan ligands and receptors, *Curr. Opin. Biotech.* **11** (2000) 42-46.

[34] K. A. Xavier, P. S. Eder, and T. Giordano, RNA as a drug target: methods for biophysical characterization and screening, *Trends. Biotech.* **18** (2000) 349-356.

[35] R-I. Stefan, J. F. Van Staden, and H. Y. Aboul-Enein, Immunosensors in clinical analysis, Immunosensors in clinical analysis, *Fresenius J. Anal. Chem.* **366** (2000) 659-668

[36] J. L. Marty, B. Leca, and T. Noguer, Biosensors for the detection of pesticides, *Analusis* **26** (1998) M144-M149.

[37] U. Schobel, C. Barzen, and G. Gauglitz, Immunoanalytical techniques for pesticide monitoring based on fluorescence detection, *Fresenius J. Anal. Chem.* **366** (2000) 646-658.

[38] T. Vo-Dinh, J. Fetzer, and A. D. Campiglia, Monitoring and characterization of polyaromatic compounds in the environment, Talanta **47** (1998) 943-969.

[39] M. A. Gonzalez-Martinez, J. Penalva, R. Puchades, A. Maquieira, B. Ballesteros, M. P. Marco, and D. Barcelo, An immunosensor for the automatic determination of the antifouling agent Irgarol 1051 in natural waters, *Environ. Sci. Technol.* **32** (1998) 3442-3447.

[40] F. S. Ligler, G. P. Anderson, P. T. Davidson, R. J. Foch, J. T. Ives, K. D. King, G. Page, D. A. Stenger, and G. P. Whelan, Remote sensing using an airborne biosensor, *Environ. Sci. Technol.* **32** (1998) 2461-2466.

[41] F. S. Ligler, Editorial, *Biosens. Bioelectron.* **14** (2000) 749.

[42] A. Strong, D. I. Stimpson, D. U. Bartholomew, T. F. Jenkins, and J. L. Elkind, Detection of trinitrotoluene (TNT) extracted from soil using a surface plasmon resonance (SPR)-based sensor platform, *SPIE-The International Society for Optical Engineering, Aerosense XIII, Proceedings*, September 1999.

[43] M. R. Darrach, A. Chutjian, and G. A. Plett, Trace explosives signatures from World War II unexploded undersea ordnance, *Environ. Sci. Technol.* **32** (1998) 1354-1358.

[44] D. Ivnitski, I. Abdel-Hamid, P. Atanasov, and E. Wilkins, Biosensors for detection of pathogenic bacteria, *Biosens. Bioelectron.* **14** (1999) 599-624.

[45] J. Grassi and R. Georgiadis, Temperature-dependent refractive index determination from critical angle measurements: Implications for quantitative SPR sensing, *Anal. Chem.* **71** (1999) 4392-4396.

[46] L. A. Lyon, W. D. Holliway, and M. J. Natan, An improved surface plasmon resonance imaging apparatus, *Rev. Sci. Instrum.* **70** (1999) 2076-2081.

[47] K. A. Peterlinz and R. Georgiadis, Two-color approach for determination of thickness and dielectric constant of thin films using surface plasmon resonance spectroscopy, *Opt. Commun.* **130** (1996) 260-266.

[48] R. P. Podgorsek, T. Sterkenburgh, J. Wolters, T. Ehrenreich, S. Nischwitz, and H. Franke, Optical gas sensing by evaluating ATR leaky mode spectra, *Sens. Act. B.* **38-39** (1997) 349-352.

[49] E. Nice, M. Lackmann, F. Smyth, L. Fabri, and A. W. Burgess, Synergies between micropreparative high-performance liquid chromatography and an instrumental optical biosensor, *J. Chrom. A* **660** (1994) 169-185.

[50] A. Bossi, S. A. Piletsky, P. G. Righetti, A. P. F. Turner, Capillary electrophoresis coupled to biosensor detection, *J. Chrom. A* **892** (2000) 143-153.

[51] P. I. Nikitin, A. A. Beloglazov, V. E. Kochergin, M. V. Valeiko, and T. I. Ksenevich, Surface plasmon resonance interferometry for biological and chemical sensing, *Sens. Act. B* **54** (1999) 43-50.

[52] L. A. Lyon, M. D. Musick, P. C. Smith, B. D. Reiss, D. J. Pena, and M. J. Natan, Surface plasmon resonance of colloidal Au-modified gold films, *Sens. Act. B* **54** (1999) 118-124.

[53] R. C. Jorgenson, S. S. Yee, A fiber-optic chemical sensor based on surface plasmon resonance, *Sens. Act. B* **12** (1993) 213-220.

[54] R. Slavik, J. Homola, and J. Ctyroky, Single mode optical fiber surface plasmon resonance sensor, *Sens. Act. B.* **54** (1999) 74-79.

[55] K. S. Johnston, T. M. Chinowsky, and S. S. Yee, Planar substrate surface plasmon resonance probe, *Proc. SPIE* **2836** (1996) 178-185.

[56] J. Homola, H. B. Lu, S. S. Yee, Dual-channel surface plasmon resonance sensor with spectral discrimination of sensing channels using a dielectric overlayer, *Electronics Letters* **35** (1999) 1105-1106.

[57] M. N. Mar, B. D. Ratner, and S. S. Yee, An intrinsically protein-resistant surface plasmon resonance biosensor based upon a RF-plasma-deposited thin film, *Sens. Act. B.* **54** (1999) 125-131.

[58] C.R. Lavers, R. D. Harris, S. Hao, J. S. Wilkinson, K. O'Dwyer, M. Brust, and D. J. Schiffrin, Electrochemically -controlled waveguide-coupled surface-plasmon sensing, J. Electroanal. Chem. **387** (1995) 11-22.

[59] K. S. Johnston, K. S. Booksh, T. M. Chinowsky, and S. S. Yee, Performance comparison between high and low resolution spectrophotometers used in a white light surface plasmon resonance sensor, *Sens. Act. B* **54** (1999) 80-88.

[60] J. Melendez, R. Carr, D. U. Bartholomew, K. Kukanskis, J. Elkind, S. Yee, C. Furlong, R. Woodbury, A commercial solution for surface plasmon sensing, *Sens. Act. B* **35** (1996) 1-5.

[61] J. Melendez, R. Carr, D. U. Bartholomew, H. Taneja, S. Yee, C. Jung, C. Furlong, Development of a surface plasmon resonance sensor for commercial applications, *Sens. Act. B* **38-39** (1997) 375-379

[62] http://www.ti.com/spreeta

[63] J. L. Elkind, D. I. Stimpson, A. A. Strong, D. U. Bartholomew, and J. L. Melendez, Integrated analytical sensors: the use of the TISPR-1 as a biosensor, *Sens. Act. B* **54** (1999) 182-190.

[64] J. Elkind, Texas Instruments, Inc., personal communication

[65] G. B. Sigal, M. Mrksich, and G. M. Whitesides, Using surface plasmon resonance spectroscopy to measure the association of detergents with self-assembled monolayers of hexadecanethiolate on gold, *Langmuir* **13** (1997) 2749-2755/

[66] Ryo Yamada, H. Wano, and K. Uosaki, Effect of temperature on structure of the self-assembled monolayer of decanethiol on Au(111) surface, *Langmuir* **16** (2000) 5523-5525.

[67] B. Persson, K. Stenhag, P. Nilsson, A. Larsson, M. Uhlen, P. Nygren, Analysis of oligonucleotide probe affinities using surface plasmon resonance: A means for mutational scanning, *Anal. Biochem.* **246** (1997) 34-44.

[68] C. T. Wittwer, K. M. Ririe, R. V. Andrew, D. A. David, R. A. Gundry, and U. J. Balis, The LightCycler: A microvolume multisample fluorimeter with rapid temperature control, *Biotechniques* **22** (1997) 176-181

[69] N. A. Friedman and D. R. Meldrum, Capillary tube resistive thermal cycling, *Anal. Chem.* **70** (1998) 2997-3002.

[70] M. Meusel, D. Trau, A. Katerkamp, F. Meier, R. Polzius, and K. Cammann, New ways in bioanalysis - one-way optical sensor chip for environmental analysis, *Sens. Act. B* **51** (1998) 249-255.

[71] H. A. Fishman, D. R. Greenwald, and R. N. Zare, Biosensors in chemical separations, *Annu. Rev. Biophys. Biomol. Struct.* **27** (1998) 165-198.

[72] S. C. Jakeway, A. J. deMillo, and E. L. Russell, Miniaturized total analysis systems for biological analysis, *Fresenius J. Anal. Chem.* **366** (2000) 525-539.

Chapter 2: Basic surface plasmon resonance theory

A *plasmon* is defined as "the quanta of waves produced by collective effects of large numbers of electrons in matter when the electrons are disturbed from equilibrium." [1] Plasmons confined to a surface are called *surface plasmons;* the existence of surface plasmons was first proposed to explain the energy loss spectra of electrons reflected from a metal surface. The frequency, and therefore energy, of these oscillations is determined by the electron density. If the plasmon energy is comparable to the energy of a photon, plasmons may be excited optically.

2.1. Causes of surface plasmon resonance

It is the presence and unusual electronic properties of the gold layer which allow the surface plasmon resonance effect to occur. The complicated physical nature of this plasma has been much studied [2]. For engineering purposes, however, the behavior of the metal's electron plasma is neatly described by the wavelength-dependent complex index of refraction of the metal.

The refractive indices of metals are notable for having large imaginary components and for being very dispersive (varying with wavelength). Fig. 2.1 shows how the real and imaginary parts of the refractive indices ***n*** of several metals vary across the visible spectrum [3]. Also shown are the permittivities ε, where index and permittivity are related by

$$n = \sqrt{\varepsilon} \tag{2.1}$$

Metals which produce a prominent SPR response have a refractive index with a large negative imaginary part and only a small real part (corresponding to a large negative real permittivity with only a small imaginary component.) By this criterion, Fig. 2.1 shows that gold, silver, copper, and aluminum are likely to show an SPR response, while lead and chrome are not. Gold is the most popular choice in modern SPR sensors due to its superior chemical inertness.

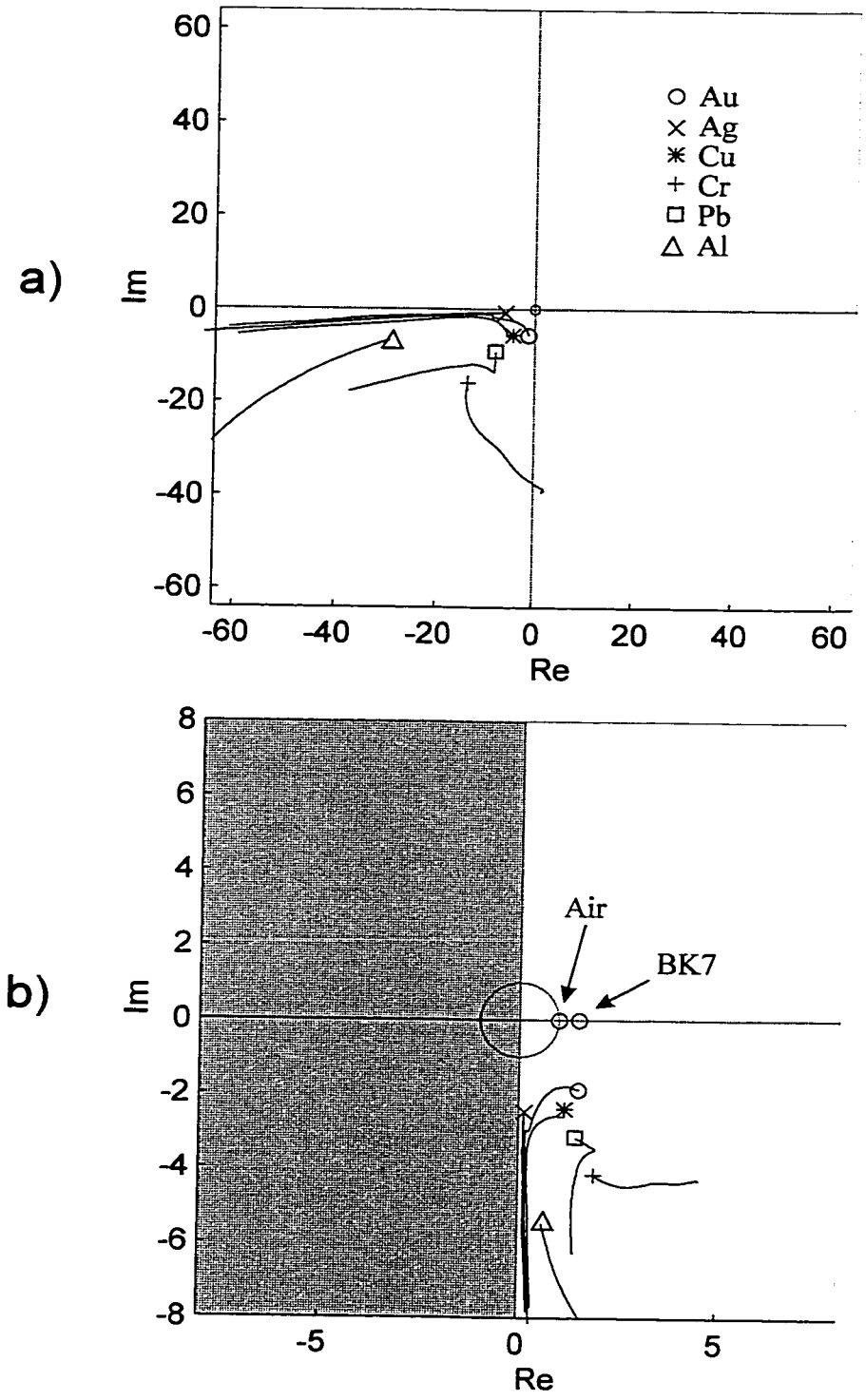

Figure 2.1. Optical constants of various metals. The locus for each metal traces its optical constants at wavelengths from 450 nm to 1150 nm. a) permittivity; b) index of refraction. The symbol for each element is placed at the 450 nm end of the locus. The locus of the optical constants of Al extends off of the scale on both graphs.

2.2 Predicting SPR in a two-layer structure

In an SPR sensor, the SPR effect results from a property of the interface between the metal and the analyte. The simplest way to predict the SPR effect is to consider a two-layer planar optical structure consisting only these two materials. (Fig. 2.2a) Both materials are considered to he half-infinite in extent.

If one searches for a plane-wave solution to Maxwell's equations for this structure such that in both regions only one wave (i.e., a forward-going or a backward-going wave) exists, one finds that a solution exists only for TM polarization, and only at wavevectors which have a component parallel to the interface equal to

$$k_{||} = k_0 \sqrt{\frac{\varepsilon_m \varepsilon_a}{\varepsilon_m + \varepsilon_a}} \tag{2.2}$$

and perpendicular components (in the metal and analyte, respectively),

$$k_{\perp m} = k_0 \frac{\varepsilon_m}{\sqrt{\varepsilon_m + \varepsilon_a}}, \quad k_{\perp a} = k_0 \frac{\varepsilon_a}{\sqrt{\varepsilon_m + \varepsilon_a}} \tag{2.3}$$

where κ_0 is the free-space wavevector and ε_m and ε_a are the complex permittivities of the metal and analyte.

If the materials in each layer are dielectrics with a positive real permittivity, this solution corresponds to the Brewster angle the angle at which zero reflectivity is observed for TM polarized-light. In this case, the wave in both layers is forward-going: radiation propagates across the interface without attenuation.

If one material instead has a *negative* real permittivity (such as that exhibited approximately by gold at optical frequencies) the solution looks quite different. The parallel component of the wavevector is real, indicating that the wave propagates along the interface, while the perpendicular component in both regions is imaginary, indicating a wave that decays with distance from the interface. Actual metals will have a permittivity with a small imaginary component in addition to the negative real part. This will give $k_{||}$ an imaginary component, indicating that the wave decays as it propagates along the interface. This is the *surface plasma wave.*

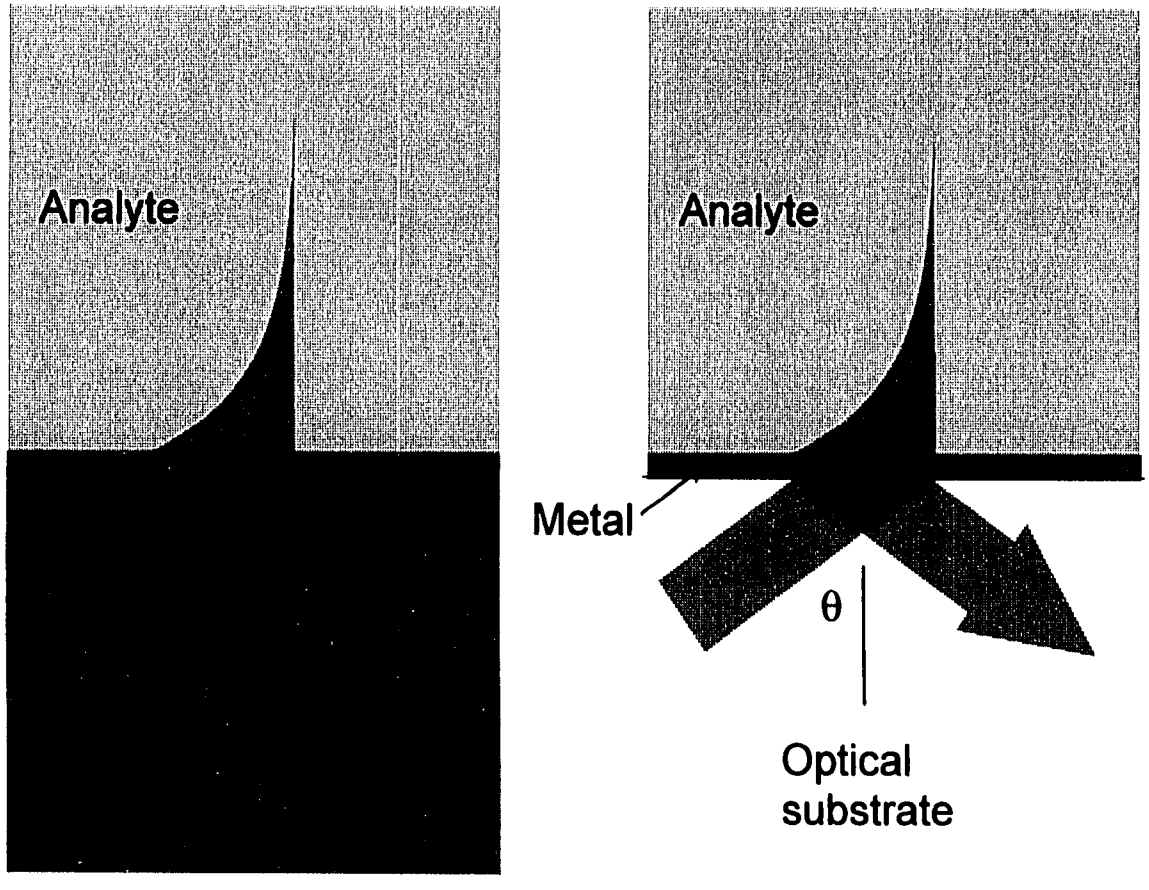

Figure 2.2. SPR in 2 and 3-layer structures. (a) In an idealized 2-layer structure, a surface plasma wave travelling along the interface between metal and analyte can be predicted. (b) In the Kretchmann configuration, if the incident wavevector matches the parallel component of the surface plasma wavevector, a dip in reflectivity is observed.

In the Kretchmann SPR sensing configuration used in this work, SPR is observed by measuring the internal reflectivity of an optical substrate coated with a thin layer (50 nm) of gold. The connection between this configuration and the two-layer result occurs because the behavior predicted for the two-layer case remains approximately true even when only a thin layer of metal is present. If the metal thickness is in the correct range, then when the parallel component of the wavevector of the incident light traveling through the substrate approaches the surface plasmon wavevector of Eq. (2.2) above, i.e.

$$\sqrt{\varepsilon_s}\sin(\theta) \approx \sqrt{\frac{\varepsilon_m \varepsilon_a}{\varepsilon_m + \varepsilon_a}} \tag{2.4}$$

then part of the incident energy is coupled into the surface plasma wave, and a decrease in reflected intensity is observed. (In Eq. 2.4, ε_S is the permittivity of the optical substrate and θ is the incident angle.)

Exact analytical expressions describing this behavior are very cumbersome to manipulate. However, exact results can easy be obtained numerically. Knowledge of the permittivities of each material, combined with thin-film optical models based on Maxwell's equations, is all that is required to simulate the SPR effect. The optical behavior of the SPR sensor shown in Fig. 2.2b may be treated as a special case of the behavior of the general thin film optical structure shown in Fig. 2.3.

The goal of these models is to determine the reflectivity, internal field strengths, transmissivity, and other parameters of this structure, given incident light (modeled as a harmonic plane wave) of a certain wavelength and angle of incidence. This may be accomplished by applying Maxwell's equations and matching boundary conditions between optical layers. An overview of the steps involved in finding a solution to Maxwell's equations for a given layer structure is shown in Fig. 2.3.

The solution is straightforward, and yields a "transmission matrix" result in which the complete solution is formed by a multiplication of 2x2 matrices, one for each layer except the first and last. (A complete derivation of this solution can be found in [5]) The derivation yields an expression relating the parallel component of the electric and magnetic fields at successive interfaces. In particular, the parallel fields at the end of the first layer and the beginning of the last ("Nth") layer are related by

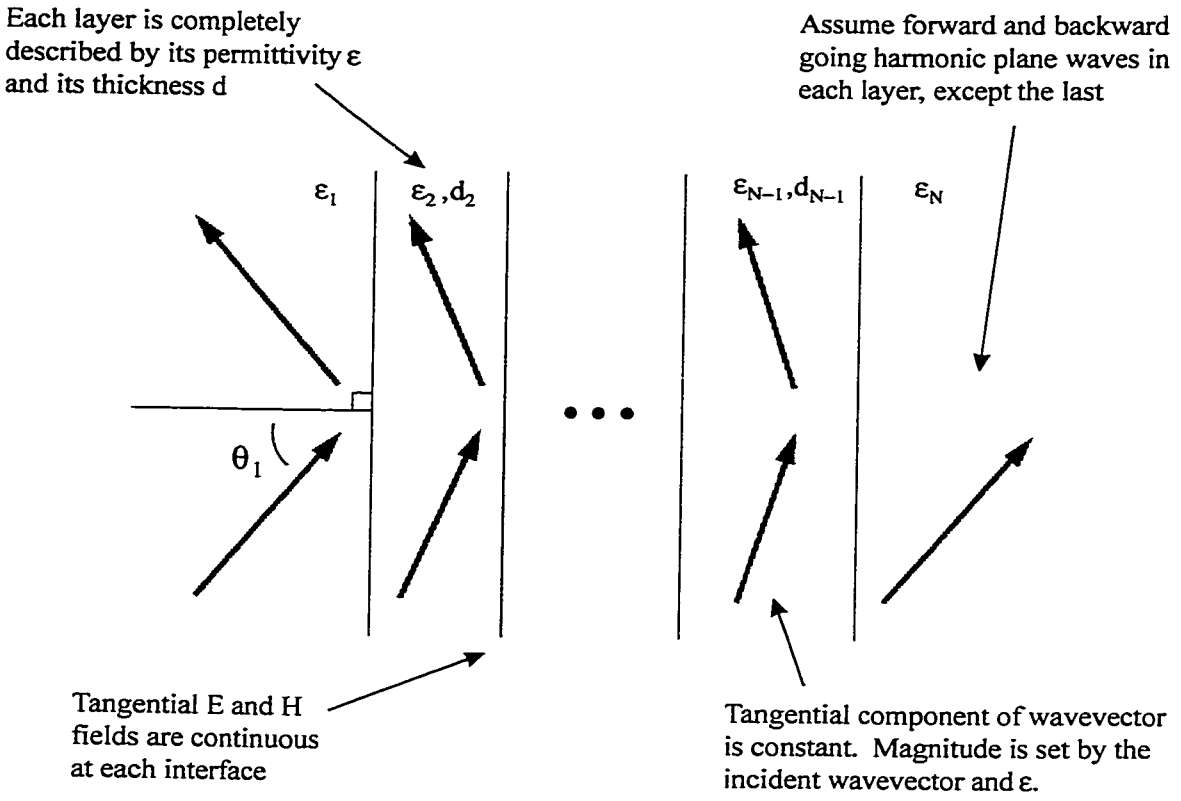

Figure 2.3: General thin-film optical structure, with key features of the method of solution

$$\begin{bmatrix} \mathbf{E}_{\parallel d} \\ \mathbf{H}_{\parallel d} \end{bmatrix}_1 = \left[\prod_{i=2}^{N-1} \bar{\bar{\mathbf{M}}}_i \right] \begin{bmatrix} \mathbf{A}_{TM}\mathbf{H}_{\parallel 0} \\ \mathbf{H}_{\parallel 0} \end{bmatrix}_N \tag{2.5}$$

where N is the number of layers and the subscripts indicate the layer for which each parameter is evaluated. The values of the parameters in Eq. (2.5) are given by

$$\bar{\bar{\mathbf{M}}} = \begin{bmatrix} \cos\boldsymbol{\kappa}_\perp d & \mathbf{j}\mathbf{A}_{TM}\sin\boldsymbol{\kappa}_\perp d \\ \dfrac{j}{\mathbf{A}_{TM}}\sin\boldsymbol{\kappa}_\perp d & \cos\boldsymbol{\kappa}_\perp d \end{bmatrix} \tag{2.6}$$

$$\mathbf{A}_{TM} \equiv \frac{\eta_0}{\kappa_0 \boldsymbol{\varepsilon}}\boldsymbol{\kappa}_\perp \tag{2.7}$$

$$\boldsymbol{\kappa}_\perp = \sqrt{\kappa_0^2\boldsymbol{\varepsilon} - \boldsymbol{\kappa}_\parallel^2} \tag{2.8}$$

$$\boldsymbol{\kappa}_\parallel = \kappa_0 n_1 \sin(\theta_1) \tag{2.9}$$

$$\eta_0 = \sqrt{\frac{\mu_0}{\varepsilon_0}} \tag{2.10}$$

$$\kappa_0 = \frac{2\pi}{\lambda_0} \tag{2.11}$$

where ε_0 and μ_0 are the permittivity and permeability of free space, λ_0 is the free space wavelength, and the complex permittivity $\boldsymbol{\varepsilon}$ and layer thickness d vary with the layer number i. Once the parallel fields have been determined from Eq. (2.5), the reflectivity may be found from

$$R_{TM} = \left| \frac{\mathbf{E}_{\parallel d} - \mathbf{A}_{TM}\mathbf{H}_{\parallel d}}{\mathbf{E}_{\parallel d} + \mathbf{A}_{TM}\mathbf{H}_{\parallel d}} \right|^2 \tag{2.12}$$

As written, these equation apply for TM-polarized incident light. The reflectivity for TE-polarized light may also be found from (2.5)-(2.12) by substituting $\mathbf{A}_{TE}$ for $\mathbf{A}_{TM}$, where

$$\mathbf{A}_{TE} \equiv -\frac{\kappa_0 \eta_0}{\kappa_\perp} \tag{2.13}$$

All simulations of SPR sensor behavior shown in this dissertation were produced using software written in the "Matlab" computing environment (Mathworks Corp., Natick, MA) by the author. A listing of this software can be found in Appendix A.

Notes for Chapter 2

[1] S. P. Parker, ed., *McGraw-Hill Encyclopedia of Physics*, New York: McGraw-Hill, 1993.

[2] H. Raether, Surface plasma oscillations and their applications, *Physics of Thin Films* **9** (1977) 145-261.

[3] E. D. Palik, ed., *Handbook of optical constants of solids*, Orlando: Academic Press, 1991.

[4] O. S. Heavens, *Optical properties of thin solid films*, New York: Dover, 1955.

[5] T. M. Chinowsky, *Combining surface plasmon resonance with electrochemistry: Instruments, experiments, and data analysis.* M. S. E. E. Thesis, University of Washington, 1997.

Chapter 3: Increasing the robustness of SPR measurements using bulk RI compensation

Interference from bulk RI effects is a serious limitation of the SPR sensing technique. Because an SPR sensor responds to any RI change within its sensing range, and that sensing range is greater than the thickness of most adsorbed films of interest, the sensor also responds to changes in the RI of the bulk analyte adjacent to the adsorbed layer. This is illustrated in Fig. 3.1. In this simulation, the formation of a 30 nm thick adsorbed layer causes a shift in the angle of the SPR minimum of 3 degrees. A subsequent increase in bulk RI from 1.33 to 1.355 results in an additional shift of about the same magnitude.

In biosensing, the analyte is typically an aqueous solution containing biologically active molecules. If the temperature or chemical composition of the solution changes, its RI will change. The sensor's response to this change can easily exceed the response resulting from binding of biomolecules.

The observed sensor response is thus a combination of the desired adsorption response and interference from bulk RI variations. We depict the nature of this "SPR arithmetic" by the equation of Fig. 3.2.

A complete solution to the problem of bulk RI effects is to measure simultaneously both the SPR response and the bulk RI of the analyte, and then use the bulk measurement to compensate the SPR response for bulk RI interference, in effect reversing the equation of Fig. 3.2. This chapter describes a new experimental technique we have developed to perform this type of compensation. Our technique, based on internal reflection refractometry (IRR), has potential advantages in robustness, ease of implementation, and cost over previously reported techniques. This chapter will discussion subtractive SPR compensation in general, and review previous techniques for SPR compensation. We then describe the basic history and theory of IRR and show how the inherent surface insensitivity of IRR makes it an attractive method for bulk RI compensation. We will then present some simulations predicting the performance of our compensation technique, and discuss in detail the sources of error which can contribute to imperfect compensation.

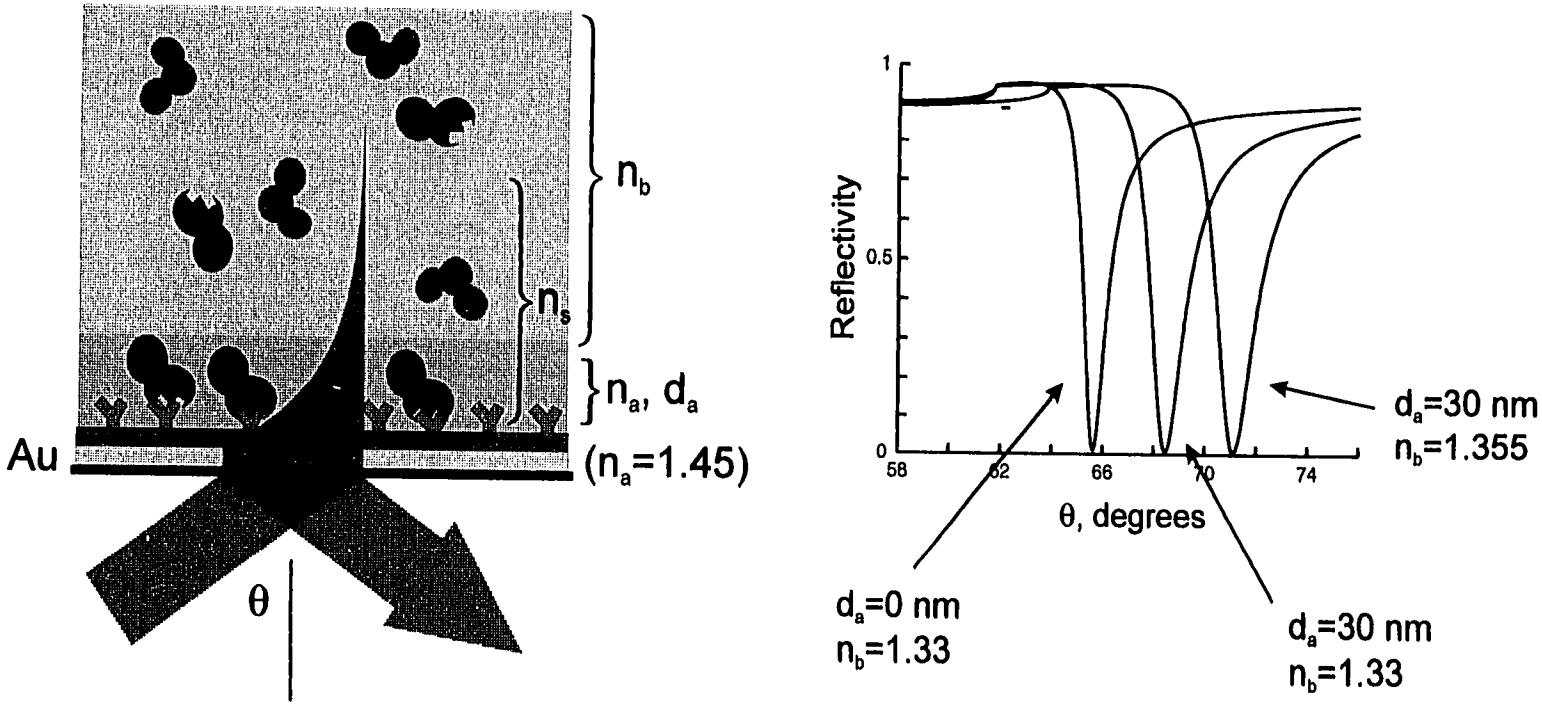

Figure 3.1. Bulk RI interference. SPR responds to all RI changes within its sensing range. Adsorption to the surface and bulk RI changes will both cause changes in the surface RI sensed by SPR.

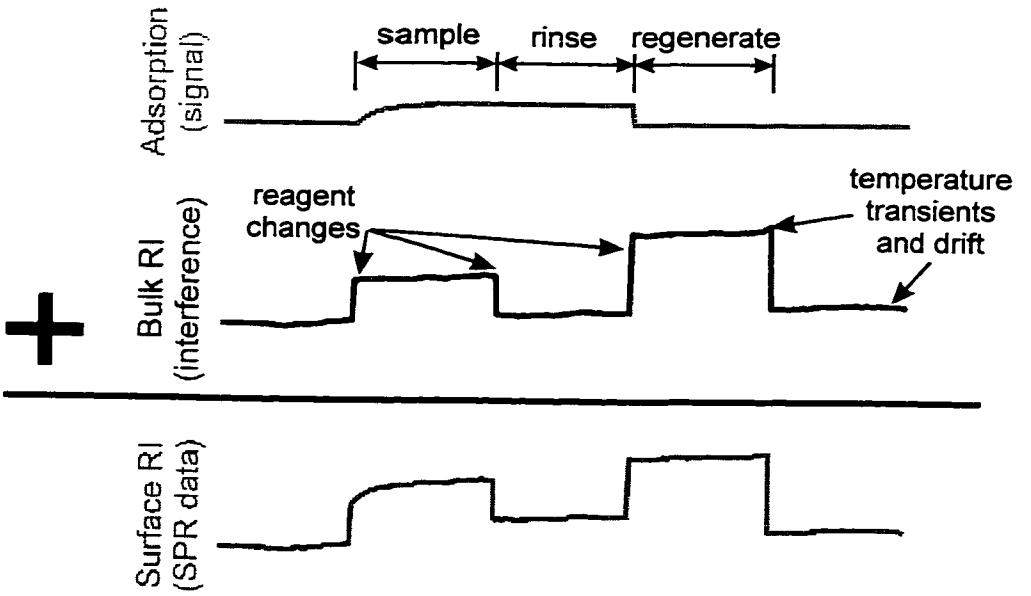

Figure 3.2. SPR arithmetic. SPR measurements of surface refractive index contain contributions from adsorbed layers and from variations in the RI of the bulk analyte above the layer. To measure adsorption independently, the bulk RI must be eliminated.

3.1. Subtractive SPR compensation

Bulk RI compensation methods seek to combine two measurements to arrive at a robust measurement of adsorption. The first measurement, the surface RI n_s, is the RI of the analyte as measured by the SPR reflection spectrum. The surface RI is defined such that when the sensor is exposed to a solution of known RI n when no adlayer is present, then $n_s=n$. If an adlayer with RI greater than n is present, the average RI near the surface with be greater than n, and $n_s>n$.

The second measurement, the bulk RI n_b, is the RI of the analyte above the adsorbed layer.

The exact relationship between n_s, n_b, and the amount of material adsorbed onto the sensor surface is complex, depending upon the detailed structure of the adsorbed layer. Some examples of these complexities are described in 3.6 and in Appendix B. However, as was suggested by Fig. 3.2, for most applications a good approximate quantification of adsorbed material can be obtained by simply subtracting n_b from n_s. We term this approximation *subtractive SPR compensation,* and define the *adsorption index* $N=n_s-n_b$ to be the difference between surface and bulk RI.

The adsorption index is the natural measurement of adsorption produced by the compensated sensor. By the definition of n_s, $N=0$ if no adlayer is present. If a high RI layer adsorbs to the SPR surface, $n_s>n_b$ and $N>0$.

The relationship between N and the actual amount of adsorbed material (measured as surface coverage Γ, in units of ng/mm^2) is typically assumed to be linear [1, 2]. The exact relationship between N and Γ depends upon the method by which the sensor surface is functionalized. To determine the relationship between N and Γ most accurately, it is necessary to perform calibration measurements in which Γ is measured directly, for instance, by radiolabeling [1]. Fortunately, because the instrument's response relative to a calibration standard is usually of interest, inability to predict the constant of proportionality between N and Γ does not interfere with interpretation of sensor data, as long as the relationship between N and Γ is repeatable and linear.

3.2. Pre-existing method of bulk RI compensation: SPR referencing

The only method of bulk RI compensation which has previously been described in the literature is the SPR referencing method. In this method, two SPR measurements of the same analyte are performed simultaneously. The first, "active" measurement is performed using a sensor surface that is functionalized normally for the desired application. The second, "reference" measurement is performed using a sensor surface which is treated to be resistant to the formation of adsorbed layers, with the goal being that the reference measurement will only respond to changes in the bulk RI of the analyte. A compensated measurement is obtained by subtracting the reference measurement from the active measurement. This method of compensation appears to have been first implemented by Biacore. Since the introduction in 1995 of the Biacore 2000 instrument, which is capable of making simultaneous SPR measurements in four separate flowcells, Biacore has recommended that one of these be used for a reference to compensate for bulk RI effects due to changes in analyte composition [3, 4].

3.2.1. Distinction between SPR referencing and IRR compensation

The IRR compensation technique of bulk RI compensation is fundamentally different from SPR referencing in that the IRR technique uses two different types of measurements to obtain measurements of surface RI and bulk RI. IRR is specifically designed to measure bulk RI, and its measurement is largely independent of conditions at the sensor surface (see 3.4.1 and 3.6.1 below). In SPR referencing, both measurements are performed using SPR, and so both will be measurements of the RI near the surface. However, because the reference measurement of surface RI is measured at a surface treated to resist adsorption, and because surface RI will be the same as the bulk RI if no adlayer is present, the reference measurement will in theory give a measurement of bulk RI.

In practice, because the reference measurement is still fundamentally surface-sensitive, it will be influenced by a number of factors other than bulk RI. The reference surface will not be completely immune to adsorption, and so some non-specific adsorption of analyte components to the reference surface may occur. Instability (such as swelling) in the reference surface can cause drift in the measurement of bulk RI.

This attribute of SPR referencing can be seen either as an advantage or as a disadvantages. The disadvantage is that these surface effects will make the reference

measurement a less stable indicator of bulk RI. The advantage is that SPR referencing has the potential to compensate the SPR measurement for interfering influences over and above bulk RI -- specifically, non-specific binding and drift due to instability in functionalization layers. If the reference surface can be designed to have the same non-specific binding and drift characteristics as the active surface, the compensated SPR measurement will be free of the effects of these interferences, as well as bulk RI interference. Thus, both types of compensation have merits. The ideal biosensor would use both types of compensation -- IRR to provide a stable and specific compensation for bulk RI, and SPR referencing to compensate for interfering surface effects.

Because compensation for surface effects is beyond the scope of this dissertation, we will restrict our discussion of SPR referencing to its use in compensating for bulk RI variations.

3.2.2. Performance of SPR referencing in compensating for bulk RI variations

3.2.2.1. Biacore implementation

Since the SPR referencing technique was introduced by Biacore in 1995, many users of Biacore instruments have used referencing without much comment or criticism [e.g., 5-10] to compensate for bulk RI interference due to variations in the RI of the various buffers and other solutions used in their experiments. Biacore does not provide specification for the quality of compensation which is typically obtainable, and most users of the technique do not present any evaluation of the benefits of the technique in their publications. Only recently have a few more detailed reports appeared. In the first paper specifically devoted to SPR referencing in the Biacore instrument, Ober and Ward [11] found that the quality of compensation varied from flowcell to flowcell within the same sensor chip, and that imperfections in compensation caused errors in kinetic constants calculated from compensated measurements. The authors did not attempt to formulate any specifications for the performance of the reference compensation, but their data show that a bulk RI change of 1.2×10^{-3} was approximately 99% compensated. This is consistent with recent publications [12, 13] by researchers at Biacore, who found that bulk RI changes of 4.5×10^{-3} were compensated to within 7.5×10^{-5}, equivalent to 98.4% compensation. They also found that supplementary calibration measurements, performed using

various concentrations of the buffer used in their binding experiments, could greatly improve the quality of compensation, increasing it to an estimated 99.9%.

Note that because the Biacore instruments are temperature-controlled, SPR referencing is not used in the Biacore instruments to remove bulk RI effects due to temperature.

3.2.2.2. Other implementations

A few other implementations of SPR referencing have appeared in the literature. Homola *et al.* [14] describe a two-channel white-light SPR sensor which uses a novel overlayer geometry to extract two SPR measurements using from one white-light reflection spectrum. In their data, bulk RI variations caused by ethylene glycol solutions covering an RI range of $8x10^{-3}$ were 99% compensated. Bulk RI variations due to slow temperature changes over a period of 7 hours ranged over $3.6x10^{-4}$ RI units and were 92% compensated. A recent refinement of this work [15] demonstrated that additional information assisting in the discrimination of bulk and surface effects can be extracted from this sensor by using the fact that the two SPR measurements performed by this sensor have somewhat different sensing ranges. This design has the potential to discriminate between bulk and surface effects without the need for a non-adsorbing layer. However, exploitation of this potential requires an additional surface calibration, which may be difficult in practice, and sufficient data has not yet appeared to allow evaluation of the capabilities of this technique.

Nenninger *et al.* [16] described a two-channel white-light SPR sensor based on a lightpipe configuration, and presented compensated binding experiments. O'Brien *et al.* [17] constructed a two-channel prism-based SPR sensor, and showed that in binding experiments SPR compensation could reduce bulk RI interference due to analyte composition and slow temperature. However, neither of these works provide enough experimental information to evaluate the sensor performance.

Finally, we note another method suggested by Melendez [18] for compensation of bulk RI interference due to temperature, which is to simply measure the temperature of the analyte and assume a relationship between temperature and RI based on knowledge of the physical properties of the analyte. This procedure was successful in compensating for 95% of bulk RI variations observed during gradual variations of temperature covering a range of 2.7C and extending over 2 days. However because

this method of compensation requires assumptions regarding analyte properties, and because it is has no ability to reduce bulk interference due to analyte composition, it is of limited utility.

3.3. Bulk RI compensation using internal reflection refractometry

The technique of bulk RI compensation by SPR referencing is capable of eliminating a great deal of bulk RI interference, as demonstrated by the high-quality Biacore measurements described above. Furthermore, the potential of SPR referencing to compensate for various surface effects in addition to bulk RI interference makes it a valuable technique. However, the SPR referencing technique requires a non-adsorbing layer on the reference surface, and the construction of such a layer which will remain stable and functional when exposed to complex analytes and , temperature changes has not been demonstrated, and may be a very difficult task. For example, pH changes may affect the bulk RI compensation ability of SPR referencing in Biacore instruments [11]. Another drawback of SPR referencing is that it requires two SPR measurements, which (unless a clever technique like that implemented by Homola [14] is used) will increase instrument complexity and cost. A low-cost implementation of SPR referencing has not been demonstrated.

We describe here an alternative method for bulk RI compensation based on IRR. Compared to SPR referencing, our method

- is inherently surface insensitive. Does not rely upon the presence of a nonadsorbing layer to measure bulk RI.
- Does not require additional measurement hardware
- Can be implemented through a simple modification to an existing inexpensive commercial SPR device, the TI Spreeta.

The concept of bulk RI compensation based on IRR had been previously mentioned in the literature [19], but never implemented before the work of this author.

IRR is a type of critical angle refractometry. Critical angle refractometry is a well established technique of RI measurement based on measurement of optical phenomena

relating to the critical angle. We will now describe the basic theory and history of critical angle refractometry and IRR.

3.4. Theory and history of critical angle refractometry

Light which travels through a material of refractive index n_i and strikes an interface with a material of different refractive index n_b will refract. The angle θ_b at which light will propagate in the second medium is given by Snell's law,

$$\sin\theta_b = \frac{n_i}{n_b}\sin\theta_i \tag{3.1}$$

where θ_i is the incident angle. If the second material has lower RI than the first, i.e. $n_b<n_i$, then for some range of incident angles $\sin\theta_b>1$. This indicates that under those conditions, no wave can propagate in the second material, and so the incident light will be completely reflected. This phenomenon is called total internal reflection (TIR). The observed reflectivity will rise to unity at the incident angle for which $\sin\theta_b=1$. This angle is called the critical angle θ_c, and

$$\theta_c = \sin^{-1}\left(\frac{n_b}{n_i}\right) \tag{3.2}$$

The exact form of the reflectivity may be determined using the 2-layer case of the reflectivity models described in Chapter 2. The results may be written compactly in closed form. The reflectivities differ for TM and TE polarizations, and are found to be

$$R_{TM} = \left|\frac{\tan(\theta_i-\theta_b)}{\tan(\theta_i+\theta_b)}\right|^2, \quad R_{TE} = \left|\frac{\sin(\theta_i-\theta_b)}{\sin(\theta_i+\theta_b)}\right|^2 \tag{3.3}$$

These equations were first discovered by Fresnel (1788-1827) in 1823 and are referred to as the Fresnel equations [20, 21]. Figure 3.3a depicts the TE and TM reflectivity

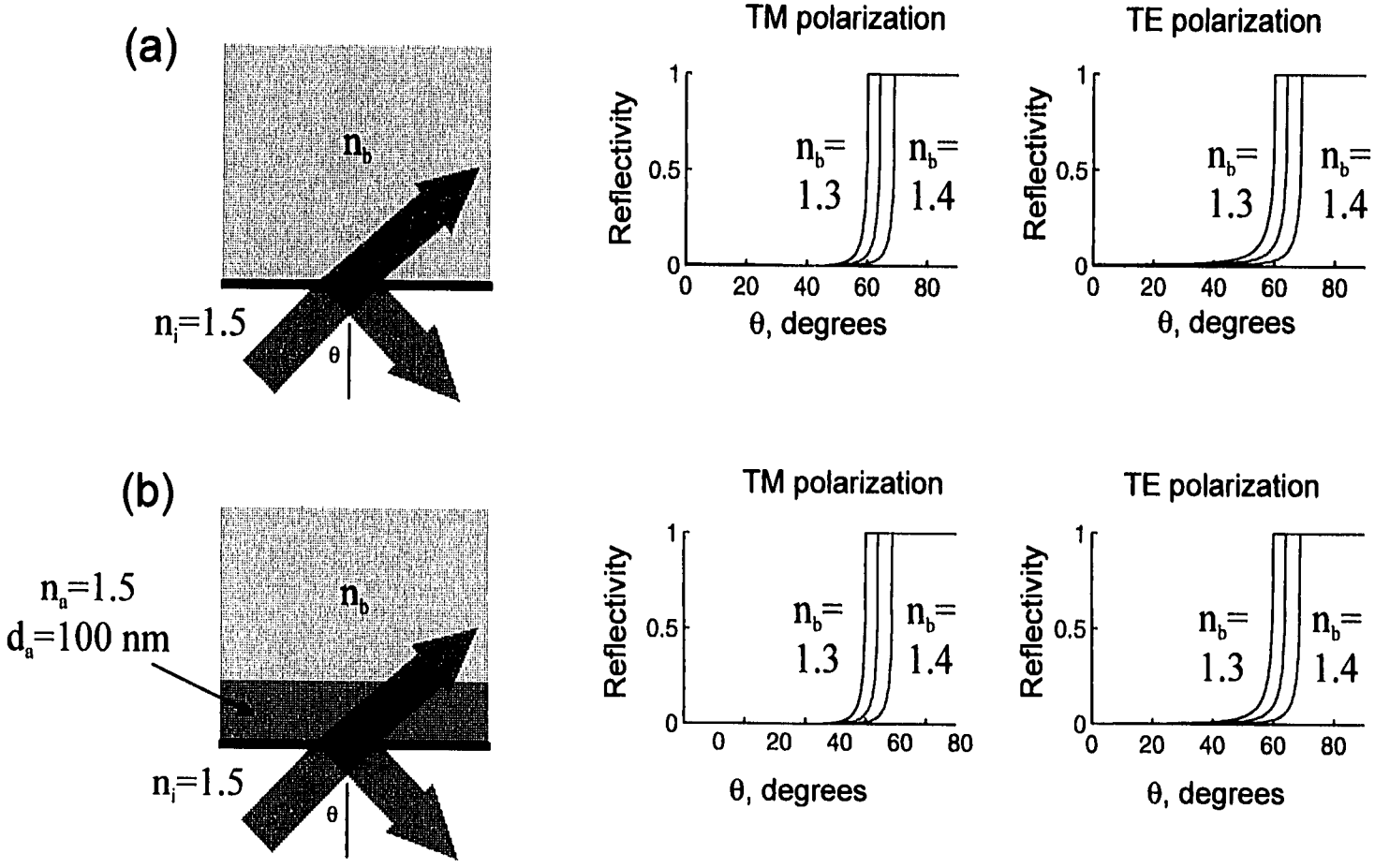

Figure 3.3. IRR sensing principle. (a) The critical angle edge observed in IRR reflection spectra varies in location with the bulk RI of the analyte (b) The IRR reflection spectrum is relatively insensitive to adsorbed layers.

predicted by the Fresnel equations for n_i=1.5 and several values of n_b=1.33, 1.35, and 1.4.

Because θ_c and the reflectivity at angles below θ_c vary with n_b, observation of internal reflectivity in the region surrounding the critical angle edge can be used to determine n_b. This is the basic principle of IRR.

Refractometry by observation of the internal reflection of a prism dates back to Wollaston (1766-1828). Various other experimental configurations for critical angle refractometry were developed, including those of Pulfrich, Hilger-Chance, and Abbe [22]. The configuration developed by Abbe (1840-1905) in 1869 became the most popular configuration for commercial instruments. In contrast to the Wollaston internal reflection method, the Abbe refractometer uses external illumination: Light shines diffusely through a material of lower RI onto a prism of higher RI, and strikes the interface at all angles. Because the greatest angle at which light can be transmitted into the prism is the critical angle, an observation of the transmitted light will reveal an edge at the critical angle. It is interesting to note while the Abbe technique has historically been the most popular, the advent of automatic digital refractometers [e.g. 23, 24] has been accompanied by a return to internal illumination. IRR is more convenient than the Abbe technique because internal illumination requires only one interface with the analyte and does not require that light be transmitted through the sample.

Some recent publications in IRR describe devices for new applications such as refractometry across the UV-visible wavelength range [25], RI measurement of biotissue [26], and measurement of RI temperature coefficients [27].

3.4.1. Surface insensitivity of IRR

Two features of IRR make it attractive for use in compensating SPR measurements for bulk RI. First, the sharpness of the critical angle edge makes IRR a sensitive technique for measuring the refractive index of a bulk solution. Second, the IRR measurement is inherently not sensitive to adsorbed biolayers. Thus, the thin layer of biomaterial that is expected to be adsorbed onto the sensor surface does not interfere with the bulk RI measurement. This is shown in Fig. 3.3b. Here, the biolayer has been modeled as a uniform thin layer of RI 1.45 and thickness 100 nm, while the bulk solution has uniform RI 1.3, 1.35, and 1.4. The reflection spectra are nearly identical

to the spectra of 3.3a. This particular feature of IRR does not appear to have been previously explored in the literature.

Note that we have assumed that the bulk solution to which the sensor is exposed is adequately modeled as having a purely real RI, and that adsorbed layers can be modeled as a uniform layer of a certain thickness and purely real RI. We know that this is not strictly true. In fact, the light scattering properties of antigen-antibody complexes have been used for sensing purposes in a technique denoted nephelometry or immunoturbidimetry [28], and the ultraviolet absorption of proteins is extensively used for quantification of protein concentration. If these loss mechanisms are strong enough, they will affect both SPR spectra [29] and critical angle measurements [25, 30, 31]. The possible presence of such effects must be kept in mind. However, researchers to date have not found it necessary to take these effects into account in explaining the optics of proteins and protein-containing solutions as investigated by optical techniques similar to ours. Characterization of adsorbed protein layers by SPR [1, 32], ellipsometry [33, 34] and waveguide-based sensors [35] found the optical effects of protein adsorption to be well modeled by a lossless layer of uniform thickness and RI. Studies of the RI of protein solutions by transmissive techniques [36] and Abbe refractometry [37] reported no loss mechanisms. RI measurements of egg protein and other biological substances performed using a technique very similar to our IRR approach found no interference due to loss mechanisms [26]. These observations are consistent with what we have observed in preliminary biosensing experiments [38] and in the experiments presented in this dissertation.

3.5. Combining SPR and IRR

IRR and SPR are both performed by observing the internal reflection of a prism (Fig. 3.4). For SPR, the prism is gold coated and the reflectivity is measured at angles above the critical angle (Fig. 3.4a). In IRR, the prism is bare, and the reflectivity at is measured at angles below and close to the critical angle (3.4b). Because the measurement configuration is so similar for the two techniques, and because the range of angles for the two techniques have a natural separation, it is easy to implement both techniques simultaneously. If the range of angles is sufficient to include the necessary range both above and below the critical angle, and if the sensor is designed such that

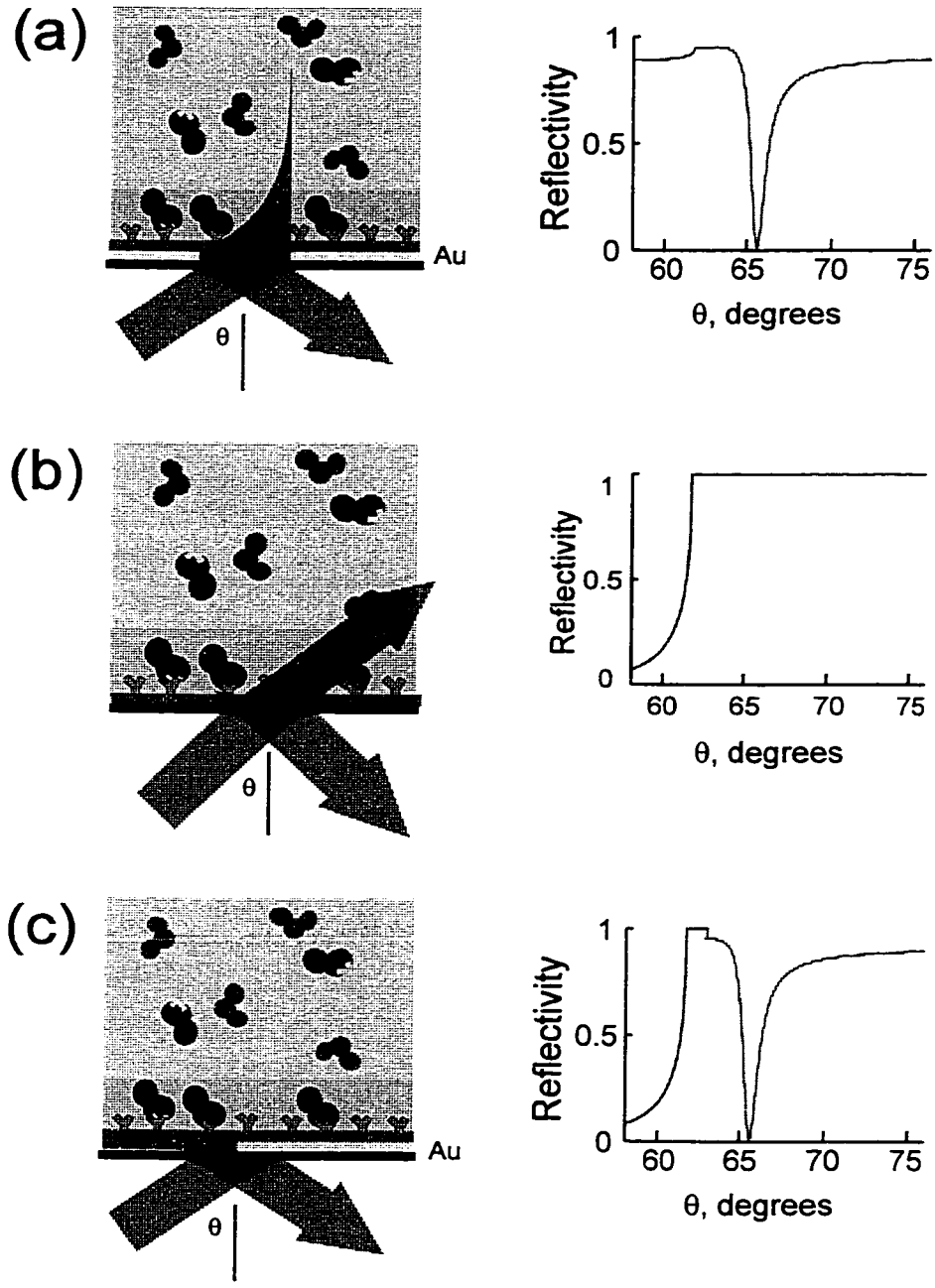

Figure 3.4. Combining SPR and IRR. (a) SPR is measured by observing the internal reflection of a gold-coated surface above the critical angle. (b) IRR is measured by observing the internal reflection of an uncoated surface below the critical angle. (c) Combination SPR/IRR measurement may be obtained on a half-coated surface.

light reflects from a gold surface above the critical angle and from a bare surface below the critical angle, a composite measurement containing both SPR and IRR measurements can be obtained (Fig. 3.4c). As will be described in Chapter 4, the geometry of the TI SPR sensor is particularly well suited for implementation of this technique.

3.6. Simulation of bulk RI compensation using SPR/IRR

A simulated experiment illustrating bulk RI compensation using the SPR/IRR method is shown in Fig. 3.5. This simulation was designed to approximate the actual experiments which will be presented in Chapter 4.

At the beginning of the simulated experiment, no adsorbed layer is present on the sensor. The sensor is then exposed to a sequence of five solutions with bulk RIs ranging from 1.328 to 1.332. Following this, the sensor is exposed to a bulk RI gradient. (As will be explained in the next two chapters, these variations in bulk RI provide calibration information which are useful in analysis of the SPR/IRR data).

Two adsorption events follow. The first event simulates the adsorption of a high-RI layer (n_a=1.45) which grows linearly in 100 s to a thickness of 8 nm, then desorbs. The second event simulates the adsorption of a layer of constant thickness 1.6 nm upon which a bulk RI gradient extending from n_b=1.3275 to n_b=1.3315 is superimposed. (The thickness and RI of this layer were chosen to approximate those of the Triton X-100 adsorbed layers investigated in the next chapter.)

Fig. 3.5a shows that only n_s, the SPR measurement of surface RI, responds to the adsorbed layer, while both the surface measurement and the bulk measurement n_b respond to bulk RI changes. The difference between the two, the adsorption index $N=n_s-n_b$ (Fig. 3.5b), is proportional to the thickness of the adsorbed layer, with proportionality constant 5.8×10^{-4} nm^{-1}. The adsorption index thus provides the desired measurement: adsorption, independent of bulk RI.

3.6.1. Effects of adsorption on critical angle

Figure 3.5 also illustrates two subtle properties of the IRR compensation technique. First, the IRR measurement is not completely independent of adsorbed layers. Thin adsorbed layers will have small effects on the reflectivity below the

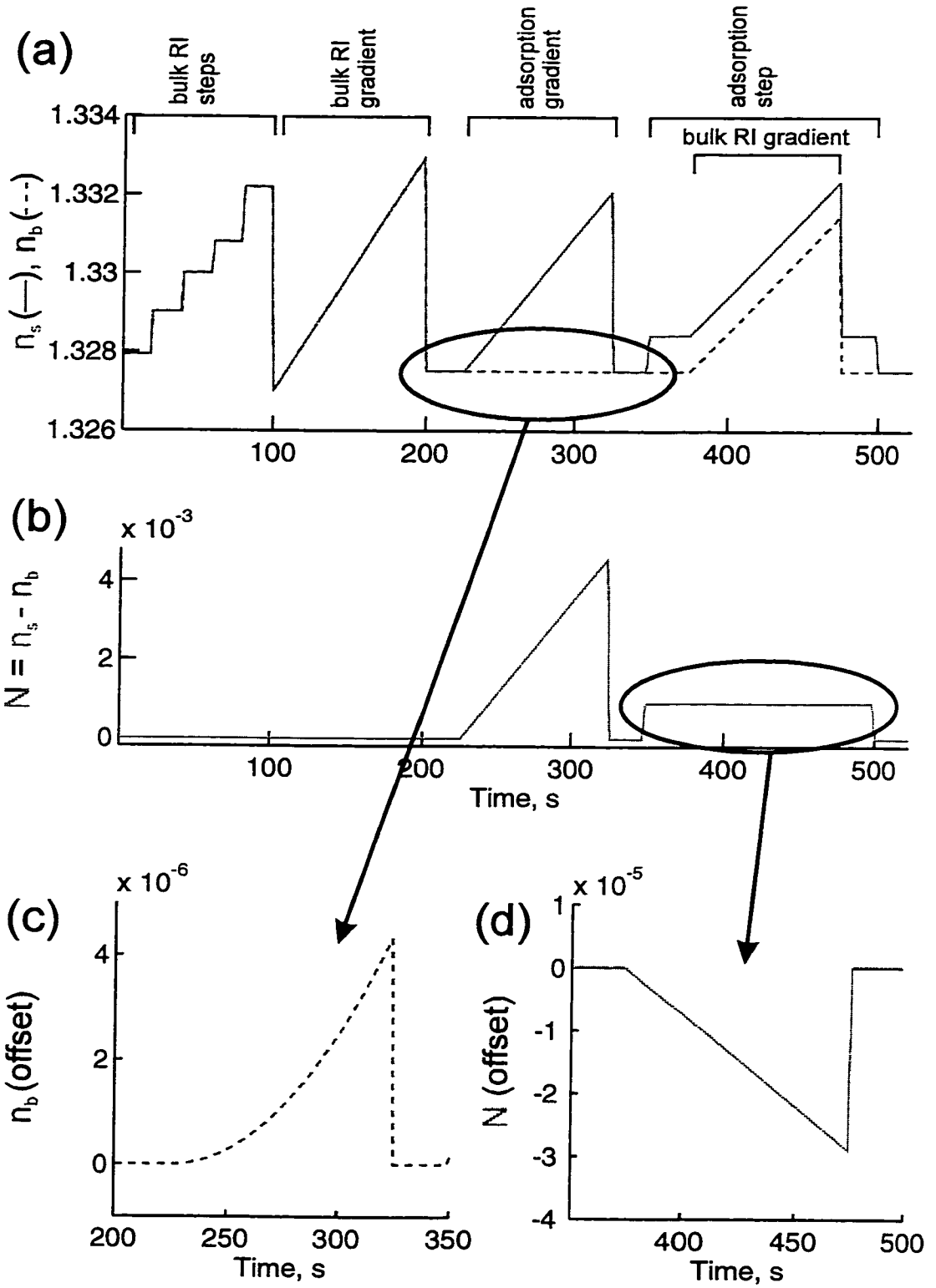

Figure 3.5. Simulation of critical angle compensation. (a) Simulated measurement of n_s and n_b. (b) Simulated adsorption index N. (c) Magnified plot of n_b, showing influence of adsorbed layer on n_b. (d) Magnified plot of N, showing influence of n_b on N.

critical angle (Fig. 3.5c). Because the degree to which these effects will be interpreted as bulk RI changes will depend upon how the data are analyzed, these effects are difficult to quantify with complete generality. For these simulated data, which are analyzed by the same method as the experimental data presented in this chapter (the method fully described in Chapter 3), the 8-nm adsorbed layer produces a change of 4.3×10^{-6} in n_b, compared to 4.6×10^{-3} change in n_s. Therefore, we may say that n_b is less than 1/1000 as sensitive to adsorbed layers as is n_s.

3.6.2. Limits of subtractive compensation

The second subtle property of the IRR technique, illustrated in Fig. 3.5d, is that the adsorption index N is not completely independent of n_b. This effect results from the shielding of the SPR measurement from bulk RI effects by the adsorbed layer. Here, a change in n_b of 4×10^{-3} in the presence of a 1.6 nm adsorbed layer of RI 1.45 causes a change in N of 3×10^{-5}, or 0.75% of the variation in n_b. If the RI of the adsorbed layer is known, the inclusion of a proportionality constant in the calculation of N, e.g. $N=n_s-cn_b$, will allow more complete compensation. Alternatively, the variation of N with n_b may be interpreted to *determine* n_a (if measurements are of high enough quality) [39].

These simulations (and all simulations of reflectivity contained in this work) were created using the Fresnel models described in Appendix A. These simulations assume mathematically perfect layers of uniform RI, and the response of an instrument to actual adsorbed layers will probably differ from these simulations. However, because the present instrument is unable to resolve effects of this small size, experimental investigation of these effects is beyond the scope of this work.

3.7. Error in compensated SPR measurements

The bulk RI variations interfering with an SPR adsorption measurement can be many times greater than the surface RI effects caused by the adsorption event of interest. For the adsorption index $N=n_s-n_b$ to be an effective quantification of adsorption, the measurements of both n_s and n_b must be of sufficiently high quality that their difference has meaning. For this reason, it is important to understand and control the factors which can introduce error in the measurements of n_s and n_b.

3.7.1. Definition of terms

The dictionary definition of *error* is defined as "the difference between an observed or calculated value and a true value." [40] Because the factors which may cause a measurement to be in error are manifold, many different concepts have been developed to describe different types of error [41]. However, researchers are not always in agreement about the meanings of these concepts. Disputes in the literature over the meanings of various terms used to describe data quality extend from at least four decades ago [42] to the present [43]. In attempts to resolve such disputes, comprehensive recommendations for procedures and terminology to be used to discuss error have been produced by organizations such as the International Federation of Clinical Chemistry (IFCC) [44] and the International Union of Pure and Applied Chemists (IUPAC). However, these guidelines do not always agree. For instance, the IFCC and IUPAC definitions of sensitivity are at odds with one another [43]. For this reason, the only way to successfully communicate what is meant in a discussion of error is to describe as completely as possible the assumptions behind that discussion.

Systematic or *determinate errors* are reproducible errors which result from flaws in experimental technique. These errors may be overcome by improvements in technique or corrections to data (if the amount of error is known). Because these errors are not described by the laws of probability, statistical analysis is not generally useful in analysis of systematic error.

Random or *indeterminate errors* are irreproducible measurement variations which result from instrumental instability or from statistical fluctuations inherent in the measurement technique. Random errors are generally assumed to follow the laws of probability and therefore are subject to quantification using statistical measures.

Precision describes how reproducible a measurement is; therefore, the precision of a measurement depends on how well random errors can be controlled. The quantification of precision is termed *imprecision*, and is generally calculated by determining the standard deviation of a group of measurements taken under the same conditions. The terms *reproducibility* and precision are often used interchangeably. It is particularly important when specifying precision to indicate under what conditions the measurements were repeated.

The *accuracy* of a measurement describes how close that measurement is to the "true" value. Accuracy depends largely on systematic error, because it is systematic error that will make a result repeatably differ from the true value. However, we agree with Bevington [41] that a given specification for accuracy implies a level of precision at least as good. For this reason, we take the quantification of accuracy, termed *inaccuracy,* of a group of measurements to be the maximum observed deviation from the "true" value. Thus, inaccuracy will have contributions from both systematic and random error.

Noise can be defined in the broadest sense as "any unwanted disturbance that obscures or interferes with a desired signal." [40] It is a term generally used to describe the behavior of electrical signals. Noise can be subdivided into *extrinsic* noise, or *interference*, which results from external factors influencing the measurement of interest, and *intrinsic* noise, which results from random fluctuations inherent in the method by which the measurement is generated [45]. Because intrinsic noise is both more fundamental and more subject to characterization than extrinsic noise, the study of noise is generally taken to mean the study of intrinsic noise.

These concepts are useful, but all sources of error do not fit neatly into these categories. For example, error caused by interference is not strictly systematic error, because it is not repeatable, but neither is it strictly random error, because one has no reason to expect that a given source of interference will follow any particular statistical law.

Drift, defined as "a gradual change in the zero reading of an instrument or in any quantitative characteristic that is supposed to remain constant," [40] is another commonly observed experimental phenomenon which is not neatly categorized. On a short time scales, error caused by drift may be viewed as a cause of systematic error, because drift does not affect the reproducibility of measurements taken close together in time. On a longer time scale, the error caused by drift is not reproducible, and so is more likely to be described as affecting the precision or reproducibility of the measurement, in spite of the fact that the measurement variations caused by drift are not due to statistical fluctuations. The existence of these ambiguities is another reason to specify as exactly as possible the conditions and assumptions used in quantifying the error in a set of measurements.

3.7.2. Example: Biacore 2000 specifications

To demonstrate how the various concepts describing errors have been applied to SPR sensing by the leading manufacturer of SPR instrumentation, we list here the relevant specifications of the BIACORE 2000 SPR instrument manufactured by Biacore AB [46].

Precision of immobilized protein	
Between flow cells on one chip	
sequential method	typically <5% CV
serial method	typically <2% CV
Between sensor chips	typically <10% CV
Baseline drift	typically <+/-0.3 RU/minute
Noise	typically <1.0 RU RMS (10 Hz) <0.3 RU RMS (1 Hz)

These specifications are notable in their incompleteness: only typical values are given, and many aspects of the instrument response (such as linearity) are not specified. The term precision is used to describe how repeatable (in relative terms) experiments are considered to be when performed on different sensing chips and on different regions of the same sensor chip. Thus, this specification goes beyond describing how the reproducibility of measurements taken in the same flow cell on the same chip (indeed, no specification is given for this) and thus, this specification incorporates all of the error which results due to the tolerances involved in the manufacturing of sensor chips.

Drift is specified as a rate of change of the instrument response, and noise is given as a root-mean-square (RMS) value in refractive index units (1 RU = 10^{-6} RI units). Noise is specified for two different sampling rates, 10 Hz and 1 Hz; the 1 Hz figure is lower because ten 10 Hz measurements are averaged to obtain the 1 Hz measurement. No information is given as to how either noise or drift was calculated or under what conditions they were measured. The fact that noise and drift are specified separately suggests that, as is conventional, noise is being used to characterize the short-term variation of the instrument response, while drift characterizes the long-term variation.

3.7.3. Characterization of error for the SPR/IRR instrument

The SPR/IRR instrument is designed to produce a measurement N which quantifies the amount of material that has been adsorbed to the sensor surface. N is the difference of the bulk and surface RIs n_b and n_s, which are calculated in turn from measured reflection spectra. What is the appropriate way to apply the above concepts regarding error to these SPR/IRR measurements?

Because of the central role of calibration in the SPR/IRR sensor, we separate the sources of observed error into instrumental error and calibration error. *Instrumental error* describes the measurement errors that result from the limits of instrumentation, and describes the error that would be observed if the instrument calibration were perfect. Instrumental error will contain both random and systematic components. *Calibration error* describes the additional systematic error that results from imperfect calibration.

We denote n_b and n_s to be the "true" values of bulk and surface RI, and n_b* and n_s* to be the observed values. n_b* and n_s* are derived using calibration functions cal_b and cal_s from "raw" values b* and s* calculated from measured reflection spectra:

$$n_b^* = cal_b(b^*)$$
$$n_s^* = cal_s(s^*) \tag{3.4}$$

Instrumental error will affect b and s, while calibration error will affect cal_b and cal_s. (Details of how the calibration functions and raw values are calculated are given in Chapter 5.) The total error in n_b* and n_s* will be a combination of instrumental and calibration error.

3.7.3.1. Instrumental error: contributions to error in raw (pre-calibration) data

Instrumental error describes the measurement errors that result due to the limits of instrumentation. If the instrument calibration were perfect, instrumental errors would be the only sources of error. The observed raw data values will be a sum of the "true" values $b(n_b)$ and $s(n_b)$ and several sources of error. We write the observed values as

$$b^* = b(n_b) + \Delta b_{noise} + \Delta b_{drift} + \Delta b_{grad} + \Delta b_{misc}$$
$$s^* = s(n_s) + \Delta s_{noise} + \Delta s_{drift} + \Delta s_{misc} \tag{3.5}$$

The sources of error enumerated here include errors due to electronic noise and other short-term fluctuations that appear random (Δb_{noise} and Δs_{noise}), slow changes in instrument response due to factors such as changing apparatus temperature (Δb_{drift} and Δs_{drift}), and miscellaneous other factors (Δb_{misc} and Δs_{misc}), such as nonuniformity of surface layers and optical absorption or scattering in the analyte. The observed raw value b^* contains an additional error component Δb_{grad}, which describes errors in b^* due to RI gradients in the analyte which cause the observed bulk RI to be different from the bulk RI adjacent to the location on the instrument surface where the surface RI is measured.

3.7.3.2. Calibration error: contributions to error in calibrated data

If the calibration functions cal_b and cal_s which calculate n_b^* and n_s^* from b^* and s^* were perfect, the instrumental noise sources listed above would be the only sources of error in n_b^* and n_s^*. Each component of instrumental error in the raw data will lead to a component of error in the calibrated data, as follows:

$$n_b^* = cal_b(b^*) = n_b + \Delta n_{b,noise} + \Delta n_{b,drift} + \Delta n_{b,grad} + \Delta n_{b,misc}$$
$$n_s^* = cal_s(s^*) = n_s + \Delta n_{s,noise} + \Delta n_{s,drift} + \Delta n_{s,misc} \tag{3.6}$$

However, because the calibration functions are derived from calibration measurements which are also subject to instrumental error, the calibration functions are not perfect and cause additional systematic error. Other factors such as imperfect knowledge of the RI of calibration solutions cause additional error in these functions. Thus, we include an additional component of error due to calibration functions:

$$n_b^* = cal_b(b^*) = n_b + \Delta n_{b,noise} + \Delta n_{b,drift} + \Delta n_{b,grad} + \Delta n_{b,misc} + \Delta n_{b,cal}$$
$$n_s^* = cal_s(s^*) = n_s + \Delta n_{s,noise} + \Delta n_{s,drift} + \Delta n_{s,misc} + \Delta n_{s,cal} \tag{3.7}$$

3.7.3.3. Quantification of measurement errors in n_b* and n_s*

Precision of n_b and n_s**. Because we reserve the term *precision* to describe components of error which appear truly random, the only components of the error in n_b* and n_s* which we describe in terms of precision are the noise components $\Delta n_{b,noise}$ and $\Delta n_{s,noise}$. The level of imprecision is quantified by the standard deviation of a group of measurements taken close together in time under the same experimental conditions. In accordance with electrical engineering terminology, we also refer to this figure of imprecision as the RMS noise level. Investigation of reproducibility from sensor to sensor (i.e. a specification of reproducibility that takes random manufacturing variations into account) is beyond the scope of this work; therefore, our definition of precision does not attempt to take these variations into account.

Accuracy of n_b and n_s**. All components of error other than the noise component are judged to be systematic (if uncontrolled) errors that are not random in nature. We view changes in the instrument response due to fluctuations in these sources of error as reflecting temporal changes in the accuracy of the instrument, rather than as components of the imprecision of the instrument. We quantify the inaccuracy of our measurements by estimating the maximum amounts by which n_b* and n_s* differ from the true values n_b and n_s during a given experiment.

3.7.3.4. Quantification of measurement errors in N*

Obviously, errors in both n_b* and n_s* will contribute to error in the measured adsorption index $N^*=n_s^*-n_b^*$, as follows:

$$N^* = N + \Delta n_{s,noise} + \Delta n_{s,drift} + \Delta n_{s,misc} + \Delta n_{s,cal} - \Delta n_{b,noise} - \Delta n_{b,drift} - \Delta n_{b,grad} - \Delta n_{b,misc} - \Delta n_{b,cal} \tag{3.8}$$

or, grouping the terms for each source of noise

$$N^* = N + \Delta N_{noise} + \Delta N_{drift} + \Delta N_{misc} + \Delta N_{cal} + \Delta N_{grad} \tag{3.9}$$

where $\Delta N_{noise} = \Delta n_{s,noise} - \Delta n_{b,noise}$, and so forth. The quantifications of the accuracy and precision of N^* follow from the corresponding definitions for n_b^* and n_s^*.

Note that the manner in which these terms subtract to give the corresponding components of error in N^* depends upon the nature of the error. For instance, because the noise components are assumed to behave as random variables with certain standard deviations, it is anticipated that their difference will be another random variable with a standard deviation equal to the square root of the sum of the squares of the two component standard deviations. In contrast, the systematic calibration error $\Delta N_{cal} = \Delta n_{s,cal} - \Delta n_{b,cal}$ is likely to be smaller than its two component errors, because $\Delta n_{s,cal}$ and $\Delta n_{b,cal}$ are determined in similar ways and are likely to be identical in sign and close in magnitude.

Note that the concept of accuracy is not necessarily the best way to quantify the quality of measurements of the adsorption index N. As mentioned in 3.1, because it generally is the instrument's response relative to a calibration standard that is of interest, inaccuracy of N does not usually interfere with interpretation of sensor data, as long as the relationship between N and Γ is repeatable and linear. Thus if N^* were related to N by the relationship

$$N^* = cN \tag{3.10}$$

then N^* would be increasingly inaccurate for increasing values of N, while the measurement quality would remain essentially the same. For this reason, we refrain from using the term "accuracy" to describe the desired quality of n_b^*, n_s^*, and N^*. Instead, we refer to the *linearity* of N^* and of the *collinearity* of n_b^* and n_s^* as the desired qualities of these measurements. For the same reason, the discussion of calibration given in Chapter 5 focuses on using calibration to achieve linearity, rather than absolute accuracy.

The next chapter of this dissertation describes an instrument built to perform SPR/IRR measurements and details experiments performed using that instrument. We will revisit the notions of accuracy and precision towards the end of that chapter to describe the performance exhibited by the instrument during these experiments.

Notes for Chapter 3

[1] E. Stenberg, B. Persson, H. Roos, C. Urbaniczky, Quantitative determination of surface concentration of protein with surface plasmon resonance using radiolabeled proteins, *J. Coll. Int. Sci.* **143** (1991) 513-526.

[2] L. S. Jung, C. T. Campbell, T. M. Chinowsky, M. N. Mar, and S. S. Yee, Quantitative interpretation of the response of surface plasmon resonance sensors to adsorbed films, *Langmuir* **14** (1998) 5636-5648.

[3] R. Karlsson and R. Stahlberg, Surface plasmon resonance detection and multispot sensing for direct monitoring of interactions involving low-molecular-weight analytes and for determination of low affinities, *Anal. Biochem.* **228** (1995) 274-280.

[4] H. Roos, K. Magnusson and R. Karlsson, Liquid handling system demands for kinetic analysis with optical evanescent field biosensors, *Proceedings of the 8th International Conference on Solid-State Sensors and Actuators and Eurosensors IX, Stockholm, Sweden, June 25-29, 1995.*

[5] T. Kaiser, P. Gudat, W. Stock, G. Pappert, M. Grol, D. Neumeier, and P. B. Luppa, Biotinylated steroid derivatives as ligands for biospecific interaction analysis with monoclonal antibodies using immunosensor devices, *Anal. Biochem.* **282** (2000) 173-186.

[6] P-O. Markgren, Markku Hamalainen, and U. Helena Danielson, Kinetic Analysis of the interaction between HIV-1 protease and inhibitors using optical biosensor technology, *Anal. Biochem.* **279** (2000) 71-78.

[7] B. M. McDermott, A. H. Rux, R. J. Eisenberg, G. H. Cohen, and V. H. Racaniello, Two distinct binding affinities of poliovirus for its cellular receptor, J. Biol. Chem. **275** (2000) 23089-23096.

[8] D. G. Myszka, R. W. Sweet, P. Hensley, M. Brigham-Burke, P. D. Kwong, W. A. Hendrickson, R. Wyatt, J. Sodroski, and M. L. Doyle, Energetics of the HIV gp120-CD4 binding reaction, *Proc. Nat. Acad. Sci.* **97** (2000) 9026-9031.

[9] G. B. Sigal, M. Mrksich, and G. M. Whitesides, "Using surface plasmon resonance to measure the association of detergents with self-assembled monolayers of hexadecanethiolate on gold," *Langmuir* **13,** pp. 2749-2755, 1997.

[10] C. Wittekindt, B. Fleckenstein, K-H. Wiesmuller, B. R. Eing, and J. E. Kuhn, Detection of human serum antibodies against type-specifically reactive peptides from the N-terminus of glycoprotein B of herpes simplex virus type 1 and type 2 by surface plasmon resonance, *J. Virol. Meth.* **87** (2000) 133-144.

[11] R. J. Ober and E. Sally Ward, The choice of reference cell in the analysis of kinetic data using BIAcore, *Anal. Biochem.* **271** (1999) 70-80.

[12] R. Karlsson, M. Kullman-Magnusson, M. D. Hamalainen, A. Remaeus, K. Andersson, P. Borg, E. Gyzander, and J. Deinum, Biosensor analysis of drug-target interactions: Direct and competitive binding assays for investigation of interactions between thrombin and thrombin inhibitors, *Anal. Biochem.* **278** (2000) 1-13.

[13] A. Frostell-Karlsson, A. Remaeus, H. Roos, K. Andersson, P. Borg, M. Hamalainen, and R. Karlsson, Biosensor analysis of the interaction between immobilized human serum albunin and drug compounds for prediction of human serum albumin binding levels, *J. Med. Chem.* **43** (2000) 1986-1992.

[14] J. Homola, H. B. Lu, G. G. Nenninger, S. S. Yee, C. T. Campbell, Novel approach to multichannel SPR sensing, *Proc. SPIE* **3857** (198-206).

[15] J. Homola, H. B. Lu, G. G. Nenninger, J. Dostalek, and S. S. Yee, A novel multichannel surface plasmon resonance biosensor, submitted to *Sensors and Actuators B,* 2000.

[16] G. G. Nenninger, J. B. Clendenning, C. E. Furlong, and S. S. Yee, "Reference-compensated biosensing using a dual-channel surface plasmon resonance sensor system based on a planar lightpipe configuration," *Sensors and Actuators B* **51**, pp. 38-45, 1998.

[17] M. J. O'Brien, S. R. J. Brueck, V. H. Perez-Luna, L. M. Tender, and G. P. Lopez, SPR biosensors: simultaneously removing thermal and bulk-composition effects, *Biosensors and Bioelectronics* **14** (1999) 145-154.

[18] J. Melendez, R. Carr, D. U. Bartholomew, H. Taneja, S. Yee, C. Jung, C. Furlong, Development of a surface plasmon resonance sensor for commercial applications, *Sensors and Actuators-B* **38-39** (1997) 375-379.

[19] M. J. Jory, G. W. Bradberry, P. S. Cann, and J. R. Sambles, A surface plasmon based optical sensor using acousto-optics, *Meas. Sci. Technol.* **6** (1995) 1193-1200.

[20] M. Born and E. Wolf, *Principles of optics*, Cambridge: Cambridge University Press, 1999.

[21] E. Hecht and A. Zajac, *Optics*, Reading: Addison-Wesley, 1979.

[22] R. S. Longhurst, *Geometrical and Physical Optics*, London: Longman Group, 1973.

[23] http://www.bs-ltd.com.

[24] http://www.leica.com.

[25] J. Raty, E. Keranen, K-E Peiponen, The complex refractive index measurement of liquids by a novel reflectometer apparatus for the UV-visible spectral range, *Meas Sci Technol.* **9** (1998) 95-99.

[26] H. Li and S. Xie, Measurement method of the refractive index of biotissue by total internal reflection, *Appl. Opt.* (1996) 1793-1795.

[27] J. H. Grassi and R. M. Georgiadis, Temperature-dependent refractive index determination from critical angle measurements: Implications for quantitative SPR, *Anal. Chem.* **71** (1999) 4392-4396.

[28] O. S. Wolfbeis, Capillary waveguide sensors, *Trends in Analytical Chemistry* **15** (1996) 225-232.

[29] G. J. Sprokel and J. D. Swalen, Attentuated total internal reflection method, in *Handbook of Optical Constants of Solids II,* Academic Press, 1991.

[30] J. E. Geake, C. S. Mill, M. S. Mohammad, A linear differentiating refractometer, *Meas Sci Technol.* **5** (1994) 531-539.

[31] G. H. Meeten, Refractive index errors in the critical-angle and the Brewster-angle methods applied to absorbing and heterogenous materials, *Meas. Sci. Technol.* **8** (1997) 728-733.

[32] L. Haussling, H. Ringsdorf, F.-J. Schmitt, and W. Knoll, Biotin functionalized self-assembled monolayers on gold: Surface plasmon resonance optical studies of specific recognition reactions, *Langmuir* **7** (1991) 1837-1840.

[33] C.-G. Golander and E. Kiss, Protein adsorption on functionalized and ESCA-characterized polymer films studied by ellipsometry, *J. Coll. Int. Sci.* **121** (1988) 240-253.

[34] J. A. DeFeijter, J. Benjamins, and F. A. Veer, Ellipsometry as a tool to study the adsorption behavior of synthetic and biopolymers at the air-water interface, *Biopolymers* **17** (1978) 1759-1772.

[35] R. G. C. Oudshoorn, R. P. H. Kooyman, and J. Greve, Refractive index and layer thickneess of an adsorbing protein as reporters of monolayer formation, *Thin Solid Films* **284-285** (1996) 836-840.

[36] G. E Perlmann and L. G. Longsworth, The specific refractive increment of some purified proteins, J. Am. Chem. Soc. **70** (1948) 2719-2724.

[37] J. Wen, T. Arakawa, and J. S. Philo, Size-exclusion chromatography with on-line light-scattering, absorbance, and refractive index detectors for studying proteins and their interactions, *Anal. Biochem.* **240** (1996) 155-166.

[38] T. M. Chinowsky, A. Strong, D. U. Bartholomew, S. Jorgensen-Soelberg, T. Notides, C. E. Furlong and S. S. Yee, Improving surface plasmon resonance sensor performance through combination with critical angle refractometry, *Proc. SPIE* **3857** (1999) 104-113.

[39] H. E. deBruijn, B. S. F. Altenburg, R. P. H. Kooyman, and J. Greve, Determination of thickness and dielectric constant of thin transparent dielectric layers using surface plasmon resonance, *Opt. Commun.* **82** (1991) 425-432.

[40] F. C. Mish, ed., *Webster's Ninth New Collegiate Dictionary,* Springfield: Merriam-Webster, 1985.

[41] P. R. Bevington, *Data Reduction and Error Analysis for the Physical Sciences,* New York: McGraw-Hill, 1969.

[42] R. B. Murphy, On the meaning of precision and accuracy, *Mater. Res. Stand.* **1** (1961) 264-7.

[43] R. Ekins and P. Edwards, On the meaning of "sensitivity", *Clin. Chem.* **43** (1997) 1824-1837.

[44] J. Buttner, R. Borth, J. H. Boutwell, and P. M. G. Broughton, IFCC approved recommendations on quality control in clinical chemistry. Part 1. General principles and terminology. *Clin. Chim. Acta* **98** (1979) 129F-143F.

[45] D. G. Fink and D. Christiansen, eds., *Electronics Engineer's Handbook*, New York: McGraw-Hill, 1989.

[46] *BIACORE 2000 Instrument Handbook*, Biacore AB, 1996.

Chapter 4: The SPR/IRR sensor: bulk RI compensated SPR measurements

The previous chapter of this dissertation described how the problem of bulk RI interference can be overcome by measuring simultaneously measuring both the SPR response and the bulk RI of the analyte. We showed that IRR was a simple and robust technique for measuring bulk RI. This chapter describes an instrument which implements the SPR/IRR technique.

Our instrument measures SPR and IRR using a modification of the design of the Spreeta SPR sensor developed by Texas Instruments. This sensor was described in section 1.5 of this dissertation.

Fig. 4.1a shows how SPR/IRR sensing can be implemented by a very simple modification of the Spreeta design. Because the sensor's light source emits a diverging beam, the beam strikes the sensor surface not at a single point, but rather at a distributed area (roughly, an ellipse). The angle at which light is incident upon this surface will vary with the location on the surface. The incident angle increases at points further away from the base of the sensor. For a given analyte, incident angles below the critical angle will strike closer to the base of the sensor, while incident angles above the critical angle will strike closer to the top of the sensor.

Because the angular of incidence varies with location on the sensor surface, a combination SPR/IRR measurement can be obtained simply by depositing gold only on the portion of the sensor surface corresponding to incident angles above the critical angle. The sensor will then deliver a composite spectrum which combines an SPR spectrum with a "IRR spectrum" which may be used for measurements of bulk RI. The range of RIs which can be examined is limited to those values for which the gold edge remains between the critical angle and the SPR dip. In simulations assuming a monochromatic light source and idealized sensor behavior, this range is approximately 3×10^{-2}. Because our experimental SPR dips are broader than ideal spectra due to the bandwidth of the LED light source and because a portion of the SPR/IRR spectra near the gold edge is occupied by a spike attributed to diffraction, the practical range will be somewhat less, closer to 1.5×10^{-2}. Simulated SPR/IRR spectra and actual spectra measured using our SPR/IRR instrument are shown in Fig. 4.1b-c.

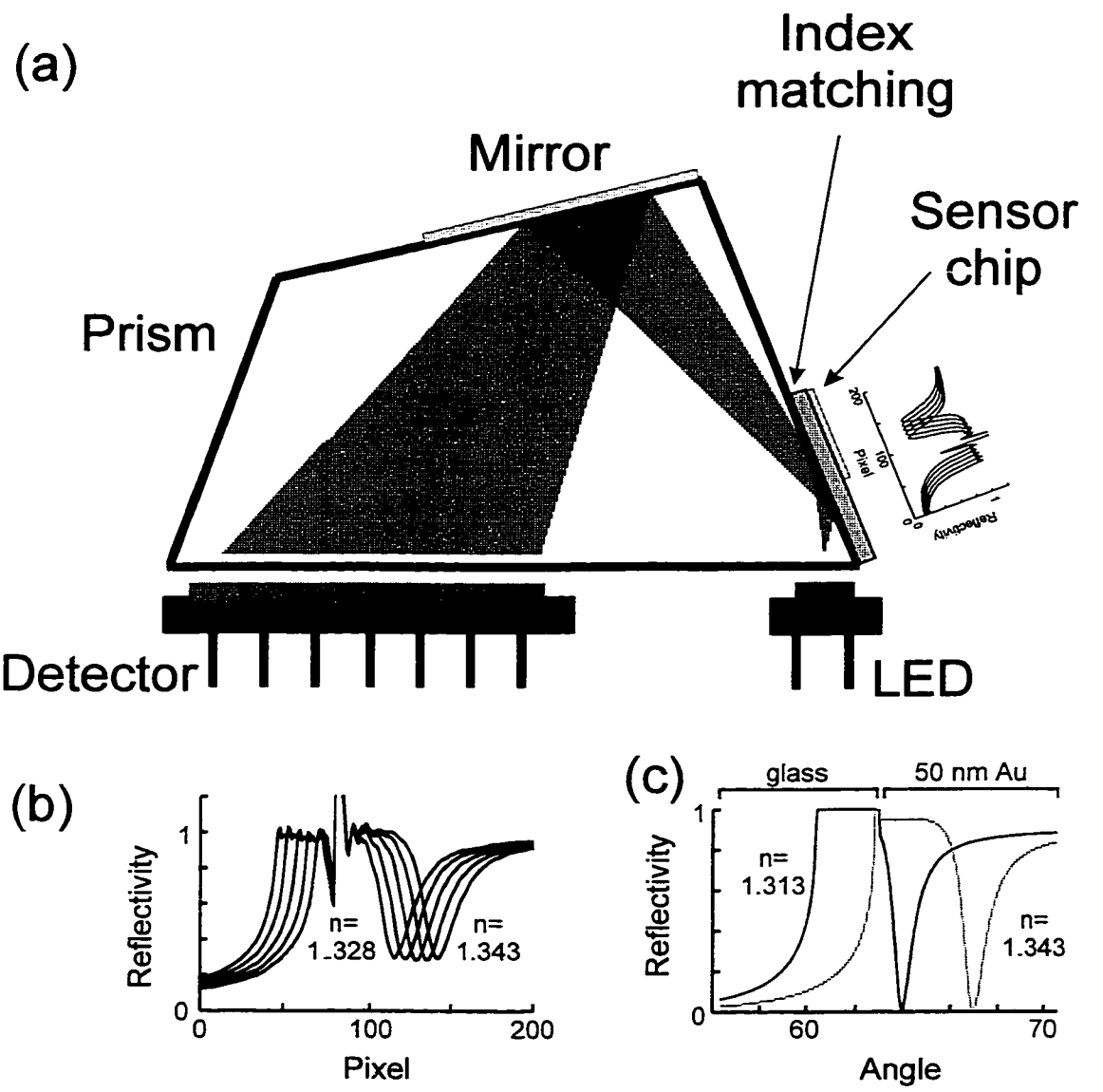

Figure 4.1. SPR/IRR sensing geometry. (a) The SPR/IRR sensor has separate LED, detector, and glass prism, compared to the one-piece molded plastic construction of TI's Spreeta. The sensor chip is half-gold-coated and index-matched to the prism with oil; in the TI device, the chip is completely gold coated and epoxied to the plastic prism. (b) Experimental SPR/IRR spectra measured in sucrose solution of varying concentration. (c) Simulated SPR/IRR spectra illustrating the theoretical range of the sensor.

4.1. Instrument design issues for bulk RI compensation

For the SPR/IRR compensation method to be as effective in practice as it is in simulations (such as that of Fig. 3.5), two aspects of the SPR/IRR instrument must be optimized: bulk RI uniformity and instrument temperature response.

4.1.1. Bulk RI uniformity

For critical angle compensation to be as effective as possible, the IRR measurement must determine the bulk RI exactly adjacent to the adsorbate measured by SPR. Because the IRR and SPR measurements take place at slightly different locations in the SPR/IRR sensor, the sensor must be designed to produce a uniform bulk RI over the sensor surface. A nonuniform bulk RI may arise from two sources: (1) variation in the chemical composition of the analyte across the sensor surface; and (2) variation in the analyte temperature. Minimization of each source of variation requires different engineering considerations.

For bulk RI variation due to composition, any changes in the bulk RI of the analyte being drawn into the sensor flow cell will result in nonuniform bulk RI along the flow channel. If the location at which bulk and surface RI are measured are separated along the direction of flow, this bulk RI at these two locations will differ. Ideally, the flow direction would be perpendicular to the separation between bulk and surface RI measurement locations; however, this would require a much wider flow channel. In the work presented here, the separation is parallel to the flow direction. The possibility of error resulting from RI nonuniformity due to composition variations must therefore be accounted for as data are interpreted.

Any nonuniformity in the temperature of the analyte may also result in nonuniform bulk RI. Liquid entering the flowcell at a different temperature than that of the flowcell itself will equilibrate as it flows, creating a temperature gradient along the direction of flow. The analyte must be allowed enough time to equilibrate in temperature before measurement. If the temperature of the analyte is to be intentionally varied by heating or cooling the flowcell, the temperature change must be uniform.

4.1.2. Instrument temperature response

Minimizing temperature nonuniformity in the analyte is necessary to achieve good critical angle compensation of bulk RI effects due to temperature. For general temperature compensation, however, this is only one consideration. If the temperature variation extends beyond the analyte to other instrument components, as it will if the instrument is in an uncontrolled environment, the instrumental effects of these temperature variations must be considered. The wavelength distribution, output flux, and output distribution of the sensor's LED light source will all have some temperature dependence. The dark current and quantum efficiency of the diode array detector will vary with temperature. The size and RI of the sensor's prism, sensing chip, and index matching fluid will all change with temperature. The aluminum fixture holding the sensor components in place will vary in size with temperature, with resulting translation of the prism, light source, and detector. These temperature effects will have a complicated influence on both SPR and IRR measurements, and must be taken into account if the instrument is to operate in an uncontrolled environment.

4.2. Optics

The apparatus used for these experiments is shown schematically in Fig. 4.2. The sensing element consists of a half gold-coated glass slide index-matched to a BK7 prism using index matching oil (Cargille). The prism refractive index and dimensions were chosen to approximate those of the plastic prism of the Spreeta sensor. A TM-polarized 830 nm LED light source and a diode array detector are mounted at the base of the prism on separate X-Y positioners. The light source was taken from an unencapsulated Spreeta sensor board obtained from TI. Because the unencapsulated detectors are fragile, an encapsulated detector was extracted from a Spreeta sensor by cutting away the plastic prism close to the detector and polishing the surface of the remaining plastic. A 0.5 mm air gap separates the LED and detector from the prism.

4.3. Flowcell

The analyte is guided across the sensor surface by a flowcell clamped to the sensor surface. The flow channel is formed by a 0.6 mm thick silicone gasket containing a

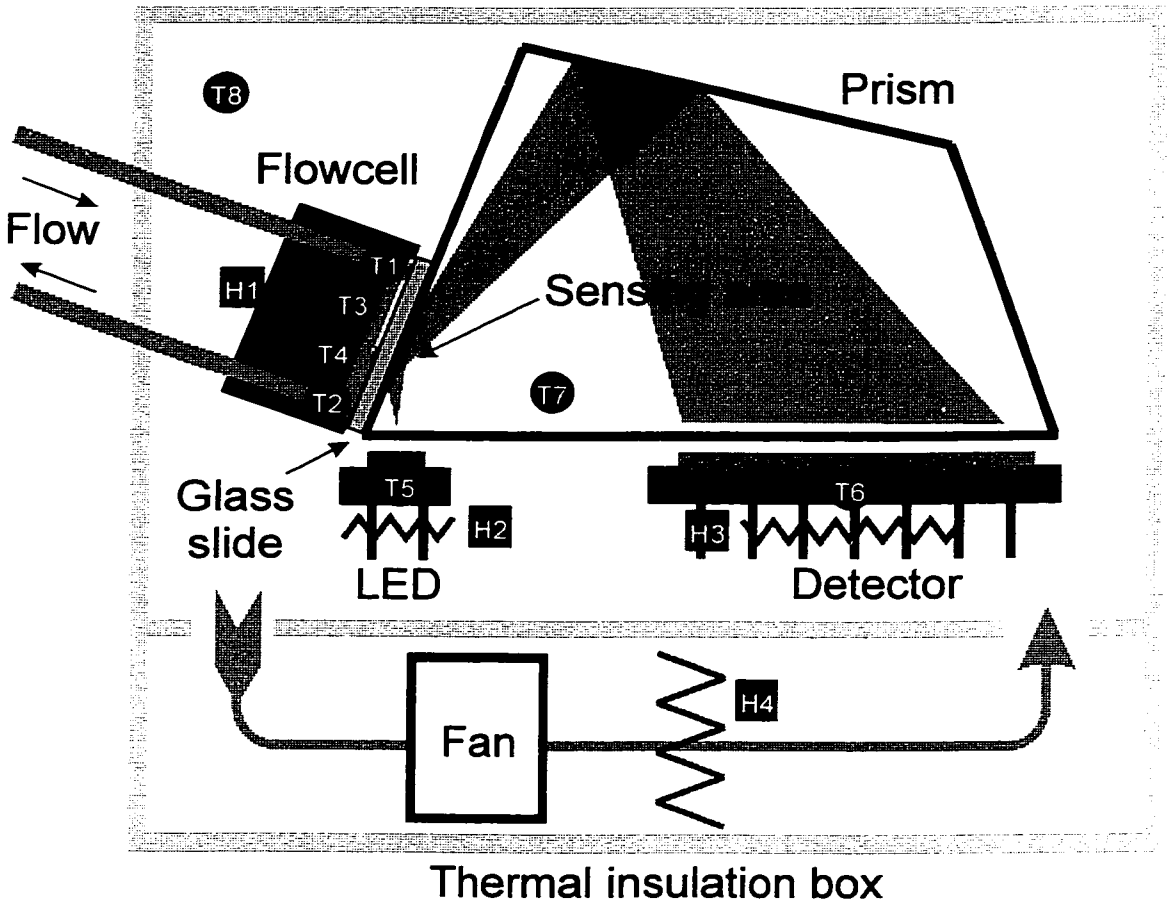

Figure 4.2. Schematic of SPR/IRR instrument, showing locations of thermocouples (T1-T8) and heaters (H1-H5).

serpentine cutout approximately 8 cm long and 2.4 mm wide (Fig. 4.3). A black Delrin block containing fluidic connectors presses the gasket against the sensor surface, forming a flow cell with a volume of approximately 115 μL.

The flow channel winds back and forth across the width of the prism, crossing the gold-glass border four times. By proper positioning of LED and detector, any of these crossing regions may be used for sensing. By placing the sensing spot in the region closest to the flowcell output, the analyte will thermally equilibrate to the flow cell and prism in the long flow length of the cell before the sensing region, and sensing disturbances due to temperature variations of the input analyte will be minimized.

To vary the temperature of the analyte, a thermoelectric heater/cooler (H1 in Fig. 4.2) is built into the flowcell. A rectangular cutout was milled in the back side of the Delrin block, leaving a thin layer of plastic at the side of the block facing the sensor surface. A 3 mm thick aluminum plate was fixed to the bottom of this cutout with thermal epoxy. A sandwich of two TE devices (Marlow DT3-4) was then placed in the cutout, and topped with a 20 mm x16 mm x 25 mm vaned aluminum heat sink . Thermal grease was placed in each joint of the heat sink/TE device/TE device/Al plate sandwich, which was then clamped together by screws mating to holes tapped in the Delrin block.

4.4. Temperature measurement and control

Eight 0.005" diameter K-type thermocouples (T1-T8 in Fig. 4.2) measure the temperature at various places in the instrument. Thermocouples were placed in the input and output fluid stream (T1, T2), on opposite sides of the aluminum plate which adjoins the flowcell wall (T3, T4), on the LED light source (T5), on the diode array detector (T6), and on the aluminum prism mount (T7). The instrument was placed in an insulating foam box. Thermocouple T8 measured the air temperature inside of the box. Temperature data were acquired using an eight channel thermocouple amplifier built using Analog Devices AD595 and Linear Technology LT1006 integrated circuits. Amplifier outputs were digitized to 12 bits.

Four heaters (H1-H4) allow control of the temperature of various instrument components. In addition to the flowcell heater (H1) previously described, small nichrome wire heaters were attached to the LED (H2) and diode array detector (H3).

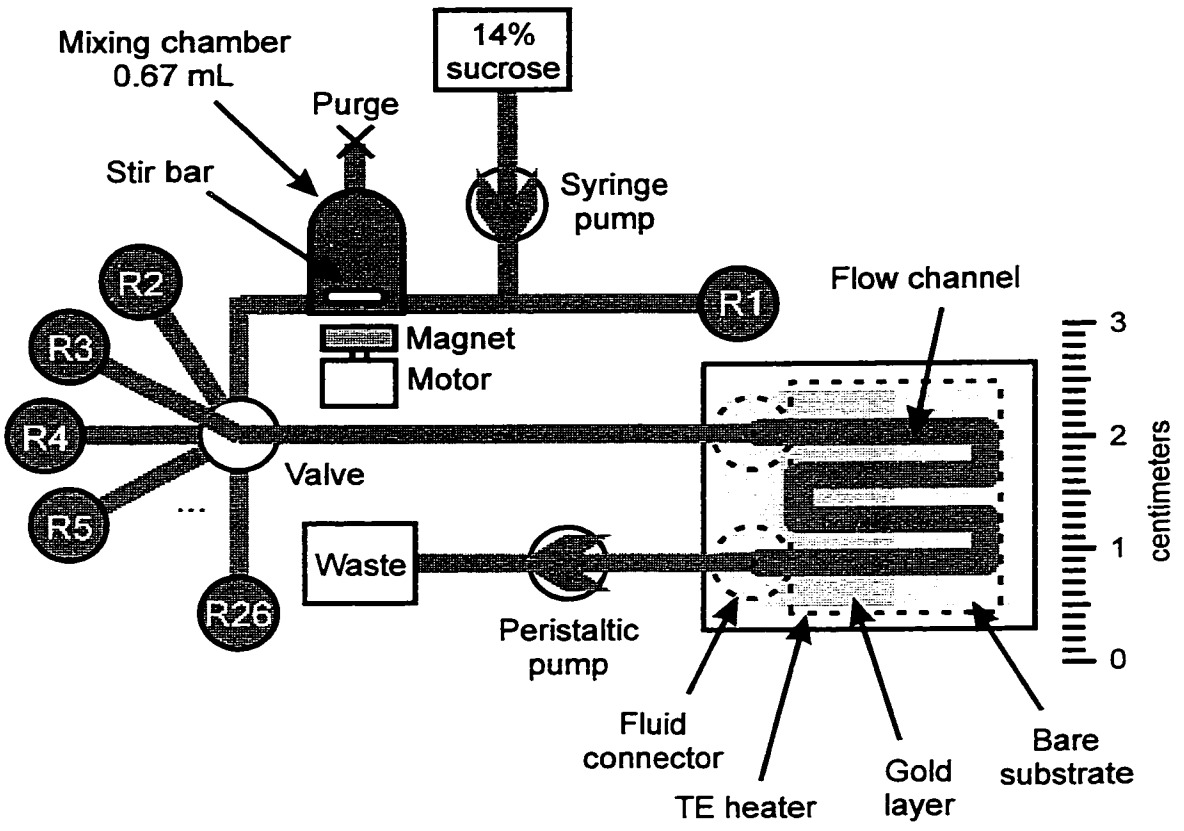

Figure 4.3. Fluid handling for the SPR/IRR instrument, including scale drawing of serpentine flowcell.

A small fan-forced space heater (H4) placed in the foam box provided a means for heating the air inside the box.

4.5. Reagent handling

A peristaltic pump (Cole-Parmer) connected to the flowcell output draws analyte through the flowcell (Fig. 4.3). A multiposition valve (Valco) at the flowcell input can select one of up to 26 sources of reagent. The valve and pump may be computer-controlled by RS-232 interface. To perform automated experiments, the valve can be programmed to switch between reagents at appropriate times, and the flow rate of the pump can be controlled.

4.5.1. Gradient calibration

One step in the sensor calibration is to expose the sensor to a solution which slowly varies over the RI range of interest (see section 5.6). To achieve this, one of the input streams (R1) is connected at a T-junction to a computer-controlled syringe pump (Yale Apparatus) containing 14% sucrose solution. When reagent stream R1 is selected, the syringe pump may be controlled to introduce an RI gradient into that stream. The stirred mixing chamber (volume V) following the T-junction serves to mix the sucrose thoroughly and to smooth out imperfections in the pumping speed of the syringe pump.

Because the mixing chamber is completely filled with liquid (the purge valve on top of the chamber helps to establish this condition) and tightly sealed except for its two fluid connections, the rate q_s at which the syringe pumps and the rate q_r at which reagent is drawn from R1 will sum to the peristaltic pump rate q_p. The syringe is controlled such that $q_s < q_p$ always, preventing backflow of sucrose solution into R1.

In this configuration, the sucrose concentration of the solution leaving the mixing chamber (and, by assumption, the uniform concentration of the solution inside the chamber) is described by the differential equation

$$\frac{dc_{out}}{dt} = \frac{q_p}{V}(c_{in} - c_{out}) \tag{4.1}$$

If a particular output concentration profile is desired, this equation must be solved to determine how c_{in} must vary to produce that profile. If a linear ramp of c_{out} is desired, a solution of Eq. 4.1 by Laplace transform predicts that a fairly simple input profile should produce this ramp (Figs. 4.4a, b, c, d). Measurements of a sucrose gradient produced using this procedure (Fig. 4.4e) shows that this procedure succeeds in producing a ramp approximately linear in refractive index. Fig. 4.4c illustrates one practical limitation of this technique -- to produce a downward linear ramp ending at zero concentration, the input concentration must go below zero, a physical impossibility. In Fig. 4.4e, this obstacle was overcome by adding a positive offset to the desired concentration. For a downward gradient in which the final concentration of zero is desired, an exponential tail is unavoidable (e.g. Fig. 4.5).

4.6. Experimental evaluation of SPR/IRR sensor performance

Our goals in designing experiments to evaluate the performance of the SPR/IRR sensor were the following:

- Examine how well the instrument compensates for bulk RI changes due to analyte composition. Compensation performance should be evaluated both with and without the presence of an adsorbed layer on the sensor.
- Examine how well the instrument compensates for bulk RI changes due to rapid and substantial changes in analyte temperature. Again, performance should be evaluated with and without the presence of an adsorbed layer.
- Examine how well the instrument compensates when the ambient temperature changes. If the instrument response changes more than would be expected from the expected changes in analyte temperature, determine the additional sources of variation.

We have not attempted to evaluate these aspects of the instrument's performance by demonstrating the instrument's performance in the biosensing applications for which we believe SPR/IRR will be useful. Rather, we have developed a simple set of experimental techniques based on detergent adsorption which we believe to be a more efficient and straightforward way of evaluating the performance of this type of sensor.

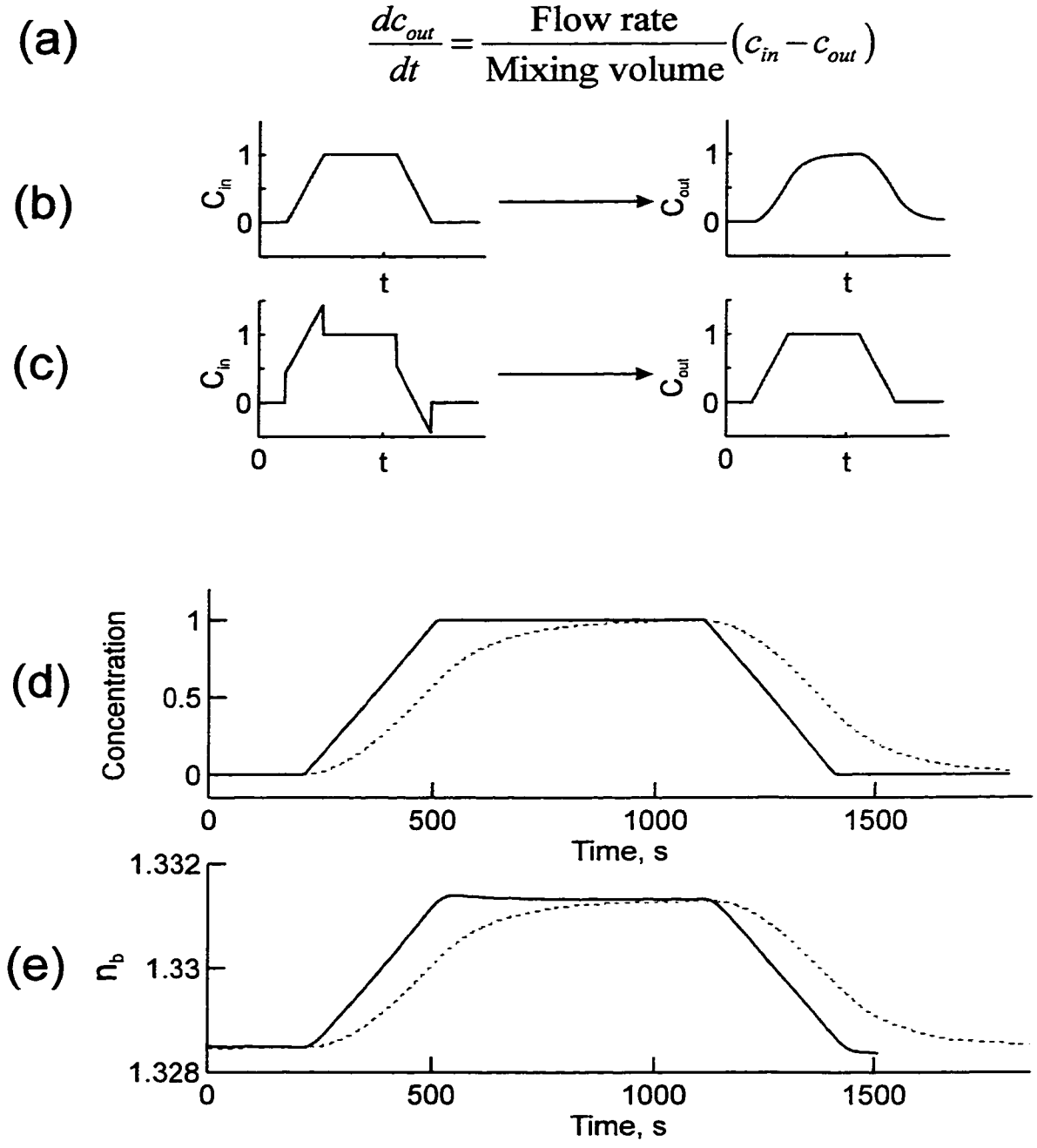

Figure 4.4. Production of linear RI gradient. (a) Differential equation relating mixing chamber input and output concentration (b) Simulated output for linear ramp input (c) Simulated output for input corrected to give linear ramp output (d) Comparison of corrected and uncorrected simulation (e) Experimental bulk RI gradients created using uncorrected and corrected concentration input.

Our techniques produce optical conditions similar to those expected to be encountered in biosensing experiments while avoiding the time-consuming and expensive biochemical complexities of those experiments. Experiments performed using our techniques can more quickly and easily be repeated than can biological binding experiments.

The use of detergent adsorption for evaluation of SPR/IRR sensor performance was inspired by our observation that when a the bare gold surface of an SPR sensor is exposed to a solution of a detergent such as Triton X-100 (TX100) or sodium dodecyl sulfate (SDS) then a thin adsorbed layer of detergent forms on the surface. When the detergent solution is replaced by a detergent-free solution, the adsorbed layer quickly washes away. Subsequently, we found that this had also been observed by Sigal *et al.* on a gold surface covered with a thiol monolayer [1]. Sigal also observed that the thickness of the adsorbed layer remained constant as long as the detergent concentration was above the critical micelle concentration (cmc) for that particular detergent. Thus, at concentrations above the cmc, adsorption of detergent provides a simple and quickly reversible way of producing an adsorbed layer of constant thickness on the sensor surface.

In the experiments presented here, we used TX100 at concentrations above the cmc to produce adsorbed layers on bare gold surfaces. The formation of this adlayer was found to cause an increase in surface RI of approximately 10^{-3}, very similar to what was observed by Sigal on thiolated surfaces. Note that this is quite a large RI effect, larger than would be expected in many biosensing experiments. Bulk RI compensation in the presence of such a substantial adsorbed layer is more difficult, because the instrument must maintain linearity across a greater range in order to achieve good subtractive compensation. Thus, our tests of bulk RI compensation are more demanding than tests conducted using thinner adsorbed layers would be.

In our experiments, we produced bulk RI variations due to composition by exposing the sensor to sucrose solutions of varying concentration. The dependence of the RI of sucrose solutions upon sucrose concentration is well known (e.g., [2]) and is often utilized for measurement of the concentration of sucrose and other sugars in the food and beverage industry. Bulk RI variation due to analyte temperature were produced using the flowcell heater. Variations in the ambient temperature of the instrument were produced using the space heater H4 described above.

Each experiment included one or more calibration steps. At the beginning of each experiment, the sensor was exposed to a bulk RI gradient to calibrate the SPR response relative to the IRR response. During selected experiments, the sensor was also exposed to five discrete RI steps to verify the absolute RI calibration.

For all experiments, the analyte flow rate was 300 µl/min. Reflection spectra were measured and recorded approximately every 2 s. Spectra were analyzed and combined with calibration information as described in Chapter 5 to extract from each spectrum a value for the bulk RI n_b and the surface RI n_s. Note that one property of the data analysis procedure is that the gradient calibration defines the range of the sensor -- data outside the range of calibration are treated as missing values. This is the cause of occasional gaps in the data that follow.

Thermocouple readings were measured and recorded approximately every second. Because much of the temperature data are redundant, only relevant data are presented.

4.6.1. Quality of composition compensation

Figs 4.5 and 4.6 illustrate the ability of the SPR/IRR sensor to compensate for bulk RI variations due to analyte composition. Fig. 4.5 shows that during sucrose gradients causing a bulk RI variation of $\sim 6 \times 10^{-3}$, bulk and surface response match to within $\sim 3 \times 10^{-5}$, or 0.5% of the variation in n_b.

The ability of the SPR/IRR sensor to compensate for bulk RI in the presence of adsorption is illustrated in Fig. 4.6. Here, following the first sucrose gradient, reagent R1 was changed from water to 3 mM TX-100, with the idea that the TX-100 would produce an adsorbed layer on the sensor surface which would retain a constant thickness while the bulk RI above the layer varied due to the changing sucrose concentration. While the TX-100 concentration will vary by 25% as the sucrose concentration changes, it was anticipated that because the concentration is always well above the critical micelle concentration (cmc) of 0.3 mM, the adsorbed layer would not be sensitive to such variations.

The results of Fig. 4.6 are consistent with these assumptions. TX-100 adsorption is found to produce an adsorption index of 9×10^{-4}, with a variation of 5×10^{-5} during bulk RI changes of 4.2×10^{-3}, or 1.2%.

4.6.2. Quality of temperature compensation, flowcell heated

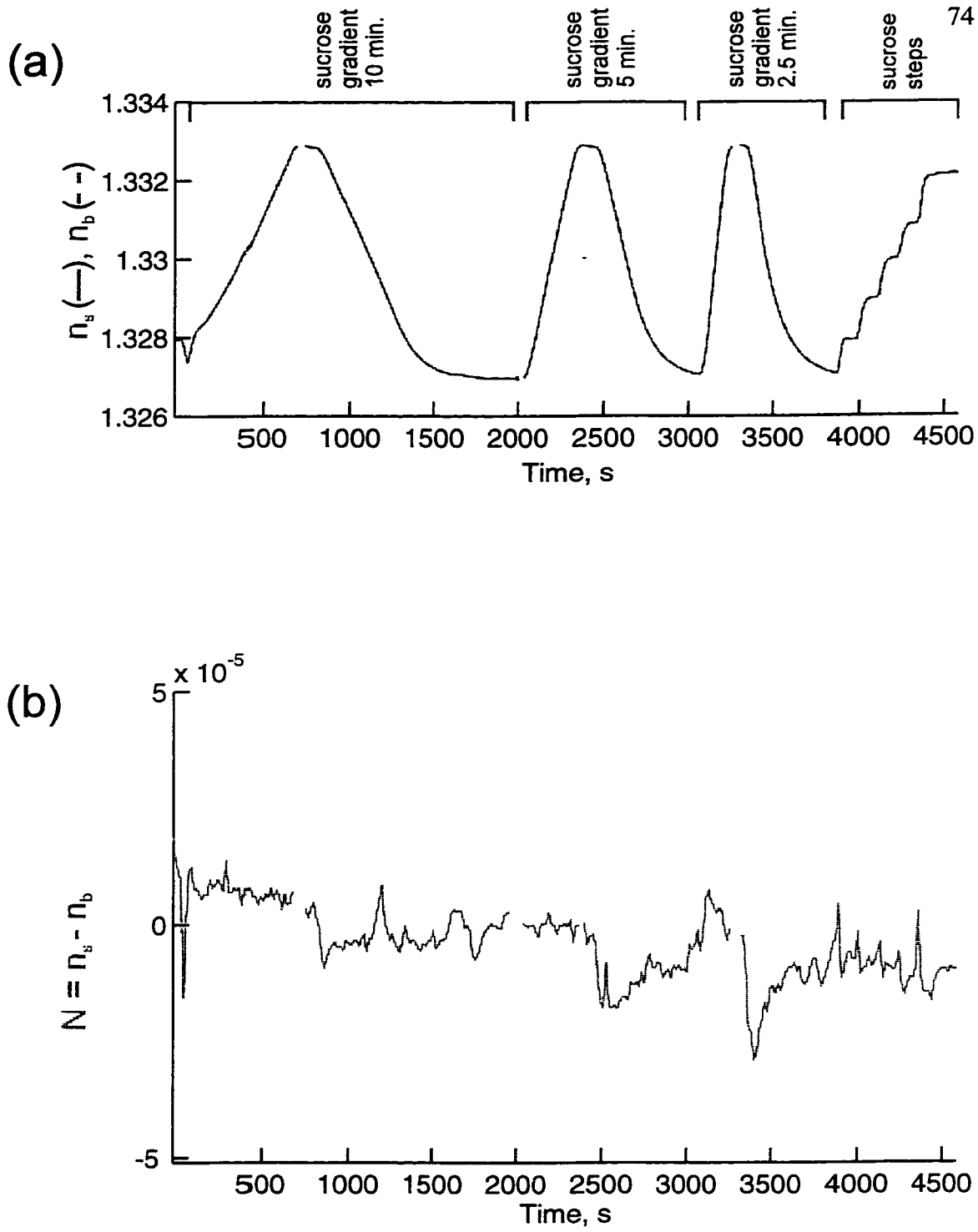

Figure 4.5. SPR/IRR composition compensation. (a) Measurement of n_a and n_b. (b) Adsorption index N.

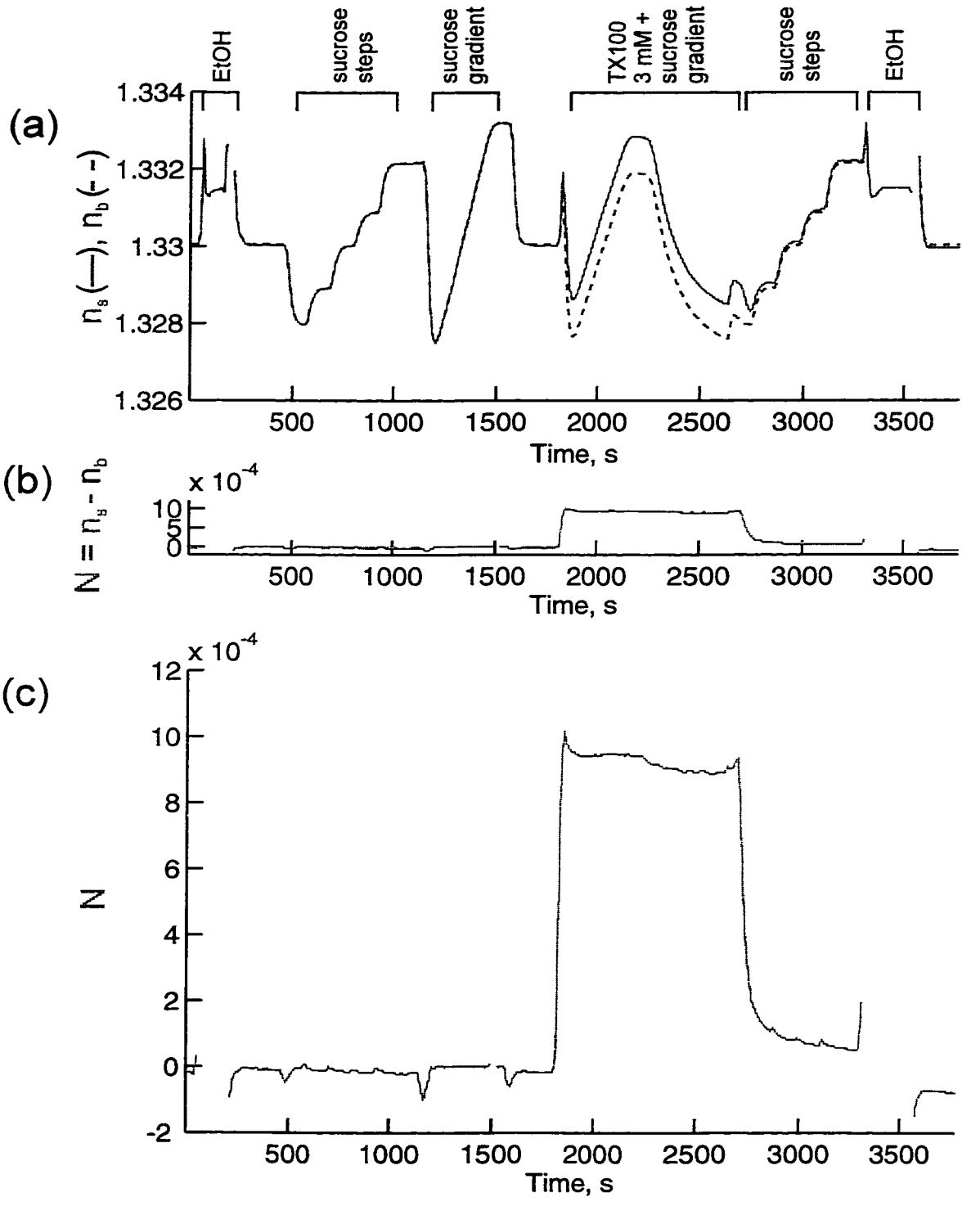

Figure 4.6. SPR/IRR compensation for composition on bare gold and with TX-100 adlayer. (a) Measurement of n_s and n_b. (b) Adsorption index N (c) N, expanded scale

Fig. 4.7 quantifies the ability of the SPR/IRR sensor to compensate for bulk RI variations due to analyte temperature. Here, heating and cooling of the flowcell during flow of 2.1% sucrose and 0.9 mM TX-100 solution produced ~1.5 x 10^{-3} variation in bulk RI. This variation is compensated fairly well, producing a variation in N of ~7 x 10^{-5}, or 4.7%, in sucrose solution, and slightly greater in TX-100.

During repeated temperature compensation experiments, compensation error was found to vary from day to day, both in sign and in magnitude, from 2% to 7%. These fluctuations suggest thermal instability in the instrument. This possibility is examined further in 4.6.5 below.

4.6.3. Quality of compensation, instrument heated

To investigate the ability of the SPR/IRR sensor to compensate for temperature variations in the instrument as a whole, experiments were performed in which the air surrounding the instrument was heated. Heating of the entire instrument from 22 C to 33 C by exposing it to heated air for 25 minutes was found to cause a change in N of -3.5 x 10^{-4} (Fig. 4.8). The shift in N caused by instrument heating is of most concern if it is accompanied by a degradation in compensation. The four flowcell temperature events measured in 2.1% sucrose are compensated to within ~ 10^{-4}, similar to compensation measured without heating. However, the measurement of N during the second sucrose gradient in Fig. 4.8 indicates that the quality of composition compensation has been affected. During bulk RI variations of 4 x 10^{-3}, bulk and surface response match to within 9 x 10^{-5}, 3 times worse than compensation measured with no heating. Near the end of the experiment, heating and cooling of the flowcell during flow of 0.9 mM TX-100 is compensated to within a variation of N of 2 x 10^{-4}, 2 times worse than previously measured with no heating.

4.6.4. Nature of LED & detector contribution to compensation error

The shift in N observed in Fig. 4.8 may be partly explained by LED and detector heating. In Figs. 4.9 and 4.10, the LED and detector, respectively, were heated, and the effect on N was observed. LED heating of 11 C resulted in a shift in N of -4.5 x 10^{-4}, while a rise of 11 C in detector temperature caused a shift of 2 x 10^{-4}. In both experiments, compensation was notably degraded. The bulk RI gradient at the end of

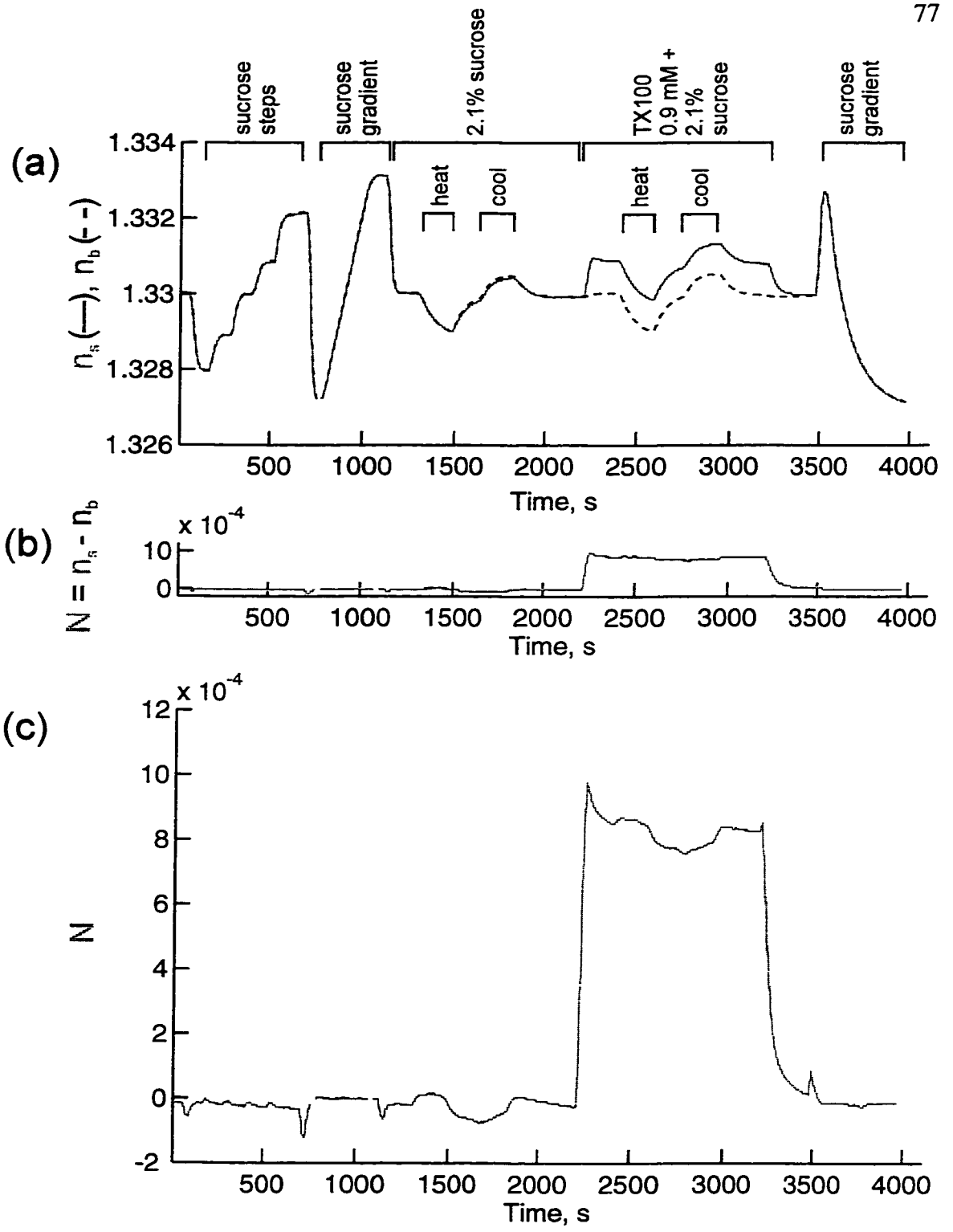

Figure 4.7. Compensation for temperature on bare gold and with TX-100 adlayer. (a) Measurement of n_s and n_b. (b) Adsorption index N (c) N, expanded scale

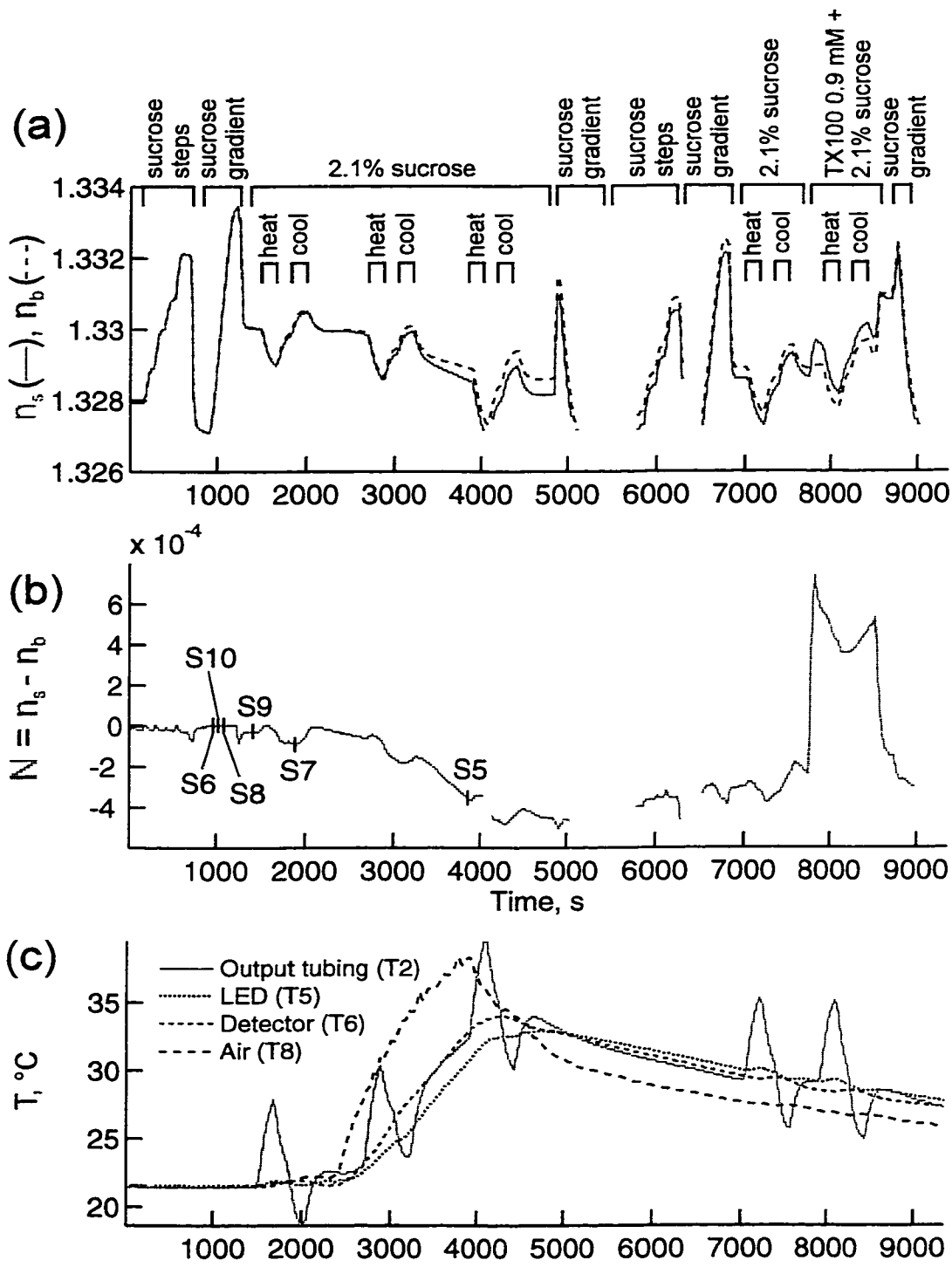

Figure 4.8. Compensation during instrument heating. (a) Measurement of n_s and n_b. (b) Adsorption index N (c) Temperature. Times of measurement of spectra S5-S10 analyzed in Fig. 2.15 are indicated.

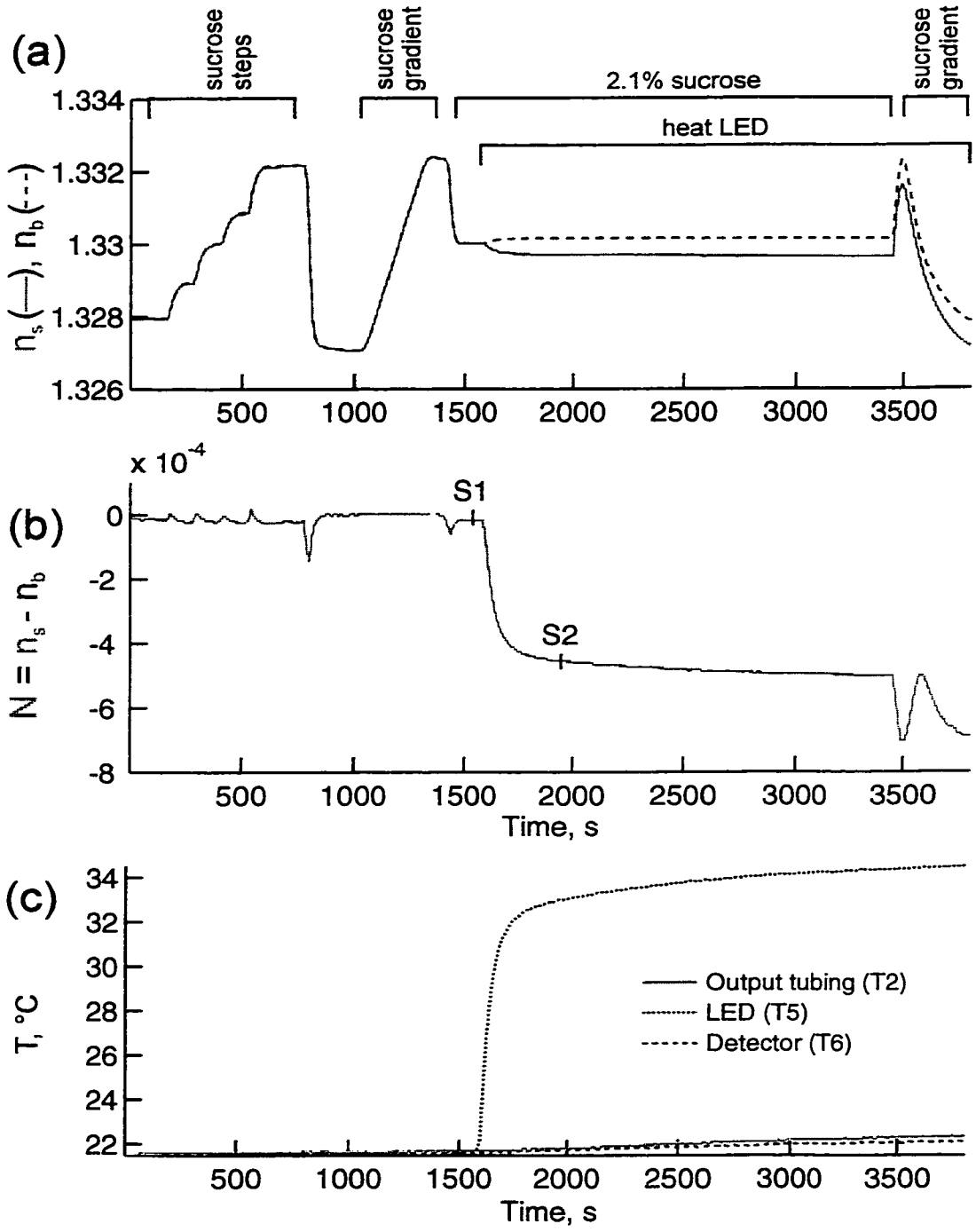

Figure 4.9. LED heating experiment. (a) Measurement of n_s and n_b. (b) Adsorption index N (c) Temperature. Times of measurement of spectra S1-S2 analyzed in Fig. 2.14 are indicated.

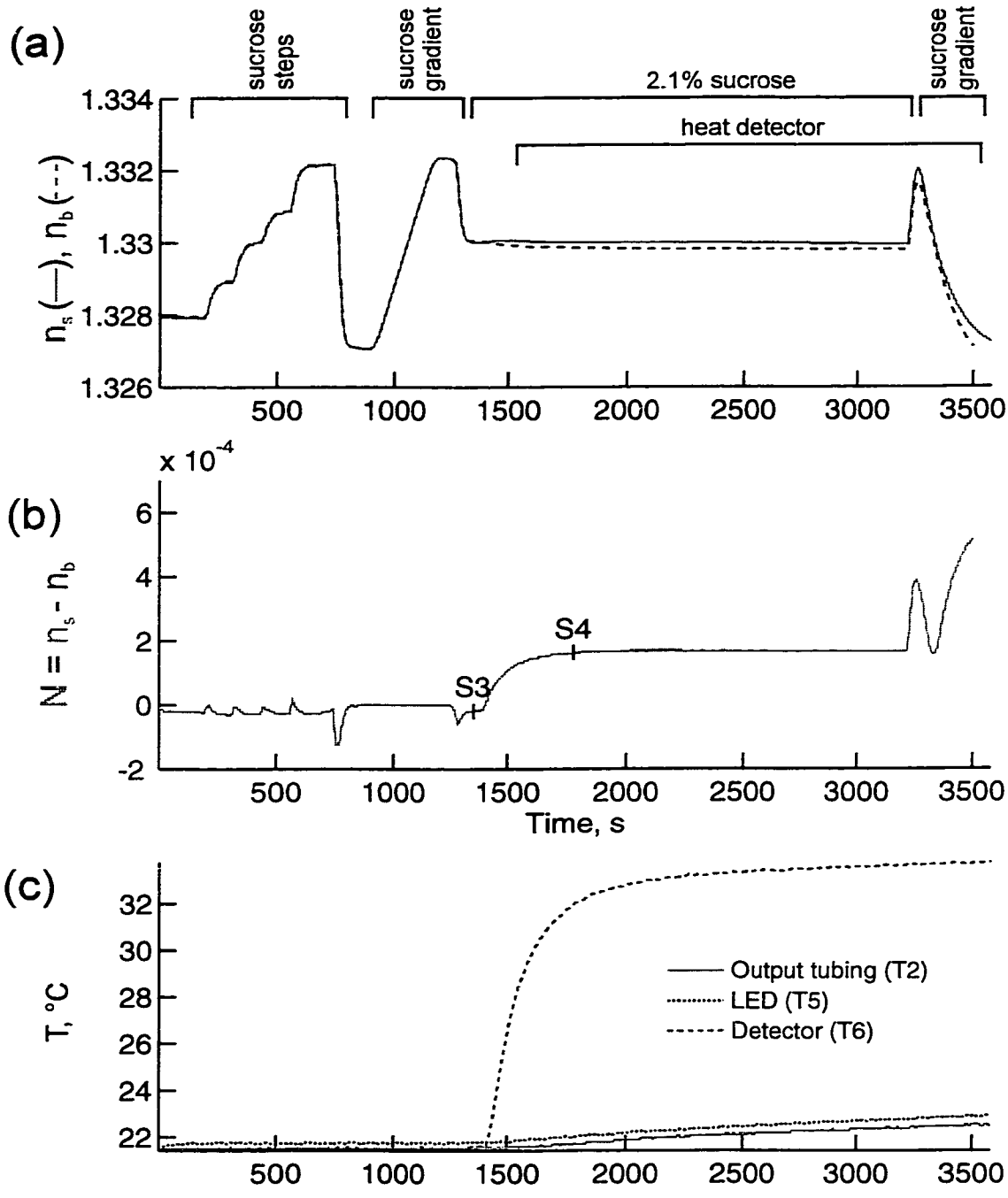

Figure 4.10. Detector heating experiment. (a) Measurement of n_s and n_b. (b) Adsorption index N (c) Temperature. Times of measurement of spectra S3-S4 analyzed in Fig. 2.14 are indicated.

each experiment, which produced a variation in n_b of 4.5 x 10^{-3}, was compensated to within 2 x 10^{-4}, 6 times worse than with no heating.

To characterize the effect of LED heating on SPR/IRR spectra, we examine simulated spectral derivatives with respect to LED intensity and wavelength (Fig. 4.11a, b). SPR and IRR spectra *S* were calculated assuming the broadband LED described in the discussion of the TI sensor in Chapter 1. The derivative dS/dI_0 with respect to incident intensity will be proportional to the spectrum itself: The measured intensity $S(\theta)$ at a given incident angle θ is the product of the reflectivity at that angle with the incident intensity at that angle. If we write the incident intensity in turn as the product of an overall intensity I_0 with a angular component $I(\theta)$ we have

$$S(\theta) = I_0 I(\theta) R(\theta) \tag{4.2}$$

then

$$\frac{dS}{dI_0} = I(\theta) R(\theta) \propto S \tag{4.3}$$

The derivative $dS/d\lambda$ was calculated numerically. The SPR portion of $dS/d\lambda$, the derivative with respect to wavelength, is very similar in form and opposite in sign to dS/dn_b, the derivative with respect to bulk RI (4.11c). The IRR portion is nonzero due to the dispersion of glass and water, but it is small compared to the SPR portion.

To compare these simulations to the observed effects of LED heating, we calculate the difference between spectra *S1* and *S2* measured before and during LED heating (Fig. 4.12a), and observe that the difference may be interpreted as a sum of the effects of changing intensity and wavelength. In the IRR portion of the spectrum, a scaled plot of *S1* fits *S2-S1* well (indicating a change in intensity). The observed decrease of 2.9% suggests a negative temperature coefficient of emission equal to -2.9%/11 C = -0.26%/C. Upon subtracting the scaled *S1* from *S2-S1*, the remainder is similar in form to $dS/d\lambda$. We estimate the wavelength shift by comparing the magnitude of this remainder with the simulated derivative. The magnitude of the remainder is approximately 0.043 peak-to-peak, compared with 0.019 peak-to-peak for the simulated derivative. This suggests that a wavelength shift of 0.043/0.019 = 2.26 nm

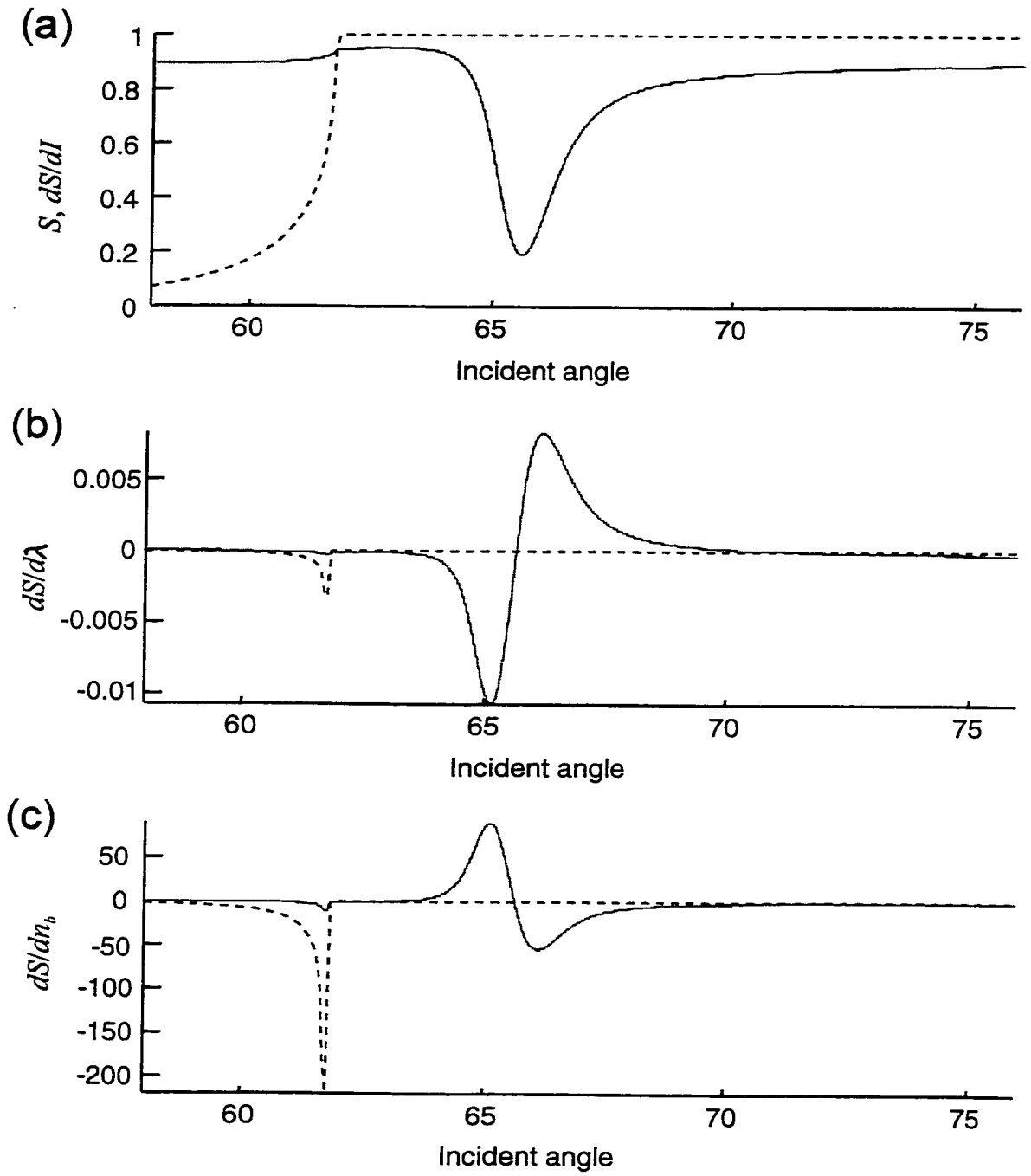

Figure 4.11. Simulated spectral derivatives. (a) S, dS/dI. (b) $dS/d\lambda$. (c) dS/dn_b. solid line: 50 nm gold layer. dashed line: no gold layer (dashed line).

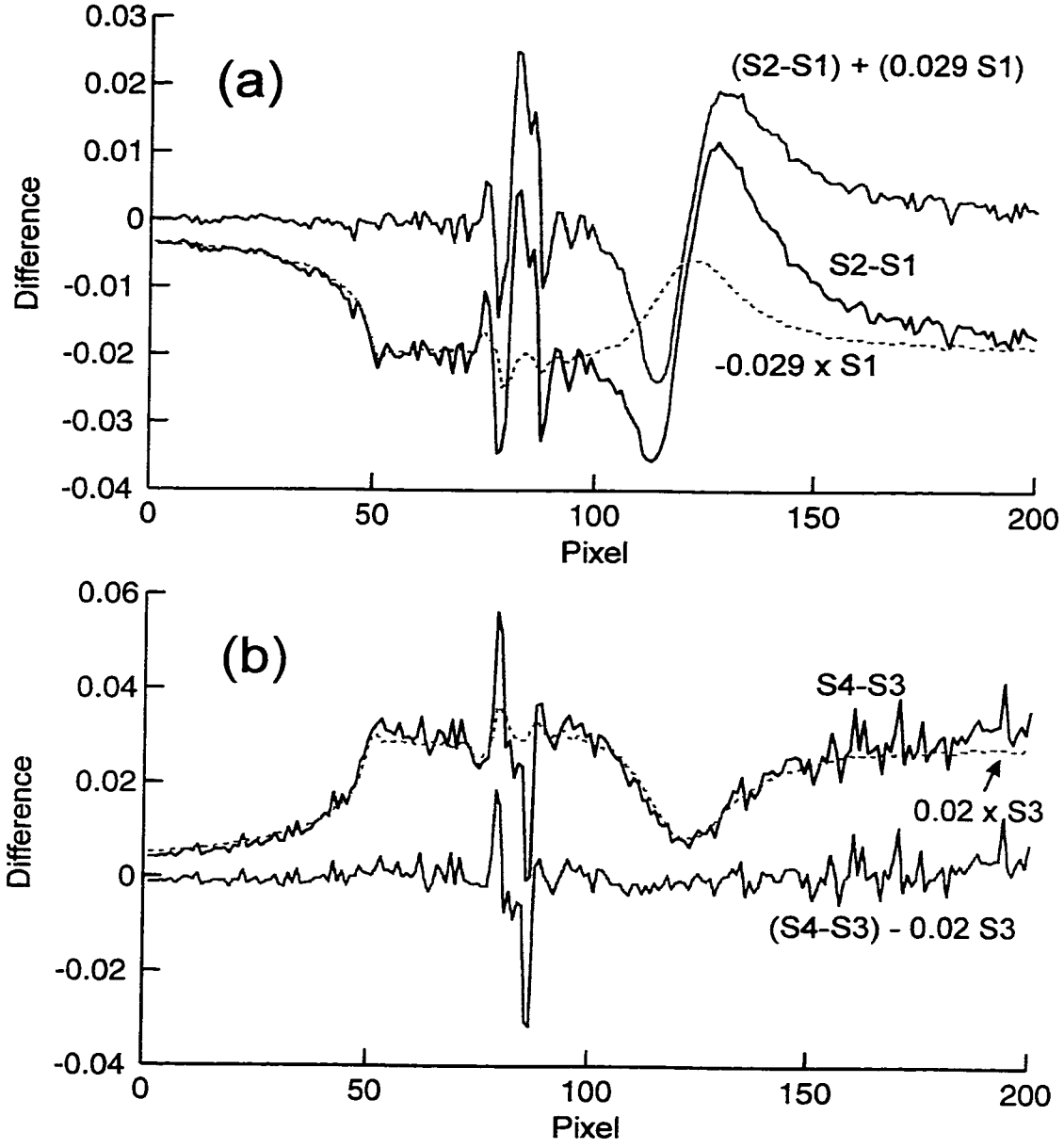

Figure 4.12. Spectral differences measured during LED and detector heating experiments. (a) LED heating. (b) Detector heating.

has occurred, indicating an emission wavelength temperature coefficient of 2.26 nm/11C = +0.21 nm/C.

A similar analysis provides an interpretation of spectral changes due to detector heating. The difference between two spectra *S3* and *S4* measured before and during detector heating (Fig. 4.12b) shows a distinct proportionality to *S3*, indicating an increase in detector sensitivity due to temperature. The difference is approximately 2% of *S3*, suggesting that the detector exhibits a positive temperature coefficient of response that is approximately 2%/11 C = 0.18%/C.

This is consistent with the literature. The detector used (Texas Instruments TSL1401) [3] is a 128 pixel silicon photodiode array with peak responsivity at ~770 nm. An inexpensive commercial device, its temperature behavior is not characterized. However, literature reports of the behavior of similar devices are consistent with the observed behavior this device. Data sheets for a family of research-grade multielement silicon photodiodes manufactured by Hamamatsu [4] show that those devices have a positive temperature coefficient of response at the upper and lower ends of their spectral ranges. For example, the S4349 device, with a peak sensitivity wavelength of 720 nm, exhibits a positive temperature coefficient of response of approximately 0.16% at 830 nm. A theoretical and experimental investigation into the temperature behavior of silicon photodiode quantum efficiency [5] similarly observed positive temperature coefficient of response at the upper and lower ends of the spectral ranges. Theoretical analysis found that the major contributions to this effect came from the temperature variations of absorption coefficients, carrier diffusion length, and the complex RI of silicon. Other researchers [6] have stated that silicon photodetectors have a positive temperature coefficient of response which extends up to 0.1%-0.2%/C, and proposed circuit configurations for compensating for this effect.

The GaAlAs LED used (Infratech INF830N14PS) is not well characterized for temperature response. Communication with the manufacturer revealed only that the temperature dependence of its peak emission wavelength is believed to be on the order of +0.1 nm/C, while the temperature coefficient of intensity is negative but of unspecified magnitude. The values we have observed are in general agreement with values published for other GaAlAs LEDs. Murtaza and Senior [7] propose a model for the variation of GaAlAs LED intensity, peak wavelength, and spectral bandwidth with temperature based on a Gaussian distribution and find that their model agrees well

with experiment. For LEDs with a peak wavelength of 875 nm they found typical values of the temperature coefficients of intensity and peak wavelength are -0.7%/C and 0.3 nm/C respectively. Marandet *et al.* [8] state that red GaAlAs LEDs show a negative TC of emission with increasing temperature and describe a detailed model which predicts a TC of -0.4%/C and which matches well with experiment.

To look for LED and detector effects in spectra measured during heating of the entire instrument, one must attempt to remove the spectral changes resulting from the accompanying change in analyte temperature. We do this by choosing a spectrum *S5* measured during instrument heating, and subtracting from it a spectrum *S6* measured during the calibration gradient prior to heating. We choose for *S6* the spectrum with the value of n_b closest to that of S5. If the actual bulk and surface RI were equal at both of these points, *and* if the measured n_b accurately measures the bulk RI irrespective of instrument heating, the subtracted spectra will indicate the spectral change caused by heating of the apparatus. This difference S5-S6, shown in Fig. 4.13a, has a form similar to 4.12a, suggesting that LED heating contributes substantially to the observed shift. Note that when both LED and detector are heated, the decrease in LED intensity will be partly offset by an increase in detector sensitivity. This accounts for the fact that S5-S6 does not present an obvious proportionality to S5.

4.6.5. Other contributions to temperature compensation error

The above results indicate that changes in LED wavelength and intensity and detector sensitivity due to heating may account for much of the compensation error observed during instrument heating. However, some of the observed spectral changes appear to have other causes. The noise-like fine structure in the data of Figs. 4.12 and 4.13 suggests a change in LED output distribution or a repositioning of instrument components due to thermal expansion resulting in small, irregular spectral changes.

LED and detector effects cannot explain the error in flowcell temperature compensation such as that observed at the beginning of the experiment of Fig. 4.7, because heating was confined to the flowcell at that point. To isolate the spectral changes which result in compensation error due to flowcell heating, we repeated the subtraction procedure described above. From the spectrum S7 measured at the point of greatest compensation error, we subtracted the spectrum S8 measured during the

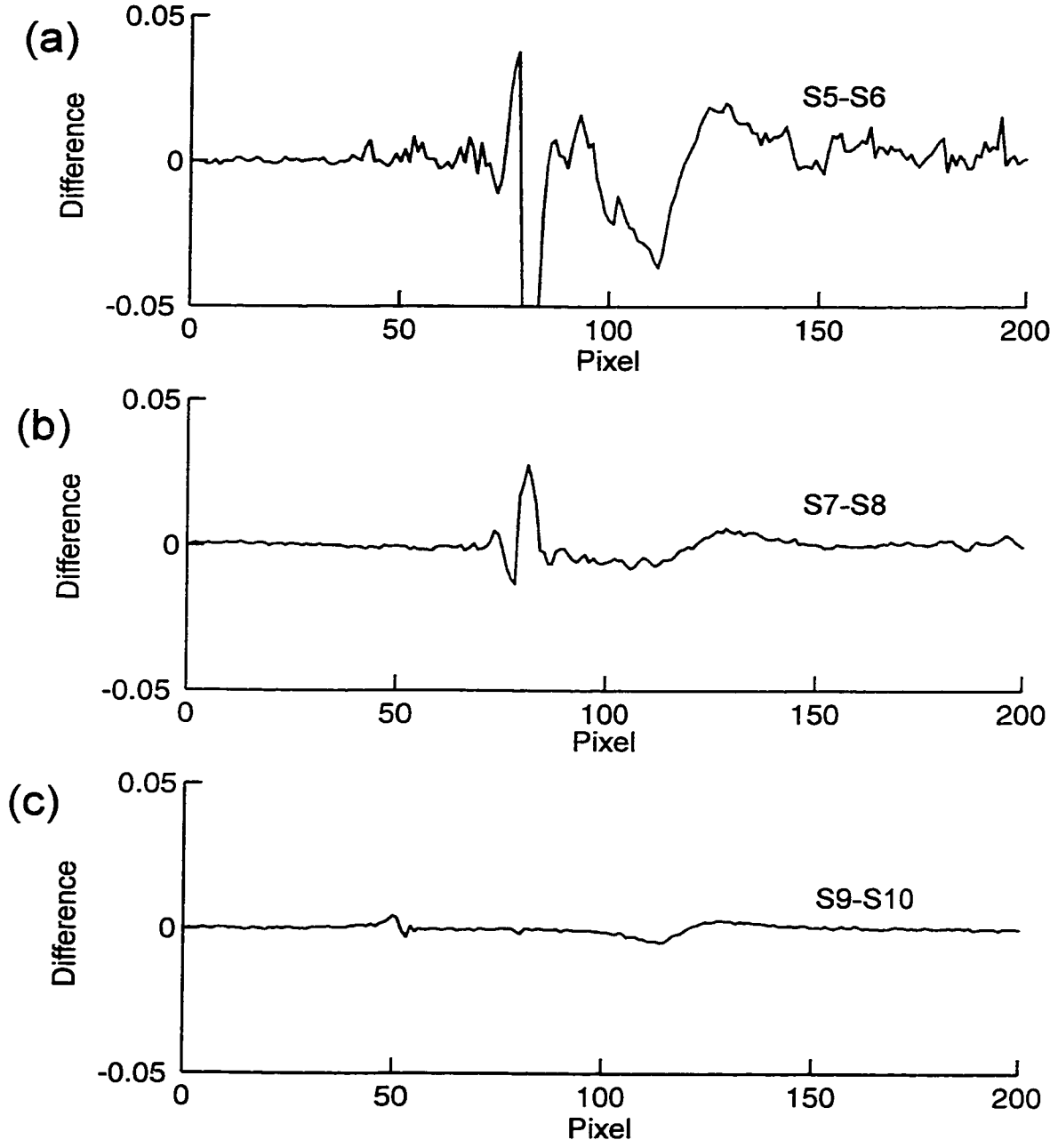

Figure 4.13. Spectral differences measured during instrument heating experiment of Fig. 2.10, using gradient spectra to isolate instrumental contribution. (a) Difference after instrument heating. (b) Difference after flowcell heating. (c) Difference with no heating.

calibration gradient with the same value of n_b as S7. The difference (Fig. 4.13b) has two main features -- an S-shaped disturbance indicating an SPR shift and a jagged peak at the gold edge.

The former is too small for definitive interpretation, because the imperfections of the subtraction procedure do not completely eliminated disturbances due to analyte RI. Fig. 4.13c illustrates this point. From the experiment of Fig. 4.8, a spectrum S9 measured prior to all heating chosen, and a spectrum S10 measured during the calibration gradient with the same value of n_b as S9 was subtracted. Small features remain around the critical angle and SPR dip.

The peak observed in 4.13b is more clearly a temperature effect, and appears to result from slight temperature-induced motion of the sensing chip. This motion, perhaps due to instability of the index-matching liquid between the sensing chip and the prism, will cause small changes throughout the spectrum, which will cause compensation error. This would be consistent with the observed nature of the error, which is independent of flow rate and varies over time, both in magnitude and in sign.

Temperature-induced changes in the RI of the gold may also contribute to the compensation error, but one would expect this effect to be more consistent than the observed error. However, little data exists on the temperature dependence of the optical constants of gold, and this effect is worthy of future study.

4.6.6. Quantification of error for the SPR/IRR sensor

In our discussions of the data presented above described the efficacy of compensation in percentage terms. For instance, we indicated in 4.6.1 above that IRR compensation removed 99% of the effect of bulk RI variations on the SPR measurement. This type of informal specification is intuitive and useful for communication, but it is not completely rigorous. Stating an error in percentage terms implies proportionality -- that is, if the bulk RI interference were to decrease, the error would be expected to decrease proportionately. Unless this is known to be true, stating error in percentage terms can be misleading.

The instrument described here is still under development, and so specifications of its performance have limited meaning. However, to explore what rigorous specifications might look like for a production instrument, we attempt here to

characterize the data presented above in terms of a specification for instrument accuracy and precision.

Precision of n_s, n_b, and N. As described in Chapter 3, we reserve the term precision to describe variations in instrument response which appear to be truly random. We obtain a value for the imprecision of a measurement by calculating the standard deviation of a group of measurements taken under the same conditions over a specified time interval. Fig. 4.14a shows the experiment from which our specification for precision was extracted. SPR/IRR measurements of five sucrose solutions with RI ranging from n_b=1.328 to n_b=1.332 were performed. (These five solutions are indicated with letters A-E in Fig. 4.14a) In each solution, 250 consecutive measurements extending over approximately 500 seconds were recorded. From each spectrum, n_b, n_s, and N were computed. For comparison, a value of surface RI, denoted $n_{s,c}$ was also computed using centroid analysis of the SPR dip. For each solution, the precision of n_b was quantified by calculating the standard deviation of the 250 measurements of n_b performed in that solution. An analogous procedure provided quantification of the precision of n_s, N, and $n_{s,c}$. The values obtained are referred to as the imprecision or RMS noise level.

The results obtained using this procedure are shown in Fig. 4.14b. The imprecision of n_s and $n_{s,c}$ are comparable and fairly constant across the RI range examined, with values that remain below 10^{-6} RI units. The imprecision of n_b and N are somewhat greater, rising from below 10^{-6} in the middle of the RI range to approximately $1.5\text{x}10^{-6}$ at the end of the RI range. (The increase in imprecision towards the ends of the RI range is an expected consequence of our data analysis method. This is described in the next chapter.) Given these observations, we specify the imprecision of n_s to be 10^{-6}, and the imprecision of N and n_b to be $2\text{x}10^{-6}$.

Accuracy of n_s and n_b. The accuracy of n_s and n_b can be evaluated if the true RI of the solution to which the sensor is exposed can be determined. In the experiments presented in this chapter, the five sucrose solutions to which the sensor is exposed at the beginning or end of the experiment serve this purpose. In all experiments, the value of n_s and n_b measured in these solutions were found to be within 10^{-4} of the RI values measured for these solutions on an Abbe refractometer. The Abbe refractometer itself has an accuracy of 10^{-4}, so the total error is within $2\text{x}10^{-4}$. To produce a conservative estimate which allows for the possibility of instrumental drift

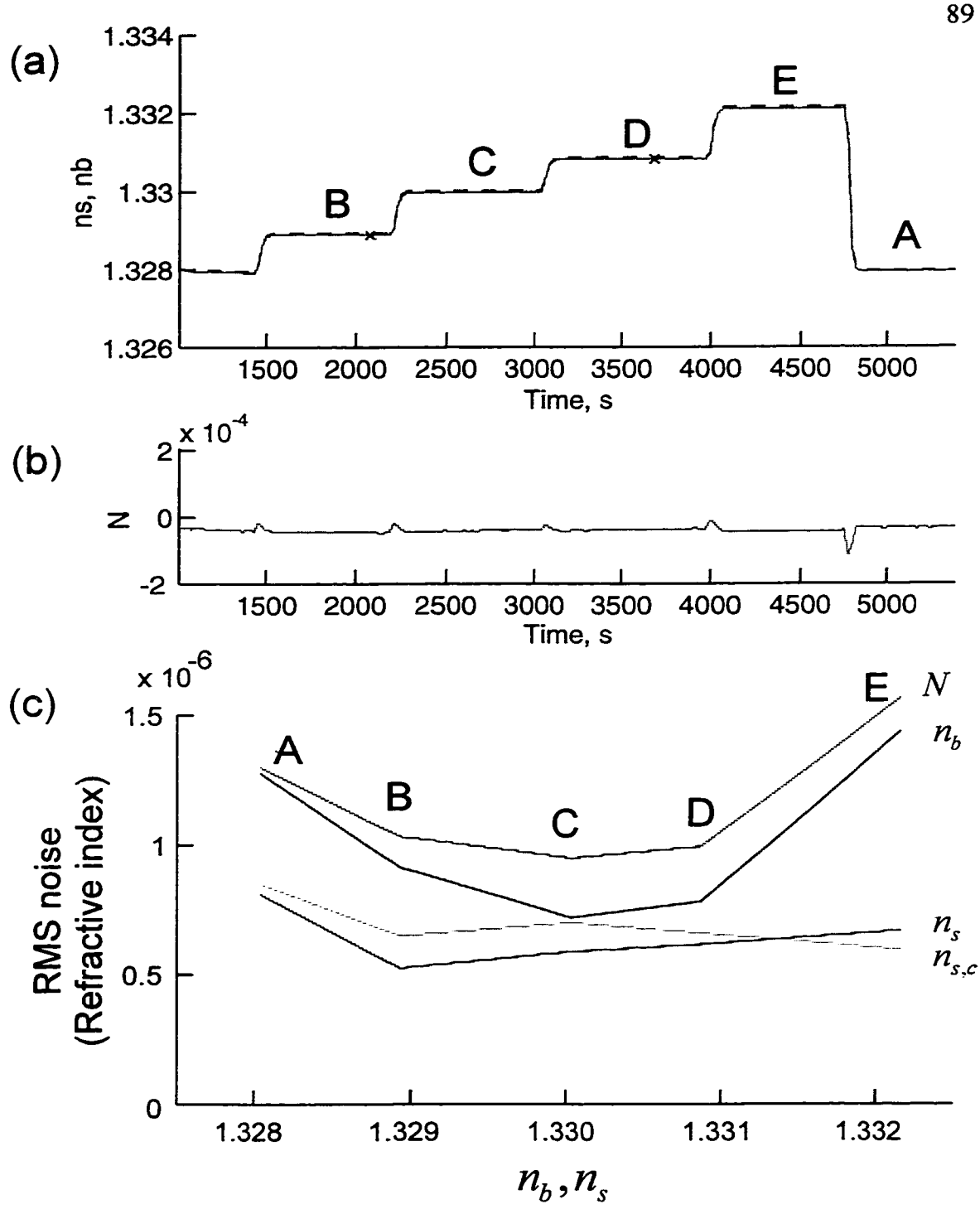

Figure 4.14. Determination of instrument precision. (a) SPR/IRR measurement of five sucrose solutions, showing n_b and n_s. (b) Adsorption index N (c) Values for precision derived from measurements. See text, section 4.6.6, for details.

such as that observed in the experiment of Fig. 4.5, we add an additional10^{-4}, arriving at a figure of inaccuracy of +/-3x10^{-4}.

Accuracy of N. When no adlayer is present, the true value of N is zero by definition; therefore, it is easy to quantify the accuracy of N. In the data of Fig. 4.5, it is seen that N remains within 3x10^{-5} of zero throughout the experiment. Thus, for N under those conditions we specify an inaccuracy of +/-3x10^{-5}. The data of Fig. 4.5 was taken at room temperature, so this specification is considered valid for room temperature experiments only. (Note that this figure is much smaller than the estimated inaccuracy of n_s and n_b. Much of the error in n_s and n_b cancels when $N=n_s-n_b$ is computed.) The data of Fig. 4.7, where the flowcell temperature was varied by approximately +/-9 C, provides a specification for accuracy which allows for temperature variations. In this experiment, N was observed to vary by approximately +/-7x10^{-5} as the temperature was changed. We take this as the value for the inaccuracy of N in conditions of changing temperature.

It is unfortunately not possible with the information available to rigorously quantify the error in N in the presence of an adlayer, because we do not have a method of determining the "true" value of N. An upper bound on the error may be obtained by summing the estimated inaccuracy of n_s and n_b, but this bound (+/-6x10^{4}) is so large as to be of little use. Until an independent determination of N can be made, the best that can be done is to extrapolate the inaccuracy determined with no adlayer to the more general case, while remaining aware of the dangers of that approach.

4.7. Conclusions

Critical angle compensation is effective in reducing the influence of bulk RI interference on SPR measurements. In the experiments presented here, during which flowcell temperature varied by over a range of 15 C and bulk RI varied over 6x10^{-3}, critical angle compensation eliminated at least 95 % of bulk RI interference. Bulk RI variations due to composition alone were 99% compensated. When the temperature of the entire instrument was raised by 11 C, a shift in N was observed and the quality of compensation was degraded, but remained better than 85% in all cases.

Further improvement of this technique is desirable. Improved compensation will allow reduced detection limits in the presence of increased interference. Considerable

improvement would be required to resolve compensation subtleties such as those simulated in Fig. 3.5. The uncertainty in N during conditions of best compensation (Fig. 4.5) is of the same order as the variation in N required to be measured. A factor of 5 to 10 improvement in compensation is necessary to examine such phenomena.

The instrument's ability to compensate for bulk RI variations due to analyte composition is already very good. Further improvements may result from optimization of flow channel dimension to reduce composition nonuniformity. Refined calibration and data analysis procedures may result in further improvements.

The instrument's compensation for bulk RI variations due to temperature is not as good as its composition compensation. The cause of this requires further investigation, but may be due to instability in the index matching oil between the sensor chip and prism. Temperature nonuniformity does not appear to be a significant problem in the experiments presented here. However, further thermal optimization of the flowcell will make the instrument yet more immune to the effects of varying reagent temperature.

The most demanding application investigated here is the use of critical angle compensation to compensate for variations in the temperature of the environment of the instrument. Temperature dependence of the instrument's LED and detector were found to account for much, but not all, of the observed variation of N with instrument temperature. The remaining effect may be due to expansion of the aluminum fixture connecting the instrument components. Effects on the order of 10^{-5} will also result from RI temperature coefficients of sensing chip and prism. Further thermal engineering is necessary to reduce these effects.

Notes for Chapter 4

[1] G. B. Sigal, M. Mrksich, and G. M. Whitesides, Using surface plasmon resonance to measure the association of detergents with self-assembled monolayers of hexadecanethiolate on gold, *Langmuir* **13** (1997), 2749-2755.

[2] B. R. Ruddick and T. G. L. Shirtcliffe, Data for double diffusers: physical properties of aqueous salt-sugar solutions, *Deep Sea Res.* **26A** (1979) 775-787.

[3] Texas Instruments, Inc., *TSL1401 data sheet,* 1996.

[4] Hamamatsu, Inc, *S4349 data sheet*, 1996.

[5] T. Appourchaux, D. Martin, and U. Telljohann, Temperature dependence of silicon photodiode quantum efficiency: theoretical and experimental results, *Proc. SPIE* **1679** (1992) 200-211.

[6] S. N. Nihtianov and D. P. Alipiev, Automatic compensation for the temperature coefficient of a photodiode in short circuit mode, *Sens. Act. A* **29** (1991) 117-120.

[7] G. Murtaza and J. M. Senior, Method for extracting thermally stable optical signals from a GaAlAs LED source, *IEEE Photon. Technol. Lett.* **7** (1995) 479-481.

[8] F. Marandet, J. Bernard, P. Garcia, J. Deforges, and D. Magnant, Effect of self-heating on the ideal static characteristics of GaAlAs light emitting diodes, *Solid State Electron.* **32** (1989) 607-614.

Chapter 5: Calibrated linear data analysis for the SPR/IRR sensor

5.1. Goals for SPR/IRR data analysis

The SPR/IRR sensor described in the previous chapter must make high quality measurements to realize the benefits of bulk RI compensation. The bulk RI variations interfering with an SPR adsorption measurement can be many times greater than the adsorption signal of interest. The measurements of surface RI n_s and bulk RI n_b must both be high quality to enable the adsorption index $N=n_s-n_b$ to be an effective quantification of adsorption. These measurements are performed under difficult conditions. The functionalized SPR sensor surface will evolve over time, causing drift in n_s. In uncontrolled environments, fouling will cause the sensor response to degrade with time. Ambient temperature variations will influence instrument components, causing additional drift.

Adding to these difficulties are the requirements of mass production. The SPR/IRR sensor is a prototype of a device intended for high-volume, inexpensive manufacturing. In that setting, trimming, testing, and fine-tolerance specifications must be minimized to achieve the lowest possible cost. Thus, sensor behavior may differ substantially from unit to unit.

This chapter describes data analysis and calibration techniques designed to produce high quality data under these challenging circumstances. This work focuses on the calculation of the adsorption index N, the natural quantification of adsorption produced by the SPR/IRR sensor.

5.2. Conventional methods of SPR and critical angle data analysis

The spectrum produced by the SPR/IRR sensor consists of a IRR reflection spectrum combined with an SPR reflection spectrum. The IRR spectrum reports the reflectivity of the interface between the transparent region of the sensor surface and the analyte at incident angles up to and including the critical angle. The SPR reflection

spectrum reports the reflectivity of the gold-coated region of the sensor surface at angles above the critical angle.

A number of methods of analyzing SPR and IRR spectra have been reported. If it is possible to construct an accurate, physically-based mathematical model of the sensor behavior, one can analyze sensor data by least-squares fitting of the model to measured spectra. This method has been used to interpret SPR and IRR spectra, with good results [1, 2]. With an accurate model, this method will give optimal noise performance [3]. However, if the sensor response varies from sensor to sensor due to manufacturing tolerances, and changes as the sensor is used, construction of a good model may be impossible.

A less formal variant of the model-fitting approach is to interpret the sensor response geometrically based on guidelines derived from a sensor model. For example, a change in the adsorbed layer on an SPR sensor causes a shift in location of the dip in the reflection spectrum, with the dip location roughly proportional to the surface RI. To determine the dip location, one can fit a polynomial to the region of the reflection spectrum surrounding the minimum and determine the polynomial minimum analytically [4]. Or, the spectrum may be characterized by setting a threshold value and finding the centroid of the portion of the spectrum which lies below that threshold [5]. The geometrical approach is the most common method of analyzing SPR data.

It is also possible to analyze critical angle data using a geometrical approach, for instance by finding the location of the peak in the derivative of the reflection spectrum at the critical angle [6], or by fitting a polynomial to the critical angle edge and calculating where the polynomial intersects unity reflectivity.

These methods are easier to apply than the model-fitting approach, but good agreement with a physical model is still necessary. An additional inadequacy of these methods is that they provide no method for predicting the performance of a given algorithm, or for selecting one over another.

5.3. Philosophy of interpretation of SPR reflection spectra

How exactly should SPR spectra be analyzed to determine the amount of material bound to the sensor surface?

The most obvious change in the SPR spectrum as the RI changes is the location of the dip in reflectivity -- the dip moves to higher angles as the RI increases. A natural method of quantifying the dip location is to determine the angle of minimum reflection. These observations have led to the conventional interpretation of SPR spectra:

The location of the SPR minimum is proportional to the average RI near the sensor surface, which in turn is proportional to the surface concentration of adsorbed material.

This interpretation is adequate for many purposes. However, it is unsatisfying in several ways. It presumes that spectra have a well defined minimum, which may not be the case. It does not describe how the minimum location should be computed from a measured spectrum. Finally, the single-minded focus on the location of the minimum obscures other spectral features -- for example, the shape of the dip and the critical angle edge -- which contain useful information (Fig. 5.1).

As the research described in this dissertation proceeded, the standard interpretation was repeatedly found to be incapable of answering questions that arose. It was necessary to develop a more general interpretation of SPR reflection spectra:

Each point of the SPR reflection spectrum contains information relating to the optical properties of the analyte and the sensor apparatus. Study of the relationship between reflection spectra and analyte properties allows optimal determination of analyte parameters.

This less concrete but more comprehensive interpretation has led to the data analysis technique described below.

In our approach to data analysis, we have sought to overcome the limitations of the conventional methods by returning to a more general approach, in which each point of the spectrum is assumed to contain information regarding the analyte. Then, with a minimum of assumptions, the optimal method of extracting the desired information regarding the analyte is sought.

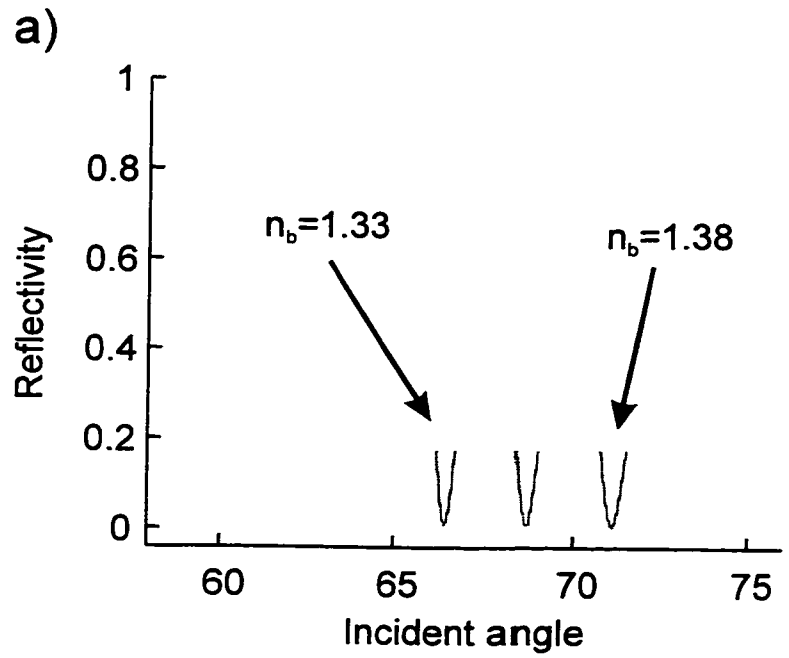

The location of the SPR minimum is proportional to the average RI near the sensor surface.

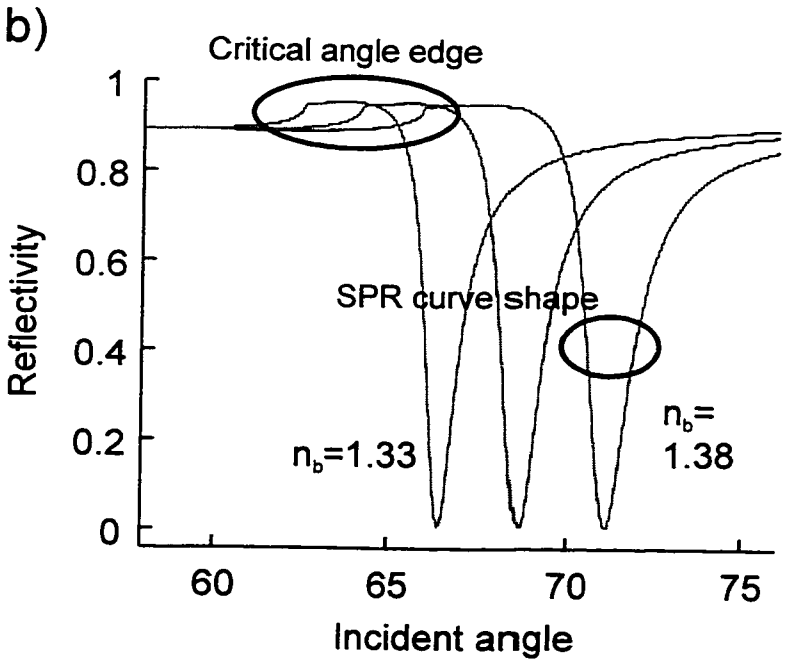

Each point of the SPR reflection spectrum contains information relating to the optical properties of the analyte and the sensor apparatus. Study of the relationship between reflection spectra and analyte properties allows optimal determination of analyte parameters.

Figure 5.1. Interpretation of SPR reflection spectra. (a) Standard interpretation focuses on location of spectral minimum. (b) Generalized interpretation encourages investigation of other spectral features, such as the critical angle edge and the shape of the SPR curve.

In designing a data analysis method following this approach, the first and most important decision that must be made is to decide which analyte parameters will be extracted from the data. For example, it is theoretically possible to extract morphological information about adsorbed layers (e.g. thickness and refractive index) from a single SPR spectrum [3]. If it were desired to extract these two parameters from a given spectrum, the data analysis method would be designed with extraction of these two parameters in mind.

We do not attempt this here. Because the exacting measurements required for such determination have not been achieved here or elsewhere, our interpretation of the information content of the SPR curve remains the same is in the standard interpretation: the SPR curve indicates the average RI near the surface. Similarly, a simple interpretation of IRR spectra is assumed: the variations in reflectivity below the critical angle are assumed to result solely from change in the real RI of the bulk analyte. Changes due to adsorption, for instance, are assumed to be absent.

These simple interpretations are appropriate given the current limitations in measurement quality. However, it is important to keep in mind the approximations inherent in these interpretations. We know that in fact the IRR measurement can be influenced by adsorbed layers, and the shape of the SPR dip will change slightly depending upon the exact structure of the adsorbed layer. If these approximations were no longer valid, for instance if the sensor were to be used to examine very thick adsorbed layers or lossy analytes, or if the instrument's performance were improved to the point where the inaccuracy of these approximations could be resolved, our approach would need to be modified accordingly.

In summary, SPR/IRR reflection spectra are assumed to be completely described by two parameters:

The bulk RI, n_b is the RI of the analyte, as measured by the IRR reflection spectrum. The method by which n_b is extracted from a IRR spectrum is designed such that when the sensor is exposed to a solution of known RI n, then $n_b=n$.

The surface RI, n_s is the RI of the analyte as measured by the SPR reflection spectrum. The method by which n_s is extracted from an SPR spectrum is designed

such that when the sensor is exposed to a solution of known RI n when no adlayer is present, then $n_S=n$.

Note that here the adlayer refers to adsorption that occurs *after* deposition of functionalization layers.

A third parameter, derived from the previous two, is of central importance for the SPR/IRR sensor:

The adsorption index N, defined by $N=n_S-n_b$, is the natural measurement of adsorption produced by the SPR/IRR sensor. By the definition of n_S, $N=0$ if no adlayer is present. If a high RI layer adsorbs to the SPR surface, $n_S>n_b$ and $N>0$.

5.4. Calibrated linear data analysis

Our data analysis method combines linear data analysis [7] with automatic calibration based on RI gradients. The extraction of values for the bulk RI n_b and surface RI n_S from a measured spectrum follows a two step process. First, the dot product of the spectrum with response vectors $\mathbf{D_b}^*$ and $\mathbf{D_S}^*$ gives values for a bulk metric b and surface metric s. These metrics are then mapped to n_b and n_S using calibration data.

Three central features of this method which makes it effective in analyzing SPR/IRR data are the following:

1) Rapid, automatic calibration allows these techniques to achieve the performance needed for good critical angle compensation.

2) The data analysis procedure is derived from the measured sensor response rather than from idealized assumptions of sensor behavior. This enables the analysis of data from a sensor with a response which changes over time or from unit to unit.

3) The data analysis procedure is designed to give low noise measurements. Under appropriate assumptions, noise performance is optimal. The relationship between

measurement noise and noise in the spectra from which the measurements are extracted is straightforward and easily quantified.

The remainder of this chapter will describe this data analysis and calibration procedure in detail.

5.4.1. Linear data analysis

Suppose one has measured an N-point SPR/IRR reflection spectrum $\mathbf{y}^* = (y_1^*, \ldots, y_N^*)^T$, and desires to calculate from those measurements $M<N$ parameters $\mathbf{x} = (x_1, \ldots, x_M)^T$ of the analyte. (Here, T is the matrix transpose operator.) In the absence of noise, we assume that $\mathbf{y}^*$ and $\mathbf{x}$ are related by a model function $\mathbf{y}$:

$$\mathbf{y}^* = \mathbf{y}(\mathbf{x}) = \left(y_1(\mathbf{x}), \ldots, y_N(\mathbf{x})\right)^T \tag{5.1}$$

which, for a parameter vector $\mathbf{x}$ close to a certain set of parameters $\mathbf{x}_0$, may be approximated by a first-order Taylor series expansion. If we assume that our measurements have an additive noise component $\mathbf{u}$, then $\mathbf{y}^*$ may be written

$$\mathbf{y}^*(\mathbf{x}) = \mathbf{y}_0 + \mathbf{D}(\mathbf{x} - \mathbf{x}_0) + \mathbf{u} \tag{5.2}$$

where $\mathbf{u}$ is a normally-distributed N x 1 vector random variable with known covariance matrix $\mathbf{V}$, and where the N x M matrix $\mathbf{D}$ is the matrix of partial derivatives evaluated at $\mathbf{x}_0$:

$$\mathbf{D} = \left[\begin{array}{ccc} \frac{\partial y_1}{\partial x_1} & \cdots & \frac{\partial y_1}{\partial x_M} \\ \vdots & \ddots & \vdots \\ \frac{\partial y_N}{\partial x_1} & \cdots & \frac{\partial y_N}{\partial x_M} \end{array}\right]_{\mathbf{x}_0} \tag{5.3}$$

The optimal method for retrieving an estimate of **x** from the noisy measurements **y*** is given by the Gauss-Markov theorem, a fundamental result of the theory of linear statistical models [8]. This theorem states that the best linear unbiased estimate of **x**, denoted by **x***, is

$$\mathbf{x}^* = \mathbf{x}_0 + \left(\mathbf{D}^T\mathbf{V}^{-1}\mathbf{D}\right)^{-1}\mathbf{D}^T\mathbf{V}^{-1}\left(\mathbf{y}^* - \mathbf{y}_0\right) \tag{5.4}$$

The variances of the elements of **x*** are contained in the diagonal elements of the covariance matrix of **x***, which is given by

$$\mathbf{C} = \left(\mathbf{D}^T\mathbf{V}^{-1}\mathbf{D}\right)^{-1} \tag{5.5}$$

The estimate (5.4) is unbiased in that the expected value of **x*** is **x**, and minimum variance in that any other unbiased estimate will yield a covariance matrix with diagonal elements greater than the corresponding elements of **C**.

This estimate provides both the optimal method of extracting an estimate of analyte parameters from our measurements and an measure of the uncertainty in that estimate. The estimation matrix in eq. (5.4),

$$\mathbf{F} = \left(\mathbf{D}^T\mathbf{V}^{-1}\mathbf{D}\right)^{-1}\mathbf{D}^T\mathbf{V}^{-1} \tag{5.6}$$

defines the optimal linear function for estimating **x** given **y***:

$$\mathbf{x}^* = F_{opt}\left(\mathbf{y}^*\right) = \mathbf{x}_0 + \mathbf{F}\left(\mathbf{y}^* - \mathbf{y}_0\right) \tag{5.7}$$

If a matrix **D** corresponding to a linear model with one parameter (say n_S, the surface RI) is used,

$$\mathbf{D} = \left[\frac{\partial y_1}{\partial n_s} \quad \cdots \quad \frac{\partial y_N}{\partial n_s}\right]^T \tag{5.8}$$

then **F** has one row, which we write as **f**. If **V** is diagonal,

$$\mathbf{f} = \left(\mathbf{D}^T\mathbf{V}^{-1}\mathbf{D}\right)^{-1}\mathbf{D}^T\mathbf{V}^{-1} = \frac{\left[\begin{array}{ccc} \frac{\partial y_1/\partial n_s}{V_{11}} & \cdots & \frac{\partial y_N/\partial n_s}{V_{NN}} \end{array}\right]}{\sum_{i=1}^{N}\frac{\left(\partial y_i/\partial n_s\right)^2}{V_{ii}}} \tag{5.9}$$

and the function which estimates n_S given $\mathbf{y}^*$ is computed by subtracting $\mathbf{y}_0$ from $\mathbf{y}^*$, calculating the dot product of $\mathbf{f}$ with the difference, and adding n_{S0} (the initial surface RI) to the result. As seen in Eq. (5.9), each element of $\mathbf{y}^*$ is weighted in proportion to the derivative of the measurement with respect to the desired parameter, and in inverse proportion to the variance of the measurement.

5.4.2. Application to SPR/IRR data analysis

To apply linear analysis to SPR/IRR data, we divide measured spectra into the SPR region and the IRR region. A one-parameter linear model is applied to the IRR region to determine n_b, and another one parameter model is applied to the SPR region to determine n_S.

Because the linear analysis of SPR/IRR spectra is followed by calibration, the calculation Eq. (5.7) may be simplified. $\mathbf{x_0}$ and $\mathbf{y_0}$ may be set to zero, and $\mathbf{D}$ need only be proportional to, rather than equal to, the derivative matrix. Then, rather than producing estimates of n_S and n_b, the linear analysis will produce a surface metric s and a bulk metric b which will be mapped to n_S and n_b by the subsequent calibration. If we further simplify $\mathbf{f}$ by assuming that $\mathbf{V}$ is proportional to the identity matrix, the analysis function becomes simply

$$\mathbf{x}^* = \mathbf{D}^*\mathbf{y}^* \tag{5.10}$$

A vector $\mathbf{D}^*$ approximately proportional to $\mathbf{D}$ may be calculated by subtracting two spectra measured at times when $\mathbf{x}$ is known to differ:

$$\mathbf{D}^* = \mathbf{y}^*(\mathbf{x}_2) - \mathbf{y}^*(\mathbf{x}_1) \tag{5.11}$$

The vector $\mathbf{D_b}^*$ for determining b is obtained from $\mathbf{D}^*$ by setting the elements of $\mathbf{D}^*$ outside the IRR region to zero. The vector $\mathbf{D_s}^*$ for determining s is obtained by setting the elements outside the SPR region to zero. The metrics b and s are then calculated from a spectrum $\mathbf{y}^*$ by

$$b = \mathbf{D}_b^{\bullet}\mathbf{y}^* \tag{5.12}$$

$$s = \mathbf{D}_s^{\bullet}\mathbf{y}^* \tag{5.13}$$

5.4.3. Limits of linear techniques for critical angle and SPR sensing

The linear model on which this data analysis method is based has a limited range of validity. As this range is exceeded, the slope of the linear estimates s and b with respect to n_s and n_b will decrease. A simulation of this is shown in Fig. 5.2a. Signal-to-noise ratio will decrease as the slope decreases; when the slope reaches zero (as it does for s in Fig. 5.2a), linear analysis can no longer be used at all. The increase in noise towards the end of the linear range can be also observed in experimental SPR/IRR data (Fig. 5.2b).

5.5. Calibration strategy

For the SPR/IRR sensor, the purpose of calibration is to create a map between the linear estimates s and b and the RIs n_s and n_b corresponding to those estimates. Calibration measurements also provide the spectra from which the response vectors $\mathbf{D_b}^*$ and $\mathbf{D_s}^*$ used to compute the linear estimates are derived. A simple, rapid calibration procedure which can be performed frequently and automatically will allow the SPR/IRR sensor to produce high quality measurements in spite of a sensor response which will drift due to surface processes and instrument temperature fluctuations.

The following diagram illustrates the path by which n_s and n_b are calculated from a spectrum $\mathbf{y}^*$:

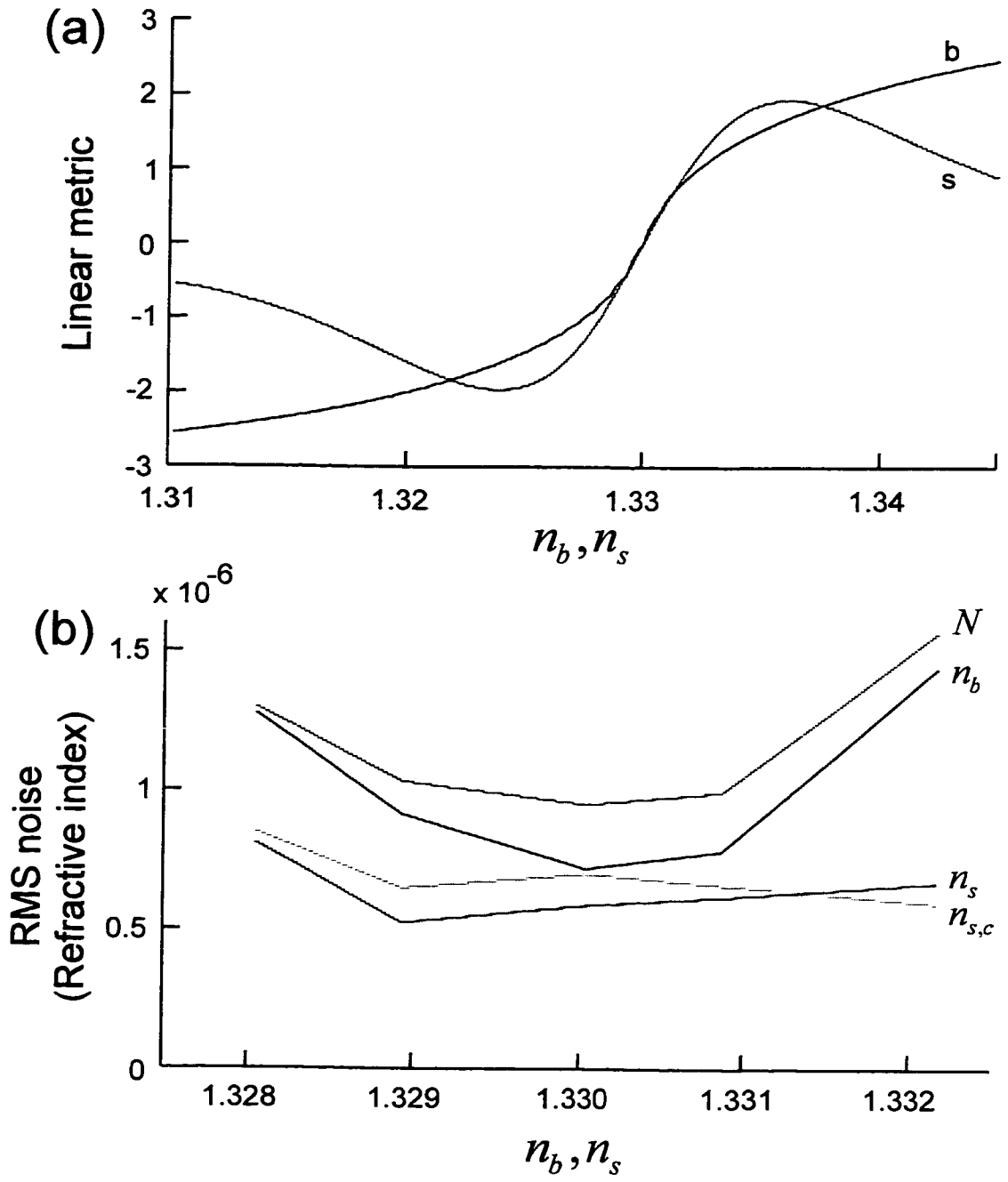

Figure 5.2. Range limits and noise behavior of calibrated linear data analysis. (a) Bulk and surface metrics as a function of RI, generated using simulated SPR/TIR spectra. For display purposes, metrics are offset to equal zero at n=1.33. (b) Experimental RMS noise values derived from SPR/TIR spectra. See text, section 4.6.6., for details.

$$\begin{bmatrix} \mathbf{y}^* \end{bmatrix} \xrightarrow[s=\mathbf{D}_s^*\mathbf{y}^*]{b=\mathbf{D}_b^*\mathbf{y}^*} \begin{matrix} b \\ s \end{matrix} \xrightarrow{h} \begin{bmatrix} b \\ b_s \end{bmatrix} \xrightarrow{g} \begin{bmatrix} n_b \\ n_s \end{bmatrix} \tag{5.14}$$

The relative calibration function h is defined as the function which maps s onto b in the absence of an adlayer. We denote $b_S=h(s)$ the "equivalent bulk metric" of s. The absolute calibration function g then maps b and b_S to n_b and n_S. Because the same function g maps b to n_b and b_S to n_S, we are guaranteed that $n_b=n_S$ if $b=b_S$.

5.6. Relative calibration: Determination of *h* using RI gradients

The function h is determined by exposing the sensor to an RI gradient covering the RI range of interest. The (b, s) pairs measured during this gradient provide data which are then used to define h. We chose to calculate h by linear interpolation between (b, s) pairs.

When interpolation is used, the noise component in each (b, s) point will cause small errors in h. An alternative would be to define h by fitting of a prechosen function (e.g. a polynomial) to the (b, s) data. Such a function may have better small scale error properties, but would require the choice of a form for h, and would introduce the possibility of larger errors due to imperfect fitting. For simplicity, and because error in h due to measurement noise was not found to be significant, the interpolation procedure was used.

For best determination of h, it is important that during calibration the changes in b and s are due solely to changes in the bulk RI. Any drift in b or s during calibration due to other effects, such as surface processes and light source and detector variations with temperature, will introduce systematic error in h.

5.7. Absolute calibration: Determination of *g*

Our objective in determining g is to ensure as high quality a measurement of the adsorption index $N=n_S-n_b$ as possible. To achieve this, one must define "high quality" and examine how the function g affects N.

Suppose the SPR/IRR sensor were exposed to a solution with bulk RI n, with no adlayer present. Then $b=b_S$, and ideally g would provide a perfect map of b and b_S back to n: $g(b) = n$. In reality, g will always contain some error, and $g(b) = n^* \neq n$.

If the sensor accumulates an adlayer, $N \neq 0$ and $b \neq b_S$. The error in g will cause the sensor to report an adsorption index N^* different from the true N. If $n^*(n)$ is the function which maps n to n^*, N^* is given by

$$N^* = n^*(n_s) - n^*(n_b) \tag{5.15}$$

Figure 5.3 illustrates the errors in N^* which can result from error in n^*. If n^* differs from n by a fixed constant (Fig 3.3a), $N^*=N$, because the constant will cancel in the calculation of N. If n^* is linearly related to n, (i.e. $n^*= c_0+c_1 n$) (Fig. 5.3b), then N^* is scaled by a constant, but otherwise unaffected in form: $N^*=c_1 N$. Because it is the instrument's relative response (e.g. response relative to an adsorbate of a given concentration) that is generally of interest, this scale error will generally not interfere with interpretation of sensor data.

If n^* is nonlinearly related to n (Fig. 5.3c), then interpretation of sensor data becomes more complicated. Suppose that at three separate times during a sensing experiment, changes in N^* of 10^{-4}, 10^{-4}, and 2×10^{-4} are observed. To what degree can one be certain that the actual changes in N in the first two measurements are equal, and that the third change is twice the previous two?

We characterize the error in N by determining the maximum factor by which two measurements of the same N may differ. We denote this factor the maximum slope ratio (MSR) α:

$$\alpha = \frac{\max(N^*)}{\min(N^*)} = \frac{\max\left(n^*(n_s) - n^*(n_b)\right)}{\min\left(n^*(n_s) - n^*(n_b)\right)} \tag{5.16}$$

where the maximum and minimum are taken over all (n_b, n_s) pairs within the sensor range. Because $N=n_s-n_b$,

$$N^* = n^*(n_b + N) - n^*(n_b) \tag{5.17}$$

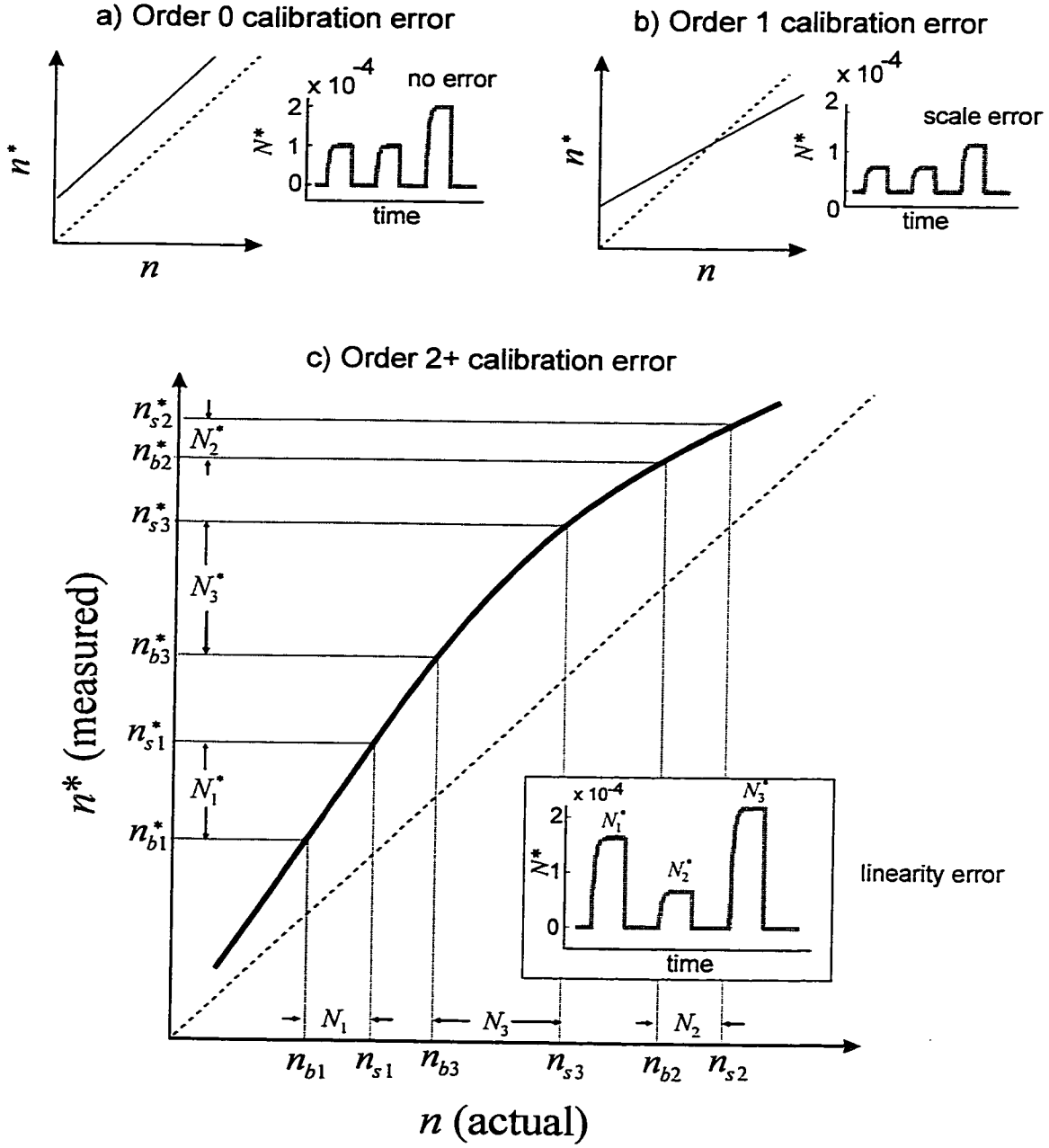

Figure 5.3. Effects of refractive index calibration error on adsorption index N. (a) A constant offset in the calibration curve cancels out in the calculation of N. (b) A linear error in the calibration curve results in uniform scaling of N. (c) Higher order error in the calibration curve causes linearity errors in N -- proportionality of N is lost.

and

$$\alpha = \frac{\max\left(n^*(n_b + N) - n^*(n_b)\right)}{\min\left(n^*(n_b + N) - n^*(n_b)\right)} \tag{5.18}$$

If $n^*(n)$ is continuous it follows from the mean value theorem of analysis

$$\alpha = \frac{\max\left(\frac{dn^*}{dn}\right)}{\min\left(\frac{dn^*}{dn}\right)} \tag{5.19}$$

The MSR α provides guidelines for the interpretation of N^*. If the ratio between two measured adsorption indices is N_2^*/N_1^*, the ratio between the true indices will be in the interval

$$\frac{N_2}{N_1} \in \frac{N_2^*}{N_1^*}\left[\alpha^{-1}, \alpha\right] \tag{5.20}$$

conversely, if the true ratio is N_2/N_1, the measured ratio will be bounded by

$$\frac{N_2^*}{N_1^*} \in \frac{N_2}{N_1}\left[\alpha^{-1}, \alpha\right] \tag{5.21}$$

If $N_1 = N_2$ and N_2^* and N_1^* are two different measurements of the same N,

$$\frac{N_2^*}{N_1^*} \in \left[\alpha^{-1}, \alpha\right] \tag{5.22}$$

Subtracting one from both sides and multiplying by N_1^*,

$$N_1^* - N_2^* \in N_1^*\left[\alpha^{-1} - 1,\ \alpha - 1\right] \tag{5.23}$$

which quantifies the size of discontinuity in N^* which may be observed due to miscalibration if n_b changes while N remains constant.

We seek a function g which will bring α as close as possible to 1. We consider two methods of determining g: linear RI gradients and centroid analysis.

5.7.1. Deriving g from linear RI gradients

If the RI gradient used for determining h is known to be linear, i.e.

$$n^* = n = c_0 + c_1 t \tag{5.24}$$

where t is time and c_0 and c_1 are constants, then n^* may be calculated at each point in the gradient. The (n^*, b) pairs measured during the gradient may then be used to construct the function g. As described above for the function h, g may be calculated from the (n^*, b) pairs by interpolation or by fitting of a function of known form.

5.7.2. Geometric derivation of g using SPR centroid

In situations where SPR/IRR spectra are of good quality, geometric analysis of the SPR dip can provide a definition for g: the location of the centroid of the SPR dip is approximately proportional to n_s. If we assume that RI is related to the centroid location x_c by

$$n^* = n = c_0 + c_1 x_c \tag{5.25}$$

where c_0 and c_1 are constants, then for each spectrum measured during the calibration gradient, b and x_c can be calculated and a set of (n^*, b) pairs calculated using Eq. (5.25). The function g may then be calculated from these (n^*, b) pairs.

5.7.3. Comparison of methods

The linear gradient method is the more versatile method for deriving g, because no specific model of sensor response is assumed. However, the sensor apparatus must be capable of making a linear gradient. Errors in gradient linearity will be exactly reflected in nonlinearity in N: If the sensor is calibrated assuming a linear gradient, i.e.

$$n^* = c_0 + c_1 t \tag{5.26}$$

but in fact the gradient is nonlinear, with a profile $n(t)$, then

$$\frac{dn^*}{dn} = \frac{dn^*/dt}{dn/dt} = \frac{c_1}{dn/dt} \tag{5.27}$$

and the MSR α is given by

$$\alpha = \frac{\max(dn/dt)}{\min(dn/dt)} \tag{5.28}$$

Compared to the linear gradient method, the derivation of g using the SPR centroid is not as versatile because it only can be used in situations where the SPR centroid gives close to a linear response. Errors in centroid linearity will result in nonunit α:

$$\alpha = \frac{\max(dx_c/dn)}{\min(dx_c/dn)} \tag{5.29}$$

For the experiments described in chapter 2, the centroid method appears to give better linearity than the gradient method. This is shown in Fig. 5.4. This data, previously shown in Fig. 4.6, examines the ability of the SPR/IRR sensor to compensate for bulk RI changes in the presence of adsorption of TX-100 detergent. We expect N to remain approximately constant while the sensor is exposed to TX-100. Analysis of the data using both centroid and gradient methods shows that the centroid method gives a more constant response.

The data of Fig. 5.5, in contrast, show little difference between the performance of the two calibration methods. In this experiment, (previously shown in Fig. 4.7) bulk RI variations due to flowcell heating and cooling were induced during flow of sucrose solution and 0.9 mM TX-100 in sucrose solution. The improved performance of the linear gradient calibration is consistent with the range of n_s and n_b being smaller than in the previous experiment. Also, n_s and n_b never approach the ends of the RI gradient, where the gradient is expected to be less linear due to transient effects.

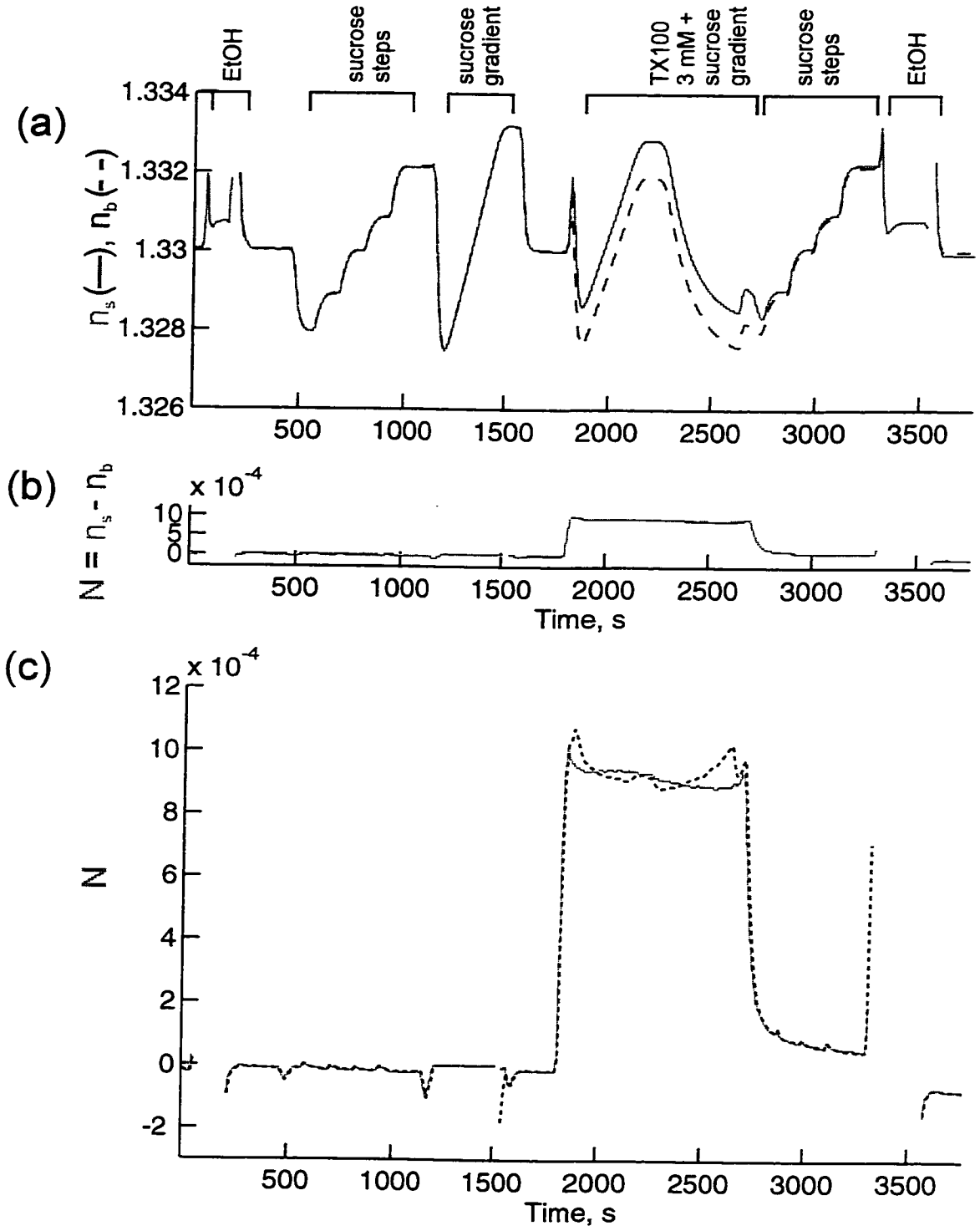

Figure 5.4. Comparison of centroid and linear gradient calibration methods in analysis of data from Fig. 2.8. (a) n_s and n_b calculated using centroid calibration. (b) Adsorption index N calculated using centroid calibration. (c) N, expanded scale, calculated using centroid calibration (solid line) and linear gradient calibration (dashed line).

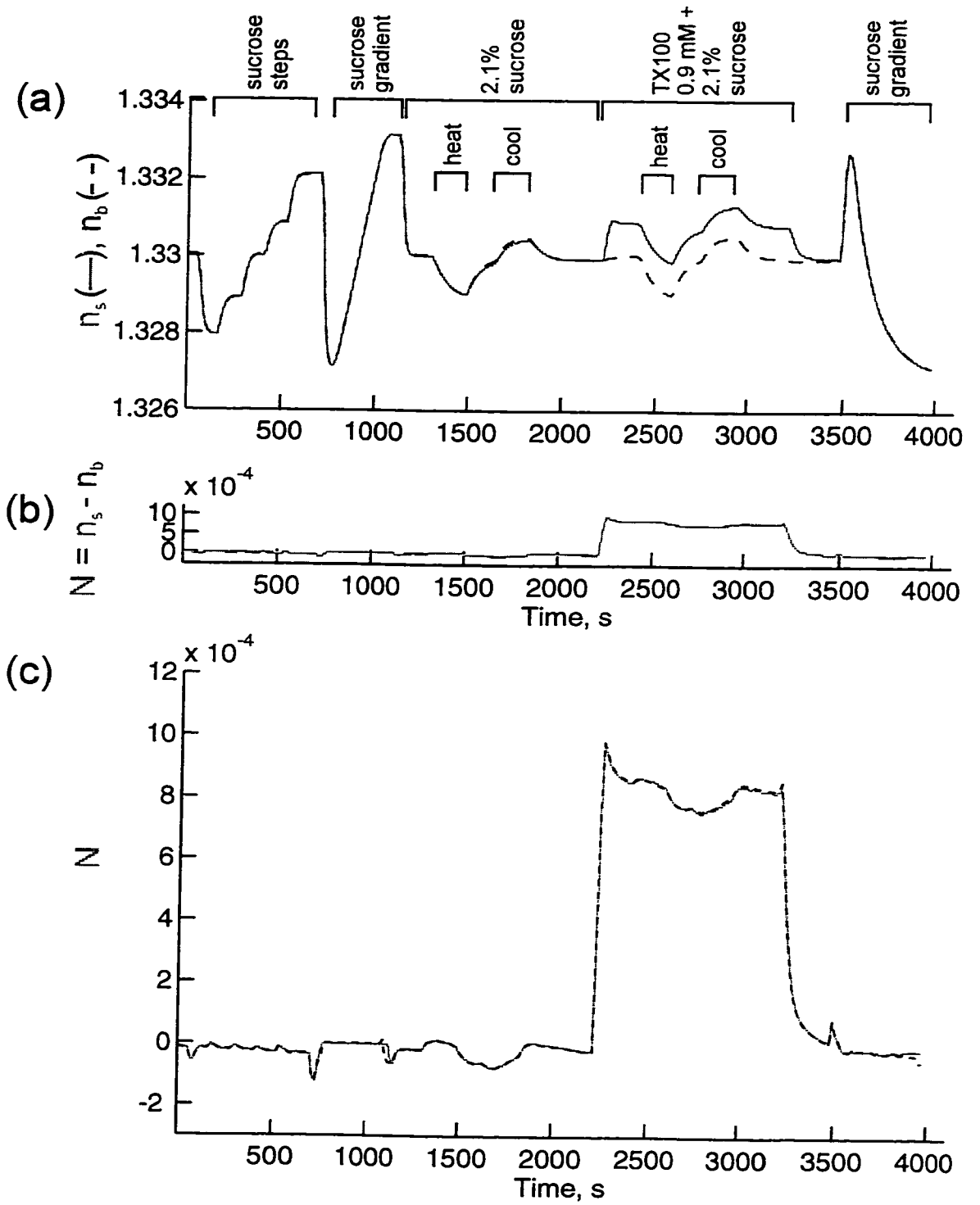

Figure 5.5. Comparison of centroid and linear gradient calibration methods in analysis of data from Fig. 2.9. (a) n_s and n_b calculated using centroid calibration. (b) Adsorption index N calculated using centroid calibration. (c) N, expanded scale, calculated using centroid calibration (solid line) and linear gradient calibration (dashed line).

5.7.4. Determination of mapping coefficients

The two methods of determining g described above assume a linear map between RI and either time or SPR centroid location. In the experiments described in Chapter 4 and in Figs. 5.4 and 5.5, the constants c_0 and c_1 defining the linear map were determined by least-squares fitting, as follows. Five sucrose solutions with concentrations ranging from 0.7% to 3.6% w/v were created. The RIs of these calibration solutions were measured on an Abbe refractometer and corrected for the sensor's 825 nm operation wavelength by assuming linear dispersion. We denote these five RI values $n_{Abbe,1}$ to $n_{Abbe,5}$.

The sensor was then exposed to each of these solutions in turn, and the data analyzed using the above procedure. The constants c_0 and c_1 were chosen such that the bulk RI values $n_{b,1}$ to $n_{b,5}$ measured by the SPR/IRR sensor best fit $n_{Abbe,1}$ to $n_{Abbe,5}$ in the least-squares sense. It was found that in all experiments the fitting residual was less than or comparable to 0.0001, the imprecision of the Abbe refractometer measurement.

The use of a linear map for n^* has the advantage that α is independent of the map chosen. If a nonlinear function is used, for instance to better describe the exact profile of the RI gradient or the relationship between n and the SPR centroid x_c, a better fit of n^* to n could be achieved. However, the function must be chosen carefully to insure that α is not inadvertently increased due to other sources of error.

This is demonstrated in Fig. 5.6. Fig. 5.6a shows the simulated relationship between the SPR centroid pixel x_c and n over the range $1.327<n<1.333$. If the relationship is assumed to be linear, a linearity error in N results, with $\alpha=1.019$. In theory, better linearity could be achieved by finding a nonlinear function which is a better fit to the actual relationship between x_c and n. Suppose, for instance, that rather than a linear function, a quadratic polynomial were fit to the five calibration points. If the Abbe refractometer measurements were very accurate and precise, this procedure would likely improve the linearity of calibration. However, because the refractometer reading has an imprecision of 0.0001 RI units, the fitting procedure is more likely to degrade the calibration than improve it. This is shown in Fig. 5.6b-d. Here, the refractometer calibration procedure described above was simulated, assuming 5, 20, and 100 calibration points evenly spread across the range of n. Refractometer error

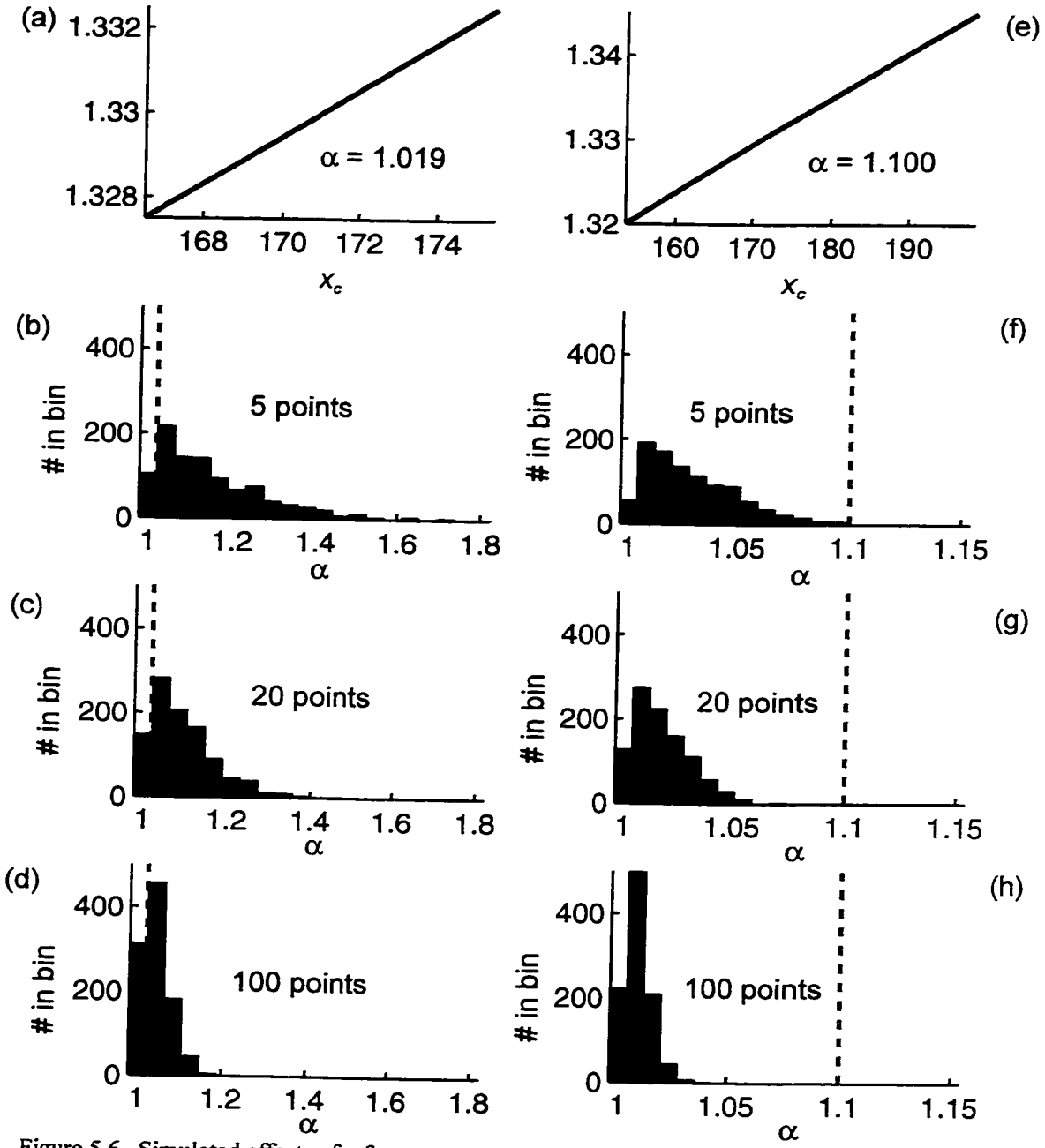

Figure 5.6. Simulated effects of refractometer measurement error on attempts to improve centroid linearity. (a) Relationship between SPR centroid pixel x_c and n for $1.327<n<1.333$, calculated from simulated SPR/IRR spectra. Assuming that the relationship is linear results in a calibration function with $\alpha=1.019$. (b) A quadratic polynomial fit to 5 evenly spaced noisy samples (standard deviation 0.0001 RI) of the n vs. x_c curve generally yields worse linearity. A histogram of the α values resulting from 1000 trials is shown. (c) Same procedure applied to 20 samples. (d) 100 samples. (e) Relationship between SPR centroid pixel x_c and n for $1.32<n<1.35$. Assuming that the relationship is linear results in a calibration function with $\alpha=1.100$. (f) The quadratic fit procedure with 5 samples now generally yields improved linearity. (g) 20 samples. (h) 100 samples.

was simulated by adding normally distributed random noise with standard deviation 0.0001 to the simulated refractometer measurements. The simulated calibration was repeated 1000 times, and a histogram of the 1000 α values characterizing the calibrations was plotted. For calibration using 5 or 20 points, we see that α almost always exceeds the value given by a linear fit. Even when 100 points are used, α is increased more than half the time.

These results show that in this case it is difficult to improve upon a linear calibration function by seeking a better fit to refractometer measurements. However, if the RI range were greater, say $1.32<n<1.35$ (Fig. 5.6e), then the centroid is less linear with respect to RI (α=1.10), and the refractometer error is a smaller proportion of the range. In this case, fitting to refractometer data will generally improve the linearity (Figs 5.6f-h).

5.8. Dependence of data quality on number of calibration points

The gradient calibration procedure provides many measurement points from which to calculate the calibration functions. For instance, in the experiment of Fig. 4.6, 167 calibration points were used. It is interesting to observe the effect of reducing the number of calibration points. Fig. 5.7 shows the data of Fig. 4.6 reanalyzed using various subsamples of the calibration points. The result for 20 calibration points is nearly identical to that obtained using the full calibration set. Some degradation can be seen with 10 calibration points. With 5 points, data is seriously degraded.

5.9. Conclusions

Figure 5.8 summarizes the method of SPR/IRR data analysis described in this chapter. This method uses simple algorithms to provide accurate, low-noise measurements. Because the analysis is based on the actual response of the instrument measured during calibration rather than on a preexisting model of sensor behavior, a detailed model of the sensor response is not necessary to achieve high quality data.

The linear technique upon which this data analysis method is based is most well suited for examining small changes in RI. Then, the assumption of linearity is most

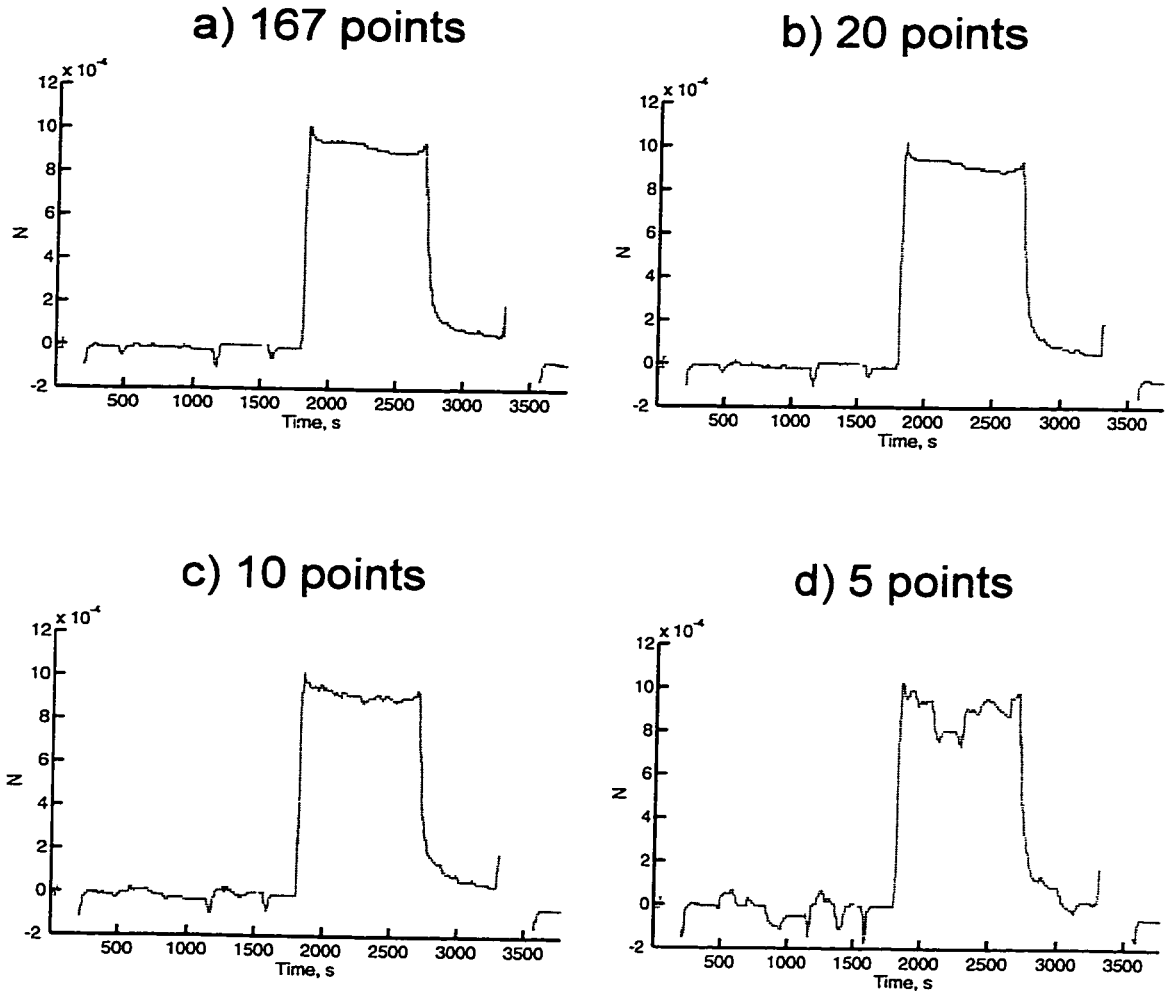

Figure 5.7. Effect of varying number of calibration points. (a) Full calibration set, 167 points. (b-d) Subsamples of calibration set. Data is for the experiment previously shown in Fig. 4.6

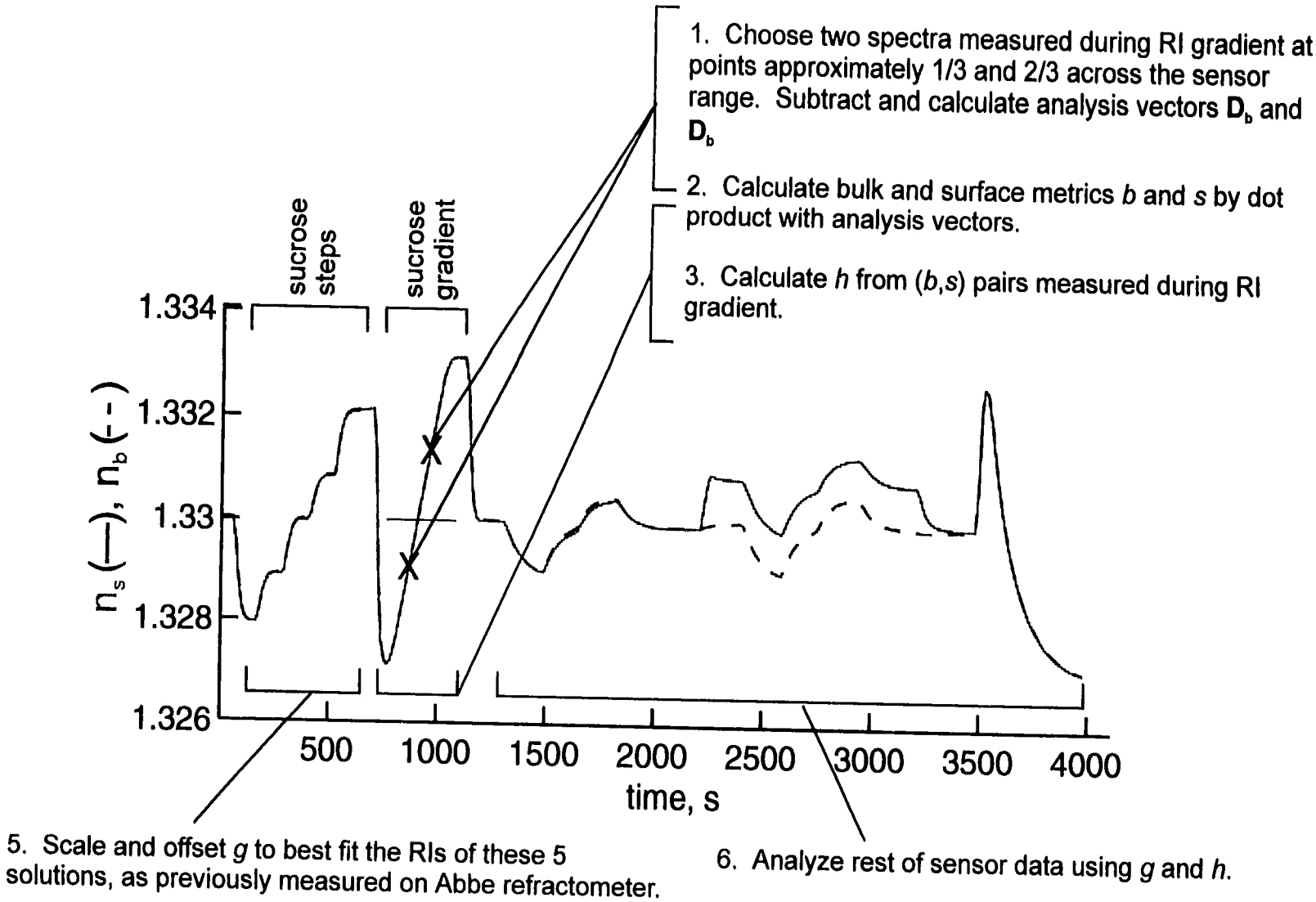

Figure 5.8. Graphical depiction of calibrated linear data analysis procedure.

valid, and the noise performance of the algorithm will be optimal. Towards the end of the linear range, noise will increase, eventually to unusable levels.

The calibration upon which this data analysis method relies uses an RI gradient generated by the instrument to determine instrument response vectors and a relative calibration function describing the relationship between the SPR and IRR measurements. If this gradient is linear, the calibration data may also be used to generate an absolute calibration which will provide linear adsorption measurements. In the data presented here, however, better linearity was obtained by using the SPR centroid data measured during calibration to linearize the RI measurements. For most effective application of calibrated linear data analysis, a simple, automatic method of generating highly linear RI gradients must be used.

Notes for Chapter 5

[1] S. Cowen, J. R. Sambles, Resolving the apparent ambiguity in determining the relative permittivity and thickness of a metal film using optical excitation of surface plasmon-polaritons, *Opt. Commun.* **79** (1990) 427-430.

[2] J. Raty, E. Keranen, K-E Peiponen, The complex refractive index measurement of liquids by a novel reflectometer apparatus for the UV-visible spectral range, *Meas Sci Technol.* **9** (1998) 95-99.

[3] T. M. Chinowsky, S. S. Yee, Quantifying the information content of surface plasmon resonance reflection spectra, *Sens. Act. B* **51** (1998) 321-330.

[4] E. Stenberg, B. Persson, H. Roos, C. Urbaniczky, Quantitative determination of surface concentration of protein with surface plasmon resonance using radiolabeled proteins, *J. Coll. Int. Sci.* **143** (1991) 513-526.

[5] T. M. Chinowsky, S. B. Saban, S. S. Yee, Experimental data from a trace metal sensor combining surface plasmon resonance with anodic stripping voltammetry, *Sens. Act. B* **35-36** (1996) 37-43.

[6] J. E. Geake, C. S. Mill, M. S. Mohammad, A linear differentiating refractometer, *Meas Sci Technol.* **5** (1994) 531-539.

[7] T. M. Chinowsky, L. S. Jung, S. S. Yee, Optimal linear data analysis for surface plasmon resonance biosensors, *Sens. Act. B* **54** (1999) 89-97.

[8] T. O. Lewis, P. L. Odell, *Estimation in Linear Models*, Prentice-Hall, Englewood Cliffs, NJ, 1971.

Chapter 6: Capillary-based SPR sensors

As described in the introduction to this dissertation, we believe that a promising strategy for biosensing is to use SPR in combination with other analytical techniques to achieve sensitive analysis of complex analytes. The SPR/IRR technique discussed in the previous chapters is one example of a combination sensing technique. A desire to expand the possibilities of biosensing techniques combining SPR with other techniques, in a format that is compatible with the eventual production of a low-cost device, motivated the invention of the capillary-based sensor described in this chapter.

Our sensor is based on capillary tubes internally coated with gold (Fig. 6.1). A focused laser beam strikes the capillary tube radially and is reflected from the interior capillary surface at a range of angles above the critical angle. The reflected beam is intercepted by an array detector, producing a reflectivity vs. angle spectrum which can be used for SPR sensing. The capillary simultaneously serves as a disposable optical element and a microvolume sample conduit, with an intrinsically protected sensor surface and an ideal flow geometry. Because the capillary is lightweight and symmetrical, its temperature can be controlled more easily than that of a prism, for instance by controlling the temperature of the surrounding air. The light source and detector are physically separated from the capillary, allowing these temperature sensitive components to be thermally isolated from the capillary itself.

Capillaries are optically versatile, ideal for fluid handling, and simple in construction. To exploit these features in a practical SPR sensor, two main technical challenges must be met. First, although the capillary design is simple, the optical behavior of its two curved surfaces is complex, and must be fully understood to best interpret the sensor data. Second, implementation of SPR sensing inside a capillary requires that the internal capillary surface be coated with a thin layer of SPR-active metal (such as gold) and further coated for biochemical functionality. The internal surface is largely inaccessible to many conventional fabrication techniques such as e-beam evaporation and sputtering. Furthermore, applications may require that the deposition be patterned, with certain segments of the capillary gold-coated and others bare, and with different segments having different biochemical functionality. To meet these demanding requirements, new fabrication techniques must be explored.

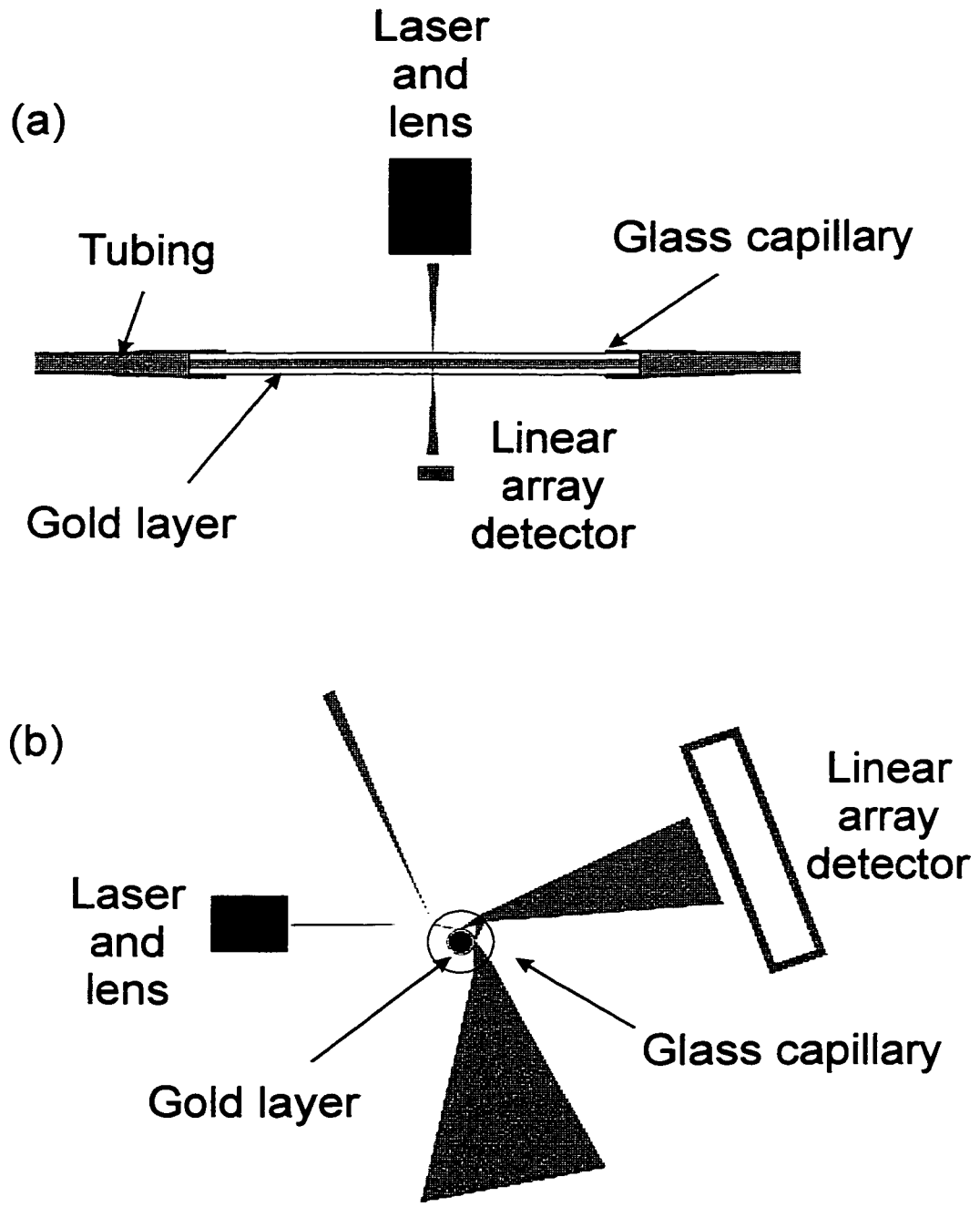

Figure 6.1. Design of capillary SPR sensor. (a) Side view. (b) End view.

6.1. History of optical capillary sensing

The optics of glass capillary tubes are interesting and useful both in the axial direction (i.e. along the length of the capillary) and radially (across the diameter of the capillary). Interest in the axial optics of capillaries was stimulated by the commercialization of low-loss solid- and hollow-core optical fibers in the early 1970's. The transmission of light in liquid-filled hollow-core fibers was first reported at this time [1]. Because the waveguiding effect and small inside diameter of these fibers allowed light to be passed through a very small quantity of liquid with a very long pathlength, liquid-core waveguides were quickly exploited to increase the pathlength available to Raman scattering measurements [2] Since then, interest in the use of capillaries for Raman scattering measurements has continued [3, 4], and the waveguiding properties of capillary tubing have been exploited for several other types of measurements, including fluorescence, absorption, and nephelometry [5].

Theoretical investigations of the radial optics of capillaries geometries goes back to Kerker and Matijevic [6] who in 1961 provided the first analysis describing the scattering of plane waves from concentric cylinders. Experimental investigation of the radial optics of capillaries began in the early 1970s, when researchers sought to measure the dimensions of solid- and hollow-core fibers by illuminating the fibers radially. Horton and Williamson [7] found that the inside and outside diameter of hollow-core fibers could be found by observing the interference pattern produced when the fiber was radially illuminated by a laser. Watkins [8] performed similar determinations with solid core fibers.

Interest in the use of the radial optics of capillaries for sensing appears to have arisen somewhat later, when the need for on-column detectors for high-performance liquid chromatography (HPLC) and capillary electrophoresis (CE) stimulated the development of sensing techniques based on the radial optics of capillaries. The UV absorption detector described by Jorgenson [9] and the refractive-index detector described by Bornhop [10] are early examples of this. The realization that radially-observed interference phenomena in forward [11] and backward [12] scattered laser light could be exploited for the sensitive detection of refractive index led researchers to develop more sophisticated optical models which could predict the

observed interference phenomena. These researchers pursued geometrical optics approaches, rather than the more rigorous but cumbersome physical optics approach of Kerker and Matijevic. These geometrical optics ray-tracing models incorporate the phase information necessary for prediction of interference. One group [13] found these models to be successful in describing interference patterns scattered from capillaries with inside diameters as small as 25 μm.

6.2. Geometrical optics of capillaries

When a radial incident ray strikes the exterior surface of the capillary with incident angle θ_o, the refracted ray strikes the interior surface at an angle θ_i given by

$$\sin\theta_i = \frac{r_o}{r_i}\frac{n_o}{n_i}\sin\theta_o \tag{6.1}$$

where r_o and r_i are the outer and inner radii of the capillary, n_i is the RI of the capillary material, and n_o is the RI of the medium surrounding the capillary (typically air, $n_o = 1$). For a thick wall capillary, defined as one for which

$$\frac{r_o}{r_i}\frac{n_o}{n_i} \geq 1 \tag{6.2}$$

θ_o may be chosen such that the refracted ray strikes the internal wall of the capillary at any angle from 0° to 90°. Thus, by changing the angles of illumination and modifying the internal surface of the capillary, different sensing techniques may be implemented. In an unmodified glass capillary, low-angle transmission/emission measurements (e.g. for absorption or fluorescence measurement) and sub-critical angle reflection measurements (e.g. for bulk refractive index measurement) are possible. In a capillary internally coated with an SPR-active metal such as gold, super-critical angle SPR reflection measurements can be performed.

Note that tubes of large or small inside diameters can be used. For high-flow process control applications, a "capillary" sensor that was actually a large tube might be useful. Small tubing, on the other hand, will reduce reagent and sample

consumption, provide better diffusion to the capillary walls, and provide capillary action that may be useful for sampling purposes.

The ray tracings of Fig. 6.2 illustrate the complexity of the optical capillary response. Each ray tracing shows the transmitted and reflected rays that result when a horizontal incident ray strikes a capillary at a given elevation y relative to the capillary center. Parameters were chosen to simulate a water filled, fused silica capillary with $r_i/r_o = 0.4$. (n_i=1.457, n_o=1.0, and n_b=1.3318, where n_b is the RI of the substance inside of the capillary.) Monochromatic, TM polarized light of wavelength 632.8 nm was assumed, and only rays with intensity greater than 0.1% of the incident intensity were retained. Depending on the input ray elevation, rays will strike the interior capillary surface either below the critical angle (6.2a-f), above the critical angle (6.2g), or not at all (6.2h-l). Note that a simple picture results when light is incident at the Brewster angle (6.2j).

A graph which concisely summarizes the range of capillary optical responses depicted in Fig. 6.2 may be produced by plotting exit angle θ vs. input elevation y for a large number of rays incident at elevations spaced over the breadth of the capillary, and indicating the intensity of each ray by the size of the plot point. This graph is shown in Fig. 6.3b. For simplicity, only rays with intensity greater than or equal to 0.5% of the incident intensity are shown.

Each ray in Fig. 6.2 corresponds to a point in a locus in the plot of Fig. 6.3b. For example, the first surface reflection R1 is observed at angles which begin at θ=180° when y=0 and decrease to 0° as the input elevation increases to y=1. A null due to the Brewster angle can be observed near y=0.8. The locus labeled R2 in Fig. 6.3b corresponds to rays which reflect from the internal surface of the capillary; these are the important rays for SPR and critical angle sensing. The critical angle is located on this locus at the cusp between the loci of transmitted ray T and ray R2 (at y ~= 0.53). This point, together with the point at the end of the locus of R2 (at y=0.58) divide the plot into three regions, corresponding to whether the ray strikes the interior surface of the capillary below the critical angle ($|y|$<.53), above the critical angle (0.53<$|y|$<0.58) or not at all ($|y|$>0.58).

Figs. 6.2 and 6.3 describe the geometrical optics of an unmodified fused silica capillary tube filled with water. The response of a capillary internally coated with gold can be simulated by calculating the reflectivity and transmissivity of the interior

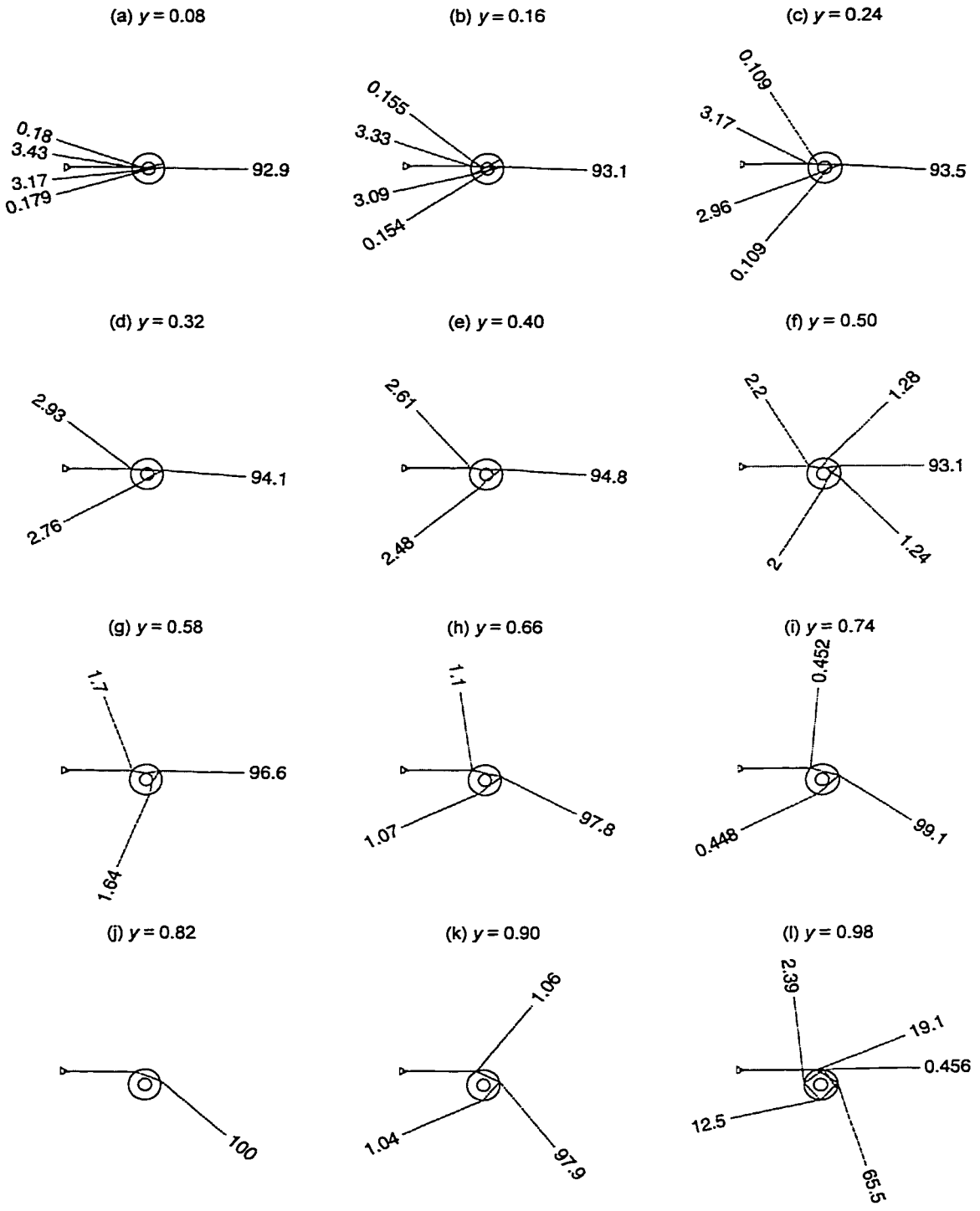

Figure 6.2. Capillary ray traces for rays of various input elevations. Input rays are marked with a triangle; output rays are marked with their intensity as a percentage of incident. Ray traces are calculated assuming TM polarization, with r/r_o=0.4, n_i=1.457, n_o=1.0, n_b=1.332.

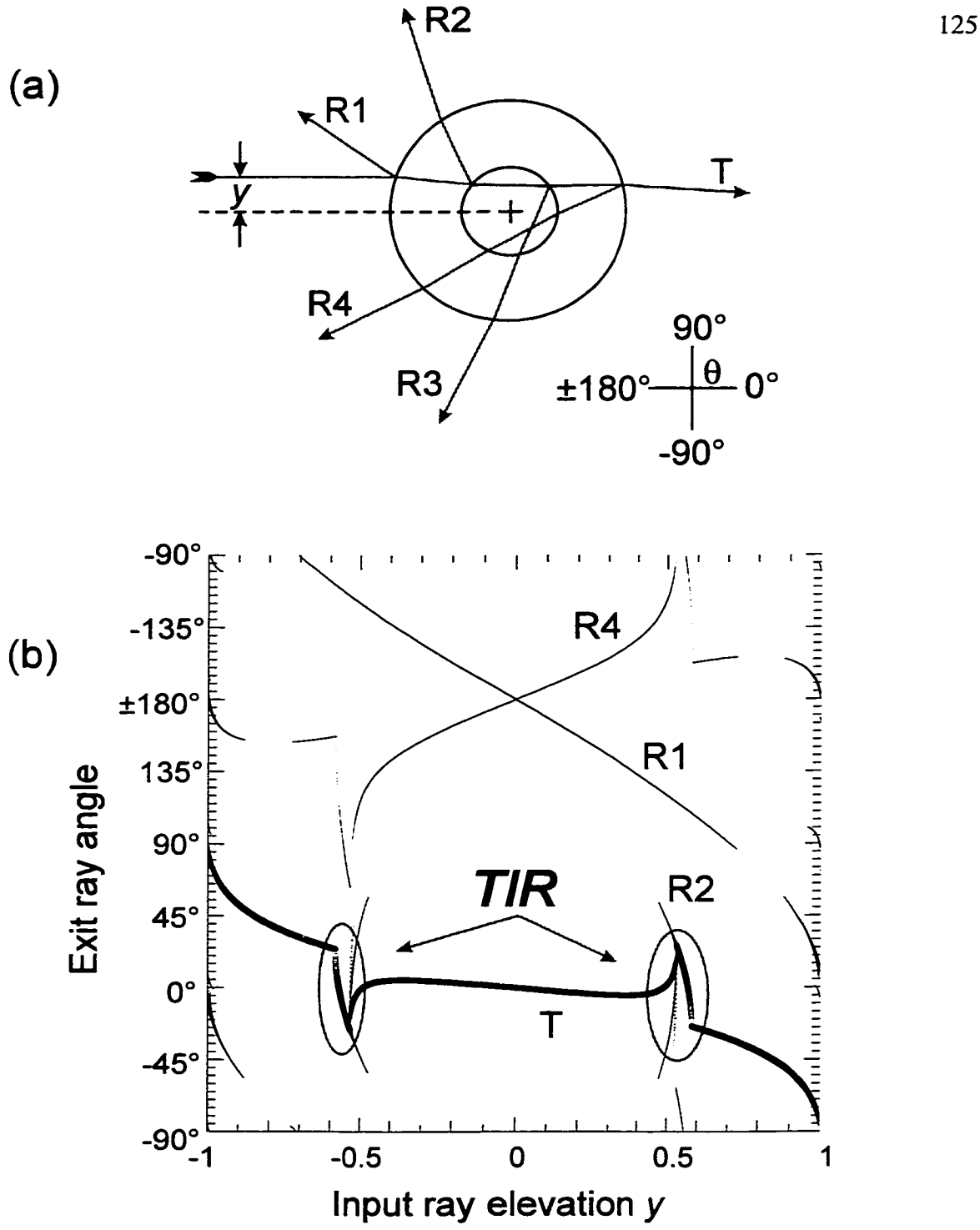

Figure 6.3. Summary plot describing capillary output rays as a function of input ray elevation. (a) Capillary ray trace showing definition of y and q, reflected rays R1-R4, and transmitted ray T. (b) Summary plot. TIR region and loci of transmitted ray and reflected rays are indicated. Ray traces are calculated assuming TM polarization, with r_i/r_o=0.4, n_i=1.457, n_o=1.0, n_b=1.332.

surface using multilayer thin film models (see Appendix A). In the result of this simulation (Fig. 6.4), the SPR phenomenon appears as a dip in intensity above the critical angle.

6.3. Capillary illumination

Fig. 6.3b shows that a single ray striking the capillary at a given elevation y, where $|y|<0.58$, will reflect from the interior capillary surface and exit the capillary at a certain discrete angle. If a *range* of y values is illuminated, rays will exit the capillary at a range of angles. Because each exit angle corresponds to a different internal angle of incidence, a detector intercepting those output angles will yield the measurement of reflectivity vs. incident angle necessary for SPR and critical angle sensing.

The plot of Fig. 6.3b guides what range of y to illuminate and where to place the detector. To monitor the reflectivity below the critical angle, one would illuminate with rays with $|y|<0.53$. To look at SPR, one would illuminate $0.53<|y|<0.58$. For the capillary of Fig. 6.2, a bundle of rays extending from $y = 0.53$ to $y = 0.58$ would strike the internal surface at angles ranging from the critical angle up to 90°, and exit the capillary at angles ranging from 30° down to -25°.

To apply these ray-tracing simulations to experiments, one must determine how they relate to the actual behavior of a capillary illuminated by a real light source. How should a "bundle of rays" be implemented experimentally?

We used a focused laser beam for capillary illumination, because a focused laser can produce a very small spot of monochromatic light. The laser beam is Gaussian, with nonzero divergence and a beam waist (i.e. focus spot size) inversely proportional to the divergence [14] (Fig. 6.5a). Given the differences between this beam and the ideal "bundle of rays," to what extent the capillary behavior can be explained by a simple geometrical model which assumes a perfectly collimated beam (Fig. 6.5b)? If this model is not sufficient, can an enhanced geometrical model (6.5c), which assumes a more complicated distribution of rays, do the job? What aspects of the capillary response can only be predicted by a more sophisticated physical optics model?

These answers to these questions are not fully known. Almost all researchers into the radial optics of capillaries have illuminated the capillary with an unfocused laser beam and modeled the incident radiation as a plane wave. The exception is Krattiger

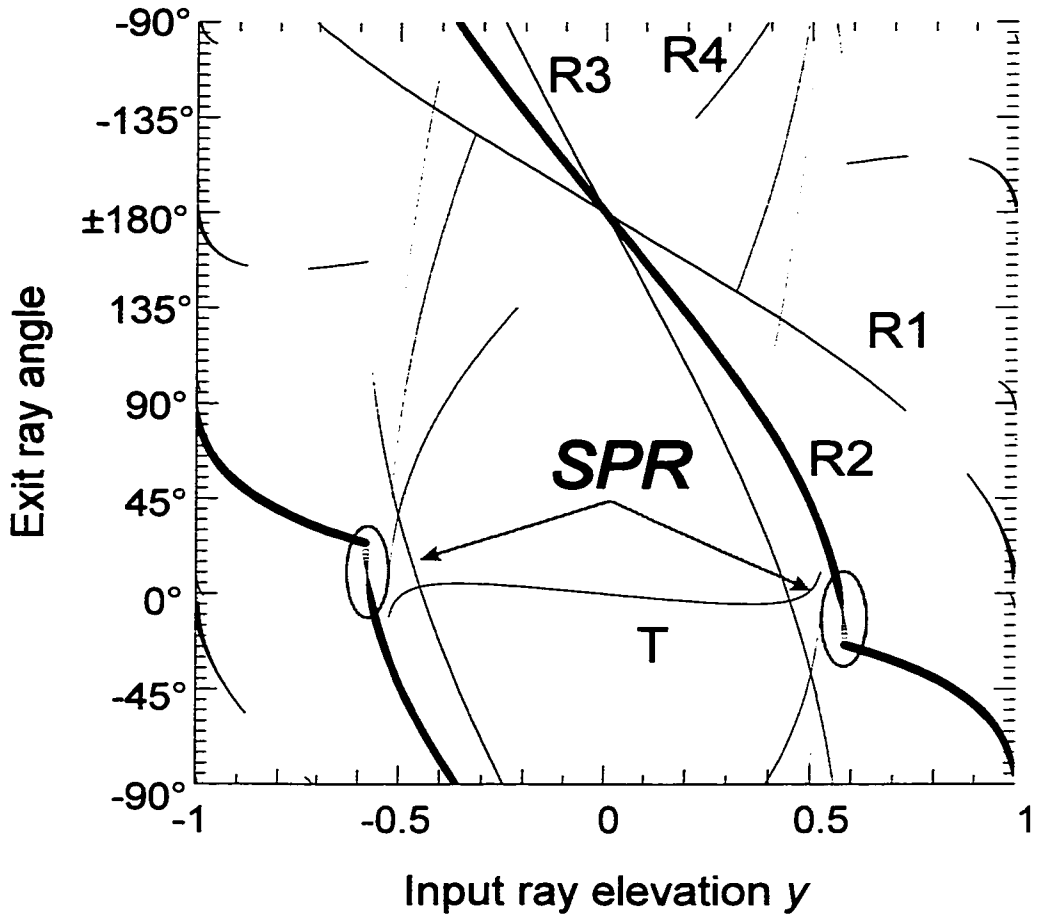

Figure 6.4. Summary plot describing response of capillary internally coated with 50 nm Au. Dip in reflectance due to SPR in the TIR region is indicated. Ray traces are calculated assuming illumination of 632.8 nm wavelength and TM polarization, with r/r_o=0.4, n_i=1.457, n_o=1.0, n_b=1.332.

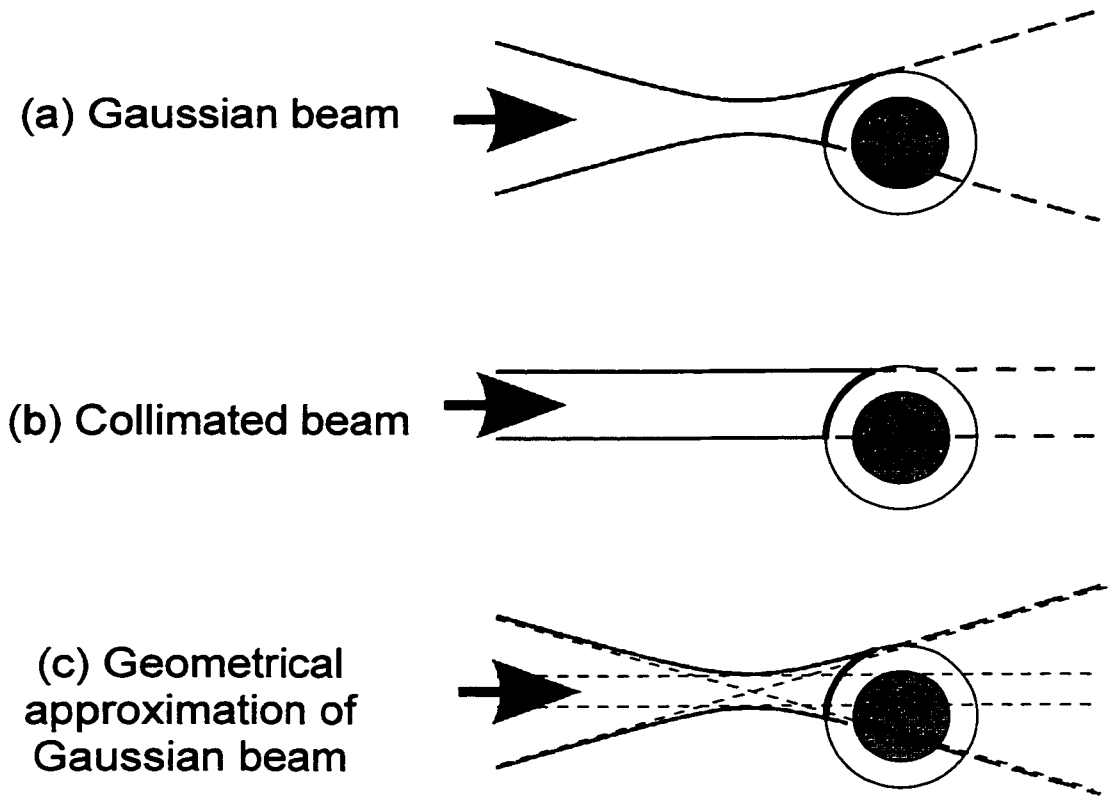

Figure 6.5. Capillary illumination and modeling. (a) The capillary SPR sensor is illuminated by focused layer beam with a Gaussian profile. (b) The simplest geometrical model assumes perfectly collimated illumination. (c) Can the Gaussian beam be better modeled by geometrical model which assumes a more complicated distribution of rays?

et al. [13] who used a focused beam, modeling it as a collimated beam with a Gaussian cross-section. They found their approach to be successful in predicting the capillary response for capillary IDs down to 25 μm. However, because the SPR effect is so dependent upon incident angle, is unclear whether this approach, which ignores the angular content of the incident beam, can fully predict the response of our capillary SPR sensor.

A full investigation of this issue is the subject of a research grant from the National Science Foundation [15]. For the work described here, however, a simple approach was found to satisfactorily describe the capillary behavior. The Gaussian laser beam was treated as a collimated beam with a width that varies with distance from the focus. Moving the capillary closer to or further from the focus decreases or increases the range of y that is illuminated. Moving the beam from side to side changes the value of y at which the illumination is centered. Interpreting the capillary illumination in this way, the capillary response was found qualitatively to agree with Fig. 6.3b. As the capillary was moved across the beam, the distribution of exit angles was found to vary in a manner consistent with Fig. 6.3b; as the capillary was moved nearer to or further from the focus, the range of output angles varied in the manner predicted from Fig. 6.3b for a narrower or wider bundle of rays.

6.4. Capillary scanner

To demonstrate the qualitative agreement of the capillary response with geometrical predictions, the capillary scanning apparatus depicted schematically in Fig. 6.6a was constructed. The capillary is mounted in the center of a black plastic cylinder mounted on an X-Y positioner. A 5 mW, 632.8 nm wavelength He-Ne laser beam passes through two linear polarizers, then is focused by a 10x microscope objective, yielding a beam of divergence 3° and beam waist 16 μm. The polarizer nearer the lens is adjusted to select the polarization of the light incident upon the capillary, and the polarizer nearer the laser is rotated to control the intensity of the incident light.

The microscope objective projects through a hole in the cylinder, illuminating the capillary. The y-axis of the capillary positioner is motorized (Motor 1 in Fig. 6.6a), allowing the capillary to be moved across the beam under computer control. The

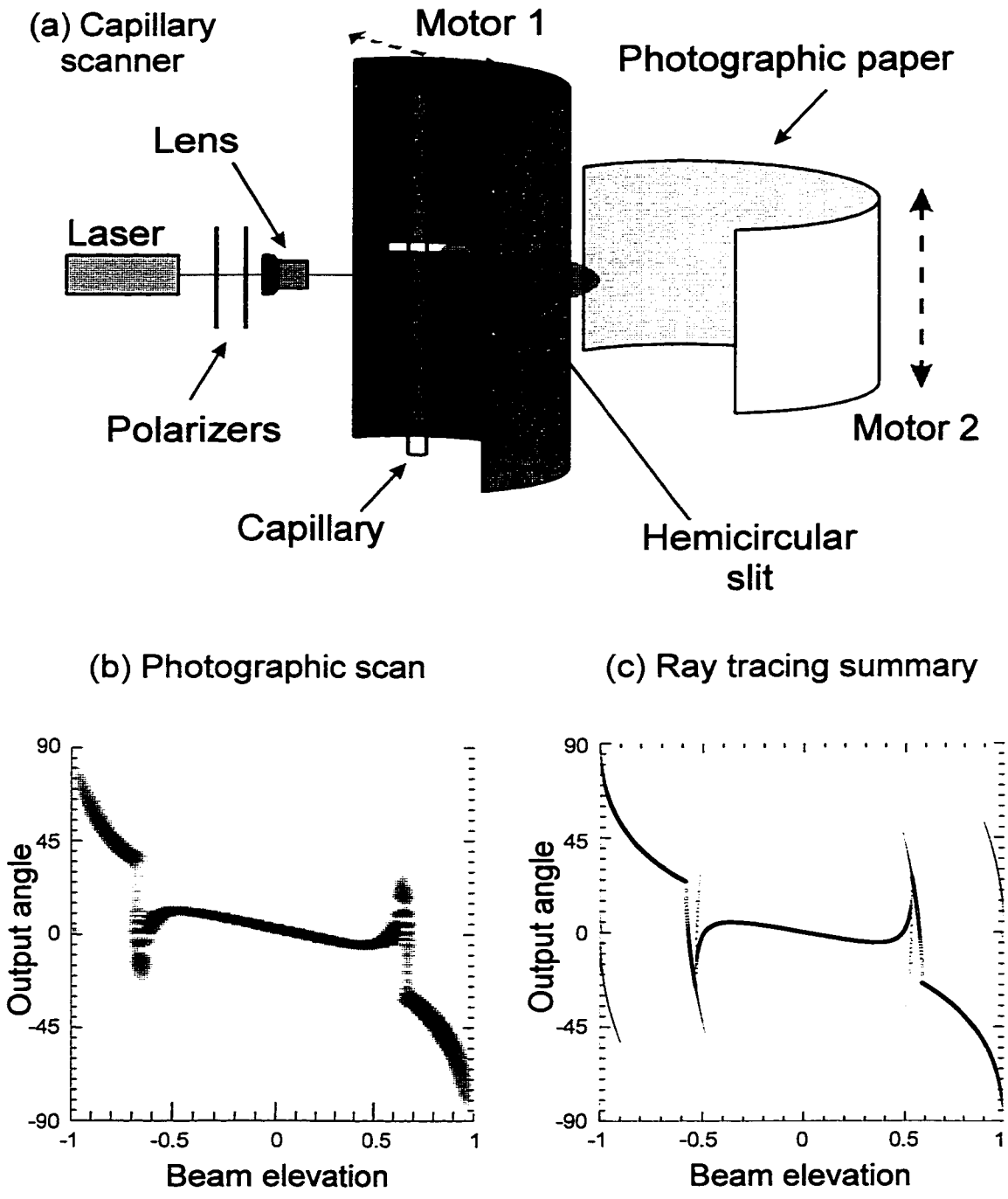

Figure 6.6. Capillary scanning. (a) Schematic of scanner. (b) Scan of unmodified fused silica capillary, 150 μm OD, 375 μm ID, water filled (c) Geometrical optics prediction of response, assuming TM polarization, r/r_o=0.4, n_i=1.457, n_o=1.0, n_b=1.332.

manual x-axis of the positioner allows adjustment of the distance of the capillary from the beam focus. For the experiments described here, the beam focus was adjusted such that the smallest output spot size was produced.

Light exiting the capillary passes through a 0.7 mm slit in the cylinder and strikes a sheet of photographic paper (Kodak Panalure) in contact with the outside surface of the cylinder. The paper is supported by a plastic hemicylinder mounted on a second motorized linear positioner (Motor 2 in Fig. 6.6a). This positioner allows the paper to be moved up and down relative to the slit, selecting the region of the paper that is exposed.

When the motion of the two positioners is synchronized such that the beam traverses the width of the capillary at the same time that the photographic paper moves, a photographic print which records how the capillary output varies over 180° as the input beam location changes is produced.

Fig. 6.6b shows a scan of a water filled fused silica capillary (Polymicro Technologies TSP150375, 150 μm ID, 375 μm OD) produced in this manner. The scan agrees well with the response predicted by geometrical optics (Fig. 6.6c), successfully predicting the three regions of the capillary response. Note that only the strongest rays predicted in 6.6b are visible in the photographic scan due to the limited latitude of the photographic paper.

The most obvious difference between 6.6b and 6.6c is the presence of interference fringes in the super-critical-angle region ($0.55<y<0.6$) of the photographic response. These fringes result because of the multiple paths that light takes inside the capillary, and are discussed further below.

6.5. Capillary sensor

For sensing, a simplified, stationary version of this apparatus was used (Fig. 6.7a) Manual positioners were used to move the capillary from side to side across the beam to select a different region of the response, and to move the capillary further from or closer to the beam focus, changing the size of the region that is illuminated. The response measured in this manner is effectively a vertical slice of the full photographic scan described above.

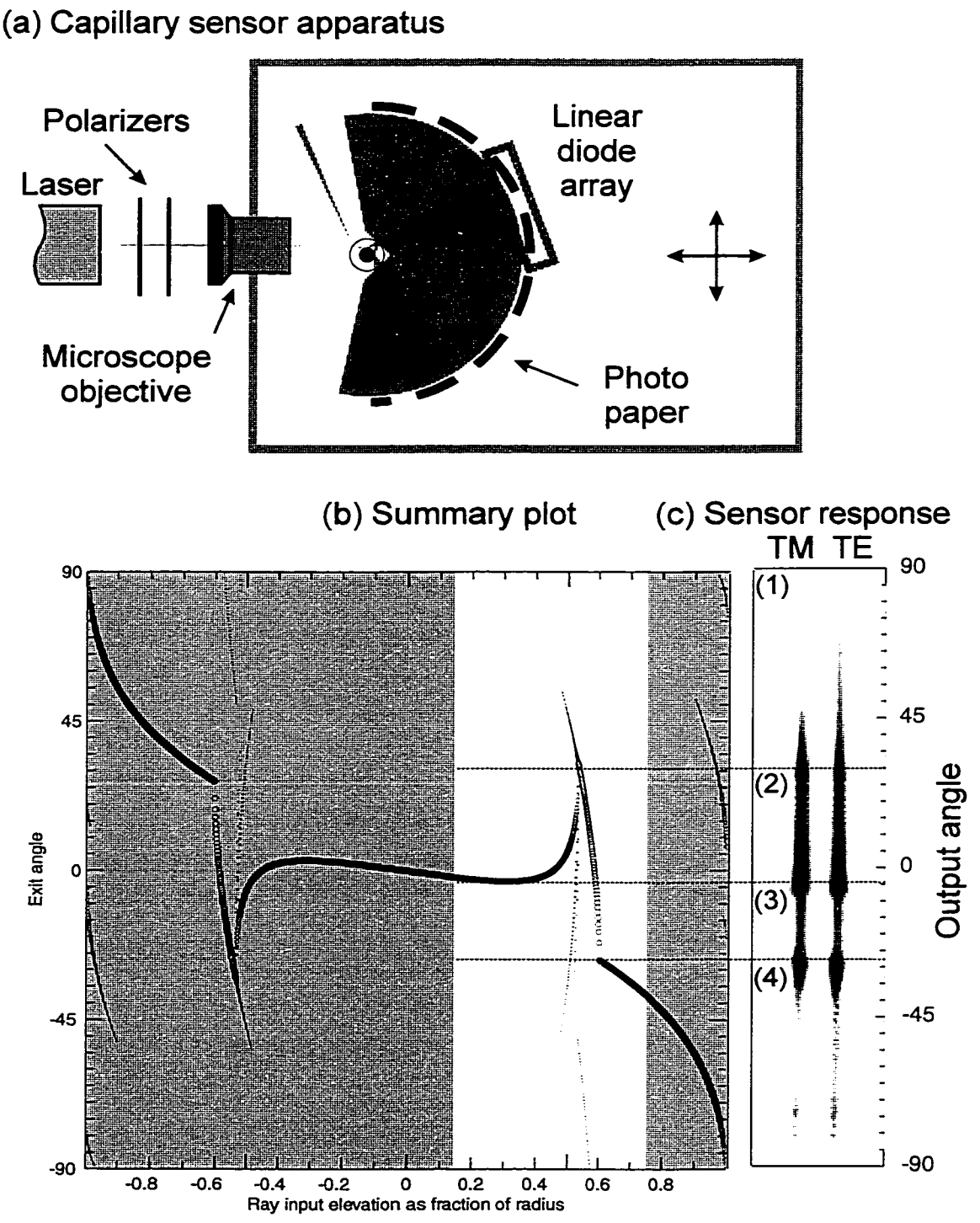

Figure 6.7. Capillary sensor apparatus. (a) Schematic (b) Summary plot predicting response of uncoated capillary. Ray traces are calculated assuming TM polarization, with r/r_o=0.4, n_i=1.505, n_o=1.0, n_b=1.332. (c) Photographic record of response of water filled soda-lime glass capillary, OD 1 mm, ID 0.4 mm, for TE and TM illumination, showing four regions of response.

For real-time sensing, a 256 pixel linear diode array (Texas Instruments, previously described in Chapter 4) was placed to intercept light exiting the capillary. When it was desired to record the capillary output over a range of angles larger than that permitted by the diode array, a fixed hemicylindrical screen of photosensitive paper was used to record emission from the capillary over 180 degrees.

Fig. 6.7c shows the photographically recorded response of a water filled, uncoated soda-lime glass capillary (Friedrich & Dimmock (FD), 0.4 mm I.D.,1 mm O.D, n_D=1.519) under both TE and TM illumination. Here, the beam position and focus were adjusted to strike a broad range of angles on one side of the capillary (approximately the unshaded region in Fig. 6.7b). The response has four distinct regions which can be correlated to features of the geometrical optics simulation shown in Fig. 6.7b.

Region 1 (30° to 90°) corresponds to sub-critical angle reflections from the interior capillary surface. Note that below the critical angle, TM reflectivity decreases faster than TE, as predicted by the Fresnel equations.

In Region 2 (-5° to 30°), both light transmitted through the capillary interior and light reflected from the capillary interior above the critical angle illuminate the photographic paper. The difference in the lengths of these two optical paths causes the interference fringes observed in this region.

Region 3 (-27° to -5°), in contrast, is illuminated by interior reflections above the critical angle, but not by transmitted light. Hence, the response is dimmer, and no fringes are visible.

Region 4 (-90 to -27°) is illuminated by light which passes through the capillary but does not strike the interior surface at all.

6.6. Fabrication techniques for SPR capillaries

These measurements of the optical behavior of glass capillaries show that the geometrical optics capillary model is useful in predicting the capillary response and in designing a method of observing the reflectivity of the interior surface of the capillary. To take the next step and implement a capillary SPR sensor requires that a high-quality gold film approximately 50 nm thick be deposited on the interior surface of the capillary. Three methods by which this can be achieved are the following:

1) *High-angle conventional evaporation.* For capillary tubes with relatively large inner diameter, the tubes may be placed in a conventional thermal or electron-beam evaporator at an angle, allowing gold to reach the inner surface (Fig. 6.8a). If the capillary is rotated during deposition, the coverage will have angular uniformity, but will vary with distance inside the capillary.

2) *Wire evaporation.* A second method for depositing gold in capillaries makes use of thin gold-coated tungsten wire threaded through the capillary (Fig. 6.8b). The gold is evaporated by passing electric current through the wire. If the wire diameter, thickness of gold on the wire, and capillary I.D. are compatible, the correct amount of gold will be deposited.

3) *Wet chemical deposition.* A wet chemical process for depositing SPR-quality gold layers on glass has been demonstrated by Lyon et al. [16]. In this technique (Fig. 6.8c), gold colloid particles are fixed to a glass surface using mercaptosilane chemistry. Additional gold is then reduced from a gold chloride solution onto these particles, causing the particles to grow together and form a uniform layer which supports SPR.

These techniques are listed in increasing order of applicability to capillaries of small inside diameter. We used high-angle conventional evaporation to deposit silver inside glass tubing of 1.8 mm ID for our first proof-of-concept experiments [17]. This method was found to be impractical for tubing of smaller size, and was not used further. The wire-evaporation method was then used to deposit gold inside 0.4 mm ID capillaries [18]. Finally, the wet chemical method was used to deposit gold inside 0.15 mm ID capillaries. Experiments performed using the latter two fabrication methods will be discussed here.

6.7. Fabrication of wire-evaporated gold layers in capillaries

FD glass capillaries ~2 cm long were treated on the interior with 3-mercaptopropyl trimethoxysilane to promote gold adhesion, following the procedure given in [16]. Gold was then deposited inside of the capillaries using 2 mil gold-coated tungsten wire (Alfa Aesar). Under low vacuum, the wire was held taut in the center of the capillary using micropositioners, and a current pulse from a capacitive discharge was sent through the wire, heating it and evaporating the gold onto the capillary interior. The

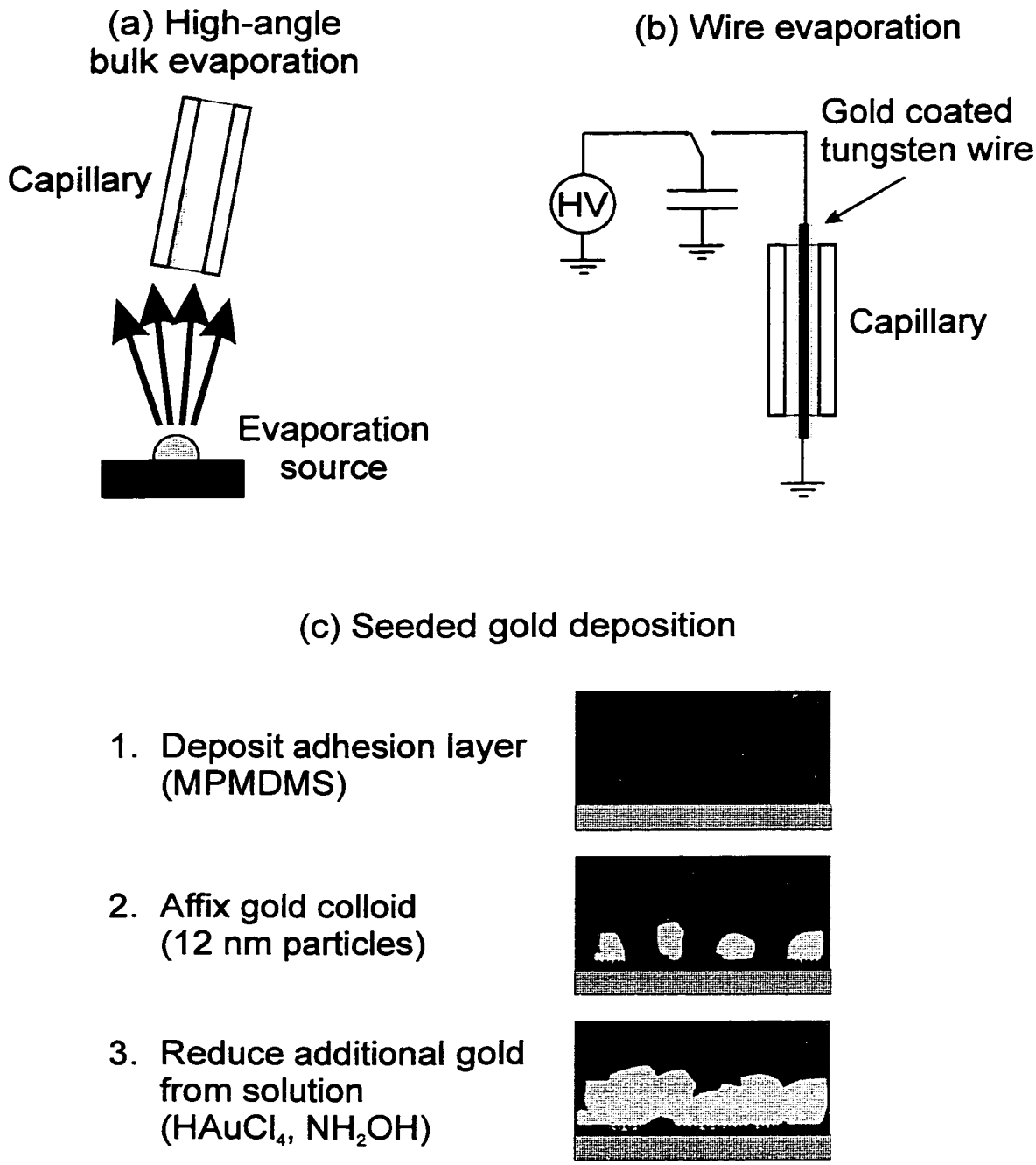

Figure 6.8. Techniques for internally coating capillaries with gold.

quantity of gold on the wire was not tightly specified (indicated only to be 3-5% by weight) and of unknown uniformity. Assuming 4% gold deposited in an even coating on the wire, and a 0.4 mm I.D. capillary, a uniform evaporation would result in a 64 nm gold deposition.

6.7.1. SPR response of wire-evaporated gold layers

After gold was deposited, capillaries were filled with water and placed in the capillary sensor apparatus described above. Because gold deposition was nonuniform, the capillary position was adjusted until a spot of suitable quality was found. Fig. 6.9a shows the response of one such capillary, recorded photographically.

The laser illumination was adjusted to strike only the region above the critical angle, and so no fringes are obvious. Under TE light, the reflectivity appears uniform, while the TM response shows the dip characteristic of SPR. When the capillary is filled with ethanol (n=1.36 compared to water's n=1.33), the dip moves to a lower angle on the screen (corresponding to a higher angle on the capillary's internal surface), consistent with the expected behavior of SPR. Measurement of these spectra by photodiode array (Fig. 6.9b) shows a well defined dip in reflectivity, and reveals that a small amount of fringing still remains in the spectra.

6.8. Wet chemical gold deposition

The wire deposition method is of limited use: capillary length and ID are constrained and deposition is nonuniform. A more promising technique, which takes advantage of the natural fluid handling capabilities of capillaries, is the wet chemical method mentioned above. To establish whether this technique could be applied to capillaries, gold layers were deposited in TSP150375 capillaries. Reagents were pumped through the capillaries using air pressure, simplifying the use of corrosive reagents by not requiring use of a mechanical pump. However, because the only way to control the flow rate was to adjust the air pressure, flow rates were not tightly controlled.

Gold colloid was manufactured following the procedure given in [19]. 100 mL 0.01% $HAuCl_4$ (Aldrich) was brought to a vigorous boil in a stirred beaker. 1.5 mL of 1% sodium citrate (Aldrich) was then added. Boiling was continued for 10 minutes

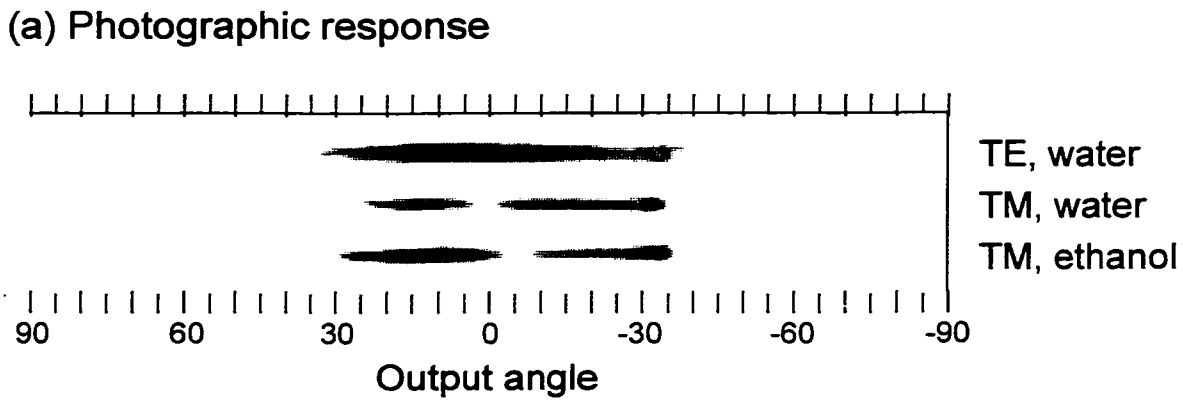

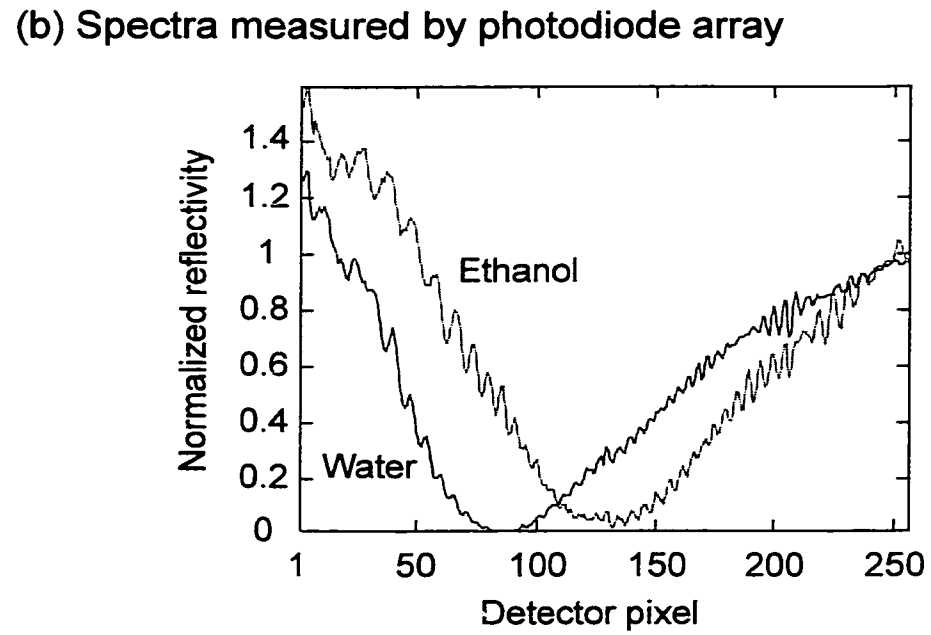

Figure 6.9. SPR response of capillary with wire-evaporated gold layer. a) Photographic recording of response. b) SPR spectra measured by photodiode array. Soda-lime glass capillary, 0.4 mm ID, 1 mm OD.

after the addition. Solution color changes were observed consistent with [19] -- a change to blackish blue in 20 s, followed by a change to deep burgundy at 60 s. Colloid was stored under refrigeration and used within 1-2 days after manufacture.

The gold deposition procedure was adapted from that described in [16]. Capillaries were cleaned by pumping piranha solution (30 % H_2O_2:H_2SO_4 1:4) through the capillary for 15 minutes at 10 µl/min. The capillary was then rinsed by pumping DI water, followed by ethanol (Pharmco) for 10 minutes each at 150 µl/min. A silane adhesion layer was then deposited. 3-mercaptopropylmethyldimethoxysilane (MPMDMS, United Chemical Technologies, 11 mM in ethanol) was pumped for 4 hours at a flow rate of 60 µl/min. Following rinses in ethanol and DI water for 10 minutes each at 150 µl/min, gold colloid was pumped for 2 hours at a flow rate of 60 µl/min. After colloid deposition, DI water was pumped for 10 minutes at 150 µl/min. At this point, the capillary interior surface could be seen to have a light burgundy color.

For the final step of the deposition, 0.5 mM hydroxylamine hydrochloride ($NH_2OH.HCl$, Aldrich, 0.5 mM) was mixed with 0.06% $HAuCl_4$ in a proportion of 5:1, and pumped for 40 minutes at 170 µl/min. As this step proceeded, capillaries were observed to become darker and more opaque. At the end of this step, capillaries were rinsed with DI water and blown dry with air.

Prior to examination, the protective polyimide coating on the outside of the capillary was removed by carefully scraping the capillary with a razor blade. Removal of the polyimide using hot sulfuric acid was much more efficient, but the high temperature involved was found to damage the gold layers.

6.8.1. SPR response of gold layers deposited by wet chemical method

Deposition results varied widely, both from capillary to capillary and also along the length of each capillary. Layers were of the highest quality near the beginning of the capillary (i.e. where fresh reagent entered). Layers decreased in thickness and in adhesion towards the end of the capillary. Optical microscopy revealed further variations in deposited layers. By transmitted light, layer color varied from red to purple to blue; by reflected light, some layers had the specular appearance expected of evaporated gold layers (Fig. 6.10a), while others appeared grainy (Fig. 6.10b).

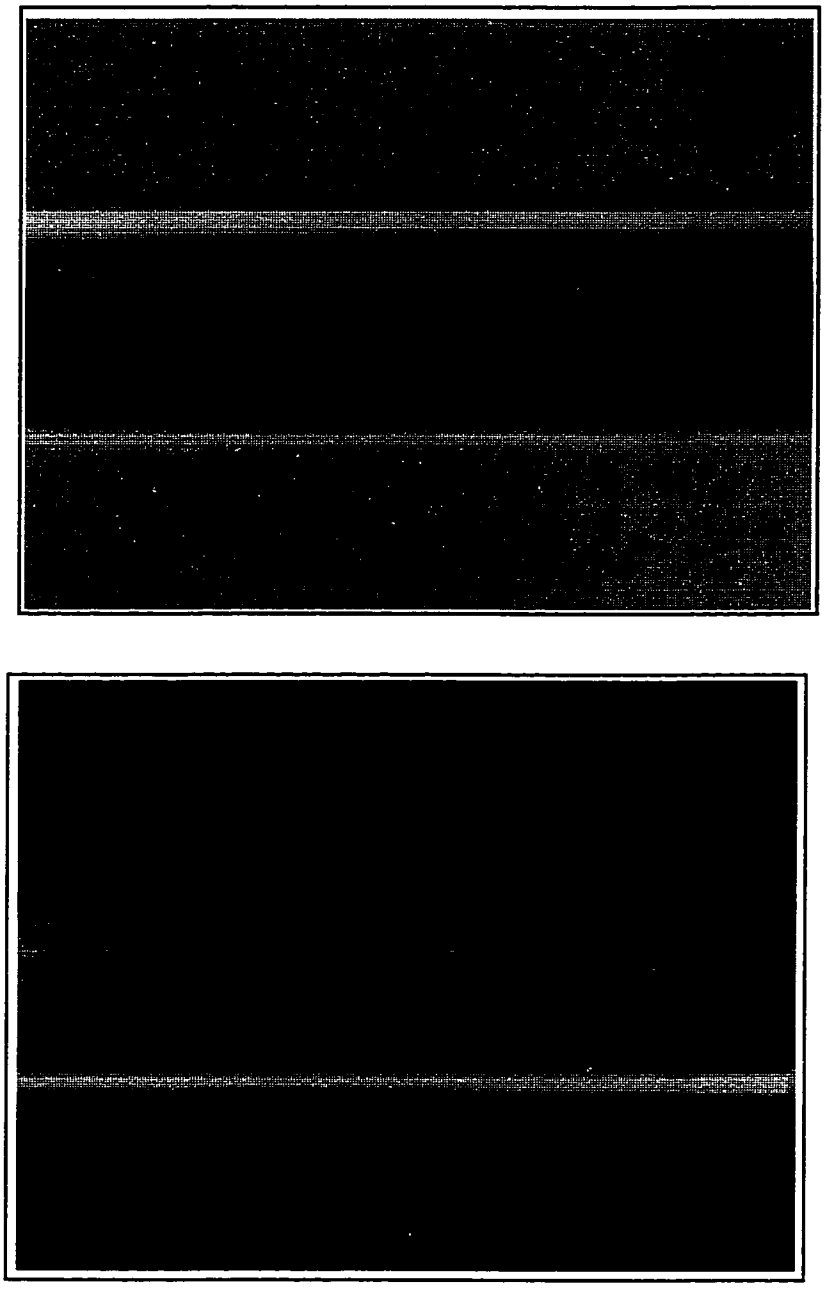

Figure 6.10. Photographs of gold deposited in capillaries by wet chemical method, showing varying surface quality. (a) Specular gold layer. (b) Grainy gold layer.

Capillaries with layers which looked similar to evaporated gold (specular reflection, blue by transmitted light) were found to exhibit behavior consistent with SPR. Fig. 6.11 shows the characterization of one such capillary (water filled) in the capillary scanner described above. A dip in reflectivity is observed above the critical angle under TM illumination, but not under TE.

To evaluate whether the observed dip could be used for sensing, the beam location was fixed at the point which illuminated the internal surface above the critical angle. Captured photographically (Fig. 6.12a), the TM spectrum exhibits a broad dip above the critical angle, and numerous interference fringes. When the TM spectrum is captured with a photodiode array and normalized to the TE spectrum, Fig. 6.12b results. The dip observed in the normalized spectrum is much less clear than the wire-evaporated capillary spectra of Fig. 6.9. However, the position of the dip was found to respond to bulk RI and adsorption consistent with SPR. This is shown in Fig. 6.12c. In this experiment, various solutions were pumped through the capillary while the SPR centroid position was monitored. Exposure to solutions of different RI (water, 1.8% sucrose, 3.6% sucrose, and phosphate buffered saline (PBS), total RI range $6x10^{-3}$) caused reversible steps in the centroid location, with higher RI corresponding to a dip in reflectivity at a higher angle of incidence. Exposure to a solution containing protein (BSA 100 μg/ml in PBS) caused a irreversible positive shift in the centroid location, consistent with protein adsorption.

6.9. Conclusions

We have presented optical theory and experimental techniques which the allow SPR sensing to be implemented in glass capillaries. The simplicity of the sensor design, the natural way in which fluid handling is intrinsic to the sensor, the variety of optical sensing techniques that have been implemented in capillaries, and the desirable thermal properties of capillaries suggest that capillary SPR sensors could become an attractive alternative to conventional prism-based SPR sensors.

The optics of capillaries are much more complicated that those of a prism, and have yet to be fully understood. The wet chemical gold deposition technique necessary for practical fabrication of capillary SPR sensors has yet to be shown capable of repeatably producing gold layers of high quality. However, the fact that the

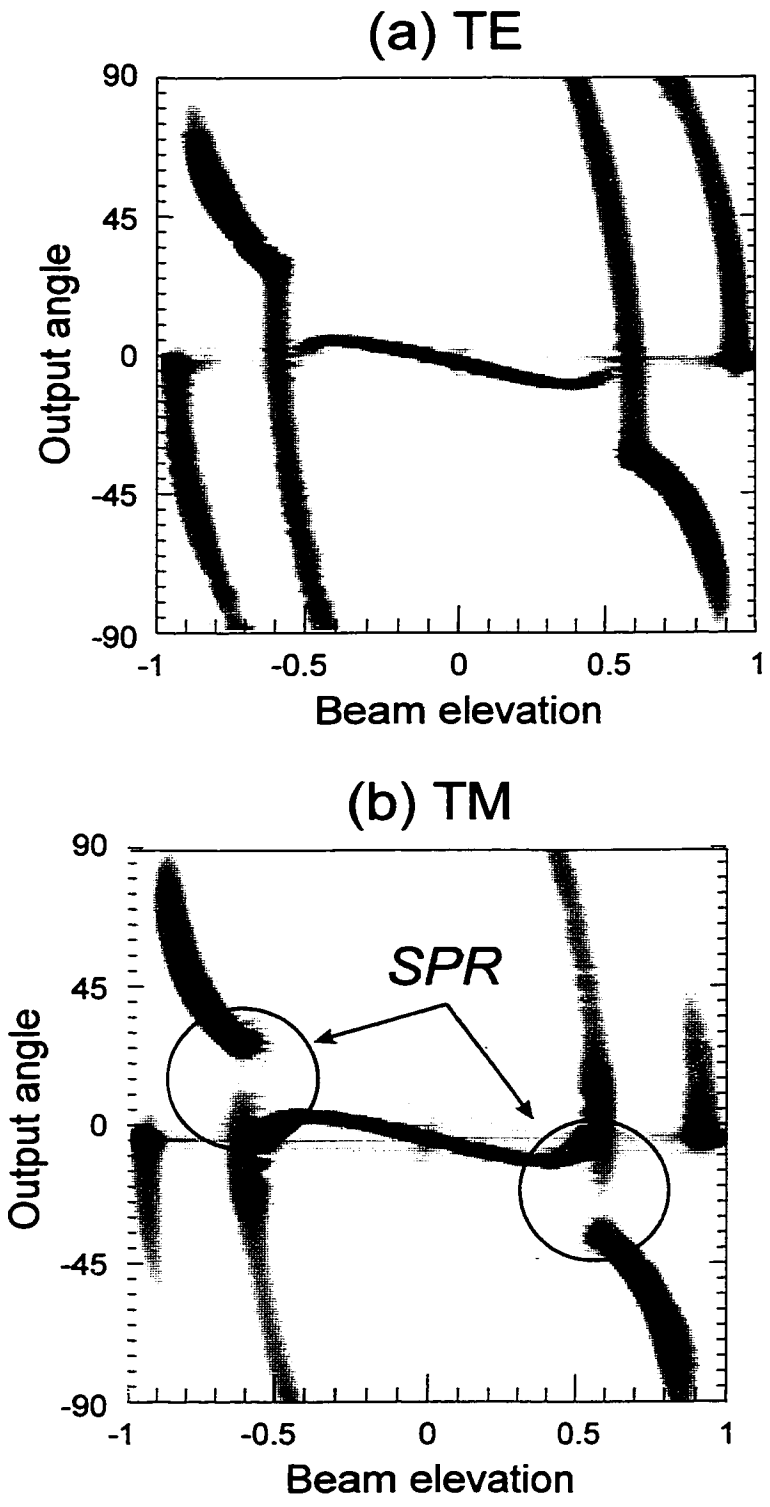

Figure 6.11. Photographic scans of water-filled, fused silica capillary coated with gold by wet chemical method. (a) TE illumination (b) TM illumination. Capillary size 150 mm OD, 375 mm ID.

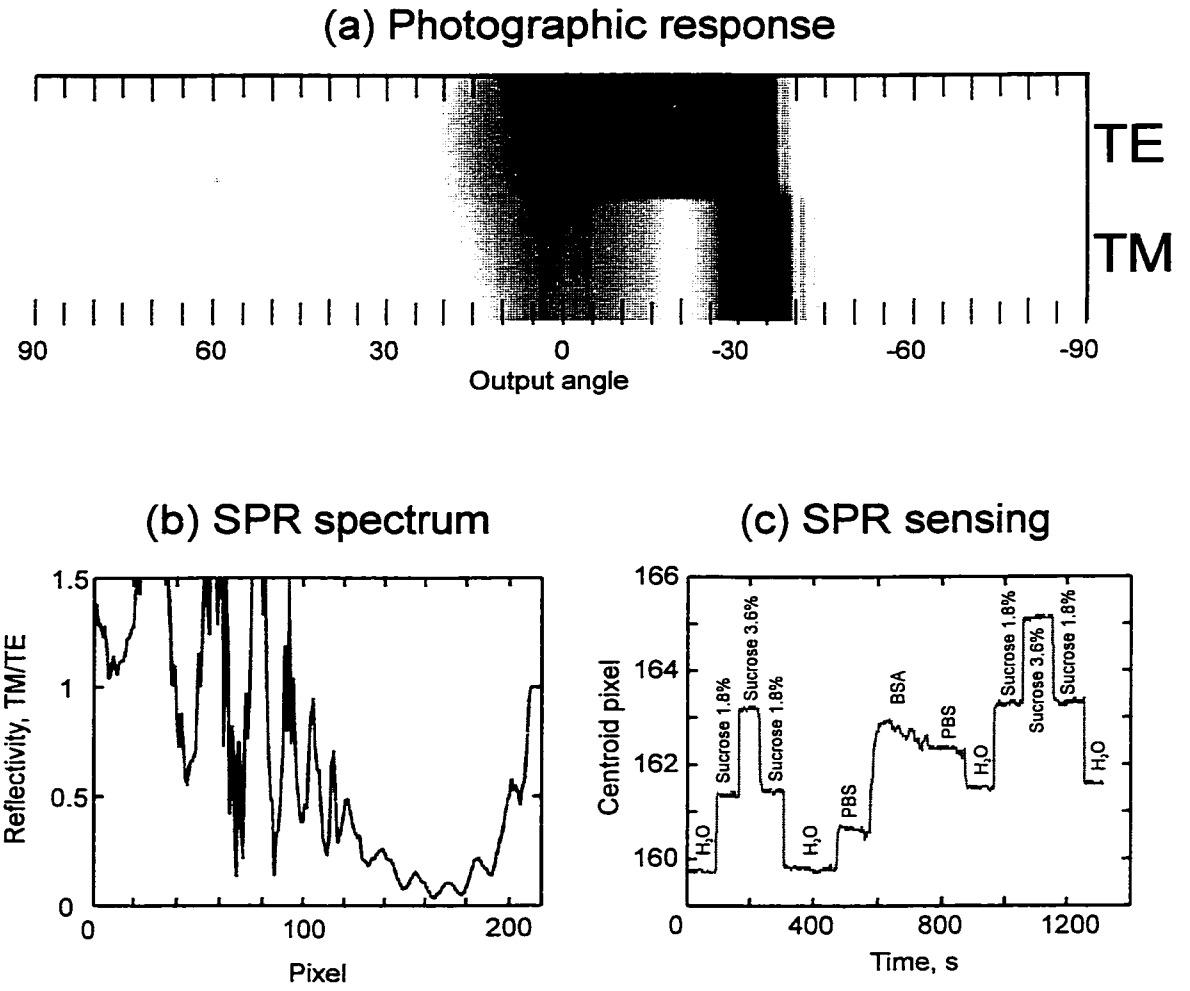

Figure 6.12. SPR spectra and sensing measured in fused silica capillary with gold layer deposited by wet chemical method. (a) TE and TM SPR spectra, recorded photographically. (b) SPR spectrum measured by photodiode array. (c) SPR sensing in capillary, showing movement of SPR centroid with bulk RI and protein adsorption.

relatively simple theory and fabrication techniques described here have allowed the construction of a functioning capillary SPR sensor is encouraging. If the interesting challenges posed by the fabrication and optics of capillaries can be mastered, capillaries may provide a powerful new platform for SPR sensing.

Notes for Chapter 6

[1] J. Stone, Optical transmission in liquid-core quartz fibers, *Appl. Phys. Lett.* **20** (1972) 239-240.

[2] G. E. Walrafen and J. Stone, Intensification of spontaneous Raman spectra by use of liquid core optical fibers, *Appl. Spect.* **26** (1972) 585-589.

[3] C. M. Stellman, F. Bucholtz, K. J. Ewing, and I. D. Aggarwal, A fiber-optic pipette for rapid long-pathlength capillary spectroscopy, *Sensors and Actuators B* **46** (1998) 56-60.

[4] S. D. Schwab and R. L. McCreery, Remote long-pathlength cell for high sensitivity Raman spectroscopy, *Appl. Spect.* **41** (1987) 126-130.

[5] O. S. Wolfbeis, Capillary waveguide sensors, *Trends in Analytical Chemistry* **15** (1996) 225-232.

[6] M. Kerker and E. Matijevic, Scattering of electromagnetic waves from concentric infinite cylinders, *J. Opt. Soc. Am.* **51** (1961) 506-508.

[7] R. Horton and W. J. Williamson, Interference patterns of a plane-polarized wave from a hollow glass fiber, *J. Opt. Soc. Am.* **63** (1973) 1204-1210.

[8] L. S. Watkins, Scattering from side-illuminated clad glass fibers for determination of fiber parameters, *J. Opt. Soc. Am.* **64** (1974).767-772.

[9] Y. Wahlbroehl and J. W. Jorgenson, On-column UV absorption detector for open tubular capillary zone electrophoresis, *J. Chrom.* **315** (1984) 135-143.

[10] D. J. Bornhop and N. J. Dovichi, Simple nanoliter refractive index detector, *Anal. Chem.* **58** (1986) 504-505.

[11] A. E. Bruno, B. Krattiger, F. Maystre, and H. M. Widmer, On-column laser-based refractive index detector for capillary electrophoresis, *Anal. Chem.* **63** (1991) 2689-2697.

[12] H. J. Tarigan, P. Neill, C. K. Kenmore, and D. J Bornhop, Capillary-scale refractive index detection by interferometric backscatter, *Analytical Chemistry* **68** (1996) 1762-1770.

[13] B. Krattiger, A. E. Bruno, H. Michael Widmer, M. Geiser, and R. Dändliker, Laser-based refractive-index detection for capillary electrophoresis: ray-tracing interference theory, *Applied Optics* **32** (1993) 956-965.

[14] K. J. Kuhn, *Laser Engineering*, Paramus: Prentice-Hall, 1997.

[15] NSF Award 0003829, *SGER: Capillary Affinity Sensors Based on Surface Plasmon Resonance*, 2000.

[16] L. A. Lyon, M. D. Musick, P. C. Smith, B. D. Reiss, D. J. Peña, and M. J Natan, Surface plasmon resonance of colloidal Au-modified gold films, *Sensors and Actuators B* **54** (1999) 118-124.

[17] T. M . Chinowsky and S. S. Yee, Capillary based SPR sensors, Invention disclosure to UW Office of Technology Transfer, 1999.

[18] T. M. Chinowsky and S. S. Yee, Surface plasmon resonance sensing in capillaries, *Electronics Letters* **35** (1999) 1659-1661.

[19] K. C. Grabar, R. G. Freeman, M. B. Hommer, and M. J. Natan, Preparation and characterization of Au colloid monolayers, *Anal. Chem.* **67** (1995) 735-743.

Chapter 7: Conclusions and future work

7.1. Research accomplishments

The research described in this dissertation has sought to improve SPR sensing technology in ways that will allow SPR to be used in a greater variety of sensing applications. We sought advances that will take SPR out of the research laboratory and allow it to be used to benefit biosensing applications such as clinical diagnostics, environmental monitoring on land on in the sea, biohazard detection, and food safety. In pursuit of this goal, we judged that the two most important aspects that a sensor must have to reach this range of applications were low cost and robustness. Accordingly, our research has focused on the design of sensors with these two characteristics.

The first sensor described in this dissertation, the SPR/IRR sensor, is a prototype of a modification to the low-cost TI SPR sensor. We discovered that a very simple modification to the sensor design allows the sensor to simultaneously measure SPR and perform IRR. The IRR measurement can be used to compensate the SPR measurement for bulk RI interference, and by doing do allow the sensor to make measurements which are largely independent of bulk RI variations due to temperature and analyte composition, and which are therefore much more robust. Because our IRR technique is inherently insensitive to adsorbed layers, it is simpler to implement and (we anticipate) more robust than the existing method of bulk RI compensation, SPR referencing, which relies on a nonadsorbing chemical layer.

We developed this new technique using a laboratory prototype which reproduced the geometry of the TI SPR sensor in a more versatile laboratory setup. Because the production TI SPR is a one-piece molded device, it is impossible to adjust or modify once it is manufactured. Because our sensor used separate components mounted on positioning stages rather than this monolithic construction, we could freely investigate each component in turn, and adjust the sensor for optimum performance. A production SPR/IRR sensor would, of course, incorporate our modifications into a molded package consistent with low cost.

Because the low-cost construction of the TI sensor leads to a device with more optical imperfections, we judged it to be important that the sensor be able to function well in spite of such flaws. For this reason, we developed data analysis and calibration techniques designed to allow the sensor to provide low-noise, well-compensated measurements under these conditions. These techniques rely upon calibration measurements measured before each experiment: The response of the sensor to an RI gradient is measured, and these measurements are used to derive the data analysis method and sensor calibration.

Because of the central role of these calibration measurements, it was important that they be quick and automatic. For this reason, we developed a simple computer-controlled method of producing RI gradients using sucrose solutions of varying concentration.

In addition to calibration, these gradients were also useful for testing of the sensor's performance. To evaluate the performance of the SPR/IRR sensor under the sorts of conditions which we felt that the sensor would experience in an actual application, we developed experimental techniques for quick and thorough evaluation of the sensor's behavior. We exposed the sensor to rapid and substantial bulk RI interference due to changes in both the composition and temperature of the analyte. Sucrose RI gradients were used to change the analyte composition, exposing the sensor to bulk RI variations over a range of $6x10^{-3}$ RI units. Rapid temperature changes induced using a flowcell heater caused bulk RI changes of $1.5x10^{-3}$, equivalent to a temperature change of 18C.

Because it is important that the sensor compensate well for bulk RI changes both with and without an adlayer present, we developed a simple method based on detergent adsorption for producing such layers. Our technique allows adsorbed layers to be quickly created and, more importantly, quickly removed, allowing experiments to be freely repeated. For this reason, we found the detergent adsorption method to be more efficient than biological binding experiments in evaluating the performance of the sensor.

We found that the SPR/IRR sensor compensates very well for bulk RI interference, eliminating over 99% of interference from bulk RI changes due to composition. This is comparable to the quality of compensation reported by users of SPR referencing on Biacore SPR instruments. The fact that our instrument exhibits performance comparable to the Biacore, which has much more sophisticated fluid handling, higher

quality optics, and much higher cost than our instrument, is very encouraging. It has recently been reported that special calibration techniques can increase the quality of the Biacore compensation to 99.9%; we anticipate that improvements in our sensor's optics and fluid handling will enable similar levels of compensation, in a much simpler and more robust sensor.

We found that our sensor eliminates 95% of interference from bulk RI changes due to analyte temperature. Because almost no previous work has been done on compensation of this type, it is difficult to compare our observations with previous work. In the one paper we have found that permits a quantitative comparison, 92% compensation for slow temperature changes due to changing room temperature was observed. We have found no previous work in which controlled variations of analyte temperature such as those used in our experiments were used to evaluate the quality of compensation; similarly, we have found no previous attempts to compensate for relatively large, rapid temperature transients such as those generated in our experiments.

To investigate the ability of the SPR/IRR sensor to function well in an uncontrolled environment, we examined its behavior as the ambient temperature was raised by 11 C. This was found to cause an offset in the instrument's response and to decrease the quality of bulk RI compensation. The modular construction of our prototype allowed us to investigate the sources of this. Small heaters and thermocouples mounted on the instrument components suspected of temperature sensitivity (the LED and detector) allowed the temperature characteristics of these components to be observed separately. Analysis of the changes in SPR/TIR spectra observed during the heating of these components revealed that the effects of instrument heating could be largely attributed to a positive shift in LED wavelength, a decrease in LED emission, and an increase in detector sensitivity. These effects were found to be consistent with behavior previously reported in the literature. Simple ways of controlling or correcting for these temperature effects are under investigation.

Our work with the SPR/IRR sensor showed that the combination of SPR with IRR enabled the construction of a more robust SPR sensor. We anticipate that a production version of this sensor could be used in a number of sensing applications which have so far been beyond the reach of SPR.

The SPR/IRR sensor combines two measurements to achieve a compensated measurement that is more robust than the SPR measurement alone. The realization that a sensor which uses combination of sensing techniques is likely to produce measurements of higher quality than a sensor which relies upon a single technique inspired the development of the second SPR sensor described in this dissertation, the capillary SPR sensor.

This sensor, based on capillary tubes internally coated with gold, has potential for facile combination with preexisting capillary- based sensing techniques such as fluorescence, as well as separation techniques such as CE and HPLC. The capillary format also has excellent fluid handling capabilities and good thermal properties. Furthermore, because the disposable capillary sensing element is very inexpensive, automated processing of many samples in the capillary format is possible.

To realize the potential of capillary SPR sensing, the optical complexities and fabrication challenges inherent in the production of such a sensor must be mastered. In pursuit of this goal, we developed modeling tools and experimental techniques for production and characterization of capillary SPR sensors.

To design and predict the response of the sensor, we developed geometrical ray-tracing models that allow the complex optical response of the capillary to be simulated and succinctly summarized. To compare the simulation results with actual capillary behavior, we constructed a capillary scanning apparatus that photographically summarizes the capillary response. We found that our models matched well with measurements produced using this apparatus.

To fabricate capillary SPR sensors, we developed two techniques for depositing gold inside of glass capillaries. The first, based on evaporation of gold from a thin tungsten wire, was limited, but sufficient to demonstrate capillary SPR sensing. The second gold deposition technique we investigated uses a recently reported wet chemical technique for deposition of high-quality gold layers. We adapted this technique for use inside capillaries, and found that it was capable of producing gold layers which exhibit SPR. Simple sensing experiments using capillaries coated with gold in this manner showed that the capillaries were usable for SPR sensing.

7.2. Future work

The SPR/IRR sensor has demonstrated the utility of IRR compensation in improving SPR measurements. Further improvement of this technique is desirable -- improved compensation will allow reduced detection limits in the presence of increased interference. Improvements may result from optimization of the flow channel to reduce composition nonuniformity. Compensation for bulk RI variations due to temperature may be improved by improving the thermal stability of the experimental apparatus.

To optimize the ability of IRR to compensate for variations in the temperature in the environment of the instrument, the effects of temperature on all instrument components must be considered. Materials with low thermal expansion coefficients and optical materials with low thermal coefficients of RI can be used to improve the thermal stability of the instrument. The temperature of sensitive components such as the LED and detector can be controlled if necessary -- these low mass components could be temperature-controlled without the expenditure of much power. Alternatively, if the temperature effects on LED and detector are highly reproducible, correction for the effects of changing LED and detector temperature could be attempted when data are analyzed.

The data analysis method used here to analyze SPR/IRR measurements uses simple algorithms to provide high quality measurements. One limitation of this method is that it is most well suited for examining small changes in RI. It may be possible to extend this technique to a piecewise linear method that would remove this restriction while retaining many of the advantages of the linear method. Further work is necessary to develop this technique and to investigate possible artifacts introduced by the construction of the piecewise linear function.

The central role of calibration in our method of data analysis allows accurate analysis of sensor data without requiring a detailed model of sensor behavior. For most effective application of calibrated linear data analysis, methods for calibration of the sensor must be further developed. Development of simple, automatic methods for creating highly linear RI gradients will improve the quality of sensor data. At the same time, improvements in data analysis procedures and instrument optical quality should be sought, in order to reduce the need for calibration.

We have found adsorption of detergent to be very convenient for creating a temporary adsorbed layer on the sensor surface in order to test the instrument's

compensation ability. To further explore the potential of this technique, its applicability to sensors employing various types of functionalized surfaces must be investigated. The compatibility of various types of detergent with these surfaces must be explored.

The capillary SPR sensor is still in its infancy. The optics of capillaries are much more complicated than those of a prism, and have yet to be fully understood. However, the fact that the relatively simple theory and fabrication techniques described here have allowed the construction of a functioning capillary SPR sensor is encouraging, and the directions in which future research must go to improve the quality of the sensor are clear. To improve the gold layers, deposition parameters must be better controlled, with flow rates and solution concentrations optimized to produce layers of the best possible surface quality and uniformity. Once uniform deposition is mastered, techniques for depositing patterned layers must be explored.

Optimization of capillary illumination is also necessary to improve the quality of capillary SPR spectra. A better understanding of how spectra vary as the beam waist and divergence of the illuminating beam are changed will allow minimization of spectral artifacts such as interference fringes, and improvement of the performance of the capillary SPR sensor.

Bibliography

F. Abeles, T. Lopez-Rios, and A. Tadjeddine, Investigation of the metal-electrolyte interface using surface plasma waves with ellipsometric detection, *Solid State Commun.* **16** (1975) 843-847.

H. Y. Aboul-Enein, R-I. Stefan, and J. F. Van Staden, Chemiluminescence-based (bio)sensors - an overview, *Crit. Rev. Anal. Chem.*, **29** (1999) 323-331.

T. Appourchaux, D. Martin, and U. Telljohann, Temperature dependence of silicon photodiode quantum efficiency: theoretical and experimental results, *Proc. SPIE* **1679** (1992) 200-211.

P. R. Bevington, *Data Reduction and Error Analysis for the Physical Sciences,* New York: McGraw-Hill, 1969.

Biacore AB, *BIACORE 2000 Instrument Handbook*, 1996.

C. B. Boring, and P. K. Dasgupta, An affordable high-performance optical absorbance detector for capillary systems, *Analytica Chimica Acta* **342** (1997) 123-132.

M. Born and E. Wolf, *Principles of optics : electromagnetic theory of propagation, interference and diffraction of light.* Cambridge: Cambridge University Press, 1999.

D. J. Bornhop and N. J. Dovichi, Simple nanoliter refractive index detector, *Anal. Chem.* **58** (1986) 504-505.

A. Bossi, S. A. Piletsky, P. G. Righetti, A. P. F. Turner, Capillary electrophoresis coupled to biosensor detection, *J. Chrom. A* **892** (2000) 143-153.

K. R. Brown, L. A. Lyon, A. P. Fox, B. D. Reiss, and M. J. Natan, Hydroxylamine seeding of colloidal Au nanoparticles. 3. Controlled formation of conductive Au films, *Chem. Mater.* **12** (2000) 314-323.

A. E. Bruno, B. Krattiger, F. Maystre, and H. M. Widmer, On-column laser-based refractive index detector for capillary electrophoresis, *Anal. Chem.* **63** (1991) 2689-2697.

J. Buttner, R. Borth, J. H. Boutwell, and P. M. G. Broughton, IFCC approved recommendations on quality control in clinical chemistry. Part 1. General principles and terminology. *Clin. Chim. Acta* **98** (1979) 129F-143F.

T. M . Chinowsky and S. S. Yee, Capillary based SPR sensors, Invention disclosure to UW Office of Technology Transfer, 1999.

T. M. Chinowsky, L. S. Jung, and S. S. Yee, Optimal linear data analysis for surface plasmon resonance biosensors, *Sens. Act. B* **54** (1999) 89-97.

T. M. Chinowsky, S. B. Saban, S. S. Yee, Experimental data from a trace metal sensor combining surface plasmon resonance with anodic stripping voltammetry, *Sens. Act. B* **35-36** (1996) 37-43.

T. M. Chinowsky, Combining surface plasmon resonance with electrochemistry: Instruments, experiments, and data analysis. M. S. E. E. Thesis, University of Washington, 1997.

T. M. Chinowsky and S. S. Yee, Quantifying the information content of surface plasmon resonance reflection spectra, *Sens. Act. B.* **51** (1998) 321-330.

T. M. Chinowsky, A. Strong, D. U. Bartholomew, S. Jorgensen-Soelberg, T. Notides, C. E. Furlong and S. S. Yee, Improving surface plasmon resonance sensor performance through combination with critical angle refractometry, *Proc. SPIE* **3857** (1999) 104-113.

T. M. Chinowsky and S. S. Yee, Surface plasmon resonance sensing in capillaries, *Electronics Letters* **35** (1999) 1659-1661.

B. A. Chrunyk, M. H. Rosner, Y. Cong, A. S. McColl, I. G. Otterness, and G. O. Daumy, Inhibiting protein-protein interactions: A model for agonist design, *Biochemistry* **39** (2000) 7092-7099.

S. Cowen, J. R. Sambles, Resolving the apparent ambiguity in determining the relative permittivity and thickness of a metal film using optical excitation of surface plasmon-polaritons, *Opt. Commun.* **79** (1990) 427-430.

E. Danelian, A. Karlen, R. Karlsson, S. Winiwarter, A. Hansson, S. Lofas, H. Lennernas, and M. D. Hamalainen, SPR biosensor studies of the direct interaction between 27 drugs and a liposome surface: correlation with fraction absorbed in humans, *J. Med. Chem.* **43** (2000) 2083-2086.

M. R. Darrach, A. Chutjian, and G. A. Plett, Trace explosives signatures from World War II unexploded undersea ordnance, *Environ. Sci. Technol.* **32** (1998) 1354-1358.

H. E. deBruijn, B. S. F. Altenburg, R. P. H. Kooyman, and J. Greve, Determination of thickness and dielectric constant of thin transparent dielectric layers using surface plasmon resonance, *Opt. Commun.* **82** (1991) 425-432.

J. A. DeFeijter, J. Benjamins, and F. A. Veer, Ellipsometry as a tool to study the adsorption behavior of synthetic and biopolymers at the air-water interface, *Biopolymers* **17** (1978) 1759-1772.

R. Ekins and P. Edwards, On the meaning of "sensitivity", *Clin. Chem.* **43** (1997) 1824-1837.

J. L. Elkind, D. I. Stimpson, A. A. Strong, D. U. Bartholomew, and J. L. Melendez, Integrated analytical sensors: the use of the TISPR-1 as a biosensor, *Sens. Act. B* **54** (1999) 182-190.

J. L. Elliott, J. Mogridge, and R. J. Collier, A quantitative study of the interactions of *bacillus anthracis* edema factor and lethal factor with activated protective antigen, *Biochemistry* **39** (2000) 6706-6713.

K. Elliott, H. Watkins, and C. S. Redwood, Altered regulatory properties of human cardiac troponin I mutants that cause hypertrophic cardiomyopathy, *J. Biol. Chem.* **275** (2000) 22069-22074.

D. G. Fink and D. Christiansen, eds., *Electronics Engineer's Handbook*, New York: McGraw-Hill, 1989.

H. A. Fishman, D. R. Greenwald, and R. N. Zare, Biosensors in chemical separations, *Annu. Rev. Biophys. Biomol. Struct.* **27** (1998) 165-198.

N. A. Friedman and D. R. Meldrum, Capillary tube resistive thermal cycling, *Anal. Chem.* **70** (1998) 2997-3002.

A. Frostell-Karlsson, A. Remaeus, H. Roos, K. Andersson, P. Borg, M. Hamalainen, and R. Karlsson, Biosensor analysis of the interaction between immobilized human serum albunin and drug compounds for prediction of human serum albumin binding levels, *J. Med. Chem.* **43** (2000) 1986-1992.

R. Gambari, G. Feriotto, C. Rutigliano, N. Bianchi, and C. Mischiati, Biospecific interaction analysis of low-molecular weight DNA-binding drugs, *J. Pharm. Experimental Therapeutics,* **294** (2000) 370-377.

C.-G. Golander and E. Kiss, Protein adsorption on functionalized and ESCA-characterized polymer films studied by ellipsometry, *J. Coll. Int. Sci.* **121** (1988) 240-253.

M. A. Gonzalez-Martinez, J. Penalva, R. Puchades, A. Maquieira, B. Ballesteros, M. P. Marco, and D. Barcelo, An immunosensor for the automatic determination of

the antifouling agent Irgarol 1051 in natural waters, *Environ. Sci. Technol.* **32** (1998) 3442-3447.

J. E. Geake, C. S. Mill, M. S. Mohammad, A linear differentiating refractometer, *Meas Sci Technol.* **5** (1994) 531-539.

K. C. Grabar, R. G. Freeman, M. B. Hommer, and M. J. Natan, Preparation and characterization of Au colloid monolayers, *Anal. Chem.* **67** (1995) 735-743.

J. H. Grassi and R. M. Georgiadis, Temperature-dependent refractive index determination from critical angle measurements: Implications for quantitative SPR, *Anal. Chem.* **71** (1999) 4392-4396.

H-M Haake, A. Schutz, and G. Gauglitz, Label-free detection of biomolecular interaction by optical sensors, *Fresenius J. Anal. Chem.* **366** (2000) 576-585.

Hamamatsu, Inc, *S4349 data sheet*, 1996.

L. Haussling, H. Ringsdorf, F.-J. Schmitt, and W. Knoll, Biotin functionalized self-assembled monolayers on gold: Surface plasmon resonance optical studies of specific recognition reactions, *Langmuir* **7** (1991) 1837-1840.

E. Hecht and A. Zajac, *Optics*, Reading: Addison-Wesley, 1979.

J. Homola, H. B. Lu, S. S. Yee, Dual-channel surface plasmon resonance sensor with spectral discrimination of sensing channels using a dielectric overlayer, *Electronics Letters* **35** (1999) 1105-1106.

R. Horton and W. J. Williamson, Interference patterns of a plane-polarized wave from a hollow glass fiber, *J. Opt. Soc. Am.* **63** (1973) 1204-1210.

O. S. Heavens, *Optical properties of thin solid films,* New York: Dover Publications, 1955.

J. Homola, S. S. Yee, and G. Gauglitz, "Surface plasmon resonance sensors: Review," *Sensors and Actuators B* **54** (1999) 3-15.

J. Homola, H. B. Lu, G. G. Nenninger, J. Dostalek, and S. S. Yee, A novel multichannel surface plasmon resonance biosensor, submitted to *Sensors and Actuators B,* 2000.

D. Ivnitski, I. Abdel-Hamid, P. Atanasov, and E. Wilkins, Biosensors for detection of pathogenic bacteria, *Biosens. Bioelectron.* **14** (1999) 599-624.

S. C. Jakeway, A. J. deMillo, and E. L. Russell, Miniaturized total analysis systems for biological analysis, *Fresenius J. Anal. Chem.* **366** (2000) 525-539.

B. Johnsson, S. Lofas, and G. Lindquist, Immobilization of proteins to a carboxymethydextran-modified gold surface for biospecific interaction analysis in surface plasmon resonance sensors, *Anal. Biochem.* **198** (1991) 268-277.

K. S. Johnston, S. S. Yee, K. S. Booksh, Calibration of surface plasmon resonance refractometers using locally weighted parametric regression, *Anal. Chem.* **69** (1997) 1844-1851.

K. S. Johnston, K. S. Booksh, T. M. Chinowsky, S. S. Yee, Performance comparison between high and low resolution spectrophotometers used in a white light surface plasmon resonance sensor, *Sens. Act. B* **54** (1999) 80-88.

K. S. Johnston, T. M. Chinowsky, and S. S. Yee, Planar substrate surface plasmon resonance probe, *Proc. SPIE* **2836** (1996) 178-185.

R. C. Jorgenson, S. S. Yee, A fiber-optic chemical sensor based on surface plasmon resonance, *Sens. Act. B* **12** (1993) 213-220.

M. J. Jory, G. W. Bradberry, P. S. Cann, and J. R. Sambles, A surface plasmon based optical sensor using acousto-optics, *Meas. Sci. Technol.* **6** (1995) 1193-1200.

L. S. Jung, C. T. Campbell, T. M. Chinowsky, M. N. Mar, and S. S. Yee, Quantitative interpretation of the response of surface plasmon resonance sensors to adsorbed films, *Langmuir* **14** (1998) 5636-5648.

Z. Junhai, C. Hong, and Y. Ruifu, DNA-based biosensors, *Biotechnology Advances* **15** (1997) 43-58.

T. Kaiser, P. Gudat, W. Stock, G. Pappert, M. Grol, D. Neumeier, and P. B. Luppa, Biotinylated steroid derivatives as ligands for biospecific interaction analysis with monoclonal antibodies using immunosensor devices, *Anal. Biochem.* **282** (2000) 173-186.

M. Kerker and E. Matijevic, Scattering of electromagnetic waves from concentric infinite cylinders, *J. Opt. Soc. Am.* **51** (1961) 506-508.

B. Krattiger, A. E. Bruno, H. Michael Widmer, M. Geiser, and R. Dändliker, Laser-based refractive-index detection for capillary electrophoresis: ray-tracing interference theory, *Applied Optics* **32** (1993) 956-965.

E. Kretchmann, Die Bestimmung optischer Konstanten von Metallen durch Anregung von Oberflachenplasmaschwingungen, *Z. Physik* **241** (1971) 313-324.

K. J. Kuhn, *Laser Engineering*, Paramus: Prentice-Hall, 1997.

L. Larsson, K. Kriz, and D. Kriz., Magnetic transducers in biosensors and bioassays, *Analusis* **27** (1999) 617-621.

C.R. Lavers, R. D. Harris, S. Hao, J. S. Wilkinson, K. O'Dwyer, M. Brust, and D. J. Schiffrin, Electrochemically -controlled waveguide-coupled surface-plasmon sensing, J. Electroanal. Chem. **387** (1995) 11-22.

T. O. Lewis, P. L. Odell, *Estimation in Linear Models*, Prentice-Hall, Englewood Cliffs, NJ, 1971.

H. Li and S. Xie, Measurement method of the refractive index of biotissue by total internal reflection, *Appl. Opt.* (1996) 1793-1795.

J. F. Liang, Y. T. Li, V. C. Yang, Biomedical application of immobilized enzymes, *J. Pharm. Sci.* **89** (2000) 979-990.

B. Liedberg, C. Nylander, and I. Lundstrom, Surface plasmon resonance for gas detection and biosensing, *Sens. Act. A* **4** (1983) 299-304.

B. Liedberg, C. Nylander, and I. Lundstrom, Biosensing with surface plasmon resonance - how it all started, *Biosens. Bioelectron.* **10** (1995) i-ix.

F. S. Ligler, G. P. Anderson, P. T. Davidson, R. J. Foch, J. T. Ives, K. D. King, G. Page, D. A. Stenger, and G. P. Whelan, Remote sensing using an airborne biosensor, *Environ. Sci. Technol.* **32** (1998) 2461-2466.

F. S. Ligler, Editorial, *Biosens. Bioelectron.* **14** (2000) 749.

R. S. Longhurst, *Geometrical and Physical Optics*, London: Longman Group, 1973.

L. A. Lyon, M. D. Musick, P. C. Smith, B. D. Reiss, D. J. Peña, and M. J Natan, Surface plasmon resonance of colloidal Au-modified gold films, *Sensors and Actuators B* **54** (1999) 118-124.

L. A. Lyon, W. D. Holliway, and M. J. Natan, An improved surface plasmon resonance imaging apparatus, *Rev. Sci. Instrum.* **70** (1999) 2076-2081.

P-O. Markgren, Markku Hamalainen, and U. Helena Danielson, Kinetic Analysis of the interaction between HIV-1 protease and inhibitors using optical biosensor technology, *Anal. Biochem.* **279** (2000) 71-78.

M. N. Mar, B. D. Ratner, and S. S. Yee, An intrinsically protein-resistant surface plasmon resonance biosensor based upon a RF-plasma-deposited thin film, *Sens. Act. B.* 54 (1999) 125-131.

F. Marandet, J. Bernard, P. Garcia, J. Deforges, and D. Magnant, Effect of self-heating on the ideal static characteristics of GaAlAs light emitting diodes, *Solid State Electron.* **32** (1989) 607-614.

J. L. Marty, B. Leca, and T. Noguer, Biosensors for the detection of pesticides, *Analusis* **26** (1998) M144-M149.

B. M. McDermott, A. H. Rux, R. J. Eisenberg, G. H. Cohen, and V. H. Racaniello, Two distinct binding affinities of poliovirus for its cellular receptor, J. Biol. Chem. **275** (2000) 23089-23096.

G. H. Meeten, Refractive index errors in the critical-angle and the Brewster-angle methods applied to absorbing and heterogenous materials, *Meas. Sci. Technol.* **8** (1997) 728-733.

J. Melendez, R. Carr, D. U. Bartholomew, K. Kukanskis, J. Elkind, S. Yee, C. Furlong, R. Woodbury, A commercial solution for surface plasmon sensing, *Sens. Act. B* **35** (1996) 1-5.

J. Melendez, R. Carr, D. U. Bartholomew, H. Taneja, S. Yee, C. Jung, C. Furlong, Development of a surface plasmon resonance sensor for commercial applications, *Sensors and Actuators-B* **38-39** (1997) 375-379.

M. Meusel, D. Trau, A. Katerkamp, F. Meier, R. Polzius, and K. Cammann, New ways in bioanalysis - one-way optical sensor chip for environmental analysis, *Sens. Act. B* **51** (1998) 249-255.

F. C. Mish, ed., *Webster's Ninth New Collegiate Dictionary,* Springfield: Merriam-Webster, 1985.

R. B. Murphy, On the meaning of precision and accuracy, *Mater. Res. Stand.* **1** (1961) 264-7.

G. Murtaza and J. M. Senior, Method for extracting thermally stable optical signals from a GaAlAs LED source, *IEEE Photon. Technol. Lett.* **7** (1995) 479-481.

D. G. Myszka, R. W. Sweet, P. Hensley, M. Brigham-Burke, P. D. Kwong, W. A. Hendrickson, R. Wyatt, J. Sodroski, and M. L. Doyle, Energetics of the HIV gp120-CD4 binding reaction, *Proc. Nat. Acad. Sci.* **97** (2000) 9026-9031.

G. G. Nenninger, J. B. Clendenning, C. E. Furlong, and S. S. Yee, "Reference-compensated biosensing using a dual-channel surface plasmon resonance sensor system based on a planar lightpipe configuration," *Sensors and Actuators B* **51**, pp. 38-45, 1998.

S. N. Nihtianov and D. P. Alipiev, Automatic compensation for the temperature coefficient of a photodiode in short circuit mode, *Sens. Act. A* **29** (1991) 117-120.

E. Nice, M. Lackmann, F. Smyth, L. Fabri, and A. W. Burgess, Synergies between micropreparative high-performance liquid chromatography and an instrumental optical biosensor, *J. Chrom. A* **660** (1994) 169-185.

P. I. Nikitin, A. A. Beloglazov, V. E. Kochergin, M. V. Valeiko, and T. I. Ksenevich, Surface plasmon resonance interferometry for biological and chemical sensing, *Sens. Act. B* **54** (1999) 43-50.

C. Nylander, B. Liedberg, and T. Lind, Gas detection by means of surface plasmon resonance, *Sens. Act.* **3** (1982/83) 79-88.

M. J. O'Brien, S. R. J. Brueck, V. H. Perez-Luna, L. M. Tender, and G. P. Lopez, SPR biosensors: simultaneously removing thermal and bulk-composition effects, *Biosensors and Bioelectronics* **14** (1999) 145-154.

C. K. O'Sullivan and G. G. Guilbault, Commercial quartz crystal microbalances - theory and applications, *Biosens. Bioelectron.* **14** (1999) 663-670.

A. Otto, Excitation of nonradiative surface plasma waves in silver by the method of frustrated total reflection, *Z. Physik* **216** (1968) 398-410.

R. G. C. Oudshoorn, R. P. H. Kooyman, and J. Greve, Refractive index and layer thickneess of an adsorbing protein as reporters of monolayer formation, *Thin Solid Films* **284-285** (1996) 836-840.

E. D. Palik, ed., *Handbook of optical constants of solids*, Orlando: Academic Press, 1991.

S. P. Parker, ed., *McGraw-Hill Encyclopedia of Physics*, New York: McGraw-Hill, 1993.

G. E Perlmann and L. G. Longsworth, The specific refractive increment of some purified proteins, J. Am. Chem. Soc. 70 (1948) 2719-2724.

B. Persson, K. Stenhag, P. Nilsson, A. Larsson, M. Uhlen, P. Nygren, Analysis of oligonucleotide probe affinities using surface plasmon resonance: A means for mutational scanning, *Anal. Biochem.* **246** (1997) 34-44.

K. A. Peterlinz and R. Georgiadis, Two-color approach for determination of thickness and dielectric constant of thin films using surface plasmon resonance spectroscopy, *Opt. Commun.* **130** (1996) 260-266.

R. P. Podgorsek, T. Sterkenburgh, J. Wolters, T. Ehrenreich, S. Nischwitz, and H. Franke, Optical gas sensing by evaluating ATR leaky mode spectra, *Sens. Act. B.* **38-39** (1997) 349-352.

S. Y. Rabbany, B. L. Donner, and F. S. Ligler, Optical Immunosensors, *Crit. Rev. Biomed. Eng.*, **22** (1994) 307-346.

H. Raether, Surface plasma oscillations and their applications, *Physics of Thin Films* **9** (1977) 145-261.

J. Raty, E. Keranen, K-E Peiponen, The complex refractive index measurement of liquids by a novel reflectometer apparatus for the UV-visible spectral range, *Meas Sci Technol.* **9** (1998) 95-99.

H. Roos, K. Magnusson and R. Karlsson, Liquid handling system demands for kinetic analysis with optical evanescent field biosensors, *Proceedings of the 8th International Conference on Solid-State Sensors and Actuators and Eurosensors IX, Stockholm, Sweden, June 25-29, 1995.*

B. R. Ruddick and T. G. L. Shirtcliffe, Data for double diffusers: physical properties of aqueous salt-sugar solutions, *Deep Sea Res.* **26A** (1979) 775-787.

U. Schobel, C. Barzen, and G. Gauglitz, Immunoanalytical techniques for pesticide monitoring based on fluorescence detection, *Fresenius J. Anal. Chem.* **366** (2000) 646-658.

S. D. Schwab and R. L. McCreery, Remote long-pathlength cell for high sensitivity Raman spectroscopy, *Appl. Spect.* **41** (1987) 126-130.

G. B. Sigal, M. Mrksich, and G. M. Whitesides, "Using surface plasmon resonance to measure the association of detergents with self-assembled monolayers of hexadecanethiolate on gold," *Langmuir* **13,** pp. 2749-2755, 1997.

S. Sjolander and C. Urbaniczky, Integrated fluid handling system for biomolecular interaction analysis, *Anal. Chem.* **63** (1991) 2338-2345.

R. Slavik, J. Homola, and J. Ctyroky, Single mode optical fiber surface plasmon resonance sensor, *Sens. Act. B.* **54** (1999) 74-79.

S. Sonezaki, S. Yagi, E. Ogawa, A. Kondo, Analysis of the interaction between monoclonal antibodies and human hemoglobin (native and cross-linked) using a surface plasmon resonance (SPR) biosensor, *J. Immunol. Meth.* **238** (2000) 99-106.

G. J. Sprokel and J. D. Swalen, Attentuated total internal reflection method, in *Handbook of Optical Constants of Solids II,* Academic Press, 1991.

R-I. Stefan, J. F. Van Staden, and H. Y. Aboul-Enein, Immunosensors in clinical analysis, Immunosensors in clinical analysis, *Fresenius J. Anal. Chem.* **366** (2000) 659-668

C. M. Stellman, F. Bucholtz, K. J. Ewing, and I. D. Aggarwal, A fiber-optic pipette for rapid long-pathlength capillary spectroscopy, *Sensors and Actuators B* **46** (1998) 56-60.

E. Stenberg, B. Persson, H. Roos, C. Urbaniczky, Quantitative determination of surface concentration of protein with surface plasmon resonance using radiolabeled proteins, *J. Coll. Int. Sci.* **143** (1991) 513-526.

J. Stone, Optical transmission in liquid-core quartz fibers, *Appl. Phys. Lett.* **20** (1972) 239-240.

A. A. Strong, D. I. Stimpson, D. U. Bartholomew, T. F. Jenkins, J. L. Elkind, Detection of trinitrotoluene (TNT) extracted from soil using a surface plasmon resonance (SPR)-based sensor platform, *Proc. SPIE* **3710** (1999) 362-372.

H. J. Tarigan, P. Neill, C. K. Kenmore, and D. J Bornhop, Capillary-scale refractive index detection by interferometric backscatter, *Analytical Chemistry* **68** (1996) 1762-1770.

Texas Instruments, Inc., *TSL1401 data sheet,* 1996.

T. Turbadar, Complete adsorption of light by thin metal films, *Proc. Phys Soc. London* **73** (1959) 40-44.

T. Vo-Dinh and B. Cullum, Biosensors and biochips: advances in biological and medical diagnostics, *Fresenius J. Anal. Chem.* **366** (2000) 540-551.

T. Vo-Dinh, J. Fetzer, and A. D. Campiglia, Monitoring and characterization of polyaromatic compounds in the environment, Talanta **47** (1998) 943-969.

Y. Wahlbroehl and J. W. Jorgenson, On-column UV absorption detector for open tubular capillary zone electrophoresis, *J. Chrom.* **315** (1984) 135-143.

G. E. Walrafen and J. Stone, Intensification of spontaneous Raman spectra by use of liquid core optical fibers, *Appl. Spect.* **26** (1972) 585-589.

L. S. Watkins, Scattering from side-illuminated clad glass fibers for determination of fiber parameters, *J. Opt. Soc. Am.* **64** (1974).767-772.

J. Wen, T. Arakawa, and J. S. Philo, Size-exclusion chromatography with on-line light-scattering, absorbance, and refractive index detectors for studying proteins and their interactions, *Anal. Biochem.* **240** (1996) 155-166.

C. Williams, Biotechnology match making: screening orphan ligands and receptors, *Curr. Opin. Biotech.* 11 (2000) 42-46.

C. Wittekindt, B. Fleckenstein, K-H. Wiesmuller, B. R. Eing, and J. E. Kuhn, Detection of human serum antibodies against type-specifically reactive peptides from the N-terminus of glycoprotein B of herpes simplex virus type 1 and type 2 by surface plasmon resonance, *J. Virol. Meth.* **87** (2000) 133-144.

C. T. Wittwer, K. M. Ririe, R. V. Andrew, D. A. David, R. A. Gundry, and U. J. Balis, The LightCycler: A microvolume multisample fluorimeter with rapid temperature control, *Biotechniques* **22** (1997) 176-181

O. S. Wolfbeis, Capillary waveguide sensors, *Trends in Analytical Chemistry* **15** (1996) 225-232.

K. A. Xavier, P. S. Eder, and T. Giordano, RNA as a drug target: methods for biophysical characterization and screening, *Trends. Biotech.* **18** (2000) 349-356.

Ryo Yamada, H. Wano, and K. Uosaki, Effect of temperature on structure of the self-assembled monolayer of decanethiol on Au(111) surface, *Langmuir* **16** (2000) 5523-5525.

C. Ziegler, Cell-based biosensors, *Fresenius J. Anal. Chem.* **366** (2000) 552-559

Appendix A: Modeling of SPR/IRR reflection spectra

The most important tools for modeling SPR sensors are the multilayer Fresnel equations [1]. These equations describe the idealized optical behavior of multilayer structures. Incident radiation is modeled as a plane wave, and each layer is modeled as a perfectly flat layer of a given thickness and refractive index. The first and last layers in the structure are assumed to be half-infinite in extent.

A complete derivation of the Fresnel equations from Maxwell's equations is given in [2]. These equations are cumbersome to manipulate symbolically but straightforward to compute numerically. All of the simulations of sensor behavior contained in this dissertations were calculated using an implementation of the Fresnel equations in the Matlab mathematical programming environment [3]. The models are used by entering a description of the multilayer structure into a Matlab data structure and then passing that structure to the function `solvefor`. To demonstrate how this is done, sample code is listed below. This code generates eight plots which model the TE and TM reflectivity of a sensor surface with and without a gold layer, as the bulk RI and the thickness of an adlayer on top of that surface are varied.

The layer structure passed to `solvefor` is an array with one multi-field element for each layer. Each element has three fields: `material`, `thickness`, and `n`. `material` is a string which names the material comprising the layer. `thickness` is the layer thickness, in nanometers. `n` is the complex RI of the layer. The first element of the layer structure describes layer 1, the incident layer -- it is half-infinite in extent and is the layer through which the incident radiation travels. In addition to the three fields possessed by every layer, layer 1 has two additional fields, `theta` and `wavelength`, which contain the incident angle of the radiation (in degrees) and the wavelength in vacuum of the incident radiation (in nanometers).

If `n` is specified directly, the same RI will be used regardless of the incident wavelength. To simulate dispersive materials, `n` is left empty and the RI is specified by `material` instead. Then, when an RI value is needed, the function whose name is contained in `material` will be called with the wavelength as an argument. The function then calculates and returns the RI at that wavelength. The functions `BK7`, `Au`, and `water` listed below implement wavelength-dependent calculations of RI for BK7 glass, gold, and water, respectively.

`solvefor` uses the multidimensional array capability of Matlab to allow the behavior of many different layers to be simulated in one function call. Any of the fields `n`, `thickness`, `theta` and `wavelength` may be vectors which extend along one dimension of a multidimensional array. (The function `vector` listed below may be used to create such a vector. For instance, `vector(2, [4 5 6])` creates a vector which extends along dimension 2 and contains the elements 4, 5, and 6.) If fields contain vectors along different dimensions, the appropriate multidimensional combination of values will be used. For example, the code listed below calculates the reflectivity of a multilayer structure simulating an SPR sensor coated with an adlayer. Layer 1 is the sensor substrate, layer 2 is the gold layer, layer 3 is the adlayer, and layer 4 is the bulk analyte. The layer structure specifies 256 incident angles, two thickness of gold, three thicknesses of adlayer, and three values of bulk RI, each varying along a different array dimension. Given this layer structure, `solvefor` will compute a 256 x 2 x 3 x 3 four-dimensional array describing the reflectivity for each combination of parameters.

If `solvefor` is called with the layer structure as its only argument, the TM reflectivity for each combination of parameters will be computed. However, `solvefor` can compute a number of properties besides TM reflectivity. The properties to calculate may specified by the second argument to `solvefor`. For example, in the code below, both TM and TE reflectivity are calculated using the function call `solvefor(layer, {'RTM', 'RTE'})`. The strings in the second argument specify which properties to calculate. The structure returned by solvefor will have two fields, `RTM` and `RTE`, containing the values of those properties. Any number of properties may be specified; a list of the properties implemented by `solvefor` is contained in the listing of that function given below.

A third argument to `solvefor`, if used, specifies which for which layers the given properties should be calculated. This capability may be used to extract electric and magnetic field parameters for each layer so that the field distribution may be plotted.

A.1. Matlab code demonstrating use of `solvefor`.

```
minang = 58;
maxang = 76
```

```
angs = linspace(minang, maxang, 256);
wavelength = 825;
metalthick = 50;
layerthicks = [0 50 100];
layern = 1.45;
bulkris = [1.33 1.355 1.38];

%-------------------------------------------------------

layer = [];

layer(1).theta = vector(1, angs);
layer(1).wavelength = wavelength;

layer(1).material = {'BK7'};
layer(1).thickness = Inf;
layer(1).n = [];

layer(2).material = {'Au'};
layer(2).thickness = vector(2, [0 metalthick]);
layer(2).n = [];

layer(3).material = {'adlayer'};
layer(3).thickness = vector(3, layerthicks);
layer(3).n = layern;

layer(4).material = {'Water'};
layer(4).thickness = Inf;
layer(4).n = vector(4, bulkris);

data = solvefor(layer, {'RTM', 'RTE'});

figure;

subplot(421);
plot(angs, squeeze(data.RTM(:,1,1,:)));
axis([58 76 0 1]);
subplot(422);
plot(angs, squeeze(data.RTE(:,1,1,:)));
axis([58 76 0 1]);
subplot(423);
plot(angs, squeeze(data.RTM(:,1,:,1)));
axis([58 76 0 1]);
subplot(424);
plot(angs, squeeze(data.RTE(:,1,:,1)));
axis([58 76 0 1]);
subplot(425);
plot(angs, squeeze(data.RTM(:,2,1,:)));
axis([58 76 0 1]);
subplot(426);
```

```
plot(angs, squeeze(data.RTE(:,2,1,:)));
axis([58 76 0 1]);
subplot(427);
plot(angs, squeeze(data.RTM(:,2,:,1)));
axis([58 76 0 1]);
subplot(428);
plot(angs, squeeze(data.RTE(:,2,:,1)));
axis([58 76 0 1]);
```

A.2. Matlab code for function `solvefor`

```
function results = solvefor(layer, wanted, whichlayers)

results = [];
if nargin<2
   wanted = { 'RTM' };
end;
if nargin<3
   whichlayers = [ 1 ];
end;

% fill out dimensions in layer structure

layer = expand(layer);

% Calculate film parameters

j = sqrt(-1);

c0 = 3e17; % nm/sec
nu0 = 120*pi; % ohms

if isempty(layer(1).n)
  nc0 = feval(char(layer(1).material), layer(1).wavelength);
else
  nc0 = layer(1).n;
end;

k0 = (2*pi) ./ layer(1).wavelength;
k02 = k0.^2;
kx = sin(layer(1).theta*(pi/180)) .* nc0 .* k0;
kx2 = kx.^2;

% loop backwards over layers

m = length(layer);

for jj = m:-1:1
```

```
fprintf(1, '%d', jj);

d = inf;

if jj == 1
  nc = nc0;
 elseif isempty(layer(jj).n)
   nc = feval(char(layer(jj).material), layer(1).wavelength);
   nc = nc - 1e-12i;
 else
   nc = layer(jj).n;
   nc = nc - 1e-12i;
 end;

 kz = sqrt(k02.*(nc.^2) - kx2);

 ATM = (nu0*kz) ./ (k0.*(nc.^2));
 ATE = - k0.*nu0./kz;

 if jj == m

   E0TM = ATM;  % normalized values for transmitted wave
   H0TM = ones(size(ATM));

   E0TE = ATE;
   H0TE = ones(size(ATE));

 elseif jj ~= 1

   d = layer(jj).thickness;
      kzd = kz.*d;

   c = cos(kz.*d);
   s = sin(kz.*d);

   E0TMt = c .* E0TM        +  j*ATM.*s.* H0TM;
   H0TM =  (j*s./ATM).* E0TM   +    c .* H0TM;
   E0TM = E0TMt;

   E0TEt = c .* E0TE           +  j*ATE.*s.* H0TE;
   H0TE =  (j*s./ATE).* E0TE   +    c .* H0TE;
   E0TE = E0TEt;

 end;

 if any(whichlayers == jj)
   for kk = 1:length(wanted)
     name = wanted{kk};
     ww = feval(name, kx, kz, E0TM, H0TM, E0TE, H0TE, ATE, ATM, d);
```

```
      results = setfield(results, {jj}, name, ww);
    end;
  end;
end;

fprintf(1, '.');

%-----------------------------------------------------------------------

% subfunctions for calculating various layer properties

function r = RTM(kx, kz, E0TM, H0TM, E0TE, H0TE, ATE, ATM, d)
% TM reflectivity
  r = (E0TM-ATM.*H0TM) ./ (E0TM+ATM.*H0TM);
  r = r.*conj(r);

function r = RTE(kx, kz, E0TM, H0TM, E0TE, H0TE, ATE, ATM, d)
% TE reflectivity
  r = ATE.*H0TE;
  r = (E0TE-r)./(E0TE+r);
  r = r.*conj(r);

function r = ZTM(kx, kz, E0TM, H0TM, E0TE, H0TE, ATE, ATM, d)
% complex TM reflection coefficient
  r = -((E0TM-ATM.*H0TM)./(E0TM+ATM.*H0TM));

function r = ZTE(kx, kz, E0TM, H0TM, E0TE, H0TE, ATE, ATM, d)
% complex TE reflection coefficient
  r = ((E0TE-ATE.*H0TE)./(E0TE+ATE.*H0TE));

function r = PSI(kx, kz, E0TM, H0TM, E0TE, H0TE, ATE, ATM, d)
% ellipsometric parameter psi
  r = (180/pi)*atan( abs(  -((E0TM-ATM.*H0TM)./(E0TM+ATM.*H0TM)) ./
...
              ((E0TE-ATE.*H0TE)./(E0TE+ATE.*H0TE)) ));

function r = DELTA(kx, kz, E0TM, H0TM, E0TE, H0TE, ATE, ATM, d)
% ellipsometric parameter delta
  r = (180/pi)*angle( -((E0TM-ATM.*H0TM)./(E0TM+ATM.*H0TM)) ./ ...
            ((E0TE-ATE.*H0TE)./(E0TE+ATE.*H0TE)) );

function r = KX(kx, kz, E0TM, H0TM, E0TE, H0TE, ATE, ATM, d)
% wavevectorin X direction
  r = kx;

function r = KZ(kx, kz, E0TM, H0TM, E0TE, H0TE, ATE, ATM, d)
% wavevector in Z direction
  r = kz;

function r = THK(kx, kz, E0TM, H0TM, E0TE, H0TE, ATE, ATM, d)
```

```
% layer thickness
  r = d;

% ------------------------------------------------------------

% TM field properties

function r = EXTMF(kx, kz, E0TM, H0TM, E0TE, H0TE, ATE, ATM, d)
% X directed electric field amplitude of forward travelling TM wave
  r = (E0TM+ATM.*H0TM)./2;

function r = EZTMF(kx, kz, E0TM, H0TM, E0TE, H0TE, ATE, ATM, d)
% Z directed electric field amplitude of forward travelling TM wave
  r = - (kx./kz).*(E0TM+ATM.*H0TM)./2;

function r = EXTMR(kx, kz, E0TM, H0TM, E0TE, H0TE, ATE, ATM, d)
% X directed magnetic field amplitude of reverse travelling TM wave
  r = (E0TM-ATM.*H0TM)./2;

function r = EZTMR(kx, kz, E0TM, H0TM, E0TE, H0TE, ATE, ATM, d)
% Z directed electric field amplitude of reverse travelling TM wave
  r = (kx./kz)*(E0TM-ATM.*H0TM)./2;

function r = HXTMF(kx, kz, E0TM, H0TM, E0TE, H0TE, ATE, ATM, d)
% X directed magnetic field amplitude of forward travelling TM wave
  r = (E0TM+ATM.*H0TM)./(2*ATM);

function r = HXTMR(kx, kz, E0TM, H0TM, E0TE, H0TE, ATE, ATM, d)
% X directed magnetic field amplitude of backward travelling TM wave
  r = -(E0TM-ATM.*H0TM)./(2*ATM);

% ------------------------------------------------------------

% TE field properties

function r = HXTEF(kx, kz, E0TM, H0TM, E0TE, H0TE, ATE, ATM, d)
% X directed magnetic field amplitude of forward travelling TE wave
  r = (E0TE+ATE.*H0TE)./(2*ATE);

function r = HZTEF(kx, kz, E0TM, H0TM, E0TE, H0TE, ATE, ATM, d)
% Z directed magnetic field amplitude of forward travelling TE wave
  r = - (kx./kz).*(E0TE+ATE.*H0TE)./(-2*ATE);

function r = HXTER(kx, kz, E0TM, H0TM, E0TE, H0TE, ATE, ATM, d)
% X directed magnetic field amplitude of reverse travelling TE wave
  r = (E0TE-ATE.*H0TE)./(-2*ATE);

function r = HZTER(kx, kz, E0TM, H0TM, E0TE, H0TE, ATE, ATM, d)
% Z directed magnetic field amplitude of reverse travelling TE wave
  r = (kx./kz)*(E0TE-ATE.*H0TE)./(-2*ATE);
```

```
function r = EXTEF(kx, kz, E0TM, H0TM, E0TE, H0TE, ATE, ATM, d)
% X directed electric field amplitude of forward travelling TE wave
  r = (E0TE+ATE.*H0TE)./2;

function r = EXTER(kx, kz, E0TM, H0TM, E0TE, H0TE, ATE, ATM, d)
% X directed electric field amplitude of backward travelling TE wave
  r = (E0TM-ATM.*H0TM)./2;

% ---------------------------------------------------------------
```

A.3. Matlab functions modeling wavelength-dependent RI of BK7 glass, gold, and water, and auxiliary function vector

```
function n = Au(w)
c = [ 5.522 - 3.154i; ...
   -2.828 - 5.537i; ...
   -3.167 + 2.166i; ...
       0.861 - 0.369i; ...
    -0.068 + 0.017i  ];
c = c .* [ 1; 1e-3 ; 1e+6; 1e+12; 1e+18 ];
n = c(1) + c(2)*w + c(3)*w.^(-2) + c(4)*w.^(-4) + c(5)*w.^(-6);


function n = BK7(w)
  c = [ 2.270567 -9.476024e-3 1.107742e-2 8.640564e-5 7.309876e-6
-1.759893e-7 ];
  w = w/1000;
  n = sqrt(c(1) + c(2)*w.^2 + c(3)*w.^-2 + c(4)*w.^-4 + c(5)*w.^-6 +
c(6)*w.^-8);


function n = water(w)
  c = [ 1.32335 3.51e-3 -5.59161e-5 ];
  w = w/1000;
  n = c(1) + c(2)*w.^-2 + c(3)*w.^-4;


function v = vector(ndim, v);

  v = v(:);
  v = shiftdim(v, 1-ndim);
```

Notes for Appendix A

[1] O. S. Heavens, *Optical properties of thin solid films,* New York: Dover Publications, 1955.

[2] T. M. Chinowsky, Combining surface plasmon resonance with electrochemistry: Instruments, experiments, and data analysis. M. S. E. E. Thesis, University of Washington, 1997.

[3] Matlab 5.2, The Mathworks, Natick, MA.

Appendix B: Modeling of protein adsorption

This appendix describes four models which have been proposed in the literature to model the optical effects of protein adsorption onto a functionalized SPR sensor surface. The purpose of these models is to predict the sensor response which is to be expected when a certain amount of protein (as measured by the surface coverage Γ, in units of ng/mm^2) is present. The four models are shown in Fig. B.1.

In the first and most simple model, the adsorbed layer forms directly on top of the gold surface, forming a uniform layer with a thickness d_a obtained from Γ by assuming a constant value for the protein density ρ (Fig. 3.1a) [1]:

$$d_a = \frac{\Gamma}{\rho} \tag{B.1}$$

Here, ρ = 1.30 g/cm^3. The RI of the layer is assumed to be known from prior measurements; here, n_a=1.57. In the second model (Fig. B.1b), the adsorbed protein layer forms on top of a functionalization layer deposited on the gold layer. This layer is modeled as a uniform layer with known RI and thickness. Here, a thiol layer is simulated with n_a=1.463 and d_a=1.5 nm.

Both of these models assume that adsorption occurs at the sensor surface, forming impermeable solid adlayers. Two different models have been proposed for a different method of functionalization, in which protein adsorption occurs within a relatively thick dextran hydrogel layer deposited on the gold surface [2]. Here the thickness of this layer is $d_{dextran}$=100 nm. The protein adsorption has been modeled both as occurring evenly throughout this layer (Fig. B.1c) (the "continuous volume" model) and as occurring in a layer that grows from the sensor surface outward (Fig. B.1d) (the "growth" model). In the growth model, the thickness of the protein layer is again calculated by Eq. B.1, but the RI of the layer is given by the sum

$$n_a = n_b + \Delta n_{protein} + \Delta n_{dextran} \tag{B.2}$$

where $\Delta n_{protein}$ is assumed proportional to ρ and $\Delta n_{dextran}$ is determined from characterization measurements. Here, $\Delta n_{protein}$=(0.18 cm^3/g) ρ, ρ=0.6 g/cm^3, and

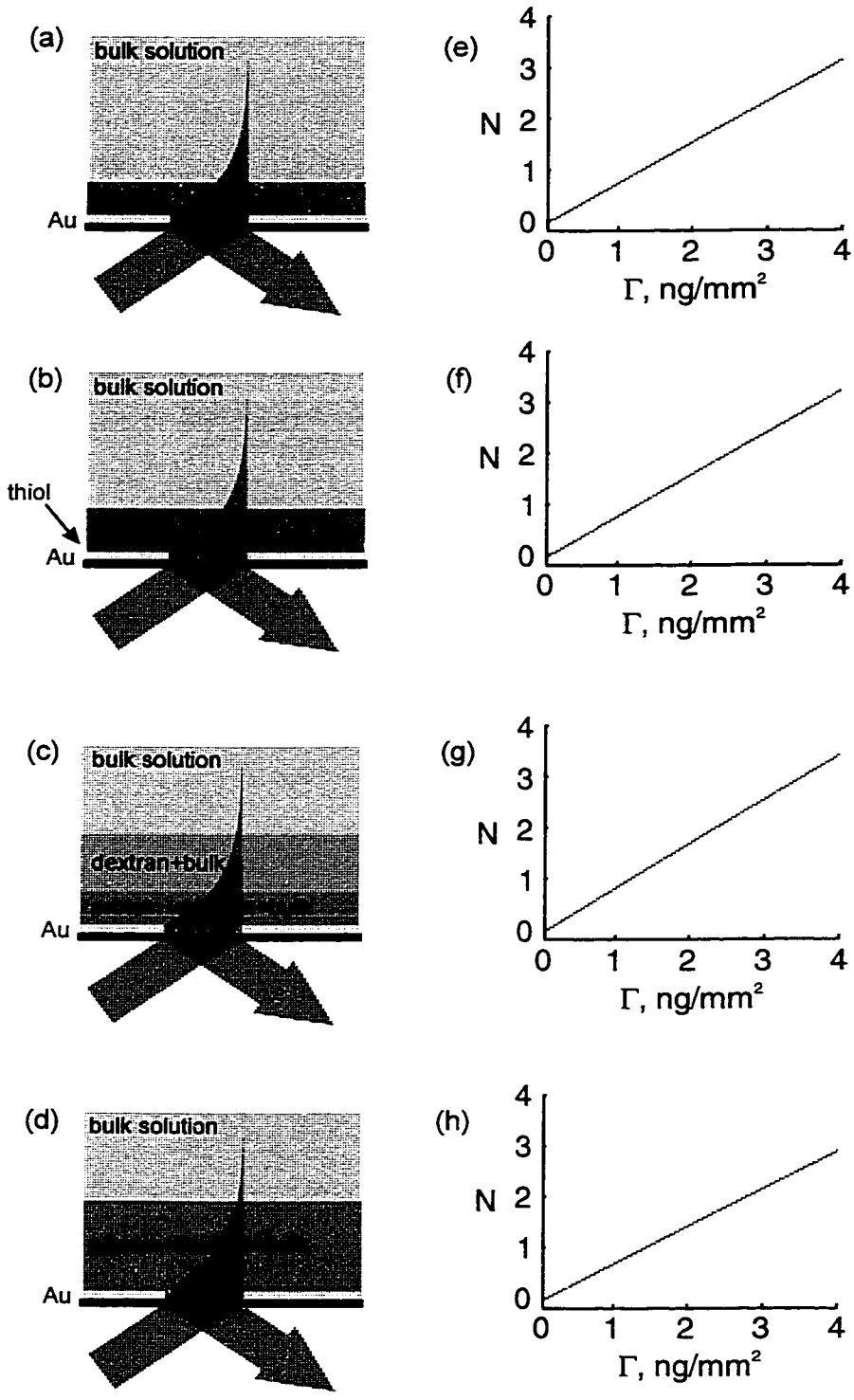

Figure B.1. Modeling of adsorption. (a) Solid film model. (b) Solid film on functionalization layer model. (c) Dextran growth model. (d) Dextran continuous volume model. (e-h) Simulated response of SPR sensors to protein adsorption, for functionalization models a-d.

$\Delta n_{dextran} = 0.00375$. If $d_a < d_{dextran}$ a layer of dextran which contains no protein is left on top of the protein layer, and is modeled to have thickness $d_d = d_{dextran} - d_a$ and RI $n_d = n_b + \Delta n_{dextran}$.

In the continuous volume model, it is assumed that protein adsorption occurs uniformly through the dextran layer, hence $d_a = d_{dextran}$. Then, by Eq. (B.1), $\rho = \Gamma / d_{dextran}$, and n_a is again calculated by Eq. B.2.

When the SPR/IRR sensor response to adsorption of a given quantity of protein is modeled in these four ways, it is seen that N is proportional to Γ in each case, but that the constant of proportionality varies somewhat (Figs. B.1e-h).

More variation is to be expected in actual measurements than in these idealized simulations. Because these models make many assumptions about the optical effects of protein adsorption, a model which accurately predicts experimental results in all circumstances is difficult to achieve. For instance, in [1], N was found to be able to determine Γ to within +/-10%. With this level of inaccuracy, the investigators were unable to establish whether the growth model or the continuous volume model is a more accurate model of protein adsorption in a dextran matrix. These measurements did show, however, that the relationship between N and Γ is linear up to much higher values of Γ than are simulated here (60 ng/mm^2).

Notes for Appendix B

[1] E. Stenberg, B. Persson, H. Roos, C. Urbaniczky, Quantitative determination of surface concentration of protein with surface plasmon resonance using radiolabeled proteins, *J. Coll. Int. Sci.* **143** (1991) 513-526.

[2] L. S. Jung, C. T. Campbell, T. M. Chinowsky, M. N. Mar, and S. S. Yee, Quantitative interpretation of the response of surface plasmon resonance sensors to adsorbed films, *Langmuir* **14** (1998) 5636-5648.

TIMOTHY MARK CHINOWSKY

EDUCATION

2000	Ph. D., Electrical Engineering, University of Washington. Dissertation title: "Optical multisensors based on surface plasmon resonance"
1997	M. S., Electrical Engineering, University of Washington. Thesis title: "Combining surface plasmon resonance with electrochemistry: Instruments, experiments, and data analysis"
1989	B. S., Electrical Engineering, and B. S., Mathematics, Massachusetts Institute of Technology.

EXPERIENCE

1995-present	Research Assistant, University of Washington Department of Electrical Engineering. Research concerns various strategies for improving surface plasmon resonance based optical chemical sensors and instrumentation. Research Advisor: Professor S. S. Yee
1990-1995	Research Engineer, University of Washington Department of Geophysics. Designed and built space physics instrumentation to be flown on high altitude balloons, sounding rockets, and satellites. Supervisor: Professor G. K. Parks

OTHER...

June, 2000	Received "Outstanding Research Assistant Award" from University of Washington Department of Electrical Engineering
May, 2000	Filed patent application, "Method for optical chemical sensing using surface plasmon resonance in capillaries," T. M. Chinowsky and S. S. Yee, co-inventors.